Investigating brittle rock failure and associated seismicity using laboratory experiments and numerical simulations

by

Qi Zhao

A thesis submitted in conformity with the requirements
for the degree of Doctor of Philosophy
Graduate Department of Civil Engineering
University of Toronto

Abstract

Investigating brittle rock failure and associated seismicity using laboratory experiments and numerical
simulations

Qi Zhao

Doctor of Philosophy

Graduate Department of Civil Engineering

University of Toronto

2017

Rock failure process is a complex phenomenon that involves elastic and plastic deformation, micro-
scopic cracking, macroscopic fracturing, and frictional slipping of fractures. Understanding this complex
behaviour has been the focus of a significant amount of research. In this work, the combined finite-
discrete element method (FDEM) was first employed to study (1) the influence of rock discontinuities on
hydraulic fracturing and associated seismicity and (2) the influence of *in-situ* stress on seismic behaviour.
Simulated seismic events were analyzed using post-processing tools including frequency-magnitude dis-
tribution (b-value), spatial fractal dimension (D-value), seismic rate, and fracture clustering. These
simulations demonstrated that at the local scale, fractures tended to propagate following the rock mass
discontinuities; while at reservoir scale, they developed in the direction parallel to the maximum *in-situ*
stress. Moreover, seismic signature (i.e., b-value, D-value, and seismic rate) can help to distinguish dif-
ferent phases of the failure process. The FDEM modelling technique and developed analysis tools were
then coupled with laboratory experiments to further investigate the different phases of the progressive
rock failure process. Firstly, a uniaxial compression experiment, monitored using a time-lapse ultrasonic
tomography method, was carried out and reproduced by the numerical model. Using this combination
of technologies, the entire deformation and failure processes were studied at macroscopic and micro-
scopic scales. The results not only illustrated the rock failure and seismic behaviours at different stress
levels, but also suggested several precursory behaviours indicating the catastrophic failure of the rock.
Secondly, rotary shear experiments were conducted using a newly developed rock physics experimental
apparatus (ERDμ-T) that was paired with X-ray micro-computed tomography (μCT). This combination
of technologies has significant advantages over conventional rotary shear experiments since it allowed
for the direct observation of how two rough surfaces interact and deform without perturbing the experi-
mental conditions. Some intriguing observations were made pertaining to key areas of the study of fault
evolution, making possible for a more comprehensive interpretation of the frictional sliding behaviour.
Lastly, a carefully calibrated FDEM model that was built based on the rotary experiment was utilized

to investigate facets that the experiment was not able to resolve, for example, the time-continuous stress condition and the seismic activity on the shear surface. The model reproduced the mechanical behaviour observed in the laboratory experiment, shedding light on the understanding of fault evolution.

Acknowledgements

Life is full of coincidences, and some of them are surprisingly nice. On my seventh year anniversary being in Canada, I passed my final Ph.D. defence, giving this long journey, from the University of Waterloo to the University of Toronto, a happy ending. This journey would not have been accomplished without the support and encouragement from many individuals, to whom I would like to express my sincerest gratitude.

First, I would like to thank my supervisor, Prof. Giovanni Grasselli, for his guidance and encouragement. His enthusiasm towards research and innovation greatly contributed to my academic achievements and personal development. The past five years of study in his group have been life-changing.

I would like to thank my co-supervisor, Prof. Nicola Tisato, who generously shared his broad knowledge and whipped me with his high standards. I owe a great deal of my academic achievements to his guidance and high expectations.

I would like to thank my former colleagues, Dr. Andrea Lisjak, Dr. Bryan Tatone, Dr. Omid K. Mahabadi, Dr. Paola Costanza Miglietta, and Dr. Scott Briggs, for their friendship and support. Special thanks to the Geomechanica folks for their remarkable work on the Irazu FDEM software that makes simulations so much more effective.

I would also like to thank my current fellow colleagues, Mr. Aly Abdelaziz, Mr. Johnson Ha, Mr. Yusheng Qiu, Dr. Wei Wei, Miss Jinghan Zhong, and Mr. Hongyuan Zhou. It has been a fun and challenging experience to be a senior member in this growing group. It was a pleasure to work with Miss Olga Kovaleva, Dr. Atena Pirayehgar, and Dr. Tai-Ming He, as colleagues and collaborators.

I also appreciate the insightful discussion, criticism, and encouragement from my Ph.D. examination committee members, for both the comprehensive exam and the thesis defences. This includes Prof. Giovanni Grasselli, Prof. Qinya Liu, Prof. Bernd Milkerite, Prof. Karl Peterson, Prof. Doug Schmitt, Prof. Nicola Tisato, and Prof. Kaiwen Xia. The quality of my research improved greatly from their generous help.

Finally, I would like to express my gratitude to my parents for their constant and unconditional support. This long journey would not have been achieved without their encouragement, and I hope I can go back home soon.

Preface

This thesis has been prepared as six separate journal articles. The original contributions by the authors are described below.

Chapter 2

    Title: Numerical simulation of hydraulic fracturing and associated microseismicity using finite-discrete element method

    Authors: Zhao, Q., Lisjak, A., Mahabadi O. K., Liu, Q., and Grasselli, G.

    Published in: *Journal of Rock Mechanics and Geotechnical Engineering*

Q. Zhao conducted the numerical simulation, analyzed results, and wrote the manuscript. A. Lisjak and O. K. Mahabadi provided the Y-Geo code and the calibrated model. O. K. Mahabadi, Q. Liu, and G. Grasselli edited the manuscript. The senior responsible author (SRA) of the publication is G. Grasselli.

Chapter 3

    Title: Influence of *in-situ* stress variations on acoustic emissions: a numerical study

    Authors: Zhao, Q., Tisato, N., Grasselli, G., Mahabadi, O. K., Lisjak, A., and Liu, Q.

    Published in: *Geophysical Journal International*

Q. Zhao conducted the numerical simulation, analyzed data, and wrote the manuscript. O. K. Mahabadi and A. Lisjak provided the calibrated model. N. Tisato, Q. Liu, and G. Grasselli contributed to the data analysis and edited the manuscript. The senior responsible author (SRA) of the publication is G. Grasselli.

Chapter 4

    Title: Understanding progressive rock failure and associated seismicity using ultrasonic tomography and numerical simulation

    Authors: He, T.-M., Zhao, Q. (corresponding author), Ha, J., Xia, K., and Grasselli, G.

    Submitted to: *Tunnelling and Underground Space Technology*

Q. Zhao conducted the numerical simulation and wrote the manuscript. T.-M., He conducted the experiment and provided the tomography results. Q. Zhao, Ha, J., Xia, K. and G. Grasselli contributed to data analysis and edited the manuscript. The senior responsible author (SRA) of the publication is G. Grasselli.

Chapter 5

Title: Rotary shear experiments under X-ray micro-computed tomography

Authors: Zhao, Q., Tisato, N., and Grasselli, G.

Published in: *Review of Scientific Instrument*

Q. Zhao calibrated the ERDμ-T apparatus, developed the experiment strategy, conducted the experiment, interpreted the data, and wrote the manuscript. N. Tisato designed the apparatus. N. Tisato and G. Grasselli edited the manuscript. The senior responsible author (SRA) of the publication is G. Grasselli.

Chapter 6

Title: Direct observation of faulting by means of rotary-shear tests under X-ray micro-computed tomography

Authors: Zhao, Q., Tisato, N., Kovaleva, O., and Grasselli, G.

To be submitted to: *Journal of Geophysical Research: Solid Earth*

Q. Zhao and N. Tisato developed the experiment strategy. Q. Zhao conducted the experiment, interpreted the data, and wrote the manuscript. O. Kovaleva carried out the segmentation and analysis of the μCT image data. N. Tisato and G. Grasselli edited the manuscript. The senior responsible author (SRA) of the publication is G. Grasselli.

Chapter 7

Title: Numerical modelling of a laboratory shear experiment using the combined finite-discrete element method (FDEM)

Authors: Zhao, Q., Abdelaziz A., Ha J., and Grasselli, G.

To be submitted to: *Computer and Geotechnics*

Q. Zhao created the numerical model, conducted the numerical simulation, data analysis, and wrote the manuscript. A. Abdelaziz provided the script to extract data from Paraview. J. Ha conducted the study of crack rupture velocity in FDEM. A. Abdelaziz, J. Ha, and G. Grasselli edited the manuscript. The senior responsible author (SRA) of the publication is G. Grasselli.

Contents

List of Tables

List of Figures

List of Symbols

A listing of the most important symbols is given in alphabetical order, first in Latin, then in Greek alphabets. Section numbers of first appearances of these symbols are given in brackets. Some symbols are used for different meanings in different chapters, but their meanings are clear within the context used.

a Intersection constant of the fitted b-value curve [2.4.2]; channel-specific scale parameter [5.3]

A Area of a BCCE with unit width [7.3.4]

A_c Real contact area [6.3.4]

A_f Fracture surface area [6.3.4]

A_i Initial surface area [6.3.4]

A_n Nominal contact area [6.3.4]

A_{nc} Non-contacting surface area [6.3.4]

A_t Total surface area [6.3.4]

b b-value [2.4.2]; channel-specific bias parameter [5.3]

c Internal cohesion [2.2]; vertical location of the centre of selected pore [6.3.3]

D_c Critical slip distance [6.4.1]

E Young's modulus [2.5]

E_e Seismic energy [2.3]; apparent normal stiffness [6.5]

E_F Friction energy loss [6.3.5]

E_G Fracture energy [6.3.5]

E_R Radiated energy [6.3.5]

E_k Kinetic energy of node [2.3]

E_s Elastic strain energy [6.3.5]

f_i Internal friction [6.2.1]

f_r	Tangential bonding stress [2.2]
f_s	Intrinsic shear strength [2.2]
f_t	Intrinsic tensile strength [2.2]
G	Shear modulus [6.3.5]
G_{Ic}	Mode I fracture energy [2.2]
G_{IIc}	Mode II fracture energy [2.2]
h	Average edge length of an element [7.2.3]
H	Hurst exponent [6.3.1]
k_s	Critical damping coefficient [7.2.3]
K_{Ic}	Mode I fracture toughness [6.2.1]
M_e	Magnitude [2.3]
M_{c}	Magnitude of completeness [2.3]
M	Torque [5.3]
N	Normal load [5.3]
P_c	Simulated confining pressure [3.1]; analogue signal of confining pressure [5.3]
P_f	Fracture penalty [7.2.3]
P_i	Analogue signal of pore fluid pressure (inlet) [5.3]
P_o	Analogue signal of pore fluid pressure (outlet) [5.3]
p_r	Seismic event rate [3.3]
R	Analogue signal of motor rotation [5.3]
S	Analogue signal of sample shortening [5.3]
T	Analogue signal of temperature [5.3]
u	Average shear displacement [5.5.1]; shear displacement [7.3.1]
v	Average shear velocity [5.5.1]
v_a	Average P-wave velocity [4.2.2]
$v_a^{\perp}$	Average P-wave velocity perpendicular to loading direction [4.2.2]
$v_a^{\parallel}$	Average P-wave velocity parallel to loading direction [4.2.2]
v_f	Crack propagation velocity [7.2.2]
v_P	P-wave velocity [7.2.3]
v_R	Rayleigh-wave velocity [7.2.2]
v_S	S-wave velocity [7.2.2]
v_T	Terminal fracture propagation velocity [7.2.2]

W_I Mechanical energy input [6.3.5]

α Channel-specific gain parameter [5.3]; viscous damping factor [7.2.3]

β Angle between the shear plane and the horizontal axis [3.4]; channel-specific offset parameter [5.3]

γ Failure mode of a cohesive crack element [7.2.2]

ΔW Released potential energy [6.3.5]

ζ Filtered tare strain gauge measurement [5.3]; source mechanism of clustered seismic event [7.2.2]

η Seismic efficiency [6.4.3]

η_c Conditioned analogue signal [5.3]

η_d Acquired digital signal [5.3]

η_f Filtered strain gauge measurement [5.3]

κ Measured physical quantity [5.3]

μ Friction coefficient [5.1]

μ_i Internal friction coefficient [2.5]

ν Poisson's ratio [2.5]

ρ Density [2.5]

σ Normal stress [5.5.1]

σ_c Uniaxial compressive strength [6.2.1]

σ_n Simulated normal stress [7.2.5]

σ_t Tensile strength [6.2.1]

τ Shear stress [5.5.1]; Simulated shear stress [7.2.5]

ϕ Internal friction angle [2.2]; porosity [6.2.1]

ϕ_a Apparent friction angle [3.5]

Ω Angular shear distance [6.3.5]

List of Acronyms

A listing of the most important acronyms is given in alphabetical order, first in Latin, then in Greek alphabets. The point of first appearance in the main text is given in brackets, which refers to a section.

AE	Acoustic emission [2.3]
ATOS	Advanced topometric sensor [6.2.2]
BCCE	Broken cohesive crack element [7.2.1]
CCE	Cohesive crack element [7.2.1]
CNC	Computer numerical control [5.4]
DEM	Discrete element method [2.2]
DFN	Discrete fracture network [2.1]
DICOM	Digital imaging and communications in medicine [5.5.2]
FDEM	Combined finite-discrete element method [2.1]
FEM	Finite element method [2.2]
FMD	Frequency-magnitude distribution [2.4.2]
FPZ	Fracture process zone [7.2.1]
GUI	Graphical user interface [5.7]
G–R law	Gutenberge-Richter law [2.4.2]
HF	Hydraulic fracturing [2.1]
ILZ	Interlocking zone [7.3.3]
KDE	Kernel density estimation [2.4.1]
LSQR	Least square [4.2.2]
MAXC	Maximum curvature method [2.4.2]
MLM	Maximum-likelihood method [2.4.2]
MS	Microseismicity [2.1]
PDF	Probability density function [2.4.1]

STL   Stereolithography [3.3]

UT   Ultrasonic tomography [4.1]

μCT   Micro-computed tomography [5.1]

Chapter 1

Introduction

1.1 Problem scope

Failure of brittle rocks involves processes including elastic and plastic deformation, microscopic cracking, macroscopic fracturing, and frictional slipping of fractures. These processes are intimately related to a number of factors, for example, rock type, fluid content, rock fabric, and stress condition (Paterson and Wong, 2005; Jaeger et al., 2007; Hudson and Harrison, 2000). In the field, the observed rock failure behaviour is a combined result of all these factors, and the role of each of them requires continued investigation to be understood.

In fractured rock masses, the macroscopic permeability is determined by the aperture and inter-connectedness of the fracture network, which is usually much larger than the permeability of the rock matrix (Jaeger et al., 2007). Therefore, the influence of rock discontinuities is of critical importance to the development of fractures (e.g., hydraulic fracturing) and associated seismicity. Understanding such an interaction is an essential aspect in optimizing hydraulic fracturing operations.

On the other hand, in order to deepen the understanding of the influence of *in-situ* stress and stress redistribution on rock failure processes, it is important to obtain a non-destructive and time-continuous observation of the rock deformation and failure. Several technologies have been utilized to achieve such a goal, for example, ultrasonic tomography and X-ray micro-computed tomography (e.g., Falls et al., 1992; Meglis et al., 2005; Desrues et al., 2006).

Moreover, understanding of the frictional behaviour has been the focus of a significant amount of research (e.g., Marone, 1998; Han et al., 2010; Reches and Lockner, 2010; Di Toro et al., 2011). Large amounts of data have been collected from these experimental studies, and constitutive laws have been

proposed to describe the dynamics of friction on earthquake faults. Although these friction laws have been successfully matching laboratory experiments and earthquake observations, they are empirical and heuristic, and lack quantitative associations with the properties and evolution of the fault (Scholz, 1998).

1.2 Approaches

1.2.1 The combined finite-discrete element method (FDEM)

Numerical simulations were carried out using the combined finite-discrete element method (FDEM) (Munjiza, 2004; Mahabadi et al., 2012a), a numerical technique that allows modelling of the material behaviour from continuum to discontinuum by explicitly simulating deformation and fracturing processes. The numerical experimentation preliminarily focused on the roles of rock discontinuities and stress conditions on rock failure and related seismicity. Simulated seismic activities were analyzed using geophysical methods including frequency-magnitude distribution (b-value), spatial fractal dimension (D-value), and fracture clustering. With the verified simulation method and analysis tools, the FDEM modelling was used to reproduce laboratory experiments and help to improve the comprehension of the experimental results.

1.2.2 ERDμ-T

X-ray micro-computed tomography (μCT), which provides a non-destructive technique to inspect the internal structure of a solid, has emerged as an important method to study geomaterials (e.g., Viggiani et al., 2004; Vanorio et al., 2011; Tisato et al., 2015; Zhao et al., 2015a). μCT discretizes the sample into three-dimensional micrometric subdomains (i.e., voxels) and obtains the X-ray attenuation coefficient of each subdomain. The attenuation coefficient is related to material thickness, density, and elemental composition. Considering the sharp density contrast between intact rock and void space (i.e., pores and fractures), μCT is ideally suited to imaging microscopic features inside rocks (Ketcham and Carlson, 2001). Therefore, a new rock physics testing system (ERDμ) that can perform experiments under μCT was designed, built and calibrated. The ERDμ system has two testing vessels: ERDμ-T for friction measurements and ERDμ-Q for seismic wave attenuation measurements (Tisato et al., 2014; Zhao et al., 2017). In this dissertation, the ERDμ-T was utilized to study the continuous evolution of a rough surface subjected to rotary shear.

1.3   Research objectives

The overall purpose of the work presented in this thesis is to use laboratory experiments and numerical simulations to study the continuous rock deformation and failure process. To achieve this goal, the following research objectives were developed:

1. Develop tools to quantitatively analyze FDEM simulated seismic activity associated with the failure process of brittle rocks.

2. Investigate the role of rock discontinuities in hydraulic fracturing and associated seismicity.

3. Investigate the influence of stress condition on rock failure processes and depict the entire deformation and failure path using laboratory experiment and numerical simulation.

4. Develop the ERDμ-T apparatus, which includes calibrating the apparatus, composing the communication and control code, and conducting a reference experiment to verify the capacity of the apparatus and suggest a routine for future tests.

5. Use the combination of ERDμ-T laboratory experiment and FDEM numerical simulation to obtain a time-continuous and non-destructive observation of fault evolution.

1.4   Thesis organization

This thesis consists of eight chapters and three appendices. Chapters 2–7 have been prepared to stand alone as separate peer-viewed journal papers. As such, each of these chapters includes an introduction, pertinent literature review, a discussion of the results, and a summary of the major conclusions. Supplementary materials associated with the manuscripts in Chapters 3, 5, and 6 were included in these chapters.

In Chapters 2 and 7, supporting materials with animated figures were provided to enhance the understanding of the corresponding chapters. These animations, embedded in the Portable Document Format (PDF) file, can be viewed using *Adobe Acrobat (Pro, Standard, or Reader) DC* under Mac or Windows operating system.

The contents of each chapter are described as follows:

- In Chapter 2, FDEM was adopted to numerically investigate the influence of bedding planes and discrete fracture network (DFN) on hydraulic fracturing (HF) and associated seismicity. Several post-processing tools, including frequency-magnitude distribution (b-value), spatial fractal dimension (D-value), and fracture clustering were utilized to interpret numerical results. Simulation

results were discussed illustrating the influence of rock mass discontinuities on the propagation of HF-induced fractures.

- In Chapter 3, FDEM models were used to study the deformation of Stanstead Granite under varying confining pressure. The seismicity associated with the deformation and failure processes (i.e., acoustic emissions) was systematically studied using fractal dimension (D-value), AE rate, and frequency-magnitude distribution (b-value). Based on these results, we suggested that the examination of seismicity should be carried out carefully, taking into consideration the deformation phase and *in-situ* stress condition.

- In Chapter 4, a laboratory experiment was coupled with ultrasonic tomography and FDEM simulation to obtain a time-lapse investigation of the progressive rock failure. The entire deformation and failure processes were studied using this combination of technologies at microscopic and macroscopic scales, and quantitative assessments of the results suggested several precursory behaviours indicating the catastrophic failure of the rock.

- Chapter 5 introduces a newly developed rotary shear apparatus (ERDμ-T) that was paired with X-ray micro-computed tomography (μCT) to inspect *in-situ* and *in-operando* deformation of the tested specimen. This technology allows for the direct observation of how two rough surfaces interact and deform without perturbing the experimental conditions. An experiment employing an aluminum alloy sample was carried out to demonstrate the capability of the apparatus.

- Chapter 6 presents, in detail, the results of an experiment conducted using ERDμ-T. Careful and quantitative analysis of the mechanical data and μCT images were carried out. Some key areas of the fault evolution and frictional behaviour were investigated, including the role of surface roughness on frictional behaviour, the shear induced fractures, and the energy budget.

- Chapter 7 used a carefully calibrated FDEM model that was built based on the experiment reported in Chapter 6 to address aspects that the experiment was not able to grasp. A new clustering algorithm was first introduced to improve the understanding of the simulated seismic activity, and then comparison and discussion on the mechanical behaviour of the shear interface and the shear induced seismicity were presented.

- Chapter 8 provides a summary of the entire thesis, outlines the major contributions and their significance. Then, some recommendations for future work are provided.

The contents of each appendix are described as follows:

- Appendix A provides the MATLAB code used for post-processing of the FDEM simulated seismic events, including b-value, D-value, and fracture clustering.

- Appendix B includes some additional notes on the calibration of the ERDμ-T apparatus.

- Lastly, Appendix C is a user manual for the graphic user interface (GUI) for the ERDμ-T apparatus. A schematic diagram of the fluid circuit system is also provided.

Chapter 2

Numerical simulation of hydraulic fracturing and associated microseismicity using FDEM

Abstract

Hydraulic fracturing (HF) technique has been extensively used for the exploitation of unconventional oil and gas reservoirs. HF enhances the connectivity of less permeable oil and gas bearing rock formations by fluid injection, which creates an interconnected fracture network and increases hydrocarbon production. Meanwhile, microseismic (MS) monitoring is one of the most effective approaches to evaluate such stimulation process. In this paper, the combined finite-discrete element method (FDEM) is adopted to numerically simulate HF and associated MS. Several post-processing tools, including frequency-magnitude distribution (b-value), spatial fractal dimension (D-value), and seismic events clustering, are utilized to interpret numerical results. A non-parametric clustering algorithm designed specifically for FDEM is used to reduce the mesh dependency and extract more realistic seismic information. Simulation results indicated that at the local scale, the HF process tends to propagate following the rock mass discontinuities, while at the reservoir scale, it tends to develop in the direction parallel to the maximum *in-situ* stress.

2.1 Introduction

The hydraulic fracturing (HF) technique has been used as a reservoir stimulation tool for more than six decades, and extensive literature has been developed on the mechanics behind the HF progress (e.g., Hubbert and Willis, 1957). However, it is the increasing demand of hydrocarbons and the exploration of unconventional reservoirs during the last two decades that spurred researchers to further develop HF techniques and to deepen the understanding of the stimulation processes.

In an HF operation, a pressurized fluid is injected through a borehole and into the target formation to overcome the overburden stress and to initiate and extend fractures into the reservoir (Jasinski et al., 1996). The fracturing fluid usually carries proppants, such as sand, glass beads, etc., which keep the fractured formation from closing under the *in-situ* stress once the injection is complete. This increases the permeability of the formation, resulting in the economical production of hydrocarbons from unconventional reservoirs. At the same time, HF operations raise environmental and safety concerns. The fluid injection could pollute groundwater (Osborn et al., 2011), and the HF process may activate natural faults, resulting in earthquake hazards (Healy et al., 1968). Therefore, it is necessary that HF operations are carefully planned and monitored.

Monitoring of fracturing processes is the key to understand, control, and optimize HF treatments. Many tools have been developed to study fracture geometry, proppant placement, and induced fracture

conductivity (Barree et al., 2002). The technique of monitoring the small-scale seismic activity induced by HF, commonly known as microseismic (MS) monitoring, is one of the very few tools that can be used to monitor the stimulation process at the reservoir scale. Examining MS activities can help track stimulation processes and reveal details of the natural discrete fracture network (DFN) (Rutledge and Phillips, 2003). Moreover, the study of HF induced seismic activities can benefit from studies concerning natural earthquakes and numerical simulations.

During the HF activity, the fracture propagation direction is controlled by the *in-situ* maximum principal stress and the local rock fabric features (Gale et al., 2007). However, conventional analysis tools typically assume the rock mass to be homogeneous, isotropic and linear elastic, and consider the HF as a bi-planar, tensile crack propagation process (Adachi et al., 2007; Dusseault, 2013). To capture the physics of discontinuous, heterogeneous, and anisotropic reservoirs, techniques based on the discrete element method (DEM) are well-suited because they inherently incorporate fabric features, such as faults and joints (e.g., Al-Busaidi et al., 2005).

In this study, a two-dimensional (2D) combined finite-discrete element method (FDEM) code developed based on Munjiza et al. (1995); Munjiza (2004); Mahabadi et al. (2012a); Lisjak et al. (2013) was used to simulate HF and associated MS activities, taking into account natural rock mass discontinuities. Also, dedicated post-processing tools were developed to analyze and interpret the simulation results.

2.2   Principles of FDEM

FDEM, pioneered by Munjiza et al. (1995), is a hybrid numerical simulation method that combines features of the finite element method (FEM) with the DEM. It inherits the advantages of FEM in describing elastic deformations, and the capabilities of DEM in capturing interactions and fracturing processes of solids (Munjiza, 2004). The progressive failure of rock material is simulated in FDEM by explicitly modelling crack initiation and propagation, employing the principles of non-linear elastic fracture mechanics (Barenblatt, 1959, 1962; Lisjak et al., 2013). Basics of FDEM and fundamental governing equations can be found in Munjiza et al. (1995); Munjiza (2004); Mahabadi et al. (2012a); Lisjak and Grasselli (2014); Lisjak et al. (2014a). In this section, only the FDEM approach to simulate HF is discussed.

A FDEM simulation uses a triangular FEM mesh to construct a model, and then the model is discretized by introducing four-node elements between each contacting triangular element pair (Mahabadi et al., 2012a). The four-node elements will be referred to as cohesive crack elements in the following discussion. Upon application of forces, the cohesive crack elements can deform elastically and break

when the slip or opening distance meet an energy based criterion.

In a 2D scenario, two fracture modes can be simulated by the cohesive crack element: mode I, the opening mode, and mode II, the shearing mode. In addition, failures involving both opening and shearing deformation components are classified as mode I-II. The fracture mode is derived from the relative displacement of the fracture edges, and the constitutive behaviours of these fracturing modes are as follows (Lisjak et al., 2013) (Figure 2.1):

(1) Mode I fracturing is simulated through a cohesive crack model similar to that originally proposed by Hillerborg et al. (1976). When the opening between two triangular elements reaches a critical value (O_p), which is related to intrinsic tensile strength (f_t), the normal bonding stress is gradually reduced until a residual opening value is reached (O_r).

(2) Mode II fracturing is simulated by a slip weakening model which resembles the model of Ida (1972). The critical slip (S_p) corresponds to the intrinsic shear strength (f_s) that is calculated according to the Mohr-Coulomb criterion:

$$f_s = c + \sigma_n \tan \phi, \tag{2.1}$$

where c is the internal cohesion, ϕ is the internal friction angle, and σ_n is the normal stress acting across the fracture surface. As the slip approaches S_r, the tangential bonding stress is gradually reduced to the residual value $f_r = \sigma_n \tan \phi$.

(3) Mode I-II (i.e., mixed mode) fracturing is defined by a coupling criterion between crack opening and slip. This mode describes a combination of shear and tensile deformation, and the failure criterion is defined by:

$$\left(\frac{O - O_p}{O_r - O_p} \right)^2 + \left(\frac{S - S_p}{S_r - S_p} \right)^2 \geq 1, \tag{2.2}$$

where O is opening distance and S is slip.

When simulating the HF induced fracturing process, a pressurized fluid exerts the driving force to propagate a fracture (Figure 2.2) (Lisjak et al., 2014b). Moreover, natural rock mass discontinuities can be incorporated into FDEM models (Lisjak et al., 2014b). For example, bedding planes can be implemented as weak interfaces, and pre-existing fractures can be simulated without introducing cohesive crack elements for triangular element pairs on both sides of the fracture.

2.3 FDEM simulated seismic events

FDEM has the ability to simulate laboratory scale acoustic emissions (AE) and field scale MS activities (Lisjak et al., 2013, 2014a; Zhao et al., 2015b). When the cohesive crack element breaks, the strain energy
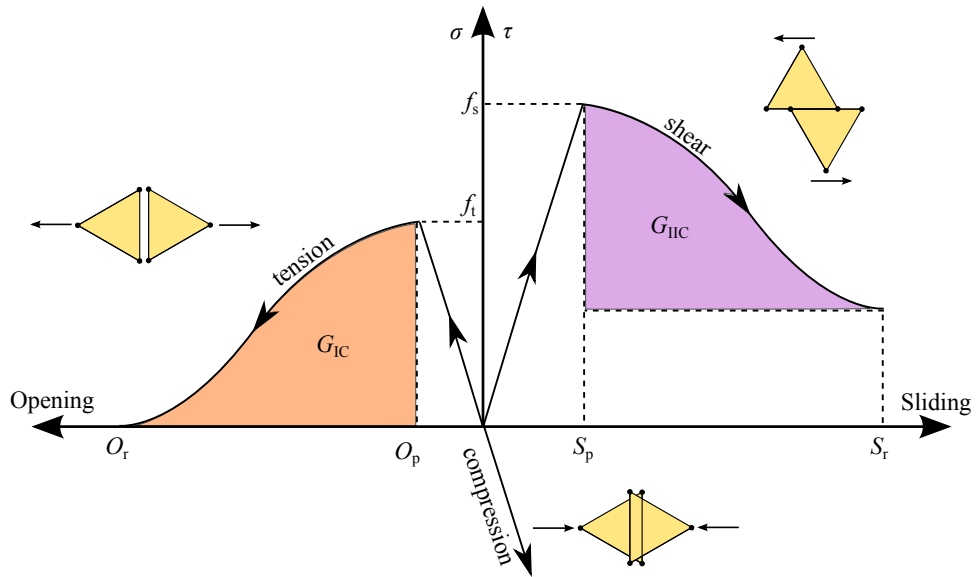
Figure 2.1: Fracture models governing the behaviour of cohesive crack elements. G_{Ic} and G_{IIc} represent the amount of energy per unit of fracture surface that mode I and mode II fractures consume during the deformation of crack elements, respectively.
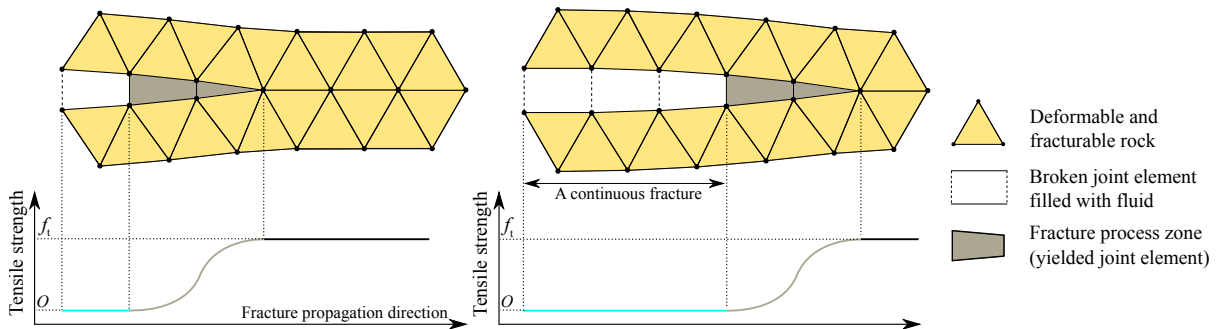
Figure 2.2: Schematic diagram of an HF induced tensile fracture propagating towards east. The continuous fracture consists of multiple broken cohesive crack elements, and these elements should be grouped together as one seismic event.

stored during the deformation is released, and the associated kinetic energy release can be captured. This energy is assessed by monitoring the relative displacement of crack surfaces and recording the kinetic energy of nodes in proximity of propagating fractures. The breakage of each cohesive crack element is assumed to be an AE/MS event, and for each event, important source parameters are numerically calculated, including initiation time, source location, fracture mode, and seismic energy.

The initial time of an event is assumed to be the time at which the cohesive crack element breaks, and its location coincides with the geometric centre of the cohesive crack element. The fracture mode is determined by the relative displacement of both sides of the fracture, as described in Section 2.2. Moreover, the associated seismic energy (E_e) is represented by the kinetic energy at the initiation time ($E_{k,f}$) calculated by the following algorithm (Lisjak et al., 2013):

$$E_{k,f} = \frac{1}{2} \sum_{i=1}^{4} m_i v_{i,f}^2,$$
(2.3)

where $i = 1$, 2, 3 and 4 represents the four nodes of a cohesive crack element, m_i and $v_{i,f}$ are the nodal mass and nodal velocity at the time of the cohesive crack element failure, respectively. Moreover, the seismic energy can be converted into magnitude (M_e) using the relation proposed by Gutenberg (1956):

$$M_e = \frac{2}{3} \left(\log E_e - 4.8 \right).$$
(2.4)

2.4 Post processing tools

Seismic processes have stochastic self-similarities in space and magnitude domains, which manifest themselves as power laws through the spatial fractal dimension (D-value) and the frequency-magnitude relation (b-value), respectively (Gutenberg and Richter, 1944; Hirata et al., 1987). A clustering algorithm is firstly introduced to overcome the limitations of FDEM (Section 2.4.1); then b-value and D-value analysis tools are utilized to interpret clustered FDEM simulation results.

2.4.1 Clustering

FDEM simulated MS, as described in the previous section, is recorded based on the assumption that each broken cohesive crack element represents a single event (Lisjak et al., 2013). This assumption is valid when simulating laboratory scale problems in which the mesh size is analogous to the mineral grain size; however, it limits the applicability of MS simulations in large scale problems where the mesh size hardly possesses any physical meaning. For example, in a HF simulation, instead of considering each

broken cohesive crack element as a single event, grouping them into one seismic event better resembles the propagating nature of the fracture (Figure 2.2).

To overcome this limitation, a clustering algorithm is introduced as a post-processing tool to ease the mesh dependency by combining broken cohesive crack elements that are close both spatially and temporally into equivalent events. Unlike typical clustering methods, the FDEM based clustering algorithm consists of two steps: (1) spatial clustering that involves the detection of continuous fractures, and (2) temporal clustering dividing continuous fractures into sub-fractures when specific criteria are met.

FDEM simulated MS events are first organized according to their spatial distribution. The geometry of a continuous fracture can be constructed by identifying and connecting cohesive crack elements that belong to this fracture. The spatial clustering helps establish the geometry of the fracture network generated by HF. A continuous fracture may contain multiple stages of fracturing, due to, for instance, asperities or stress drops. Different stages of fracture propagation should be divided into separate MS events. Therefore, for broken cohesive crack elements in continuous fractures, a non-parametric Gaussian kernel density estimation (KDE) method is used for temporal clustering (Botev et al., 2010).

Density estimation is an important tool for the statistical analysis of data, and the KDE is one of the best developed density estimation methods (Botev et al., 2010). The adaptive Gaussian KDE method, based on a linear diffusion process, reduces some well-known biases of KDE and has the ability to conduct a non-parametric bandwidth selection.

Given P independent observations $\chi_P \equiv X_1, ..., X_P$ from an unknown continuous probability density function (PDF) on $\mathbb{Z}$, the Gaussian KDE is defined as:

$$\hat{f}(x;t) = \frac{1}{P} \sum_{i=1}^{P} \phi(x, X_i; t) \quad (x \in \mathbb{R}), \tag{2.5}$$

where ϕ is the Gaussian kernel of x at location X_i with t being the bandwidth parameter bandwidth$= \sqrt{t}$, and it is expressed as:

$$\phi(x, X_i; t) = \frac{1}{\sqrt{2\pi t}} e^{-(x-X_i)^2/(2t)}. \tag{2.6}$$

Equation 2.5 offers a unique solution to the diffusion partial differential equation (PDE), i.e.,

$$\frac{\partial}{\partial t} \hat{f}(x;t) = \frac{1}{2} \frac{\partial^2}{\partial x^2} \hat{f}(x;t) \quad (x \in \mathbb{Z}, t > 0), \tag{2.7}$$

with $\mathbb{Z} \equiv \mathbb{R}$ and initial condition of:

$$\left.\begin{aligned} \hat{f}(x;0) &= \Delta x \\ \Delta x &= 1/P \sum_{i=1}^{P} \delta(x - X_i) \end{aligned}\right\}, \tag{2.8}$$

where Δx gives the empirical density of the data χ_P, and $\delta(x - X_i)$ is the Dirac measure at X_i. Botev et al. (2010) interpreted Equation 2.5 as the Green's function of Equation 2.7; thus, $\hat{f}(x;t)$ can be represented by the solution of Equation 2.7 up to time t.

There are several advantages of such interpretation over the traditional Equation 2.5. Firstly, it can be used to construct a density estimator for a domain with unknown density distribution; secondly, it has a smooth density estimation at the boundary; moreover, a completely data-driven bandwidth selection is available for such density estimator (Botev et al., 2010).

In practice, the KDE first evenly discretizes the domain (i.e., time duration of the continuous fracture) into L (e.g., $L = 2^{14}$ by default) grids, and this discretization is smoothed using the computed optimal bandwidth ($\sqrt{t^*}$), then the PDF of each grid is estimated. The resulting cumulative density of the entire domain, which is the equivalent of the area covered by the PDF, is unitary (Botev et al., 2010). The bandwidth defines the resolution (h) of the clustering; meaning that, with larger bandwidth, the events temporally more separated will be clustered together. Although the applied clustering method is non-parametric by default, it can be toggled to use specific bandwidth to satisfy certain interpretation purposes. For example, when a specific resolution is required, h can be controlled by modifying L. Knowing the initial time (t_1) and ending time (t_2) of a continuous fracture, one can use the calculated grid number (L_c) to achieve such resolution:

$$L_c = \frac{t_2 - t_1}{h}. \tag{2.9}$$

Temporally adjacent broken cohesive crack elements in a continuous fracture with temporal spacing $\Delta t < h$ will be included into one cluster.

Local minima of the PDF are used as dividing points, and each cluster of broken cohesive crack elements is considered to be an equivalent seismic event. Source parameters of such event are calculated using the following routine: (1) Time of the equivalent event is the time when the first cohesive crack element fails at t_1, as mentioned above. (2) Its location is where the energy release starts (i.e., coordinates of the first cohesive crack element), which gives an analogy to the hypocenter of a natural earthquake. (3) The source mechanism of this event is the weighted average of mechanisms of all broken cracks in

this fracture, based on the kinetic energy they release. (4) The energy release is calculated as the total kinetic energy of all cohesive crack elements in the cluster.

From a fracture propagation point of view, HF-induced fracture propagates when the intrinsic strength of the rock has been overcome. Once the fracturing process proceeds, the fracture volume increases, and the fluid pressure will decrease accordingly, causing fracture propagation to halt. On the other hand, HF operations are usually conducted in stages, and fluid pressure varies during different stages. The two-step clustering algorithm introduced herein (1) helps understand the geometric and temporal distribution of HF-induced fractures and (2) illustrate how these fractures respond to the variation of geological background and injection procedure. Further analysis will be discussed based on clustered results.

2.4.2   b-value

The Gutenberge–Richter law (G–R law) states that the frequency-magnitude distribution (FMD) of seismic activities in a given volume can be approximated by a simple power-law (Gutenberg and Richter, 1944):

$$\log_{10} N \left(> M \right) = a - bM \tag{2.10}$$

where N(>M) refers to the number of seismic events with magnitude larger than M, and a and b are constants.

The G–R law has been extensively used for describing HF-induced MS (Utsu, 1999; Grob and van der Baan, 2011). In this linear expression, b-value is given by the slope of the FMD curve which is usually around 1. The b-value has been considered an important parameter that characterizes the seismicity of a region.

The maximum-likelihood method (MLM) provides the most appropriate way to estimate the b-value (Aki, 1965; Woessner and Wiemer, 2005):

$$b = \frac{\log_{10} e}{\overline{M} - \left[M_{\mathrm{c}} - \frac{\Delta M_{\mathrm{bin}}}{2} \right]}, \tag{2.11}$$

where e is Euler's number; M_{c} is the magnitude of completeness, which is defined as the lowest magnitude at which all the events in a space–time volume are detected (Woessner and Wiemer, 2005); $\overline{M}$ is the arithmetic average magnitude for $M > M_{\mathrm{c}}$; and ΔM_{bin} is the binning width of the catalogue. MLM is essentially controlled by the smallest events and is less affected by events at the large-magnitude-end which may not fit the G–R law (Amitrano, 2012).

The choice of M_c, beyond which AE events should be excluded in the b-value estimation, directly impacts the evaluation of the b-value, and in turn influences the estimation of the overall seismicity rate (Mignan and Woessner, 2012). In order to provide a robust b-value estimation, we estimate M_c by employing the maximum curvature method (MAXC) (Wiemer and Wyss, 2000). In this method, M_c represents the point in the magnitude domain where the seismic event population is most concentrated. Moreover, binning width in this work is chosen to be 0.1 (i.e., ΔM_{bin}) so that the estimation is not biased due to large bin size (Bender, 1983).

MAXC was criticized for underestimating M_c, especially for gradually curved FMD that does not fit the G–R law (Rydelek and Sacks, 1989; Woessner and Wiemer, 2005). However, we use it for consistency and comparison between different simulations.

2.4.3 D-value

The correlation integral, $C(r)$, is used to quantitatively study the spatial distribution pattern of seismic events (Hirata et al., 1987):

$$C(r) = \frac{2}{N(N-1)} N_r (R < r), \tag{2.12}$$

where $N_r (R < r)$ is the number of seismic source pairs separated by a distance smaller than r, and N is the total number of events. If the source distribution has a fractal structure, then we have:

$$C(r) \propto r^D, \tag{2.13}$$

where D is the fractal dimension of the distribution, which is linear in a log-log scale.

In a 2D situation, $D = 2$ indicates complete randomness in the source location distribution, and lower values suggest the presence of clustering. Note that D-value does not carry any information about the shape of the spatial distribution, and the fractal analysis must be accompanied with a visual inspection of the actual source pattern.

2.5 Numerical simulation examples

Three HF simulation examples are demonstrated in this section. In Section 2.5.1, the first example demonstrates the clustering algorithm and the KDE. In Sections 2.5.2 and 2.5.3, the influences of bedding planes and natural fractures (i.e., DFN) to the HF treatments are studied. Geotechnical parameters of the rock mass and cohesive crack elements used for these examples are the same (Table 2.1). In addition

to b- and D-values, other aspects of interest to engineers and geophysicists that can be calculated by FDEM are also shown in these examples, for instance, magnitude of principal stresses and seismic wave radiation.

Table 2.1: Geotechnical properties of the rock mass and cohesive crack elements.

Property (unit)	Value
Density, ρ (kg·m^{-3})	2500
Young's modulus, E (GPa)	20
Poisson's ratio, ν (-)	0.18
Internal friction coefficient, μ_i (-)	0.6
Internal cohesion, c (MPa)	20
Intrinsic tensile strength, f_t (MPa)	3
Mode I fracture energy, G_{Ic} (J·m^{-2})	100
Mode II fracture energy, G_{IIc} (J·m^{-2})	150

2.5.1 Example 1: demonstration of the clustering algorithm

A small-scale numerical model with a simple geological setting was used in this example. Significant geotechnical properties used for the rock mass and cohesive crack elements are listed in Table 2.1. This example is an ideal case to illustrate the clustering algorithm (Figure 2.3) and the ability of FDEM to capture stress wave radiation (Figure 2.4a).

To simulate the constant flow rate used in HF operation more realistically, the installation of a stiff casing (i.e., steel and cement) was explicitly simulated. In this example, the borehole was perforated towards the east and the model setup is illustrated in Figure 2.4b. Moreover, the *in-situ* stresses in the vertical and horizontal directions were assumed to be equal (i.e., $\sigma_v = \sigma_h = 25$ MPa).

The clustering algorithm successfully identified and connected broken cohesive crack elements that belong to the east-propagating fracture, and then the non-parametric KDE divided them into three segments (i.e., events I, II, and III) according to their temporal distribution (Figure 2.3). After each cluster of events, extra fracture volume created by HF caused a pressure drop, and the fracture propagation halted until the fluid pressure accumulated high enough to fracture the rock again.

The propagation speed of each event can be estimated by dividing the total length of the fracture by the propagation duration of the fracture (i.e., $t_2 - t_1$). The first fracture segment, between 2.8 ms and 3.8 ms, propagated at a velocity of 870 m/s, and the second segment propagated at a velocity of 630 m/s between 4.4 ms and 5.1 ms. The last segment of the fracture consists of only one broken cohesive crack element, thus no propagation speed was calculated. Moreover, Figure 2.4a shows the seismic wave radiated from the propagating fracture corresponding to the second segment. The seismic energy radiated from the crack tip is clearly captured by the model, including its variation due to the
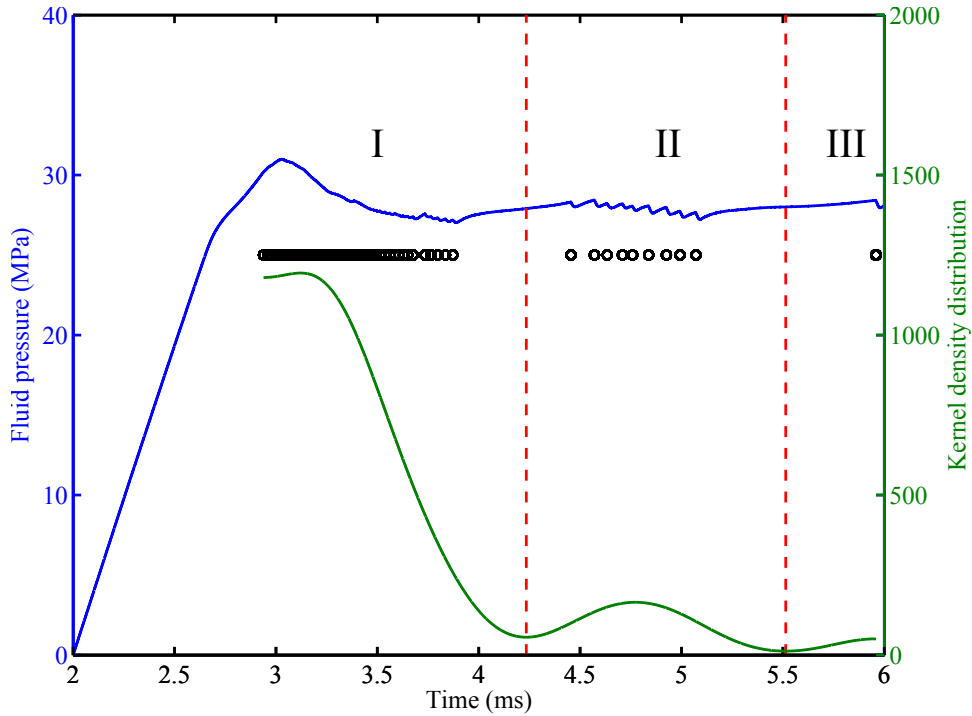
Figure 2.3: Demonstration of the clustering algorithm and non-parametric KDE. The fluid pressure (blue) and density estimation (green) of broken cohesive crack elements are plotted versus time. A total number of 72 broken cohesive crack elements are clustered into three equivalent events, and the dividing points are local minima of the density estimation (red dashed line).

fractured surface.

2.5.2 Example 2: influence of bedding planes

In this example, the *in-situ* stress condition was assumed to be $\sigma_v = 65$ and $\sigma_h = 50$ MPa, which corresponds to a completion depth of about 2.5 km with a stress ratio $K_0 = \sigma_h/\sigma_v = 0.77$. Horizontal bedding planes were implemented in the model and the borehole was perforated in six directions. The dominant propagation direction of the fracture was controlled by the *in-situ* stresses, particularly the maximum principal stress direction. However, it was clearly demonstrated that bedding planes add complexity to the fracture pattern (Figure 2.5). Fractures penetrated into bedding planes adjacent to the main fracture and generated MS events. The importance of natural rock mass fabrics to HF was clearly highlighted by FDEM simulation. Moreover, MS observed in this model resulted in $b = 1.20$ (Figure 2.6) and $D = 0.47$.
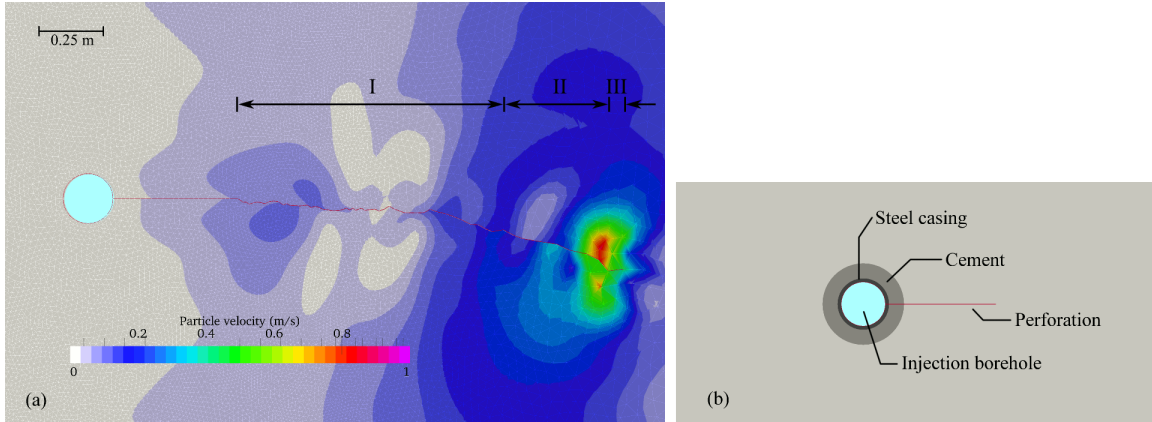
Figure 2.4: The east-propagating fracture induced by HF and associated wave radiation. (a) The seismic wave radiated by the second segment of the propagating fracture, and (b) casing and perforation of the borehole. Red line represents the free surface created by the perforation shot and fracturing.

2.5.3 Example 3: influence of DFN

The third model was used to investigate HF in a horizontal well placed within a naturally fractured formation. The same *in-situ* stress condition as Example 2 was used. A simplified DFN, consisting of two fracture sets inclined at ±45° to the directions of the principal stresses, was embedded into the model (Figure 2.7a). The strength parameters of these natural fractures were chosen such that they were partially open under the given *in-situ* stresses.

The simulated fracturing pattern shows the crucial role of the pre-existing rock mass discontinuities. The emergent fracturing process consisted of a combination of breakage through the intact rock (Figure 2.7b) and shearing along the pre-existing discontinuities (i.e., DFN) (Figure 2.7c). At the local scale, the fluid pressure induced fracture tended to follow the DFN, while at the global scale it tended to align with the maximum *in-situ* stress. These results are in agreement with the conceptual model proposed by Dusseault (2013).

The reactivation of DFN generated low magnitude events that were distinguished from the HF-induced MS, and were thus analyzed separately. HF-induced MS reported a b-value of 0.61 (Figure 2.8), and the reactivation of natural fractures resulted in a b-value of 1.59 (Figure 2.9). We speculate that the significant departure between magnitude ranges of HF-induced MS and reactivation of natural fractures, as well as their b-values, may be useful indicators for interpreting field data and depicting the structure of the DFN in the field.

In the case of the spatial distribution of MS, events located on the main HF-induced fracture had a D-value of 0.27, which was lower than that reported in Section 2.5.2. From the visual inspection of the fracture pattern depicted in Figures 2.5 and 2.8, one can interpret that there are fewer branches in
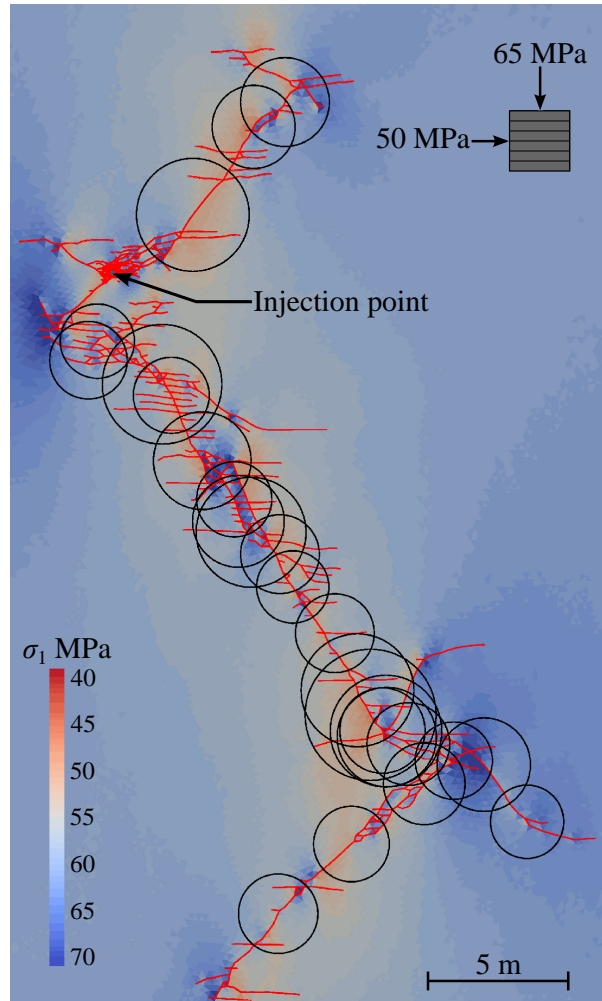
Figure 2.5: Simulated HF-induced fracture network and its interaction with the bedding planes. Seismic events occurring during the HF are shown as circles, with their sizes proportional to their energy and centers corresponding to the location of events. While the magnitude ranges from -7 to -1, only events with magnitude larger than -1.5 are plotted. Background of the figure is the magnitude of the maximum principal stress (σ_1).
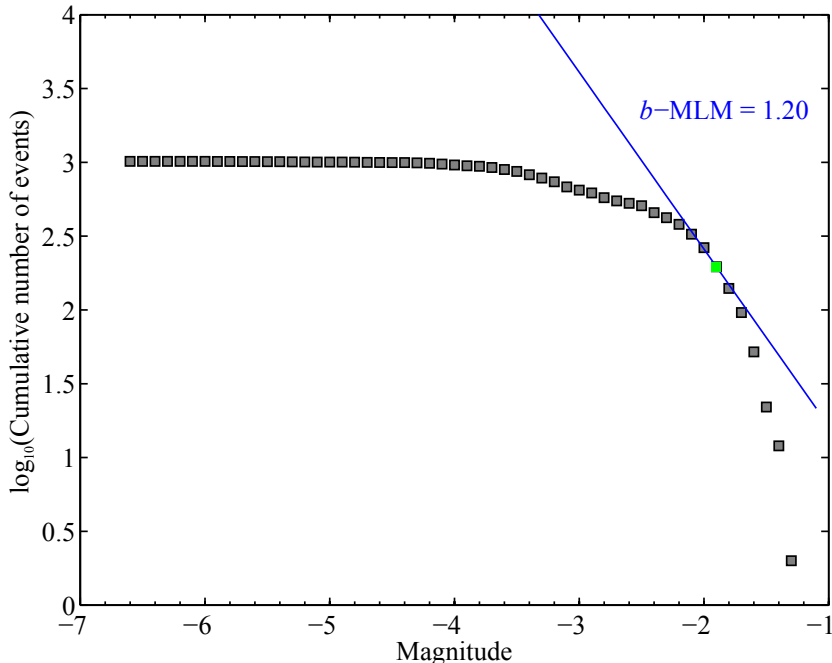
Figure 2.6: FMD of MS of the example in Section 2.5.2 ($\Delta M_{\text{bin}} = 0.1$) and the estimated b-values by MLM (blue). Green square denotes M_{c}, the b-value estimation does not perform well due to the gradually curved FMD.

the model with DFN, and the events are more concentrated, resulting in a lower D-value. If the MS events from the activation of pre-existing fractures are taken into account, the D-value increases to 1.69, indicating a higher order of randomness of the spatial distribution of MS due to the presence of the DFN.

2.6   Conclusions

Numerical simulation can be used as an additional tool to solve geophysical and geotechnical engineering problems. The FDEM introduced in this paper can simulate the mechanical behaviour of the reservoir under HF operations and associated seismic activities. Moreover, it can simulate the underground environment more realistically by considering natural rock mass discontinuities, compared to continuum methods.

A non-parametric clustering algorithm was developed to ease the mesh dependency of FDEM-simulated events, resulting in more realistic MS predictions. The b- and D-values were carefully assessed based on the geological background of the model. The FDEM of HF simulation appears to be promising for its unique ability in obtaining geomechanical and geophysical insights into HF under realistic rock mass conditions. Moreover, FDEM demonstrated a potential for forward modelling of MS, owing to its
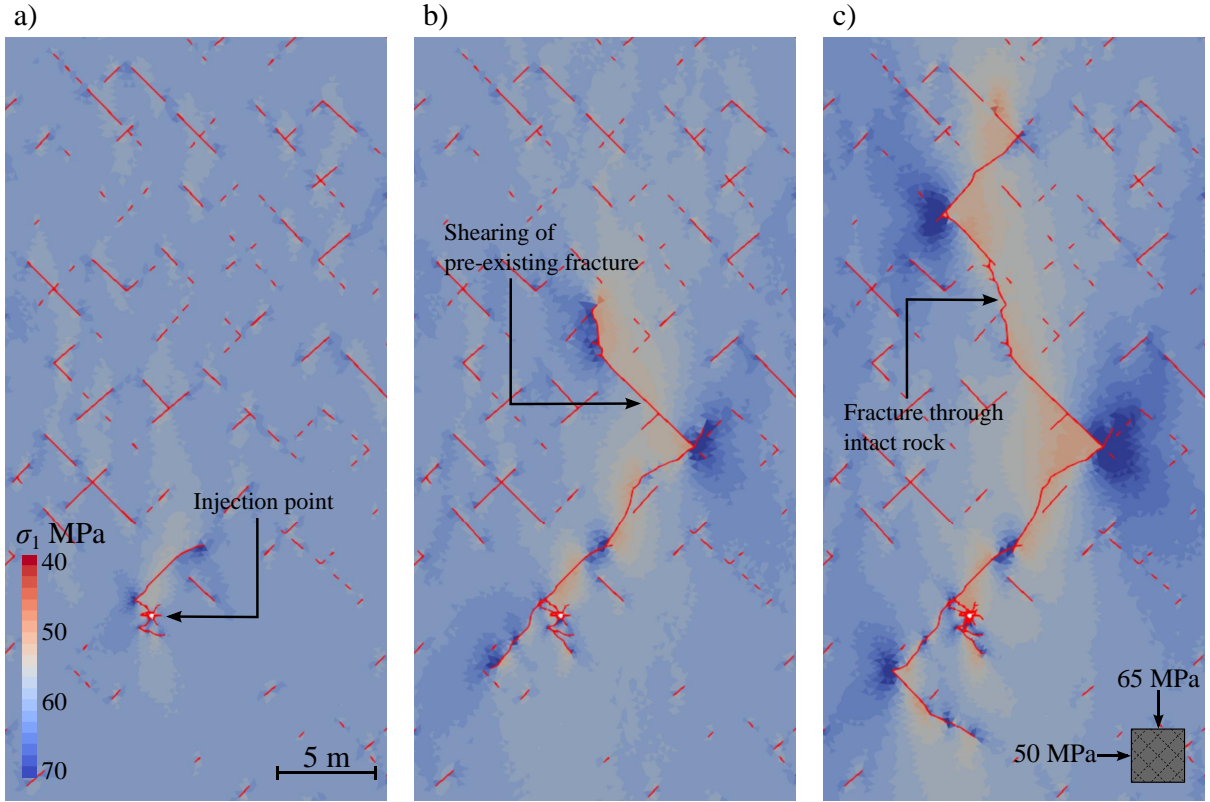
Figure 2.7: The evolution of the fracture during the HF treatment with DFN. The variation of the maximum principal stress, σ_1, is shown accordingly. Note the stress concentration at pre-existing fractures.
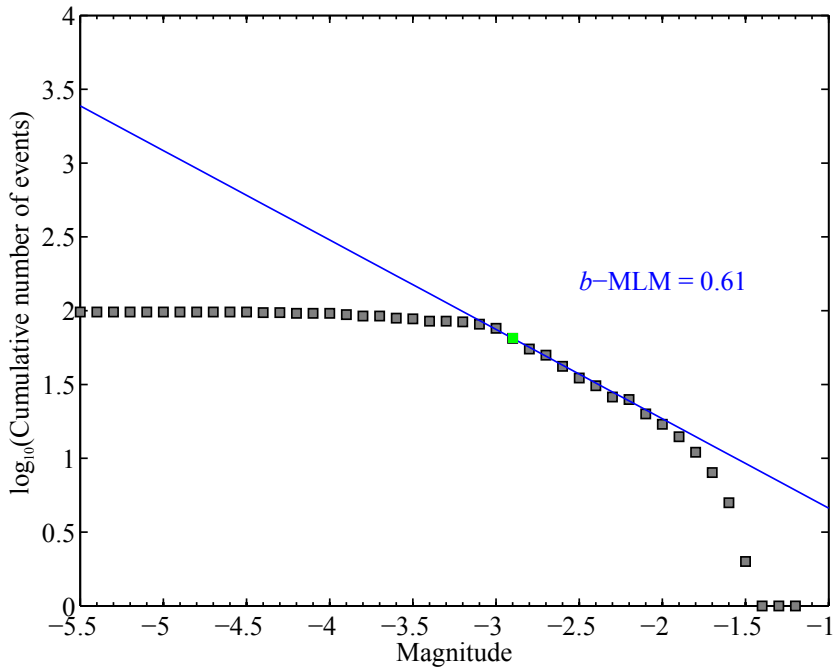
Figure 2.8: FMD of MS events along the main fracture of the example in Section 2.5.3 ($\Delta M_{\mathrm{bin}} = 0.1$) and the estimated b-values by MLM (blue). Green square denotes M_c.
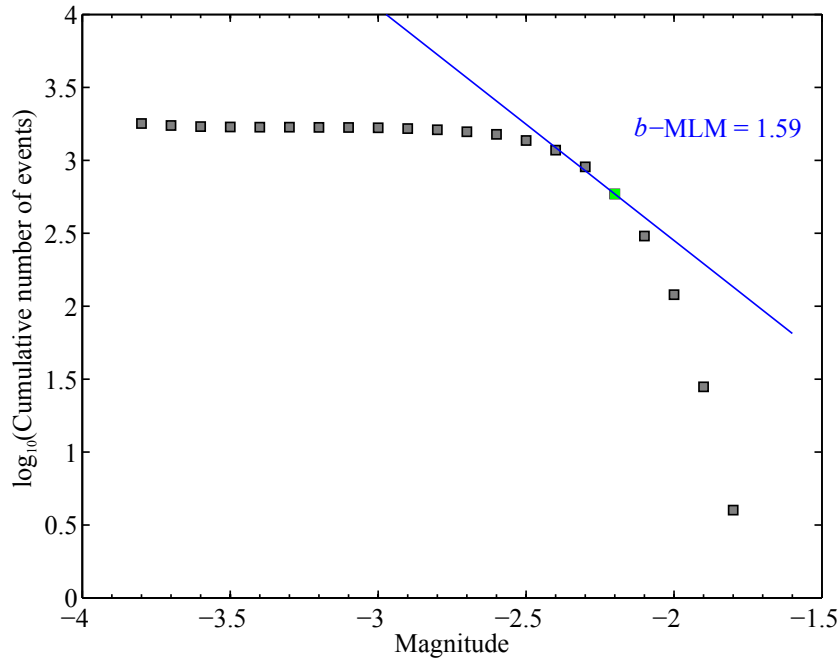
Figure 2.9: FMD of MS from reactivation of natural fractures of the example in Section 2.5.3 ($\Delta M_{\text{bin}} = 0.1$) and the estimated b-values by MLM (blue). Green square indicates M_{c}. Note the low estimation quality due to the gradually curved FMD.

inherent ability to generate synthetic seismic events from a geomechanical aspect, which may provide valuable insights for interpreting MS data observed in field.

Supporting material[*]

Figure 2.10: Animated view of the simulated hydraulic fracturing process and the influence of bedding planes, as presented in Figure 2.5. Fractures are represented by red lines.

---

[*]Animations can be viewed using *Adobe Acrobat (Pro, Standard, or Reader) DC* under Mac or Windows operating system.

Figure 2.11: Animated view of the simulated hydraulic fracturing process and the influence of pre-existing joint sets, as presented in Figure 2.7. Fractures are represented by red lines.

Chapter 3

Influence of *in-situ* stress variations on acoustic emissions: a numerical study

Summary

The study of acoustic emissions (AEs) is of paramount importance to understand rock deformation processes. AE recorded during laboratory experiments mimics, in a controlled geometry and environment, natural and induced seismicity. However, these experiments are destructive, time consuming, and require a significant amount of resources. Lately, significant progress has been made in numerical simulations of rock failure processes, providing detailed insights into AE. We utilized the two-dimensional (2D) combined finite-discrete element method (FDEM) to simulate the deformation of Stanstead Granite under varying confining pressure (P_c), and we demonstrated that the increase of P_c (i) shifts failures from tensile towards shear dominated, and (ii) enhances the macroscopic ductility. We quantitatively describe the AE activity associated with the fracturing process by assessing the spatial fractal dimension (D-value), the temporal distribution (AE rate), and the slope of the frequency-magnitude distribution (FMD) (b-value). Based on the evaluation of D-value and AE rate, we defined two distinct deformation phases, Phase I and II. The influence of P_c on the spatial distribution of AE varies according to the deformation phase: for increasing P_c, D-value decreases and increases during Phase I and II, respectively. In addition, b-value decreases with increasing P_c during the entire experiment. Our numerical results show for the first time that variations of D- and b-value as a function of *in-situ* stress can be simulated using the finite-discrete element approach. We demonstrate that the examination of seismicity should be carried out carefully, taking into consideration the deformation phase and *in-situ* stress conditions.

3.1 Introduction

Understanding how confining pressure (P_c) influences the damage and failure processes in rocks is valuable for many disciplines, including mining activities, hydrocarbon explorations, volcanic, and earthquake studies (Lockner, 1993; Hardy, 2003; Goebel et al., 2012). These anthropogenic activities and natural processes are difficult to monitor in situ; however, they can be studied by quantifying the induced and natural seismicity and assessing the associated seismic energy release.

Acoustic emissions (AEs) are elastic vibrations generated by fracture nucleation and propagation, which are broadly utilized to investigate rock damage and failure in laboratory tests (Lockner, 1993). As fracturing processes at laboratory and crustal scale are found to obey similar statistics, a primary purpose of AE studies is to characterize damage patterns, which provide important clues when studying larger phenomena, such as earthquakes (Hanks, 1992; Lockner, 1993).

AE generated in laboratory tests mimic, at a smaller scale and controlled environment, the seismicity

occurring in the Earth's crust. Laboratory experiments are essential for the study of fracturing processes in rocks; however, they are destructive, time consuming, and require significant resources. In comparison, numerical methods, which are capable of simulating crack nucleation and propagation, can provide detailed insights into AE activities and can be effectively used to understand the influence of each parameter (e.g., Hazzard and Young, 2000; Lisjak et al., 2013).

In this study, we utilized the two-dimensional (2D) combined finite-discrete element method (FDEM) to simulate AE generated by fracturing processes in Stanstead Granite under varying P_c. FDEM has the ability to explicitly capture the entire loading and failure path and the associated seismic activity (Mahabadi et al., 2012a; Lisjak et al., 2013; Zhao et al., 2014). The use of a 2D plane stress approach to reproduce triaxial tests is limited with respect to laboratory studies as it disregards the three-dimensional (3D) character of the tests. However, it has the merit of reducing the computational demand, and it has been verified to provide insights into the failure processes of rocks and associated AE (Lisjak et al., 2013). In addition, the adopted 2D methodology using a micromechanical brittle failure model is able to recreate realistic emergent rock failure behaviours (Mahabadi et al., 2012b, 2014).

In the following sections, we will first outline the simulation procedures of FDEM and our model setup, and then explain the various parameters used for AE analysis. We located the first peak point of each stress-strain curve and divided the test into pre- and post-peak stages. We then quantitatively examined the failure mechanisms, the spatial fractal dimension (D-value), the temporal distribution (AE rate), and the slope of the frequency-magnitude distribution (FMD) (b-value) of pre- and post-peak AE.

Our simulations demonstrate that high P_c promotes shear failure and suppresses tensile failure. Meanwhile under the same P_c, pre-peak AE have a higher order of spatial randomness than post-peak AE, while post-peak AE release more energy and are spatially and temporally more concentrated than pre-peak AE. According to the spatial and temporal distributions of AE, we defined two distinguished phases of deformation (Phase I and II). These results are consistent with the literature, and for the first time we show that a numerical simulation approach, based on FDEM, can accurately capture the D- and b-value variations under varying P_c.

3.2   Model setup and simulation procedure in FDEM

The numerical experiments simulated confined triaxial tests performed on a 2D model that consisted of a 54 mm × 108 mm longitudinal section, representing the rock sample (Supporting Information, Figure 3.6). The model was discretized using an unstructured triangular finite-element mesh (i.e., Delaunay triangulation) with an average element size of 0.8 mm. The model reproduces a Stanstead

Granite specimen whose mineral grains were represented by elastic triangular elements connected to each other by four-node cohesive crack elements, representing grain boundaries (Munjiza, 2004; Mahabadi et al., 2012a). These cohesive crack elements can deform elastically and break when the slip or the opening distance exceeds assigned energy-based thresholds (Zhao et al., 2014). This modelling approach enables FDEM to capture the elastic deformation of different solids, together with crack propagation and corresponding particle motions (Munjiza, 2004; Mahabadi et al., 2012a). In FDEM simulations, the breakage of cohesive crack elements can occur in tensile mode (mode I), shear mode (mode II), or a combination of the two (i.e., mixed mode, mode I-II).

Properties of the Stanstead Granite were assigned to the model and the spatial heterogeneity of mineral phases was stochastically generated based on a discrete Poisson distribution of the rock mineral composition (Mahabadi, 2012). Stanstead Granite properties were chosen according to Mahabadi (2012) and Lisjak et al. (2013) (Table 3.1). Mineral interfaces between biotite and other minerals are mechanically weak and their fracture energies (i.e., intergranular fracture energy) were assigned to be lower than those between feldspar and quartz. Detailed model calibration procedure and laboratory compression test results can be found in Mahabadi (2012).

Two rigid loading platens located at both ends of the rock specimen were used to load the sample at a constant velocity of 0.25 m/s, which corresponds to a strain rate of 2.31. The imposed loading speed, although significantly higher than those used in laboratory experiments, has been verified to ensure a quasi-static loading condition while allowing the simulations to run in a reasonable time (Mahabadi, 2012). Confining pressure was applied to both left and right sides of the sample throughout the simulations. AE events were recorded using the approach developed by Lisjak et al. (2013), and their magnitudes were calculated based on the release of energy at the breakage of grain boundaries. Two software packages, Y-GUI and Y-Geo, were used to build the model and run the FDEM simulations, respectively (Mahabadi et al., 2010, 2012a).

3.3 AE analysis methods

During the deformation of brittle rocks, AE are released by localized inelastic deformations, such as microcracking and grain boundary slip. In FDEM, the energy associated with these processes can be directly measured by monitoring the deformation of the cohesive crack elements allowing, for each AE event, the source location, failure mode, event time, and magnitude to be recorded.

We systematically studied the stochastic self-similarities of AE in space, time, and magnitude domains using the spatial fractal dimension (D-value), AE rate, and frequency-magnitude relation (b-value),

Table 3.1: Rock properties used in the FDEM simulations for Stanstead Granite, after Mavko et al. (1998); Mahabadi (2012).

Parameter (unit)	Quartz	Biotite	Feldspar
Volume fraction (%)	21	8	71
Density, ρ (kg/m^3)	2600	2800	2600
Young's modulus, E (GPa)	83.1	17.2	56.4
Poisson's ratio[1], ν (-)	0.26	0.30	0.45
Internal friction angle, ϕ (°)	51.8	51.8	51.8
Internal cohesion, c (MPa)	24.2	24.2	24.2
Tensile strength, f_t (MPa)	11.4	4.2	5.5
Mode I fracture energy, G_{Ic} (J/m^2)	907	599	310
Mode II fracture energy, G_{IIc} (J/m^2)	1814	1198	620

[1] ν of elements representing minerals in the numerical model was obtained through an iterative calibration process so that the emergent mechanical behaviour of the model resembled the laboratory test.

respectively (Gutenberg and Richter, 1944; Hirata, 1987; Hirata et al., 1987; Lockner, 1993). Due to the difference between simulated and real time, AE rate was investigated on a relative base.

FMD for natural seismicity is essential for earthquake source studies, and is usually described by the Gutenberg-Richter (G–R) law (Gutenberg and Richter, 1944):

$$\log_{10}(N) = a - bM, \tag{3.1}$$

where N is the cumulative number of seismic events with magnitude larger than M, and a and b (i.e., b-value) are constants. Spatial and temporal variations of the b-value provide important information regarding the earthquake source region. Wyss (1973) suggested that the b-value reflects the stress conditions in the crust and varies with depth. He indicated that b-value for the shallowest part of the crust is significantly higher than that for the lower part of the crust. This hypothesis was also verified by field studies (e.g., Wyss, 1973; Gerstenberger et al., 2001)

However, the estimation of b-value can be controversial because the transition from the horizontal to the inclined portion of the FMD is often concealed. This transition point is termed as the magnitude of completeness (M_{c}), and AE events with magnitude smaller than M_{c} should be disregarded from the b-value estimation. Therefore, the choice of M_{c} has a direct impact on the evaluation of the b-value, which in turn influences the estimation of the overall seismicity rate (Mignan and Woessner, 2012). In order to provide a robust b-value estimation, we determine the M_{c} using the maximum curvature method (Wiemer and Wyss, 2000), and we employ the maximum likelihood method (MLM) to estimate

the b-value (Aki, 1965; Bender, 1983):

$$b = \frac{\log_{10}(e)}{\overline{M} - \left(M_c - \frac{\Delta M}{2}\right)}, \tag{3.2}$$

where $\overline{M}$ is the mean magnitude of the catalogue used for b-value estimation, and ΔM is the linear incremental magnitude bin width. The FMD is represented by a histogram of the number of AE within each magnitude bin.

In this study, we adopted the bootstrap approach to obtain the standard error (SE) in b-value estimations (Efron and Tibshirani, 1986; Amorese et al., 2010), which was applied using the following procedure:

(1) a bootstrap sample was generated based on the FDEM simulated FMD catalogue;

(2) b-value for this bootstrap sample (b^{BT}) was calculated using MLM (Equation 3.2);

(3) step 1 and 2 were repeated B times, where B was the number of bootstrap sampling replications. In this work, we chose $B = 1000$ to provide a robust SE estimation (Efron and Tibshirani, 1986); and

(4) SE of b-value was then calculated by the standard deviation of b^{BT} values:

$$\text{SE} = \sqrt{\frac{1}{B-1} \sum_{i=1}^{B} \left(b_i^{\text{BT}} - \bar{b}_i^{\text{BT}}\right)^2}. \tag{3.3}$$

On the other hand, we employed the two-point correlation integral to evaluate the spatial distribution pattern of AE (Hirata et al., 1987):

$$C(r) = \frac{2N_r(R < r)}{N(N-1)}, \tag{3.4}$$

where $N_r(R < r)$ is the number of hypocentre pairs separated by distances shorter than r, and N is the total number of AE. If the hypocentre distribution has a self-similar structure, $C(r)$ is proportional to r^D, where D is the D-value.

Moreover, we utilize the relative AE rate (p_r) to analyze the temporal distribution of pre- and post-peak AE:

$$p_r = \frac{N_t}{tp_{max}}, \tag{3.5}$$

where N_t is the AE event number recorded during the time period t, and p_{max} is the highest observed AE rate.
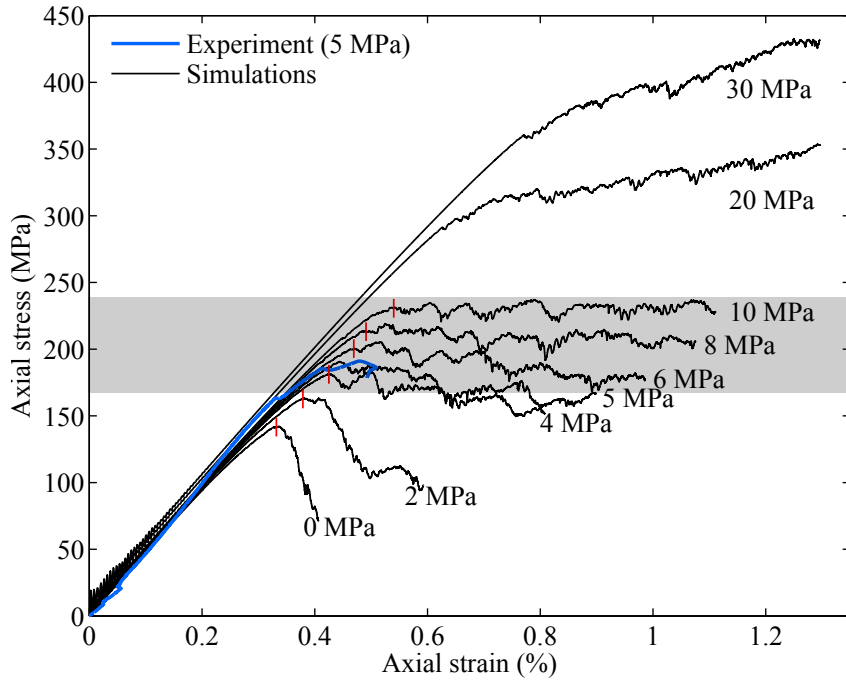
Figure 3.1: Stress-strain curves of compression tests of simulations with P_c ranging from 0 to 30 MPa and laboratory experiments with P_c=5 MPa (see Supporting Information Figure 3.7 for the complete comparison of stress-strain behaviour between laboratory tests and numerical results). Between 4 and 10 MPa, we observe a transition of macroscopic deformation behaviour, from brittle to ductile (shaded zone). Simulations with P_c=20 and 30 MPa can sustain up to 2% strain without major stress drops. Red vertical bars indicate the location of the peak points.

3.4 Simulation results and data analysis

We computed numerical simulations with P_c ranging 0–30 MPa. We adopted the nomenclature proposed by Handin (1966) to describe the stress-strain behaviour. Increasing P_c modifies the macroscopic deformation of the rock from brittle to ductile (Figure 3.1) where three distinct behaviours were observed:

(1) below 4 MPa, the rock can be considered brittle;

(2) between 4 and 10 MPa, the rock undergoes a transitional phase, changing its apparent (i.e., macroscopic) deformation behaviour from brittle to ductile; and

(3) ≥10 MPa, prior to the stress-peak, the rock endures a significantly higher axial strain than that observed in behaviour (1), and the apparent deformation regime becomes ductile.

Here we restricted our analysis to macroscopic brittle failure (i.e., $P_c \leq 10$ MPa), and based on the stress-strain behaviour, we divided each simulation into pre- and post-peak stages, according to the peak axial stress. Knowing that the cumulative number of events indicates the overall damage (Lockner, 1993), our simulations demonstrated that, regardless of P_c, the total number of pre-peak events was
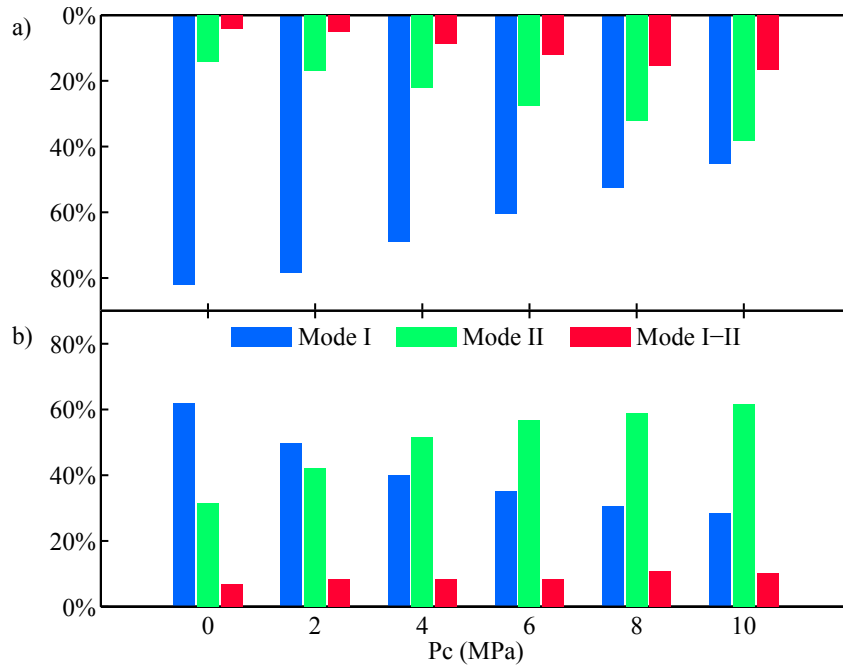
Figure 3.2: The variation of the percentage of each failure mode in simulations with increasing P_c. Both (a) pre-peak and (b) post-peak failure modes of AE events are examined.

consistently between 270 and 370; thus similar amounts of damage was accumulated prior to the peak.

Microscopically, the increase of P_c promoted mode II failure and restricted mode I failure (Figure 3.2). For $P_c \leq 4$ MPa, mode II failure became more dominant during the post-peak stage. Macroscopically, the unconfined specimen tended to fail by longitudinal splitting; however, once P_c was applied, longitudinal splitting was limited and AE occurred along inclined shear bands (Figure 3.3). We studied the macroscopic fracturing process by examining the angle between the shear plane and the horizontal axis (β) (Jaeger et al., 2007). β varies gradually from 60° to 70° with increasing P_c. The orientation of the failure plane is in agreement with the Mohr-Coulomb failure criterion assuming that the internal friction angle (ϕ) is 51.8° (Mahabadi, 2012) (see Supporting Information Figure 3.8 for the comparison of fracture patterns between laboratory tests and numerical results).

We quantitatively assessed the spatial distribution of AE utilizing D-value (Supporting Information, Figure 3.9), accompanied with a visual inspection. During the pre-peak stage, AE tends to be more clustered as P_c increases from 0 to 10 MPa (Figure 3.3a–d), and accordingly, D-value drops from 1.58 to 1.48 (Figure 3.4a). On the other hand, during the post-peak stage, events were more clustered at $P_c < 4$ MPa (e.g., Figure 3.3e) than at $P_c > 4$ MPa (e.g., Figure 3.3h), with D-value increases from 1.35 to 1.54 as P_c increased from 0 to 4 MPa, and then dropped to 1.48 with P_c continuously increased to 10 MPa (Figure 3.4a).
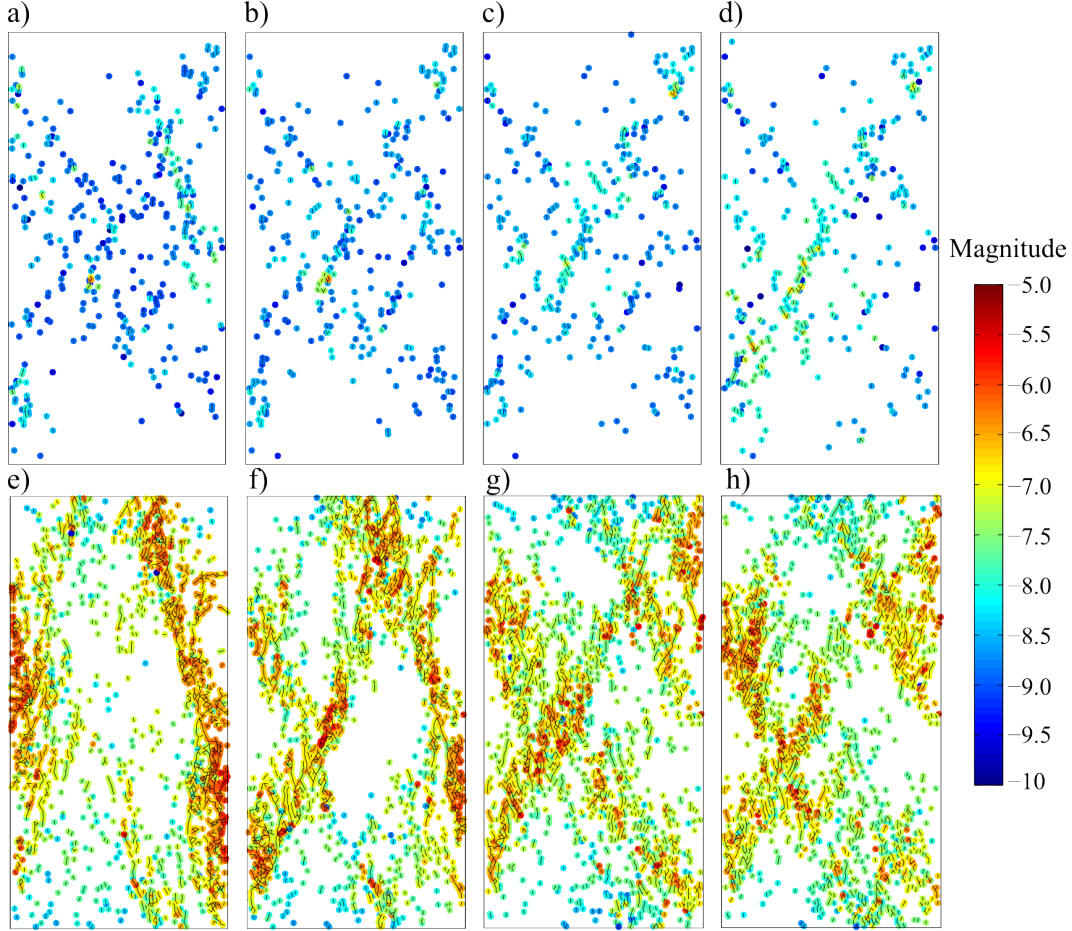
Figure 3.3: Locations and magnitudes of AEs under different P_c. AE events are plotted as colour-coded circles according to their magnitudes, overlapping with their associated cracks. (a)–(d), pre-peak stage of simulations with $P_c = 0$ MPa, 2 MPa, 6 MPa, and 10 MPa, respectively; and (e)–(h), post-peak stage of simulations corresponding to (a)–(d). Note the significantly elevated magnitude range at the post-peak stage.

To investigate this transition in D-value variation with the increasing P_c, we considered also the variation of the relative AE rate (p_r), based on the duration of each stage (Figure 3.4b). Pre-peak p_r increased gradually with increasing P_c; however, it remained very low (< 0.06). On the other hand, at $P_c < 4$MPa, post-peak p_r were exponentially higher than those measured at $P_c > 4$ MPa (Figure 3.4c).

Under the same P_c, the microcrack population, which has a high degree of randomness in space at the pre-peak stage, becomes more clustered at the post-peak stage (lower D-value), accompanied by higher magnitudes (Figure 3.3). Moreover, the variation of D-value between pre- and post-peak stage decreases as the P_c increases. According to the variation of p_r and D-value, we define two different deformation phases:

(1) Phase I (the slow and diffused deformation phase) was defined for $p_r<0.1$ and D-value> 1.45; and,
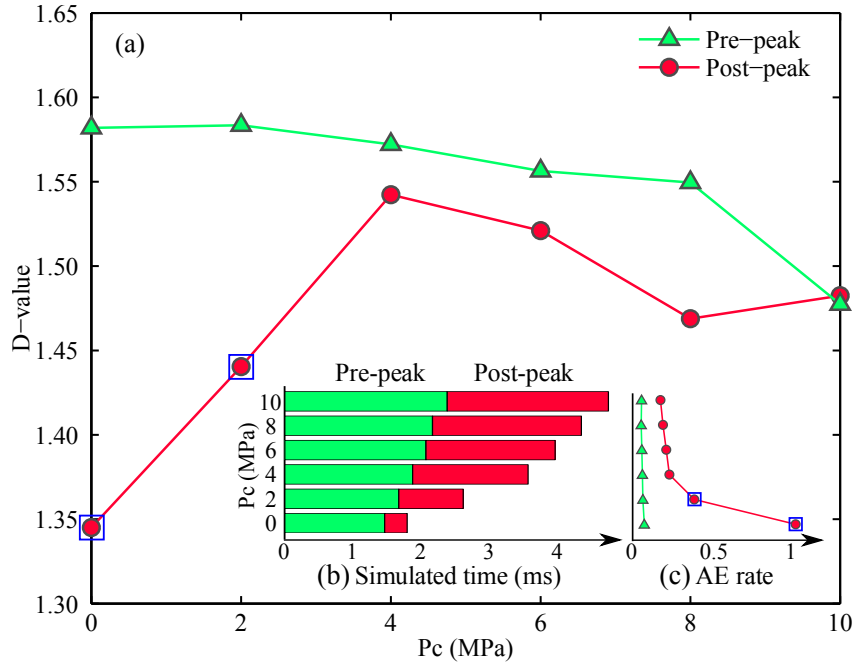
Figure 3.4: (a) Variation of D-value with increasing P_c for pre- and post-peak stages. (b) Time duration of the pre- and post-peak stages of each simulation. (c) Relative AE rate (p_r) at pre- and post-peak stages. The significant drop of D-value and increase of p_r indicate Phase II deformation (indicated by blue squares).

(2) Phase II (the rapid and clustered deformation phase) was defined for $p_r > 0.1$ and D-value< 1.45.

The significant differences in AE statistics between Phase I and II indicate the variation of damage processes in the specimen, which is the focus of this study.

Moment magnitude of AE recorded at laboratory scale are usually in the range between -8 and -5 (e.g., Sellers et al., 2003; McLaskey et al., 2014; Goodfellow and Young, 2014), and our simulation show very good agreement with this range. The b-value of the simulated AE decreases from 1.17 ± 0.09 to 0.84 ± 0.07 with increasing P_c (Figure 3.5). b-value estimation for pre-peak events has significant error (i.e., $\sim 25\%$), which is due to the limited event catalogue size and the uncertainty in defining the peak location. Therefore, in order to obtain representative b-values, we chose to estimate the b-value using all the events recorded in the simulations (Supporting Information, Figure 3.10). b-value estimated from simulated AE showed a range which is similar to that observed in the laboratory and the field (e.g., Lei et al., 2004; Amorese et al., 2010).

To investigate the variations of D- and b-value with time, we divided the AE catalogue into equal time segments (Supporting Information, Figure 3.11). At low P_c (< 4 MPa), D- and b-value have relatively large fluctuations as a function of time; whereas, at high P_c (> 4 MPa), D- and b-value are rather stable. A clear spatial clustering trend, indicated by the decreasing D-value, can be observed at
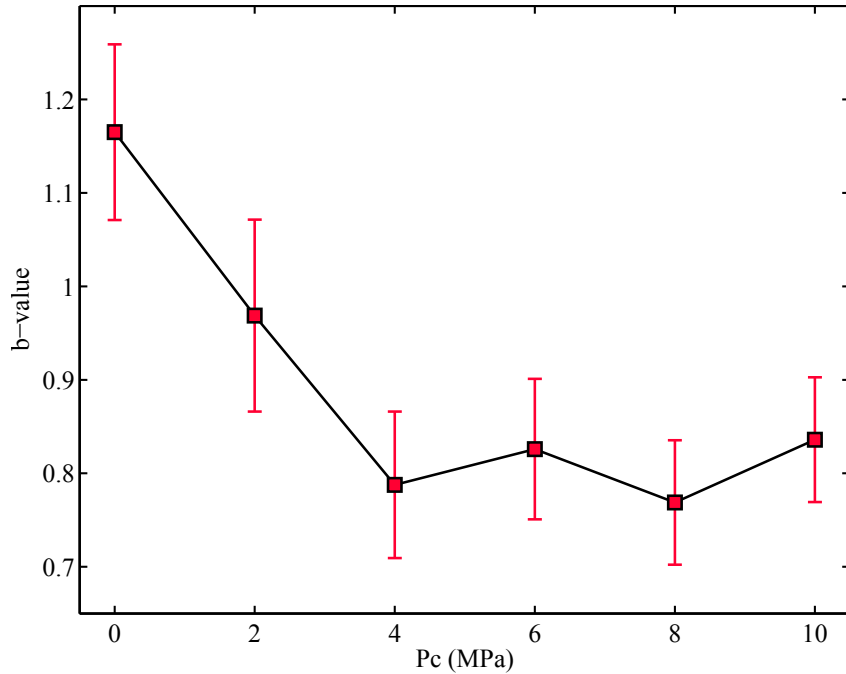
Figure 3.5: b-value, estimated using MLM, as a function of P_c and the associated standard error estimated by the bootstrap approach.

simulations with low confinement. More interestingly, we demonstrate a positive correlation between D- and b-value (Supporting Information, Figure 3.12).

3.5 Discussion

The present study reports numerical simulations of rock failures under varying confining pressures. Microscopically, we investigated grain boundary breakages; and macroscopically, we examined the stress-strain behaviour. These observations resemble laboratory investigations. In addition, the statistical analysis of synthetic seismic events agrees with laboratory (i.e., AE) and field (i.e., earthquake) observations, revealing details about the evolution of seismic activity at different deformation phases and confining pressures.

At low P_c (i.e., < 4 MPa), the rock exhibited brittle behaviour and only a small amount of strain occurred before the microcracks coalesced and formed throughgoing fractures. On the other hand, at high P_c (i.e., > 10 MPa), the rock was, from a macroscopic point of view, ductile, and significant shortening ($> 2\%$) took place before sample failure. The macroscopic ductile stress-strain behaviour, associated to the pervasively distributed microcracking, agrees with laboratory observations and numerical simulations (Paterson and Wong, 2005; Amitrano, 2003; Mahabadi, 2012). However, such transition of macroscopic behaviour should be distinguished from the brittle-ductile transition discussed in rock physics literature.

In particular, the brittle-ductile transition involves grain-scale deformation mechanisms such as crystal plasticity, diffusional flow, and granular flow, which in turn, cause the deformation pattern to shift from being microcracking dominated to dislocation dominated (Paterson and Wong, 2005). These dislocation mechanisms usually require an increase of temperature; however, as we considered room temperature in our simulation, the microscopic ductile deformation can be considered negligible (Tullis and Yund, 1977). The decreases of β from 60° to 70° with increasing P_c was associated to the increased mobilization of friction, resulting in the decrease of the apparent friction angle ϕ_a, where $\beta = 45° + \phi_a/2$ (Amitrano et al., 1999; Jaeger et al., 2007).

Before the stress-peak, the cumulative counting of AE, which is commonly used in the laboratory to estimate the accumulated damage, was not significantly influenced by P_c. However, the lower the P_c, the less the time was required for similar numbers of AE to occur, resulting in higher p_r.

The drop in D-value occurring between the pre- and post-peak stage can be explained by the coalescence of microfractures, which leads to the spatial localization of the fracturing process (Kranz, 1983). The larger the P_c, the smaller the drop in D-value, which indicates that at higher confinement, microfractures tend to be more homogeneously distributed spatially (Johnson, 1992).

D-value and p_r are inversely correlated. In fact, the significant drop of D-value, observed between pre- and post-peak stages, corresponds to the significant increase of p_r. Considering the throughgoing failure planes generated at P_c=0 and 2 MPa, the drop of D-value and the rapid increase of p_r may be considered precursors to the failure of the rock (Hirata et al., 1987; Lei et al., 2004). On the other hand, for simulations with $P_c \geq 4$ MPa, the variations of D-value and p_r from pre-peak to post-peak are relatively small. Observations suggest that during Phase I, increasing P_c favours localized damage, and during Phase II, P_c promotes diffused damage. It is worth noticing that for $P_c \geq 4$ MPa, Phase II never occurs, even after the peak point (Supporting Information, Figure 3.13).

The decrease of b-value, with increasing P_c, can be explained by the fact that shear events, which release higher energy than tensile events, are more frequent at $P_c \geq 4$ MPa. Similar decrease in b-value was observed in previous studies including field observations and numerical simulations (Wyss, 1973; Gerstenberger et al., 2001; Amitrano, 2003), confirming that the b-value behaves as a stressmeter and low b-values indicate high *in-situ* stresses (Schorlemmer et al., 2005). In this study, by utilizing the combined finite-discrete element method, we obtain variations of b-value as a function of P_c as an emergent property of the model instead of imposing it through a stress dependent modulus reduction algorithm as required in a finite element code (Amitrano, 2003). Moreover, the positive correlation between D- and b-value agrees with the literature (e.g., Henderson et al., 1999; Chen et al., 2006).

3.6 Concluding remarks

We utilized 2D FDEM based AE modelling algorithm to obtain insights into the mechanical and seismic behaviour of rock failure processes. Simulated results provide accurate descriptions of microscopic and macroscopic damage patterns of rocks under different P_c. Simulated AE, which are emergent behaviours associated with the explicit simulation of fracturing processes, captured the variations of D- and b-value, as a function of P_c, similar to what was observed in several published laboratory tests.

Two indicators for the failure of the intact rock were identified: (i) the significant drop of D-value (damage localization), and (ii) the sharp increase of event rate. Both phenomena are known to occur concurrently before earthquakes, and we successfully simulated these anomalies before sample failure. The decrease of b-value with increasing P_c and its positive correlation with D-value are also captured by the simulations. Interestingly, we also found that P_c promotes more clustered damage during Phase I deformation and more diffused damage during Phase II deformation.

Observations performed at laboratory scale resemble those carried forward on regional and crustal scales, and our numerical results suggest that the seismic behaviours (i.e., spatial, temporal, and magnitude distributions) are mainly controlled by two factors: (i) the *in-situ* stress and (ii) the damage phase. These two factors should be carefully assessed when monitoring natural and induced seismic activity. For instance, during the hydraulic fracturing operation, a decrease in D-value and increase in seismic rate may indicate that the induced fractures are rapidly developing.

Numerical simulations can provide an effective tool to assist laboratory experiments and field studies to obtain further insights into the rock failure processes. Our simulations demonstrate the potential of our approach to help monitor and even forecast earthquakes. Moreover, the ability to systematically evaluate the influence of confining pressure on seismic activity suggests that numerical simulations can help elucidate regional/crustal stress information held in the seismic activity.

Supporting information
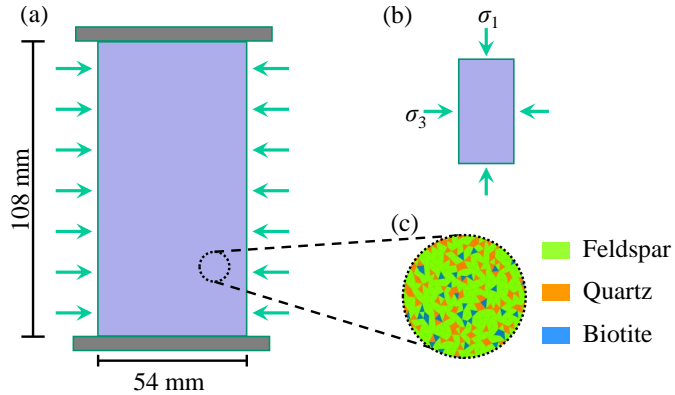
Figure 3.6: (a) Configuration of the numerical simulation. (b) Confining conditions. (c) Mineral phases assigned to the rock specimen.
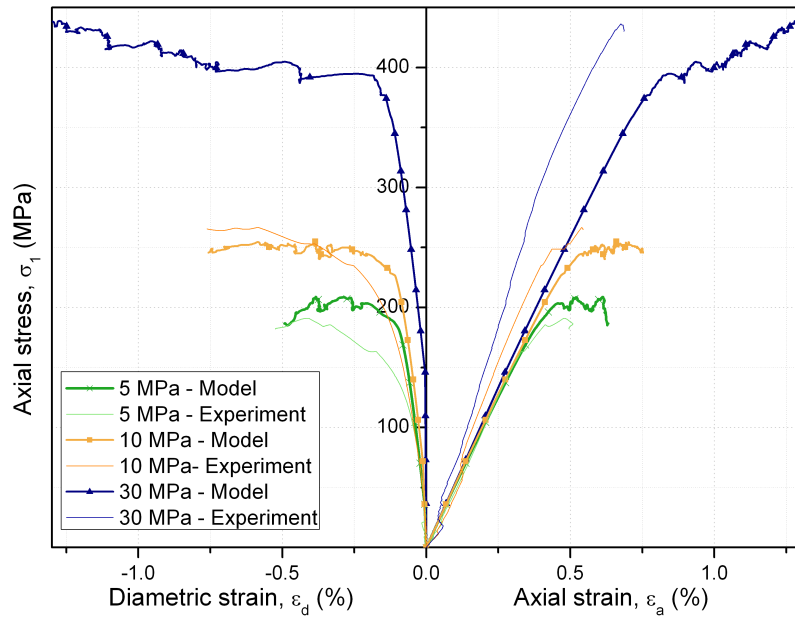
Figure 3.7: Stress-strain curves for the confined compression tests of the laboratory experiments and the numerical simulations. The diametric strain data for $P_c = 30$ MPa test is missing (from Mahabadi, 2012).
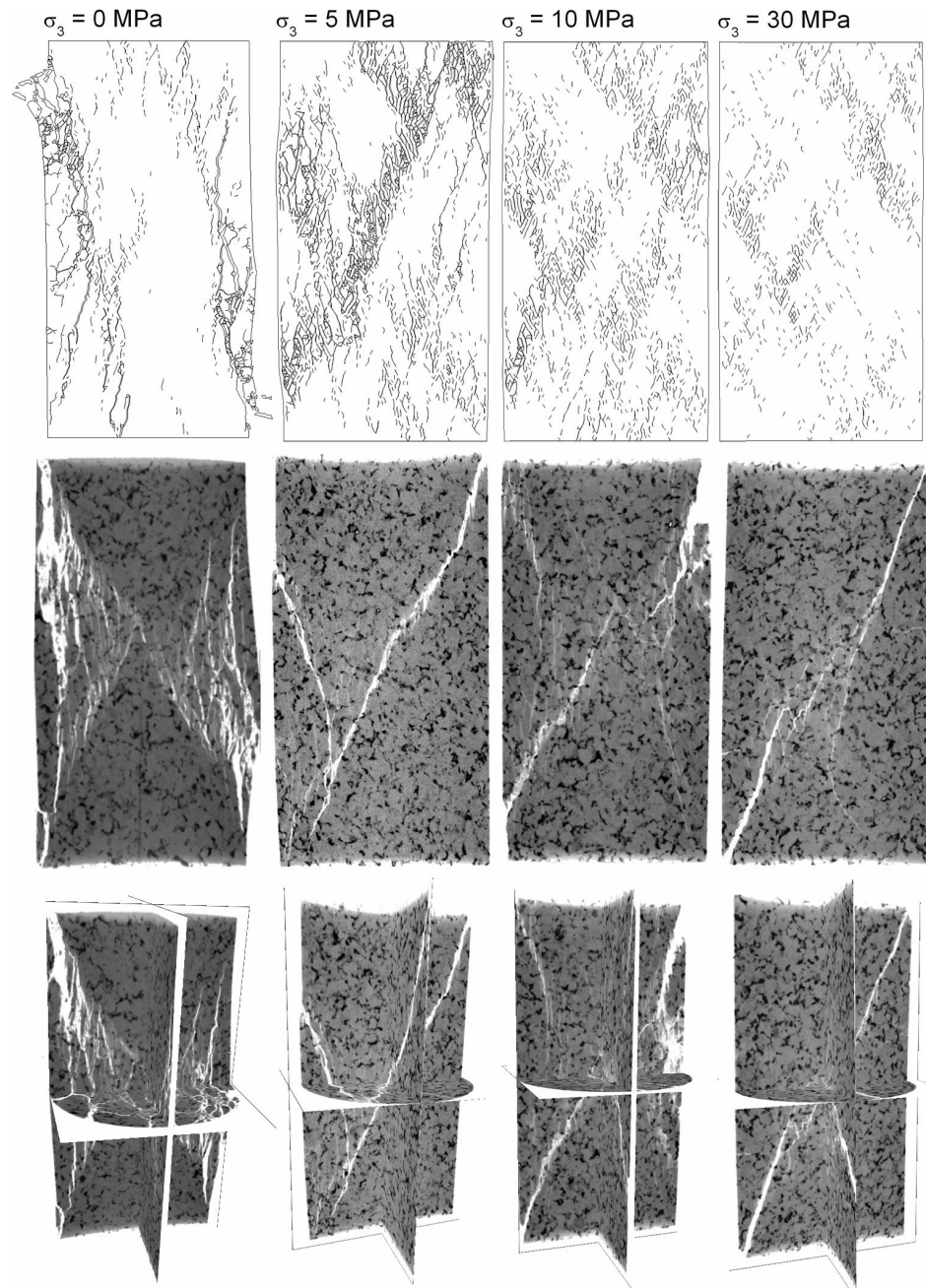
Figure 3.8: Fracture patterns for confined compression tests with $P_c = 0$ (unconfined), 5, 10, and 30 MPa in the numerical simulations (top row), and µCT images of failed laboratory specimens (middle and bottom rows) (from Mahabadi, 2012).
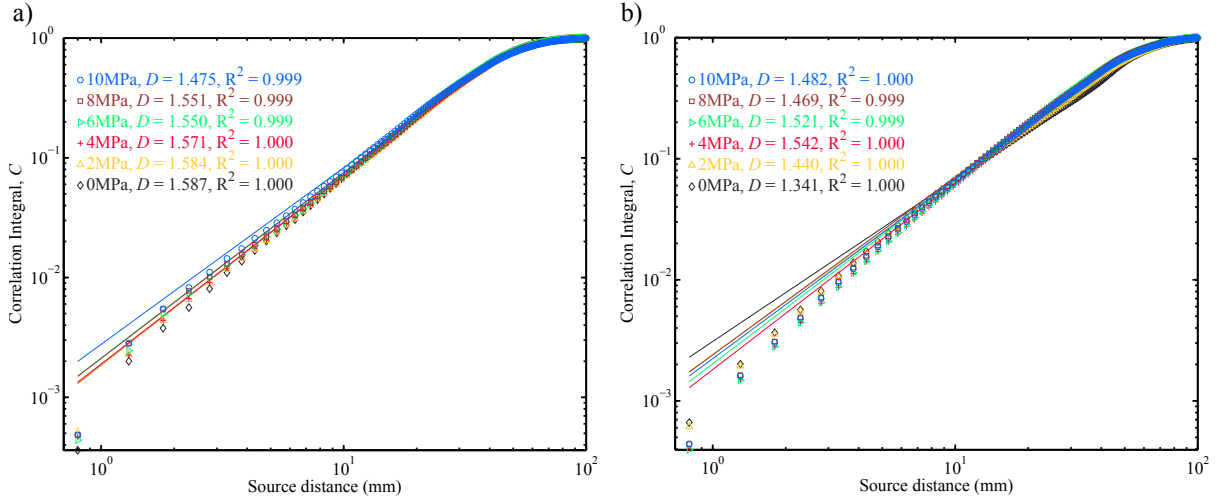
Figure 3.9: D-value estimation using correlation integral analysis. Curve fitting results between correlation integral ($C(r)$) and source distance (r) and their fitted lines are visualized in log-log scale, for (a) pre-peak stage and (b) post-peak stage, respectively.
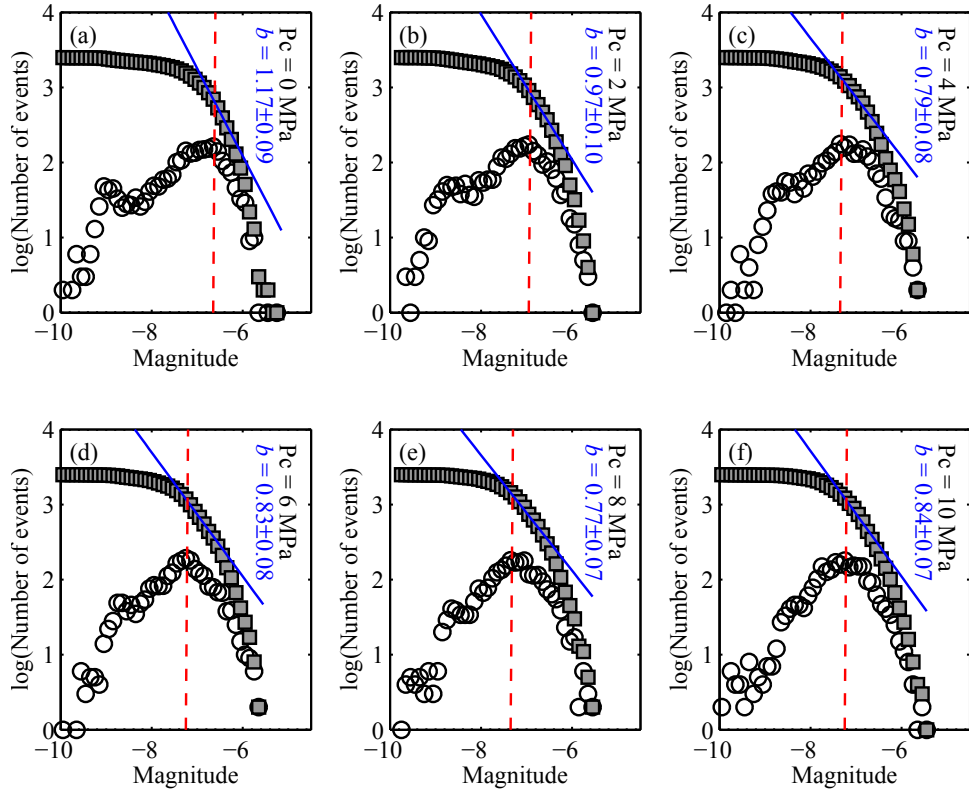
Figure 3.10: b-value estimation for simulated AE for simulations with P_c from 0 to 10 MPa. Filled squares are cumulative number of AE, and hollow circles are non-cumulative number of AE. The maximum likelihood method (MLM) was utilized, where the dashed vertical lines indicate the magnitude of completeness (M_c) and the blue straight lines show the estimated G–R relation.
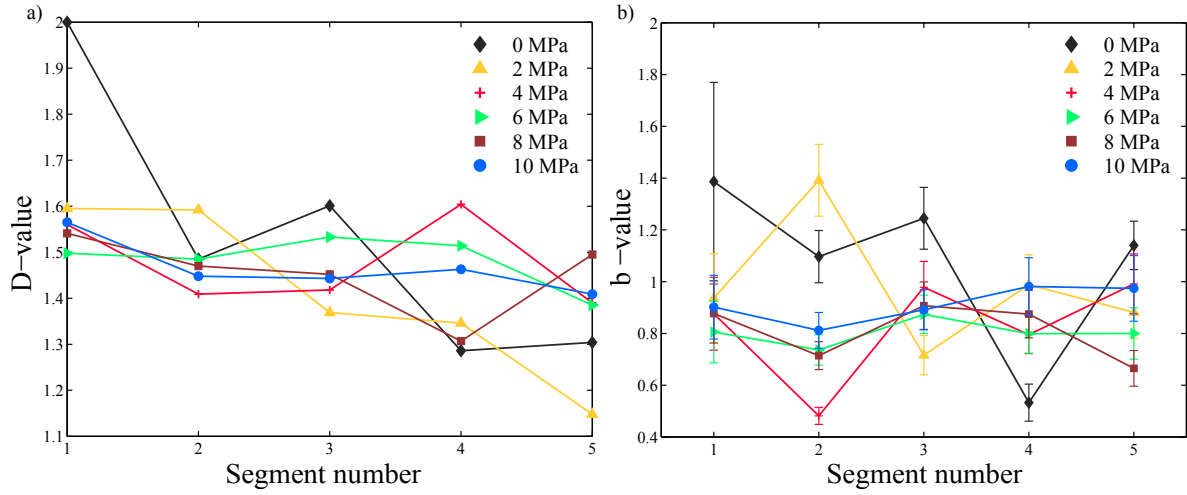
Figure 3.11: Time variation of (a) D-value and (b) b-value. Simulated AE in each simulation are evenly divided into 5 time segments, and D- and b-value are calculated for every segment to obtain their time variation patterns.
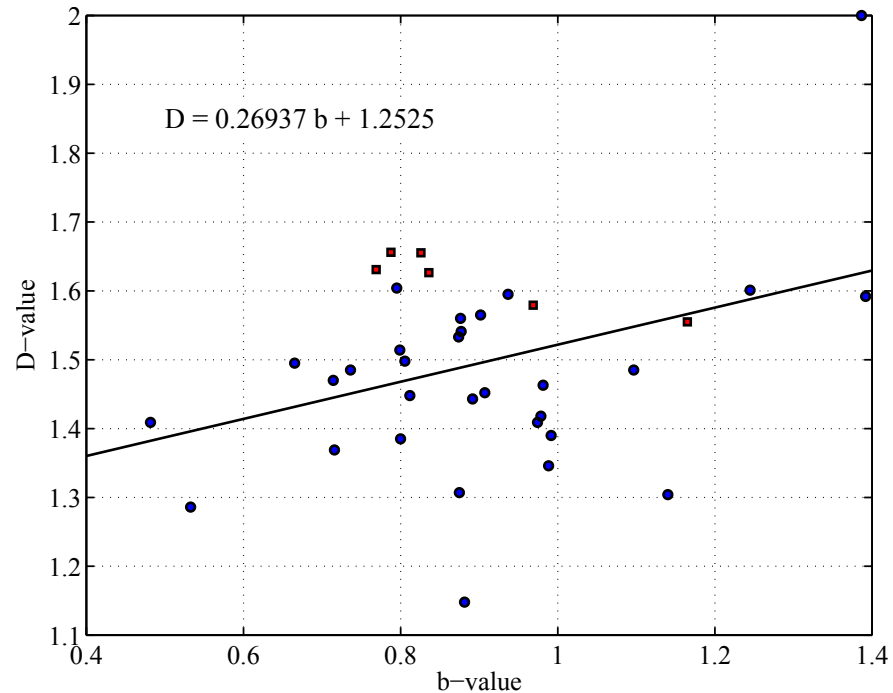
Figure 3.12: Correlation between D-value and b-value. A positive correlation is found between D-value and b-value. Blue circles are values calculated from aforementioned segmented data, and red squares are values calculated from the overall catalogue at each simulation.
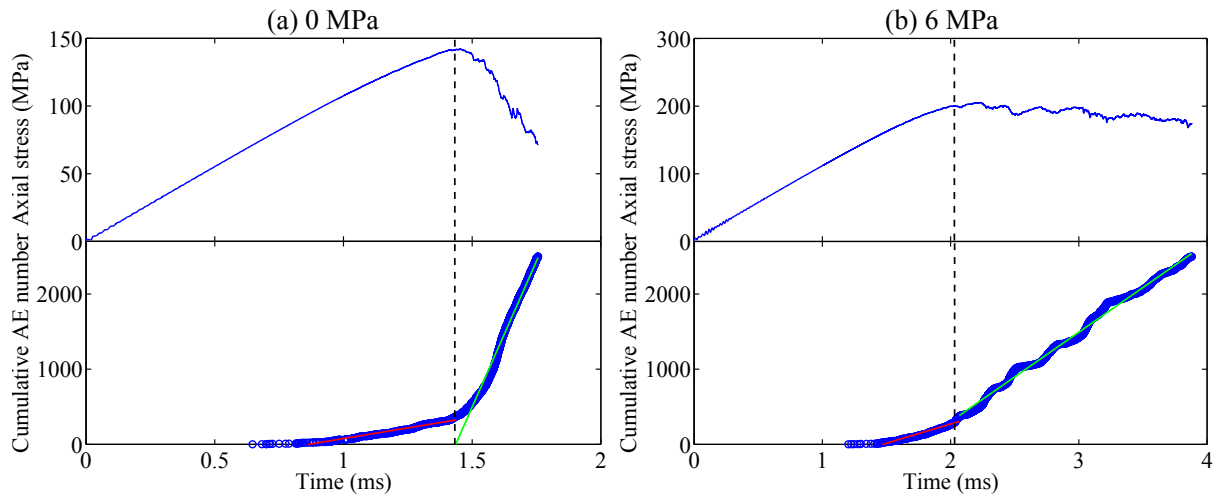
Figure 3.13: Stress-strain behaviour, cumulative AE counting, and deformation phase, taking (a) P_c =0 and (b) 6 MPa as examples. Dashed black lines mark the location of the peak points. In the bottom panel, the red line is the best fitting line to pre-peak events, and the green line is the best fitting line to post-peak events. Their slopes represent AE rates. The P_c =0 MPa simulation experienced Phase II deformation after the peak point, while the 6 MPa simulation remained in Phase I deformation.

Chapter 4

Understanding progressive rock failure and associated seismicity using ultrasonic tomography and numerical simulation

Summary

Monitoring the stability of underground rock excavation zones, such as tunnels and underground mines, is critical to their operational safety. The stability of these structures is related to the stress redistribution introduced by the excavation process and disturbance during the operation. Therefore, the characteristics of progressive rock failure behaviour at different stress conditions must be investigated. In this study, we address this problem using a laboratory experiment, coupled with ultrasonic tomography (UT) and numerical simulation. A time lapse two-dimensional (2D) UT observation was conducted on a granite slab under uniaxial compression. This test was then reproduced by the combined finite-discrete element method (FDEM). The entire deformation and failure processes were studied using this combination of technologies at macroscopic and microscopic scales. Quantitative assessments of the results suggested six precursory behaviours indicating the catastrophic failure of the rock: (1) decrease of the average wave velocity, (2) increase of the heterogeneity and anisotropy of wave velocity, (3) exponential increase of seismic rate, (4) spatial localization of damage onto the failure plane, (5) increase of the dominance of shear failure, and (6) slight recovery of b-value, followed by a significant drop. An integrated monitoring and analysis of these indicators, accompanied by carefully calibrated numerical simulations, may provide vital information regarding the stability of underground structures.

4.1 Introduction

Many tunnels and underground structures are constructed through highly stressed brittle rocks. Under high-stress conditions, stress redistribution occurs during and after the excavation which generates energy imbalance in the rock mass. The resultant formation, propagation, and coalescence of microcracks alter the properties of the surrounding rock mass and impact the stability of underground structures (Chang and Lee, 2004). Therefore, fundamental studies evaluating the failure and damage mechanisms of rock at different stress states are of great importance to geo-hazard assessment and operational safety of underground structures.

Under this motivation, we conducted a time lapse ultrasonic tomography (UT) observation on a granite slab subjected to a uniaxial compression test. UT has been used in medical science since the seventies (Greenleaf et al., 1974), but it was only in the eighties that Neumann-Denzau and Behrens (1984) applied this technology to rocks. UT utilizes ultrasonic wave signals (> 20 kHz) to penetrate the sample and image the velocity structure of the sample interior (i.e., tomography). Due to the high scattering and attenuation nature of the ultrasonic wave, UT is typically used for laboratory and small

scale field applications (Falls et al., 1992; Jansen et al., 1993; Lo et al., 1988; Meglis et al., 2005; Michaels, 2008).

Ultrasonic wave velocity is influenced by a number of factors including: pressure, crack density and orientation, and pore fluid properties (Johnston and Toksöz, 1980; Lockner et al., 1977; Sayers and Kachanov, 1995; Stanchits et al., 2006). Extracting information regarding such factors from elastic wave velocity using tomography provides a non-destructive approach to study the rock interior and is ideal to study the property changes of the rock during compression tests (Paterson and Wong, 2005).

In order to improve our understanding of the laboratory observations, we used the two-dimensional (2D) combined finite-discrete element method (FDEM) to numerically reproduce the uniaxial compression test. The FDEM model synthesizes the macroscopic behaviour of materials from the interaction of micro-mechanical constituents, and provides insights into the failure processes of rocks and associated seismic activities (Lisjak et al., 2013; Mahabadi et al., 2014; Tatone and Grasselli, 2015a; Zhao et al., 2014, 2015b). This innovative combination of technologies allowed us to characterize the deformation and brittle failure processes of the rock at macroscopic and microscopic scales. We quantitatively analysed the velocity anomaly and simulated acoustic emission (AE), and six evident precursors of the rock failure were identified. Based on the laboratory test and simulation results, we suggested that these indicators, which can also be obtained from field seismic monitoring, can aid in improving the assessment of the stability of underground structures.

4.2   Material and methods

4.2.1   Material and experiment set-up

The rock sample investigated in this study is a Fangshan granite slab 110 mm wide, 220 mm long, and 30 mm thick. Fangshan granite is a coarse grain rock consisting of three main mineral phases: feldspar, quartz, and biotite, with an average grain size of 2.6 mm. A uniaxial compression test was conducted on this sample using a MTS-1000KN hydraulic test system (Figure 4.1a). During the compression test, the axial load is applied by means of a moving cross-head, which was increased at a rate of 6 kN/min (∼1.82 MPa/min). At the initial (i.e., 0 MPa), and every 20 MPa incremental stress level, an UT test was performed.

4.2.2   Ultrasonic tomography (UT)

The UT system used in this study consists of five main components (Figure 4.1):
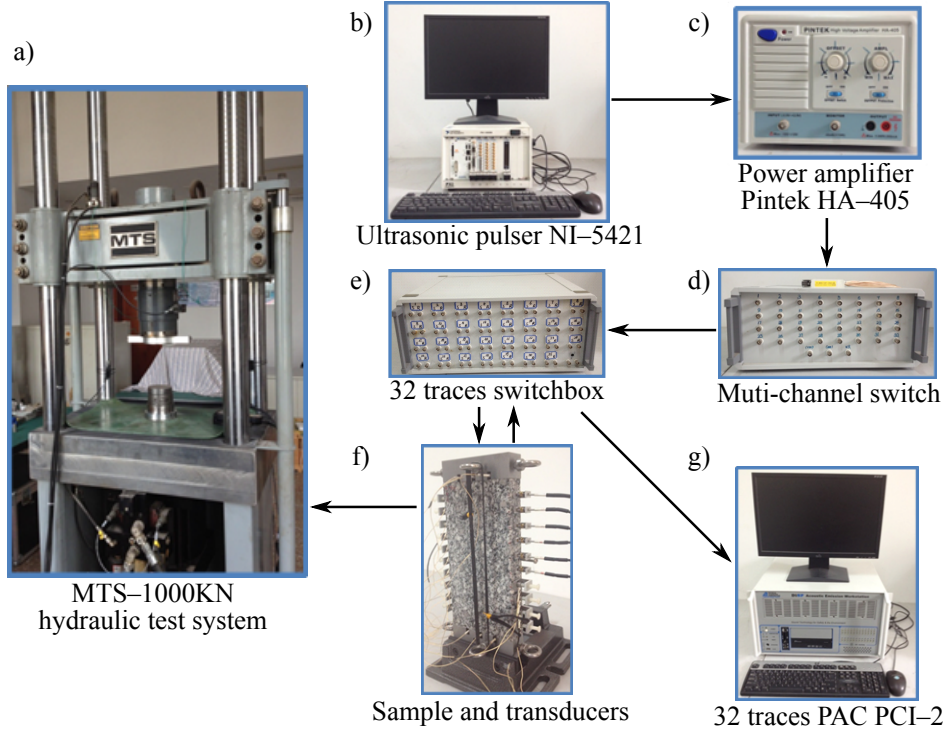
Figure 4.1: Illustration of the experiment set-up. (a) The MTS-1000KN test system, (b) the computer controlled ultrasonic pulser, (c) power amplifier, (d) multi-channel switch, (e) the 32 traces switchbox, (f) the sample with transducers attached on it, and (g) the 32 traces PAC-PCI-2 data acquisition device.

(1) Ultrasonic transducers. Two types of transducers were used in this study, Physical Acoustics Corporation (PAC) Nano-30 and Valpey-Fisher Pinducer model VP1093. The PAC Nano-30 transmitter has a bandwidth of 125–750 kHz, while the VP1093 transmitter has a bandwidth of 10–10000 kHz. The mixed usage of transducers was due to the limited number of either type readily available in our laboratory; however, as received signals showed no significant quality difference between the two types, we did not consider the error associated with the differences in used transducers. Ten transducers were placed on the left and right sides of the slab, with 20 mm vertical spacing, and three transducers were placed at the middle of the top and bottom sides of the slab, with 25 mm lateral spacing (Figure 4.2a&b). These transducers were coupled to the sample using epoxy. Transducers on the top and bottom sides of the sample were embedded in specially designed slots on the loading platens.

(2) An ultrasonic waveform generator (National Instrument NI-5421). The NI-5421 board, which was configured with the PXI-1000B chassis, has a frequency range from <1 mHz to 43 MHz. We used a computer to control the digital-to-analogue channel of this device to generate a square wave signal at a frequency of 1 MHz with a peak-to-peak voltage of 1 V, which was then amplified by

an amplifier (Pintek HA-405) to 100 V.

(3) A custom multi-channel switch was used to replicate multiple identical ultrasonic signal traces from the amplified signal.

(4) A custom ultrasonic switchbox, operated by an NI-2567 device (not shown in the figure). The ultrasonic switchbox was used for switching sensors between transmitting signal and receiving signal during the experiment. Each UT test consisted of four stages, and during each stage, transducers on one side of the sample acted as transmitters while transducers on the other three sides acted as receivers. This operation started from the left side (i.e., transducers 1–10) and carried on counterclockwise (Figure 4.2b).

(5) A 32-channel data acquisition system, which consists of 16 PAC PCI-2 boards. This system can acquire analogue signals from the transducers, convert them to digital signals and transmit them to the computer. The P-wave wave velocity between a source and receiver transducer pair can be directly estimated using the source-receiver distance divided by the travel time. This velocity is the result of the effects of the media along the wave path (i.e., raypath), and it only indicates the overall variation of velocity. In the following discussions, we refer to it as averaged velocity (v_a). We calculated the averaged P-wave velocities between transducer pairs perpendicular ($v_a^\perp$) and parallel ($v_a^\parallel$) to the loading direction and examined their variations against the stress condition. Note that at high stress levels, transducers 11 and 13 became loosely coupled due to sample deformation, and in order to study $v_a^\parallel$, we examined v_a between transducer 12 and transducers 24, 25, and 26.

In order to obtain spatial variation of wave velocity in the rock, inversion of the velocity taking into consideration the rock heterogeneity (i.e., tomography) was required (Aki and Lee, 1976). Tomography was performed on grids with a grid cell size of 10 mm × 10 mm, resulting in a 2D velocity map of the sample. The raypath lengths were estimated using a wave front ray-tracing technique, and the damped least square (LSQR) iterative inversion method was applied, using a damping factor of 10 with 20 iterations (Paige and Saunders, 1982; Zhao et al., 1992). To obtain the initial velocity values of the iterative inversion, a linear fit of travel time and the travel distances between all source-receiver pairs at each stress level was carried out, and the slope of this fitted curve was used as the initial value in the inversion. Moreover, to constrain the inversion, velocity of each grid was limited to the range of 3500–5500 m/s.
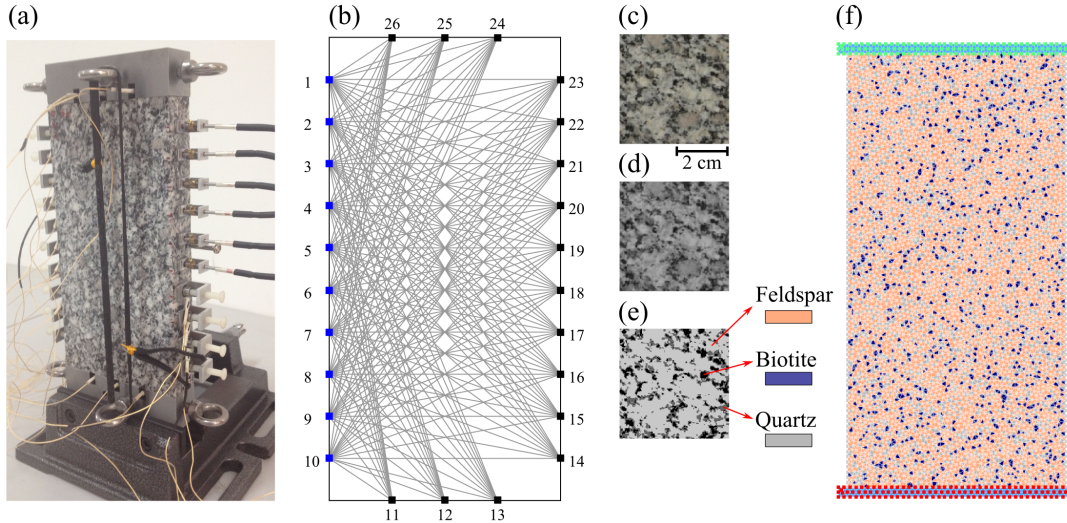
Figure 4.2: (a) Ultrasonic signal transducers attached to the sides of the specimen. (b) Schematic diagram of the raypath at the first stage of the UT test. Blue and black squares indicate transducers, and transducers 18–23 are VP1093 and the others are Nano-30. (c)–(e) Procedure of estimating the relative abundance of minerals in the rock specimen. (f) FDEM model of the rock specimen.

4.2.3   Combined finite-discrete element method (FDEM)

The FDEM model consisted of a 220 mm × 110 mm longitudinal section representing the rock sample and two rectangles at the top and bottom of the rock sample representing the steel loading platens. The model was discretized using a finite-element mesh with an average element size comparable to the rock sample grain size (i.e., 2.6 mm). The model recreated the Fangshan granite sample whose mineral phases were represented by approximately 10,000 elastic triangular elements connected to each other by four-node cohesive crack elements that represent grain boundaries. These cohesive crack elements can deform elastically, yield, and break when the deformation exceeds assigned energy based thresholds (Mahabadi et al., 2012a; Munjiza, 2004). The breakage of cohesive crack elements can occur in tensile mode (mode I), shear mode (mode II) or a combination of the two (mixed mode, mode I-II).

In order to incorporate the heterogeneity of the Fangshan granite in the model, the relative percentage of the three major mineral phases were estimated by employing an image based analysis approach and then assigned to the model. A photograph of the specimen was taken (Figure 4.2c) and converted to an 8-bit grayscale image (Figure 4.2d). A segmentation process based on visual inspection of grayscale values of different minerals was carried out: grayscale values > 100 and < 68 were considered feldspar and biotite, respectively, while the remaining mineral phases were considered quartz (Figure 4.2 e). The segmentation showed that the Fangshan granite sample consists of 67% feldspar, 23% quartz and 10% biotite. Elements in the FDEM model were assigned according to such percentages with stochastic

spatial distribution (Figure 4.2f). Properties of minerals and boundaries between different minerals (intergranular boundaries) were assigned using typical values from the literature and fine tuned to match the laboratory results (Table 4.1). Two loading platens were assumed to be rigid and they loaded the sample at a constant velocity of 0.2 m·s^{-1}, which corresponds to a strain rate of 0.91 s^{-1}. The loading rate, although significantly higher than in the actual test, has been verified to ensure a quasi-static loading condition while allowing the simulation to run in a reasonable time (Mahabadi et al., 2012a; Tatone and Grasselli, 2015a). In order to reproduce the effect of the friction between the platens and the rock, a friction coefficient of 0.2 was assigned to the interfaces between them. The software package Irazu 2.0.0 (Geomechanica Inc.) was used to build the model and run the simulation.

Table 4.1: Mineral properties and intergranular boundary properties used in the FDEM model for the Fangshan granite sample, adapted from Mavko et al. (1998); Lisjak et al. (2013).

Mineral property (unit)	Feldspar	Quartz	Biotite
Volume fraction (%)	67	23	10
Density (kg·m^{-3})	2600	2600	2800
Young's modulus (GPa)	56.4	83.1	17.2
Poisson's ratio (-)	0.32	0.07	0.36
Internal friction coefficient (-)	1.27	1.27	1.27
Internal cohesion (MPa)	37	37	37
Tensile strength (MPa)	5.5	11.4	4.2
Mode I fracture energy (J·m^{-2})	310	907	599
Mode II fracture energy (J·m^{-2})	620	1812	1198
Intergranular boundary property (unit)	Feldspar-quartz	Feldspar-biotite	Quartz-biotite
Friction coefficient (-)	0.82	0.82	0.82
Cohesion (MPa)	37	37	37
Tensile strength (MPa)	0.235	0.235	0.235
Mode I fracture energy (J·m^{-2})	0.6	0.05	0.05
Mode II fracture energy (J·m^{-2})	1450	382	382

4.2.4 Simulated acoustic emission (AE)

Energy release event associated with the microscopic cracking process in the rock is usually referred to as AE (Lockner, 1993). Understanding AE activities can help us link microscopic damage to observed macroscopic behaviour of the rock sample, and it has been commonly used together with UT to understand rock damage (Falls and Young, 1998; Stanchits et al., 2006).

In this study, AE activities during the laboratory compression test were considered noise and not analysed. Combining UT and AE monitoring is challenging because of the significant differences between the two types of signals. To accomplish such a functionality, two instrumentation systems may require (Jansen et al., 1993), which is beyond the capability of the current set-up. On the other hand, FDEM is a proven tool to study laboratory AE, and based on the calibrated model, we can investigate damage

process in the rock by quantitatively studying simulated AE (Lisjak et al., 2013; Mahabadi, 2012; Zhao et al., 2014, 2015b). Similar to the UT observation, we have examined AE between stress points at each 20 MPa interval; additionally, the peak stress point was also taken into consideration. The AE count in each interval was associated with the correspondent stress-strain behaviour. The failure mode and spatial density of the simulated AE pre- and post-peak were studied based on a grid with a grid cell size of 5 mm × 5 mm.

The distribution of AE in the magnitude domain, that is, the frequency magnitude distribution (FMD), was estimated using the Gutenberg–Richter (G–R) law (Gutenberg and Richter, 1944). Variation of b-value provides important information regarding the earthquake source region. In order to study the evolution of the characteristics of b-value during the deformation and failure process, we evaluated temporal variation of b-value using a sliding time window method (Nuannin et al., 2005). This method examines AE in a time window that contains N AE events, and the window slides through the AE catalogue in a timely order by increments of s event counts. In this study, we chose $N = 200$ as the window size and $s = 20$ (i.e., $s = N/10$) as the incremental step size. b-value within each window was calculated using the maximum likelihood method (Aki, 1965; Bender, 1983), with a bin size of 0.1 unit magnitude. The magnitude of completeness (M_c), which is the cut-off magnitude below which events are not considered into the b-value estimation, was obtained by applying the maximum curvature method to the complete AE catalogue (Wiemer and Wyss, 2000). The error associated with b-value was estimated using a bootstrap approach (Efron and Tibshirani, 1986; Zhao et al., 2015b).

4.3   Results

4.3.1   Compression test results

The Fangshan granite sample had a uniaxial compression strength (σ_c) of 136 MPa, a Young's modulus (E) of 57 GPa, and a Poisson's ratio (ν) of 0.20. These results, as well as the fracture pattern of the failed sample, were used to calibrate the FDEM model. The calibrated simulation resulted in emergent σ_c, E, and ν values of 138 MPa, 61 GPa, and 0.21, respectively. These values matched well with the respective experimental values.

The stress-strain relation from the laboratory test was not linear at the initial portion (i.e., 0 to 50 MPa), which is related to the closure of microcracks in the sample. However, the influence of microcracks was not considered in the FDEM modelling and the initial portion of the stress-strain curve was linear, which resulted in a difference in strain of approximately 0.02% (Figure 4.3). The rock sample failed
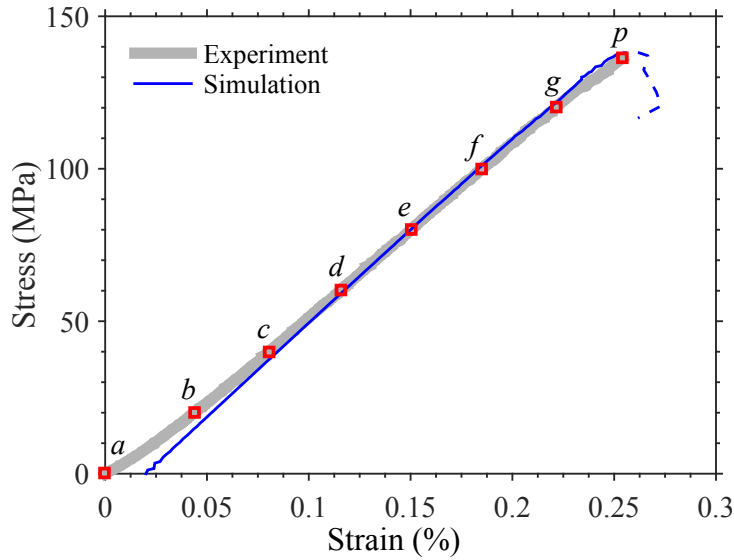
Figure 4.3: Stress-strain behaviour of the tested Fangshan granite (thick grey curve) and the FDEM simulation result (thin blue curve). The simulated strain is shifted to the positive strain direction by approximately 0.02% to compensate for the difference in the initial portion of the stress-strain curves. Points a–g indicate stress conditions where UT observations were carried out. Point p represents the peak stress, at which the laboratory test was stopped. The dashed portion of the blue curve represents the post-peak stage of the simulation.

abruptly at peak stress during the laboratory test, and the test was stopped at this point. This abrupt failure was reproduced in the simulation where the stress dropped immediately after the peak stress; however, the simulation was stopped shortly after the peak stress point, when a catastrophic macroscopic failure occurred.

4.3.2 Tomography results

The recorded waveforms showed that as the rock deformed with increasing stress, signal to noise ratio decreased, which may be related to (i) the flawed coupling between transducers and the sample and (ii) increased AE activities (Figure 4.4). Automated arrival picking techniques could not consistently detect arrivals and waveforms of waves, especially at high stress levels. Therefore, hand-picked arrivals of P-waves were used for tomography analysis in this study.

The averaged velocity perpendicular to the loading direction, $v_a^\perp$, calculated from all transducer pairs across the sample laterally increased when the axial stress increased from 0 to 60 MPa (Figure 4.5). After 60 MPa, $v_a^\perp$ tended to decrease, reaching values lower than the initial (i.e., 0 MPa) values at 120 MPa. On the other hand, the averaged velocity parallel to the loading direction, $v_a^\parallel$, kept increasing with increasing compressional stress, and reached ∼5300 m/s at 120 MPa. The difference in the averaged velocities in different directions, quantified by the velocity anisotropy, k (Babuška, 1984; Kern, 1993),
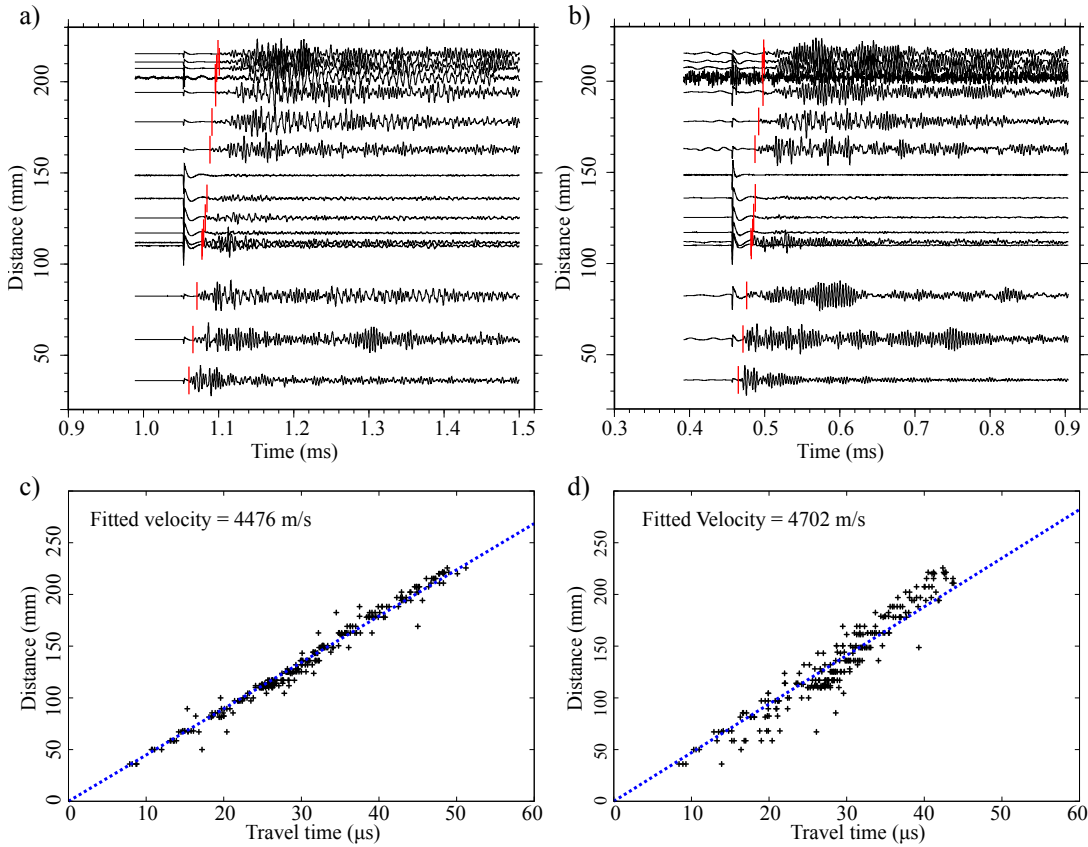
Figure 4.4: Waveforms recorded by transducers 11–26 (from top to bottom) at the first stage of the UT test under (a) 0 MPa and (b) 120 MPa axial stress. Red bars indicate the manually picked P-wave arrival times. Note that due to the crosstalk between circuits, a wiggle appeared in the beginning of each trace; although considered noise in most applications, it indicated the "zero" for wave travel time. (c) and (d) are P-wave velocities estimated from arrival time pickings by simple linear fittings at 0 MPa and 120 MPa, respectively.

increased from 10% to 36% when the axial stress increased from 0 to 120 MPa. Moreover, from 0 to 80 MPa, k increased in a logarithmic fashion and the rate of change decreased gradually; whereas, from 80 MPa to 120 MPa, k increased linearly at a higher rate of change.

The initial velocity values of the iterative inversion, obtained by a linear fitting of travel time and distances between all source-receiver pairs at stress points a–g were 4476 m/s, 4599 m/s, 4716 m/s, 4891 m/s, 4814 m/s, 4815 m/s, and 4702 m/s, respectively (e.g., Figure 4.4c&d).

Tomography results showed that velocity of the sample at 0 MPa was relatively uniform and consistent with the averaged velocity (Figure 4.6a). As the stress increased to 20 MPa, small areas with high and low velocities started to develop (Figure 4.6b). In fact, two low velocity areas ($<$ 4500 m/s) developed at the north-east and south-west parts of the sample, while the remaining parts had slightly increased velocity ($>$ 4500 m/s). The size of this high velocity zone was relatively unchanged between 20–60 MPa; however, the velocity in this area increased consistently (Figure 4.6b–d). From 80–100 MPa, the size of
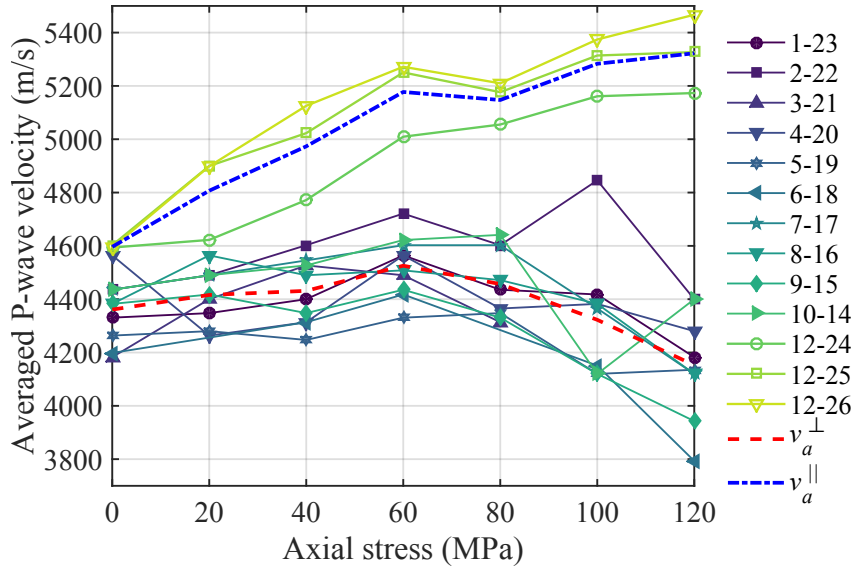
Figure 4.5: Averaged P-wave velocity measurement from source and receiver pairs across the sample laterally (solid markers) and vertically (hollow markers). The averaged values of these velocities at different stress levels, calculated using transducer pairs at the same orientation, are represented by $v_a^{\perp}$ (blue dash-dot curve) and $v_a^{\parallel}$ (red dash curve), respectively.

the high velocity zone shrank towards the centre of the sample (Figure 4.6 e–f). At 120 MPa, the low velocity zones were enlarged with further deceased velocity, and the high velocity zone shrank to the north-middle part of the sample (Figure 4.6g).

4.3.3 Simulated AE and quantitative analysis

Comparison of the simulated AE against the mechanical behaviour (Figure 4.7) shows that the first AE occurred at ∼40 MPa (point c) and very few events were generated prior to 60 MPa (point d). From 60 to 100 MPa (point d–f), AE occurred at a relatively stable rate (∼50 events per interval). Between 100 MPa and the peak stress point (point f–p), AE rate increased rapidly to 150 events per interval. Finally, after the peak stress point (point p–h), the AE rate increased rapidly to 530, suggesting an exponentially increased AE rate. The variation of AE rate suggested that the crack initiation stage occurred at approximately 60 MPa, and the unstable cracking stage started at approximately 100 MPa (Martin, 1993).

For the complete AE event catalogue, we obtained a M_c of -6.6 and an overall b-value of 0.82 ± 0.09. This M_c value was used in the sliding time window method to evaluate the time variation of b-value as a function of time. In general, b-value decreased throughout the deformation of the specimen (Figure 4.7), from an initial value of 1.3 at ∼100 MPa to 0.8 at 130 MPa. From 130 MPa to the peak stress point, b-value then recovered to 1 (point p). After the peak point, b-value rapidly dropped to 0.7.
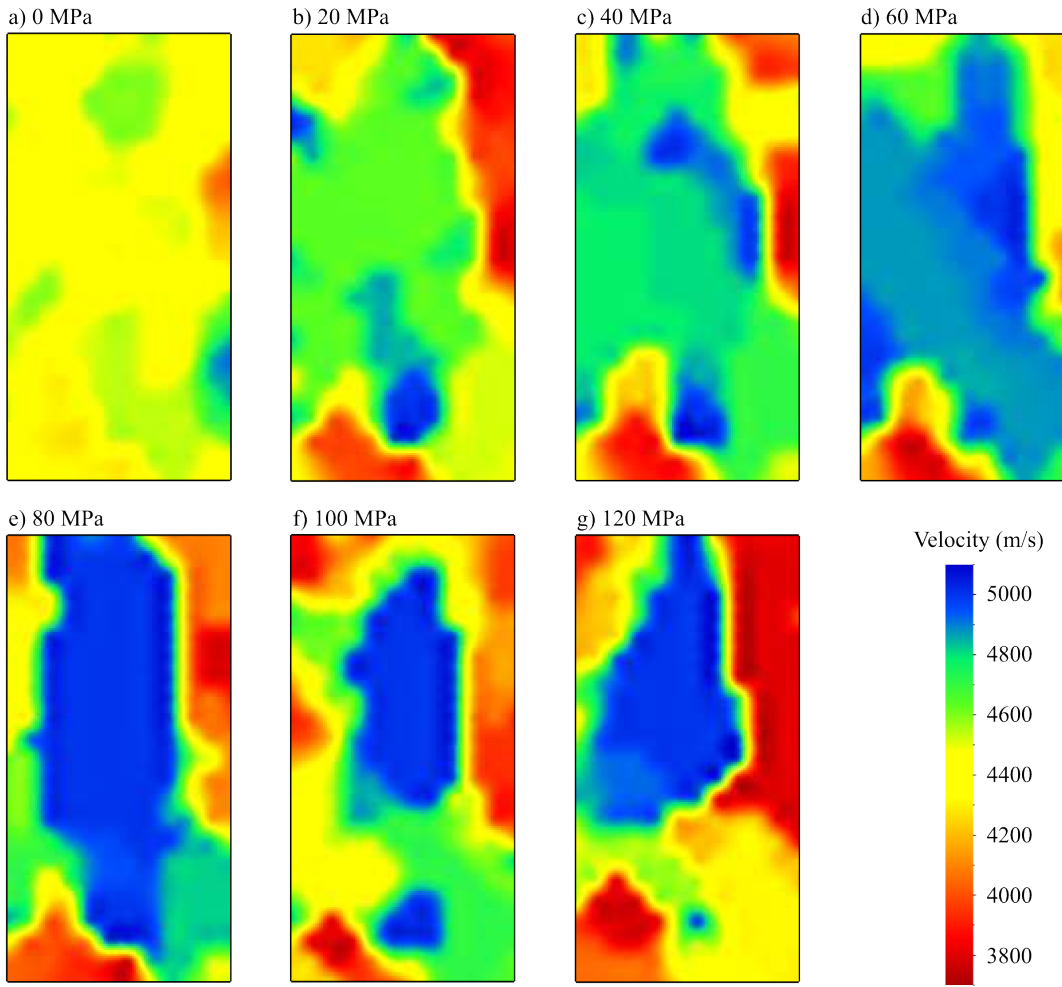
Figure 4.6: UT velocity inversion results. (a)–(g) correspond to UT observations conducted at stress conditions 0, 20, 40, 60, 80, 100, and 120 MPa, respectively.

To further investigate the significant change of AE behaviour before and after the peak stress point, we divided AE activities into pre-peak and post-peak stages and examined their spatial distribution and failure mode separately (Figure 4.8). The majority of the AE occurred in the pre-peak stage were in tensile failure mode, evenly distributed throughout the sample, and sub-vertically oriented (Figure 4.8 a). Event density at this stage was < 5 counts/grid throughout the sample. AE occurred in the post-peak stage were mainly shear events localized along a shear band oriented approximately 70° with respect to the horizontal direction (Figure 4.8b). Event density on the shear band was > 10 counts/grid, while the remaining parts of the sample were relatively quiescent with few AE recorded. Comparing the simulated fracture pattern with the compression tests result, the inclined throughout fracture was successfully reproduced by the simulation (Figure 4.8c).
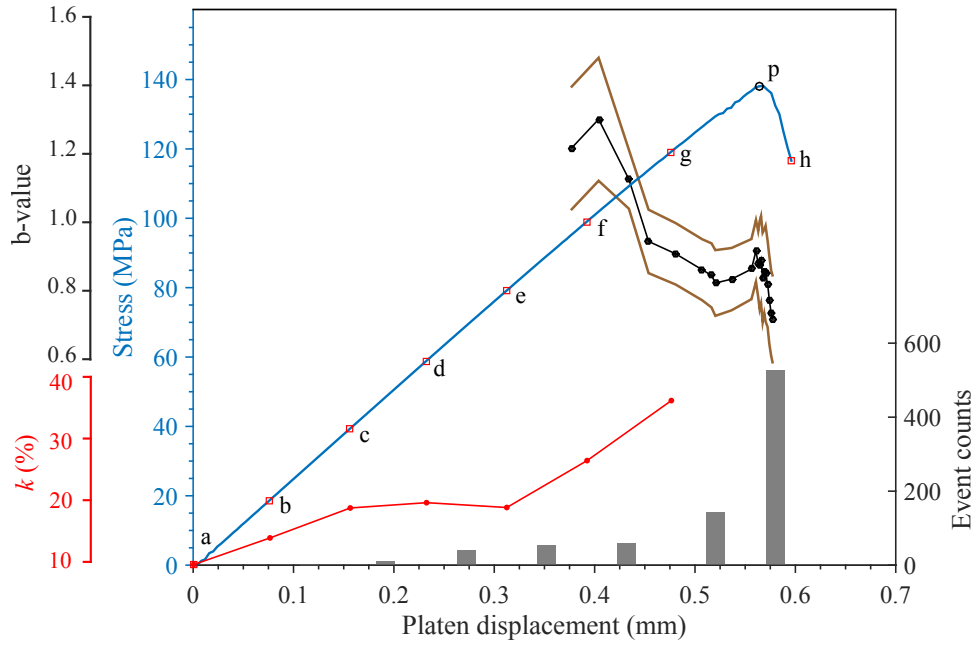
Figure 4.7: Simulated axial stress (blue curve), non-cumulative AE event counts (columns), b-value (black curve), and velocity anisotropy (red curve) examined against the loading history. Note that in order to avoid the overlapping strain after peak stress, we use platen displacement as the horizontal axis. Brown lines indicate the errors associated with the b-values. Points a–g (red squares) correspond to stress points at 20 MPa intervals, h is the failure point. Peak stress point p is marked by the black hollow circle.
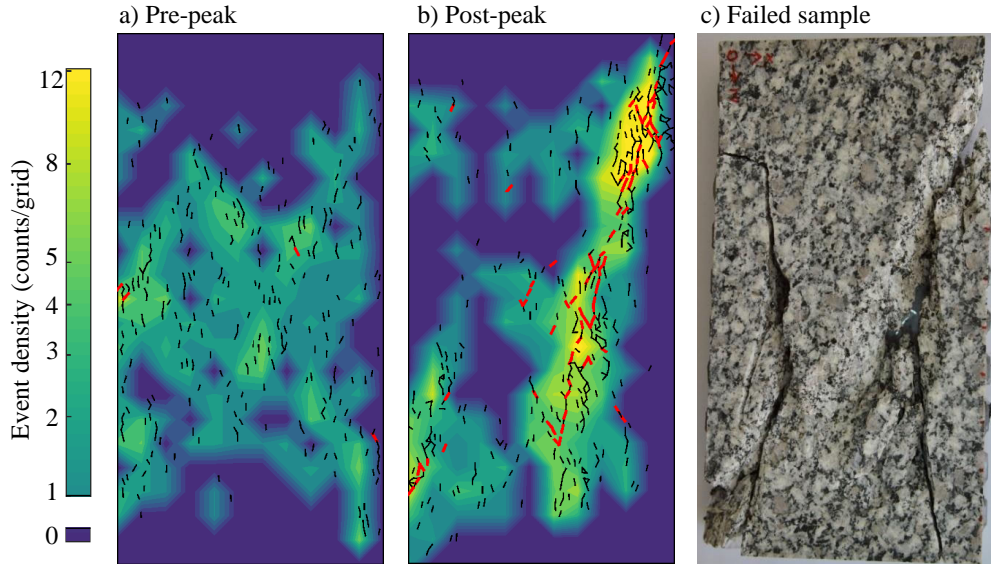
Figure 4.8: (a) and (b) show the location and failure mode of simulated microcracks (i.e., AE) that occurred pre- and post-peak, respectively, overlapping their spatial density maps. Density maps are in log scale for better illustration. Tensile dominant cracks are marked by thin black dashes and shear dominant cracks are marked by thick red dashes. (c) The tested rock specimen after the abrupt failure. Note the similarity in macroscopic fracture pattern between (b) and (c).

4.4 Discussion

4.4.1 Damage process characterized by wave velocity and simulated AE

The variation of velocity is related to the change in elastic modulus at macroscopic scale, while the AE is associated with the degree of damage at microscopic scale (Diederichs et al., 2004; Lockner, 1993; Nur and Simmons, 1969). Combining the two provides detailed insight into the deformation and failure processes of the brittle rock.

The influence of closure of pre-existing microcracks on the elastic properties of the rocks was suggested as early as (Adams and Williamson, 1923). Later laboratory studies observed that this effect causes velocity anisotropy that seismic waves travel faster in the direction of the applied stress (Tocher, 1957; Nur and Simmons, 1969). We characterized the wave velocity difference in different directions using velocity anisotropy (k) and described regional velocity difference in the sample using velocity heterogeneity.

The increase of $v_a^\perp$ and $v_a^\parallel$ with increasing axial stress prior to 60 MPa was related to the closure of pre-existing microcracks. The UT observations not only captured the increase of the overall velocities, but also provided details of the velocity heterogeneity in the sample. The velocity heterogeneity, observed as high and low velocity zones, may have two origins: (1) heterogeneity of the mineral phases and microcracks in the rock sample and (2) end effect between the sample and platens stemming from the relatively high friction between them.

After 60 MPa, $v_a^\parallel$ kept increasing with increasing axial stress, but $v_a^\perp$ started to decrease, causing k to increase. This suggests that new microcracks were developing in preferred orientations and failure modes, and they had a more significant impact on the elastic modulus in the lateral direction than in the vertical direction. This interpretation was confirmed by the numerical simulation: most AE events occurred during this period were oriented in conjugate sub-vertical directions and in tensile failure mode. These AE events (i.e., microcracking) divided the sample into high and low velocity regions. As the damage accumulated and covered more regions of the sample, the areas of the high velocity zones decreased and the areas of the low velocity zones enlarged, causing more significant velocity heterogeneity.

Velocity anisotropy has been suggested to be meaningful to rock burst prediction (Tocher, 1957). The observed k variation as a function of loading history resembles other laboratory studies (Goodfellow et al., 2014), and by comparing it with the stress-strain relation and simulated AE (Figure 4.7), we have been able to understand the origin and development of the velocity anisotropy.

Upon 120 MPa where the last UT observation was carried out, the numerical simulation has successfully explaine the tomography results. After this point, laboratory observations were limited and our

interpretation relied on the numerical simulation. As the axial stress continued to increase, the shear band became evident. After the peak stress, shear dominant cracking and the linkage between them became the major mechanism of crack interaction (Lei et al., 2000). The throughout fault that failed the sample, observed in the laboratory test and the simulation, verified such interpretation (Figure 4.6g & Figure 4.8c).

4.4.2 Rock failure precursors

Several precursors of the catastrophic failure of the rock were identified: (1) decrease of the overall (i.e., averaged) elastic wave velocity, (2) increase of the heterogeneity and anisotropy of elastic wave velocity, (3) exponential increase of AE rate, (4) spatial localization of damage onto the failure plane, (5) an increase of the dominance of shear failure, and (6) slight recovery of b-value, followed by a significant drop.

The decrease of the average velocity (indicator 1) suggests that significant amount of damage has occurred resulting in a reduction in the apparent elastic modulus of the rock sample. As the damage continued to accumulate and new microcracks formed, high and low velocity zones developed with the increase of elastic wave velocity anisotropy (indicator 2). Our study suggested that indicators 1 and 2 may appear at approximately 45% (i.e., 60 MPa) and 60% (i.e., 80 MPa) of the compressive strength of the rock, respectively, providing meaningful hints for intermediate- to long-term prediction of rock failure.

At the unstable cracking stage, damage accumulates rapidly along the shear band (indicators 3, 4 and 5). These indicators became evident after 80% of the compressive strength of the rock (i.e., 100 MPa), and as the microcracks started to grow and coalescence, the throughout fault that catastrophically failed the rock sample formed quickly (Cai et al., 2004; Diederichs et al., 2004). Therefore, indicators 3, 4 and 5 may be considered as short-term prediction parameters.

The rapid drop of b-value (indicator 6) has been suggested by the work of Main et al. (1989) based on fracture mechanics, which was in agreement with laboratory and field earthquake studies (Weeks et al., 1978; Imoto, 1991; Lockner et al., 1991). Our results demonstrated that it can be an intermediate- to long-term prediction tool as it gradually decreases along with the failure process. However, the slight recovery and significant drop right before the failure was more evident, making it a useful short-term prediction parameter.

Other failure indicators were also suggested by researchers, such as increasing energy release rate, increase in spatial correlation length, and increase in scattering attenuation (Lei and Satoh, 2007; Main

et al., 1989). These failure indicators, in addition to the indicators we identified, are closely related, and each of these aspects may have complicated evolution due to the heterogeneity of the rock. Therefore, it is important to integrate the analysis of several parameters to successfully predict rock failure.

4.5 Conclusion

In this study, we employed ultrasonic tomography observations and FDEM numerical simulation method to investigate the progressive failure process of a rock sample under uniaxial compression. Six indicators related to critical behaviours prior to rock failure were identified. These precursory behaviours can be obtained from field monitoring, for example, from seismograms, and with the support of carefully calibrated numerical models, they can improve the accuracy of stability assessment of underground structures. In addition, these observations may also be useful to the forecast of mining and tunnelling induced seismicity. In future studies, the combination of technologies can be further developed by (1) recording induced AE during the compression test, (2) taking wave waveform information and attenuation into account to enhance the tomography results, and (3) using validated numerical models to simulate field scale problems.

Chapter 5

Rotary shear experiments under X-ray micro-computed tomography

Abstract

A rotary shear apparatus (ERDµ-T) was designed, assembled and calibrated to study frictional behaviour. We paired the apparatus with X-ray micro-computed tomography (µCT) to inspect *in-situ* and *in-operando* deformation of the tested specimen. This technology allows us to observe how two rough surfaces interact and deform without perturbing the experimental conditions (e.g., pressure, temperature and sample position). We performed an experiment employing an aluminum alloy sample to demonstrate the capability of the apparatus. The sample was sheared at incremental steps, and during shearing, normal force, sample shortening, torque, and shearing velocity were measured. The measurements were associated to the µCT imagery, giving a comprehensive understanding of the deformation processes of the samples. The present contribution demonstrates that the ERDµ-T allows (1) linking the variation of physical parameters to the evolution of internal structures of the sample and (2) shedding light on fracturing and frictional sliding processes in solid materials.

5.1 Introduction

The study of friction in rocks is of great interest to many disciplines including civil engineering, mining, hydrocarbon exploration, and earthquake studies (Byerlee, 1978; Zoback et al., 2012; Di Toro et al., 2004). Friction, or frictional strength, is expressed as friction coefficient (μ), which can be expressed as the ratio of the measured shear stress to the measured normal stress on two counteracting surfaces. It has been reported from laboratory and field observations that during a frictional sliding process, the friction varies as a function of stress, sliding velocity and distance, contact geometry, and time (Brace and Byerlee, 1966; Scholz, 1998). Such a complex behaviour controls, for instance, the initiation, propagation, and termination of the slip on a seismogenic fault (Scholz, 1998; Reches and Lockner, 2010; Di Toro et al., 2011).

Due to the difficulty of inspecting natural faults and rock joints, the study of rock friction takes advantage of laboratory tests, among which direct shear and rotary shear tests are the most common (Jing and Stephansson, 1995). Rotary shear tests have two distinct advantages over direct shear tests: (1) unlimited shearing distance in a constrained volume and (2) constant nominal contact area during the rotation so that the testing conditions (i.e., normal and shear stresses, pore pressure, and confining pressure) can be well controlled (Jing and Stephansson, 1995). For these reasons rotary shear is suitable to study the frictional behaviour associated with faults slipping.

Over the past four decades, rotary shear tests have been conducted on a large range of rock types

with varying velocities, sliding distances, stresses, and temperature conditions (Reches and Lockner, 2010; Tisato et al., 2012; Togo and Shimamoto, 2012; Chambon et al., 2002; Di Toro et al., 2004; Beeler et al., 1996). These studies utilized conventional techniques which measure the rock bulk properties and assume they are representative properties of the rock. However, frictional behaviour is intimately related to rock microscopic features, such as mineral composition, grain orientation, microscopic asperities, microcracks, and gouge material properties (Kanamori and Heaton, 2000; Goldsby and Tullis, 2011). During laboratory tests, none of these aspects can be easily observed.

On the other hand, in recent years, X-ray techniques have been used extensively to study geomaterials (Ketcham and Carlson, 2001; Tatone and Grasselli, 2015b; Jackson et al., 2008; Zhao et al., 2015a; Johns et al., 1993; Viggiani et al., 2004; Renard et al., 2004; Fusseis et al., 2014; Renard et al., 2016; Ritman, 2004). X-ray can penetrate materials and undergo attenuation during this process, and the magnitude of the attenuation can be considered, in first approximation, proportional to the density of the penetrated material (Raynaud et al., 1989). The internal structure of geomaterials is often defined by density and/or phase variations (i.e., gas, fluid and solids) and chemical composition (i.e., minerals); therefore, X-ray is well suited to image the interior of geomaterials (Vervoort et al., 2004).

Traditionally, rotary shear experiments are performed with incremental strain steps. Characterizing the surface for every step leads to gouge mass loss and potential misalignment of asperities. Therefore, restarting the experiment at the exact same condition is nearly impossible, and commonly a new sample is used to achieve increment of total strain. This approach is arguably problematic if slight heterogeneities exist between samples and repeatability tests are necessary. X-ray micro-computed tomography (μCT), on the other hand, provides a non-destructive technique that can inspect the three-dimensional (3D) internal structure of the sample at micro-metric resolution, without perturbing the sample.

Under such a motivation, a new X-ray transparent vessel (ERDμ-T) was designed, assembled, installed, and calibrated at the University of Toronto. Coupled with the X-ray μCT system (Phoenix|X-ray v|tome|x, General Electric Sensing and Inspection Technologies), the ERDμ-T allows performing rotary shear experiments inside the μCT machine cabinet so that the tested samples can be scanned *in-situ* and *in-operando*. The variations of physical parameters including normal force, sample shortening, friction and rotation velocity can be measured during the experiment, and then compared against the μCT imagery, resulting in better comprehension of the evolution of the frictional surface.

An experiment was conducted employing an aluminum alloy sample, and the preliminary results showed that the ERDμ-T can correctly measure friction and link its variations to the wearing and fracturing processes that occur on the frictional interface. This experiment also helped to establish a workflow to conduct rotary shear experiments using the ERDμ-T and acquire high-quality data.
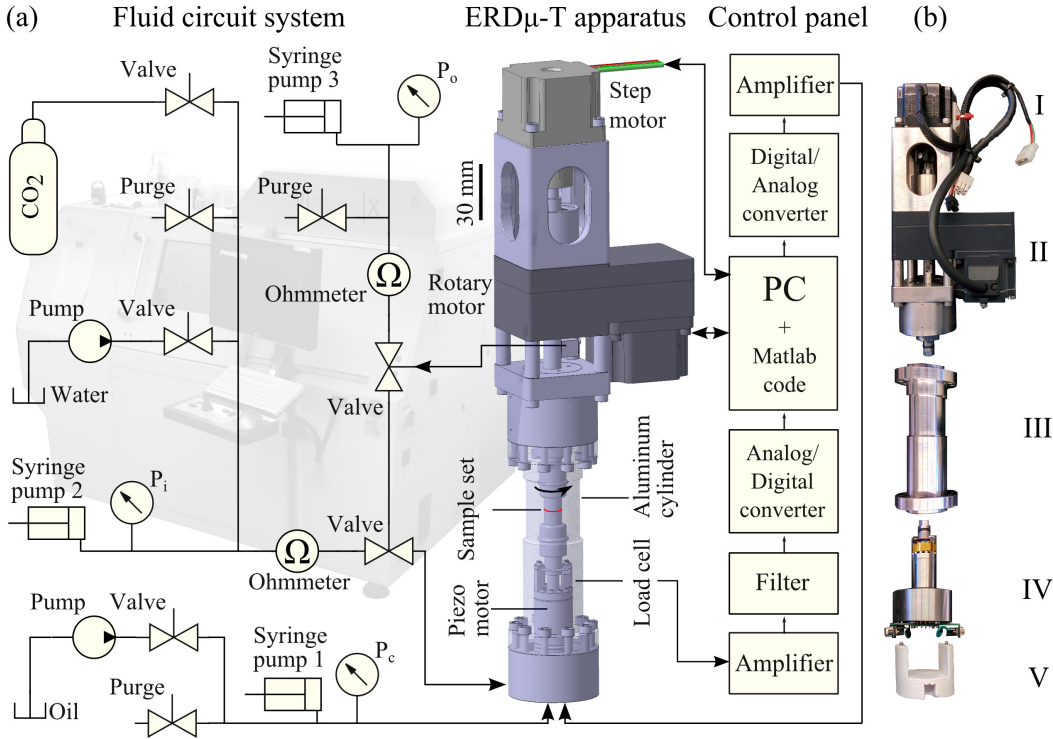
Figure 5.1: The X-ray transparent rotary shear test apparatus ERDµ-T. (a) Schematics of the ERDµ-T system, with the µCT machine in the background (Tisato et al., 2014). (b) The ERDµ-T apparatus. From top to bottom, (I) the linear electromechanical motor, (II) the rotary motor, (III) the cylindrical aluminum alloy pressure vessel, (IV) the load and torque cell and piezoelectric motor, and (V) the apparatus support.

5.2 Specimen preparation and design of the apparatus

The ERDµ-T system has three parts: the ERDµ-T vessel, the fluid circuit system, and the control panel (Figure 5.1a). In Sections 5.2.1–5.2.3, we first introduce the specimen preparation for ERDµ-T tests (Section 5.2.1), followed by the ERDµ-T apparatus (Section 5.2.2), the fluid circuit system, and the control panel (Section 5.2.3).

5.2.1 Specimen preparation

The physical and mechanical properties of aluminum alloy are well documented (Ezazi et al., 2014; Lakshmipathy and Kulendran, 2014; Sudhakar et al., 2015); therefore, it is a suitable material for a reference test. The sample was composed of two 12 mm diameter cylindrical semi-samples, which were placed one above the other during the test. The top semi-sample was 18 mm long and the bottom semi-sample was 15 mm long. The contacting surfaces of the two semi-samples (i.e., the bottom surface of the top semi-sample and the top surface of the bottom semi-sample) were prepared with lathe and

then polished manually with 400 grit sandpaper with average particle diameter of 23 μm. A cone-shaped indentation of 3.8 mm diameter and 2 mm depth was prepared at the centre on each surface. These indentations were created because of the concern that the center area undergoes too little or null displacement that the material may fail due to compression, instead of shearing. However, this effect has very limited impact on the test results.

Prior to the test, the semi-samples were glued onto sample holders with Loctite 454 Prism Instant Adhesive Gel, which secured the semi-samples to the top and bottom part of the apparatus. The sample was covered with a plastic shrink tube to prevent material from escaping from the frictional interface.

5.2.2   The ERDμ-T apparatus

The top semi-sample was mounted to the top part of the apparatus through a vertical cylindrical shaft that transmits to the sample the shear and normal stresses generated by two actuators (Figure 5.1b). The first actuator is a linear electromechanical actuator (Haydon Kerk 57H4A-3.25-807) that can apply, through an angular contact ball bearing system and the cylindrical shaft, up to 890 N of normal force to the sample. This normal load translates to 8 MPa normal stress on a 12 mm diameter sample. The actuator is able to extend or retract with a minimum step of 0.12 μm, allowing for accurate control of the normal load. A pressure compensated piston is located between this actuator and the vertical shaft, which permits the capability of applying hydrostatic pressure, if confining fluid is applied.

The second actuator (Oriental Motor BLE23CR200F) is a rotary motor that can apply torque to the vertical shaft while allowing the shaft to move vertically. This actuator is capable of applying up to 17 N m of torque, resulting in a shear stress of 30 MPa on the sample, which is adequate to deform most sedimentary and metamorphic rocks (Barton, 1974).

The bottom semi-sample was directly mounted to the stainless steel (SS304) load and torque cell. This load and torque cell serves as the pressure vessel enclosure, and together with a piezoelectric motor (PI P-016.10H, with stiffness 270 N/μm), forms the bottom part of the apparatus (Figure 5.2). The load and torque cell uses strain gauges to measure normal load, torque, and sample shortening. Strain gauges for normal force and torque measurements are directly glued onto the stainless steel body of the load and torque cell; whereas, strain gauges for sample shortening measurements are attached on two arc-shaped beryllium copper cantilevers.

The detailed strain gauge configurations are described as follows: (1) the normal force is measured by means of a Wheatstone (full) bridge, which is composed of two strain gauges (HBM 1-LY11-1.5/350) and two fixed resistors (Figure 5.2d); (2) the torque is measured by a Wheatstone bridge consisting of

two half bridge torsion strain gauges (HBM 1-XY21-1.5/350). Each half bridge torsion strain gauge has two measuring grids which are placed at 45° inclination with respect to the vertical axis to capture the deformation caused by torque applied to the vertical axis of the load and torque cell; and (3) the sample shortening is measured by a Wheatstone (full) bridge consisting of four strain gauges (HBM 1-LY11-1.5/350) (Figure 5.2e), and these stain gauges deform with the cantilevers while the sample undergoes shortening.

The piezoelectric motor is placed beneath the load and torque cell. The length of this motor can be controlled by changing the voltage supplied to it ($\sim$0.015µm/V), allowing for accurate and quick control of the normal load, which is used to test the normal stiffness of the sample. In addition, this motor is capable of generating signals at seismic frequencies (Tisato et al., 2014), which could be used to study seismic wave attenuation through the rock interface.

A hollow aluminum alloy (7075-T6) cylinder connects the top and bottom parts of the apparatus and serves as a pressure vessel that encloses the sample. This cylinder is considered X-ray "transparent" due to its relatively low density. The inner diameter of this cylinder is 26 mm, and the outer diameter is 40 mm, resulting in a wall thickness of 7 mm. Specially, at the position where the sample sits, a 40 mm high "imaging window" is created by reducing the wall thickness to 5 mm (Figure 5.1b III).

An electronic board with two DB9 connectors that transmit the data between the apparatus and the control panel is placed at the bottom of the apparatus. A temperature sensor (Texas Instruments LM35, having accuracy of 0.5°C) is placed on this electronic board to capture the ambient temperature and eventually correct for the temperature dependence of all acquired measurements.

5.2.3 The fluid circuit system and the control panel

The fluid circuit system consists of ten ON/OFF fluid valves and three syringe pumps controlled by linear electromechanical actuators (Haydon Kerk 57H4A-3.25-815) (Figure 5.3a). Two syringe pumps and seven valves form the saturation circuit that allows for injection and extraction of the fluid flowing through the sample (e.g., water and CO_2). The third syringe pump, along with three valves, forms the high-pressure oil circuit providing the confining pressure to the sample up to 30 MPa. These motors control the syringe pumps and allow the manipulation of fluid volumes with an accuracy of 2.43 nL, providing precise control of the pore and confining pressures. Moreover, three pressure sensors (Honeywell MLH05KPSB01B) are mounted on the syringe pumps to accurately measure the confining and pore pressure. These pressure sensors have errors of 3% when pressure <2.1 MPa and 2% when pressure ≥2.1 MPa.

The control panel, which controls and monitors the ERDµ-T system, is equipped with three signal
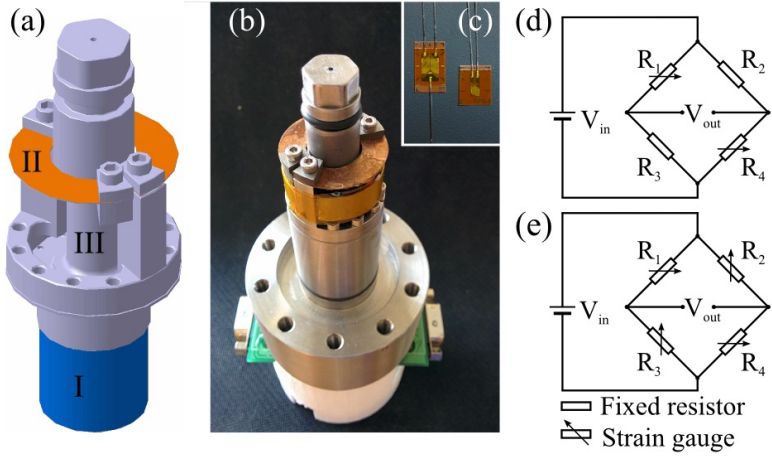
Figure 5.2: (a) Design of the load and torque cell. (I) The piezoelectric motor, (II) a pair of cantilevers where strain gauges for sample shortening measurement are attached, and (III) stainless steel rod where strain gauges for normal load and torque measurements are attached. (b) The bottom part of the ERDµ-T apparatus. (c) HBM 1-XY21-1.5/350 torsion strain gauges (left) and HBM 1-LY11-1.5/350 strain gauge (right). (d) Strain gauge configuration for the normal force measurement. (e) Strain gauge configuration for the torque and shortening measurements.
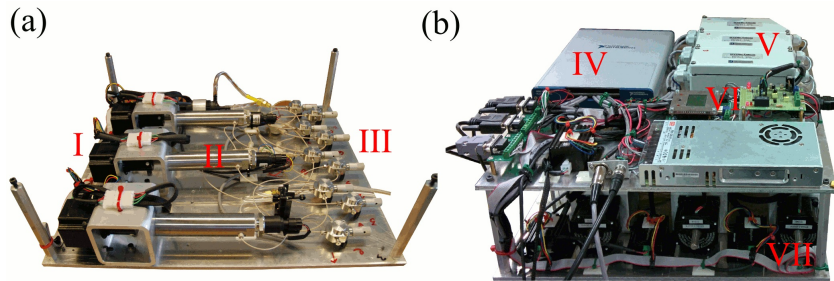
Figure 5.3: (a) The fluid circuit system: (I) electromechanical motors, (II) syringe pumps, and (III) ON/OFF valves. (b) The control panel: (IV) the NI USB-6351 device, (V) signal conditioners, (VI) the Olimex microcontroller, and (VII) the rack that contains the control panel (top) and the fluid circuit system (bottom).
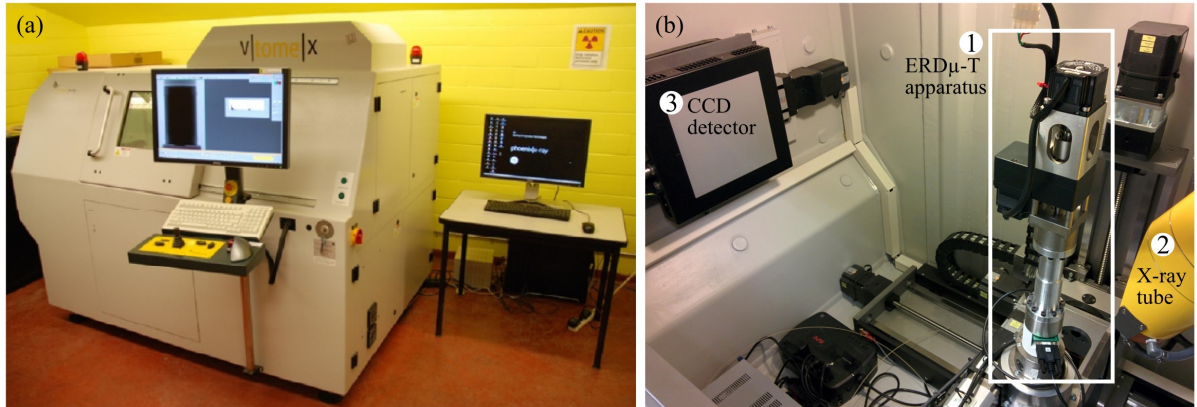
Figure 5.4: (a) Phoenix|X-ray v|tome|x μCT. (b) (1) The ERDμ-T apparatus placed inside the X-ray μCT machine, mounted on the CNC rotation stage; (2) the X-ray tube; and (3) the CCD detector.

conditioners (Durham Instruments Model SGA), an analogue-to-digital and digital-to-analogue converter (National Instrument, NI USB-6351) and an Olimex microcomputer (Figure 5.3b).

The signal conditioners condition the strain gauge signals before they are acquired by the NI USB-6351 device, and the signal conditioning and acquisition processes are reported in the following section. The microcomputer monitors pressures every second and triggers an alarm when confining or pore pressure overcomes a pre-defined threshold. Moreover, the fluid circuit system and the control panel are installed on a compact rack, and together with the ERDμ-T vessel, are placed inside the cabinet of the X-ray μCT machine (Figure 5.4).

Three USB cables connect the ERDμ-T apparatus to the controlling PC that is located outside the μCT cabinet. The first cable converts the signal to RS-485 standard and controls the four linear electromechanical actuators in the system, the second cable controls the rotary motor, and the third cable establishes the communication between the NI USB-6351 device and the computer that allows data transfer. Custom MATLAB codes are used to realize all the functionalities, including apparatus control, data acquisition, and data processing.

5.3 Signal conditioning, acquisition, calibration and error assessment

Analogue signals of strain gauge measurements for normal force (N), sample shortening (S) and torque (M) are first filtered by signal conditioners with 5 kHz low pass filters, and then conditioned using:

$$\eta_c = \alpha(\eta_f + \beta\zeta), \tag{5.1}$$

Table 5.1: Signal conditioning parameters.

η_c	α (mV/V)	β (%)
N	0.39	+30
S	0.39	+76
M	0.80	-15

where η_f is the filtered strain gauge measurement during testing, ζ is the filtered strain gauge measurement while the load cell is not under loading (i.e., tare), α and β are channel-specific gain and offset parameters (Table 5.1), and η_c is the conditioned analogue signal (Interface, Inc., 2007).

The three conditioned analogue signals, along with other analogue signals including pore pressures (inlet, P_i, and outlet, P_o), confining pressure (P_c), temperature (T), and motor rotation (R), are acquired by the NI USB-6351 device. The NI USB-6351 device has a resolution of 16-bits and can acquire data at 1.25 MHz for single channel acquisitions and 1.00 MHz for multi-channel acquisitions. This device converts analogue signals to digital signals and transmit them to the computer. The full scale errors related to the analogue to digital conversion by the NI-6351 device of N, S, M, pressures (P_i, P_o and P_c) and T are 95 μV, 1520 μV, 180 μV, 800 μV and 180 μV, respectively. During the stiffness test, N, S and M are acquired at 250 kHz per channel, and during the rotary shear test, R is acquired additionally at the same rate.

Acquired digital signals (η_d) are converted to physical quantities (κ) according to the calibrations:

$$\kappa = a\eta_d + b, \tag{5.2}$$

where a and b are channel-specific scale and bias parameters (Table 5.2). a and b for pressure and temperature measurements are from sensor specifications, whereas for N and M, these values are obtained using calibrated laboratory instruments. The shortening signal is currently uncalibrated, and shortening can be evaluated qualitatively using voltage data.

N was calibrated using the ELE Digital Tritest 50 Load Frame (Figure 5.5) with two cycles of normal force ranging from 50 N to 850 N. M was calibrated using a Tohnichi 9BTG-A torque gauge (Figure 5.6) with two cycles of torque up to 1 N m in the counterclockwise direction (positive) and clockwise direction (negative). a and b were obtained using a first order polynomial fitting of the value obtained from the calibrated instrument and the voltage reading from the ERDμ-T (Table 5.2).

Relative errors at full scale (%F.S.) including non-linearity error (e_l), repeatability error (e_r), hysteresis error (e_h) and total error (e_t) were assessed systematically (Lipták, 2013). e_l, e_r and e_h of N are 3.80%, 4.84%, and 4.27%, respectively; and these errors of M are 3.77%, 5.13%, and 3.16%, respectively.
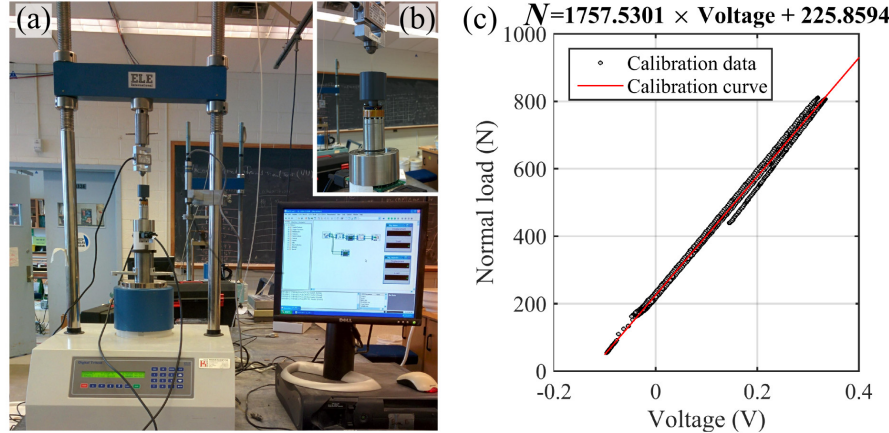
Figure 5.5: Calibration of the normal load using the Digital Tritest 50 load frame. (a) The calibration set-up. (b) Zoom-in view of the calibration set-up, note the PVC cap was used to ensure a stable contact between the press and the load cell. (c) Calibration raw data of normal force measurement and the calibration curve.

Table 5.2: Signal conditioning and calibration parameters and the associated total relative error at full scale.

κ	a	b	e_t (%F.S.)	Unit
N	1757.53	225.86	5.43	N
S	1	0	-	V
M	-2.81	0.03	4.28	N m
P_i	8.98	-8.80	2.02	MPa
P_o	8.98	-8.79	2.02	MPa
P_c	8.98	-8.92	2.02	MPa
T	100	273.15	1.02	K
R	1	0	-	V

e_t of N and M are 5.43% and 4.28%, respectively. e_t of pressures (P_i, P_o and P_c) and T, which are the results of sensor measurement errors and analogue to digital conversion errors, are 2.02% and 1.02%, respectively.

The rotation monitoring signal, R, consists of voltage pulse generated by the rotary motor at each 0.06° of rotation. This signal is converted to the total amount of rotation while conducting the rotary shear test and used to monitor and control the shearing distance. The error associated with the rotation monitoring is ±0.06°.

5.4 Experiment procedure

Here we report the workflow of a ERDμ-T experiment, using the test conducted on the aluminum alloy sample as an example (Figure 5.7):

(1) Test preparation. The testing sample was prepared and mounted in the ERDμ-T apparatus, which
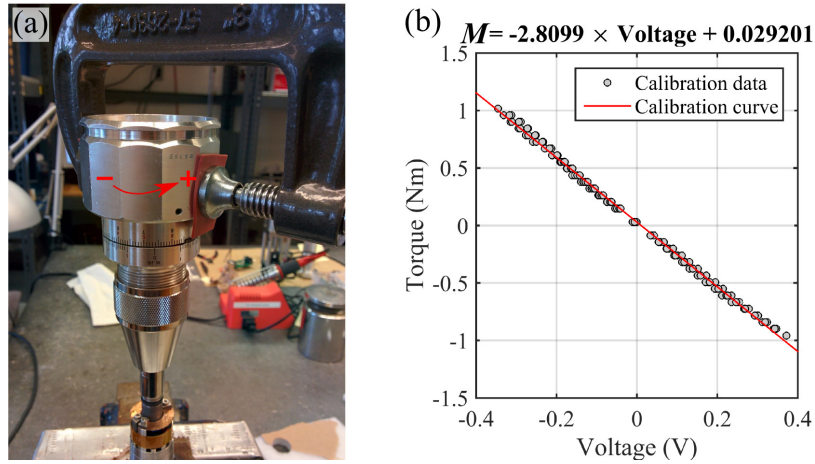
Figure 5.6: Calibration of torque measurement for ERDμ-T. (a) Calibration set-up, the clamp was used to apply torque without introducing normal force. The red arrow indicates counterclockwise rotation, which corresponds to positive voltage. (b) Calibration raw data of the torque measurement and the calibration curve.

was placed onto the 5-axis computer numerical control (CNC) rotation stage inside the X-ray μCT machine (Figure 5.4). The stage was moved to a distance from the source that allowed a resolution of 25 μm for the μCT imagery. The ERDμ-T system was powered on for 15 minutes to warm-up electronic devices and assess stable readings.

(2) Torque baseline test. (i) The torque required to overcome the frictional resistance of the apparatus components, (ii) the torque resistance offered by the shrink tube covering the sample and (iii) the electronic noise introduced by the operation of the rotary motor were measured. These systematic errors were 0.02 N m in total, which was subtracted from the torque measurement when calculating the friction.

(3) X-ray μCT scan. Prior to the experiment, the undisturbed specimen was imaged with the X-ray μCT. During the scan, the ERDμ-T vessel was rotated 360° in 1080 equally spaced increments; meanwhile, the X-ray beam irradiated through the ERDμ-T vessel. At each angle, 5 projections were acquired using 800 ms exposure time and averaged to obtain a 2D 16-bit gray scale image, representing the attenuated X-ray amplitude (Figure 5.8a). The scan was carried out at 100 kV voltage and 249 μA current. All the scans here reported were carried out using the same parameters.

(4) Joint closure. The top semi-sample was carefully lowered using the linear electromechanical motor to a position close to the bottom semi-sample (∼0.5 mm gap).

(5) Initialization. The initialization was used to establish the contact (touch point) between the top
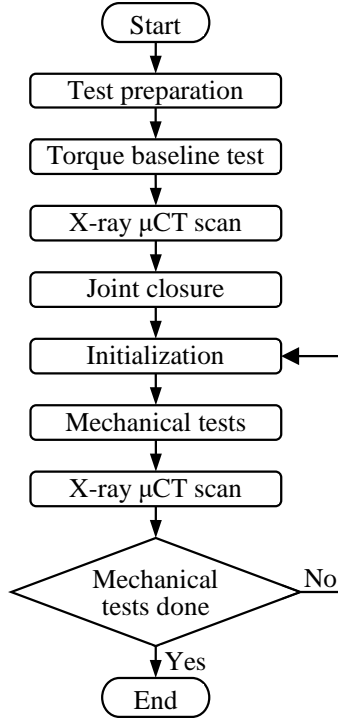
Figure 5.7: Test workflow of the ERDμ-T experiments.

and bottom semi-samples and zero the normal force reading (zeroing). The unzeroed normal force reading was first acquired, and the electromechanical motor was slowly driven down until the normal force reading increased by ∼25 N. Then the top semi-sample was retracted back slowly until the normal force reading stabilized. This stabilized value was then subtracted from the normal force reading to zero it. After first initialization, a normal load of 560 N was applied to the sample. Given the sample dimensions, the resultant normal stress was approximately 5 MPa. The undeformed sample at this initial stress condition was recorded with the μCT.

(6) Mechanical tests. Stiffness test and rotary shear test can be carried out using the ERDμ-T apparatus.

(i) The stiffness test can be conducted by applying cycles of voltage steps to the piezoelectric motor. Custom MATLAB code controls a digital-to-analogue channel of the USB-6351 device to generate an analogue signal as voltage steps, which is amplified by a piezo controller (PI E-501.00 HVPZT-AMPLIFIER) to the operating voltage of the piezoelectric motor (0–1100 V). These voltage steps applied to the piezoelectric motor can generate loading and unloading cycles causing little strain ($\lesssim 0.02\%$) across the sample, allowing for the estimation of effective samples stiffness without inducing plastic deformation.

(ii) The rotary shear test was conducted at a rotation speed of 10°/s. The top semi-sample was rotated incrementally for 8 steps at 180° per step. During each rotation, the sample was accelerated to the desired speed in 0.1 second and stopped instantaneously at the desired shear distance. The small rotation step size allowed for imaging the morphological evolution of the slipping surfaces and the formation/evolution of the gouge layer. Note that normal force was not controlled during the rotation and the emerging values of the normal force were recorded.

During the mechanical tests, the apparatus was kept stationary (i.e., the CNC stage was not rotating) and two-dimensional (2D) X-ray radiographies (i.e., shadow projections) of the sample were acquired at 4 FPS frequency.

(7) X-ray µCT scan. After each incremental rotation step, an X-ray µCT scan was carried out.

(8) Steps 5-7 were repeated until all the desired mechanical tests were finished.

5.5   Data processing

5.5.1   Mechanical data processing

During the post processing, the normal load (N), sample shortening (S), and torque (M) data were filtered with moving average filters with window sizes of 125 data points to improve the signal-to-noise ratio. As a consequence, the acquisition rate was considered to be 2 kHz. The filtered N and M data are used to calculate the friction coefficient (μ) using:

$$\mu = \frac{\tau}{\sigma} = \frac{3M(R^2 - R_0^2)}{2N(R^3 - R_0^3)},$$

(5.3)

where τ is the shear stress, σ is the normal stress, R_0 is the inner radius of the sample and R is the outer radius. When $R \gg R_0$, this equation can be simplified as:

$$\mu = \frac{3M}{2NR},$$

(5.4)

and the error associated with μ ($\sigma\mu$) can be estimated using error propagation:

$$\sigma\mu = \mu\sqrt{\left(\frac{\sigma M}{M}\right)^2 + \left(\frac{\sigma N}{N}\right)^2},$$

(5.5)

where σM and σN are the errors associated with torque and normal force measurements, respectively. $\sigma\mu$ is proportional to μ, and when $\mu = 1$, $e_t = 6.91\%$.

Angular rotation speed (ω) during each 0.06° rotation interval was calculated by the ratio between the rotation amount and time duration. The averaged velocity (v) on the shearing surface was calculated using

$$v = \frac{\omega\pi\left(R + R_0\right)}{360°}.$$

(5.6)

We calculated the average friction value in each 0.06° rotation interval and examined it against the velocity data to study the relation between friction and sliding velocity. Moreover, for the stiffness test data, in addition to the moving average filtering, the average values of N and S acquired at each strain step were calculated.

5.5.2 μCT imagery data processing

The μCT scan generated 1080 images that were 794 by 1024 pixels at 25 μm resolution (Figure 5.8a), and these images were reconstructed into a 3D volume (Figure 5.8b) using the Phoenix X-ray datos-x-reconstruction software (v.1.5.0.22). Parameters used for reconstruction were: a beam hardening correction of 3/10, an automatic ring artifact reduction, and a scan optimization which compensates for small translations of the specimen during scanning and accurately locates the center of reconstruction (Tisato et al., 2015).

Reconstruction produced an image stack formed by 1024 16-bit grayscale images with dimensions of 794 by 794 pixels. In this reconstructed imagery, different grayscale values can be approximated as different densities, which can be associated to specific materials or phases. Based on such information, the reconstructed volume was then segmented to produced a 3D model of the specimen using the free version of the commercial software Mevislab (Ritter et al., 2011). The following steps were taken for the segmentation process:

(1) The reconstructed image stack was cropped to the volume of interest. Particularly, the volume adjacent to the shearing surface was used for the segmentation.

(2) A Digital Imaging and Communications in Medicine (DICOM) imagery file was generated from the cropped image stack (Figure 5.8b).

(3) Using a "2D marked view editor", an original seed representing aluminum was manually placed on the DICOM imagery.
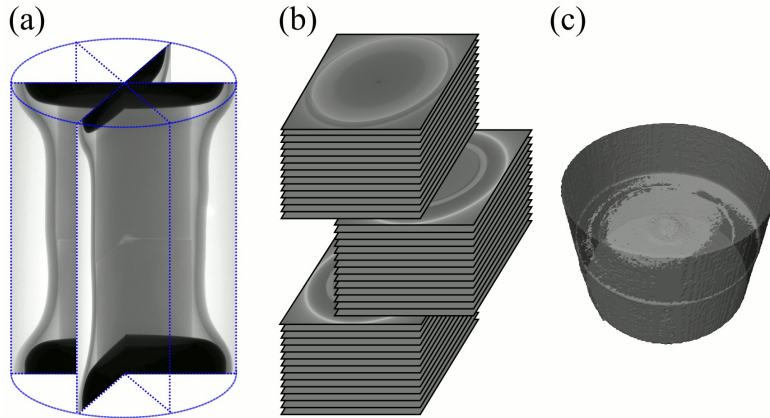
Figure 5.8: Example of the X-ray μCT acquisition, reconstruction, and segmentation process. (a) Acquisition of 16-bit grayscale images. (b) Reconstructed 3D volume, viewed as an image stack, in which the middle part is the area of interest. (c) 3D visualization of the middle part of the segmented sample volume.

(4) A "region growing" segmentation procedure was applied to search for voxels adjacent to the original seed that have grayscale level within the user defined threshold (2.18%). The new identified voxels became new seeds and the "region growing" procedure was repeated until no new seeds were found. The segmentation threshold was obtained by increasing the initial threshold value (1%), at incremental steps of 0.01%, until the segmentation satisfied the following criteria: (i) the segmented region covers the entire sample volume, and (ii) the segmented region does not over-estimate the sample volume by, for example, including the covering shrink tube. This segmentation procedure generated a volume representing the sample.

(5) The segmented volume was rendered and captured as images using the "WEM inspector" toolbox, and microscopic structures on the shear surface could be visually inspected (Figure 5.8c).

5.6 Preliminary results and discussion

The friction coefficient of the aluminum alloy surface ranged between 0.2 and 0.5 which is in agreement with the literature (Figure 5.9) (Ezazi et al., 2014; Lakshmipathy and Kulendran, 2014; Sudhakar et al., 2015). However, during the rotation between 5π to 6π, the friction coefficient increased above 1, which is similar to the friction reported on aluminum alloy surface with manually introduced micro-structural roughness (Sanchez-Santana et al., 2006).

The segmented μCT imagery showed that a narrow ring-shaped high density zone formed when the normal force was applied, which suggested compaction on the frictional surface (Figure 5.10a). This
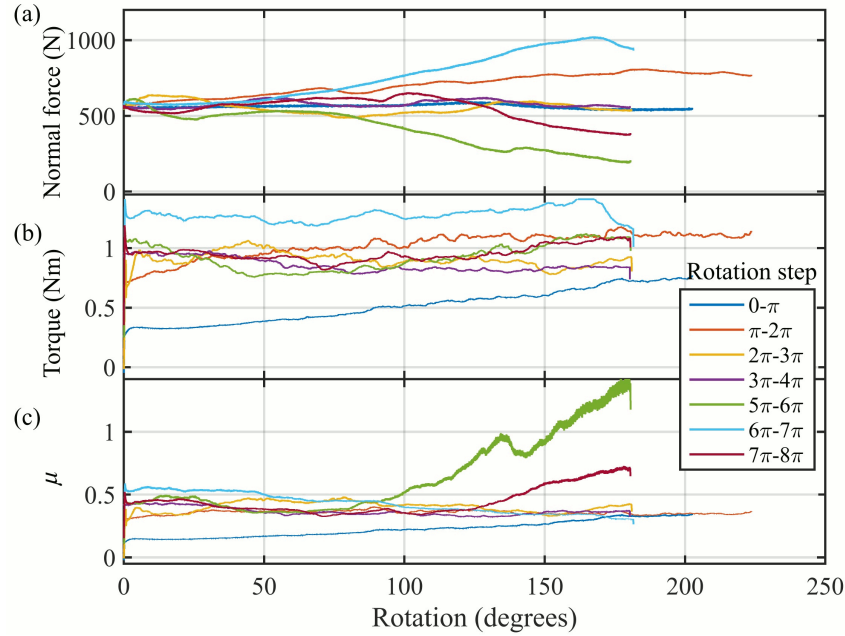
Figure 5.9: The variations of (a) normal force and (b) torque recorded during the rotary shear test, and (c) the calculated friction coefficient. Note that the data during rotations between 4π–5π are missing.

narrow area endured high normal stress during testing and after a complete turn (i.e., 2π of rotation), a wearing zone was formed, characterized by a ring-shaped striae and two spots of fragments (Figure 5.10b). The fragments indicates adhesive wear behaviour, which is a common frictional behaviour of metals (Rabinowicz, 1965; Aghababaei et al., 2016). The accumulation of fragments during rotation introduced micro-structural roughness to the sliding surface, which may have resulted in dilatation of the shearing interface (Figure 5.10c&d), change in actual contact area (Figure 5.10e&f), and abnormally high friction (e.g., rotation between 5π to 6π).

Assessing the real contact area is essential to the understanding of friction, and it is convention-ally studied using transparent materials, such as polymethyl methacrylate (PMMA) (Ben-David et al., 2010b). We demonstrate here that ERDμ-T is capable of observing this important feature.

To confirm theses interpretations from mechanical data and μCT imagery, the specimen was removed from the apparatus at the end of the experiment and a micrograph of these distinguished features on the sliding surface was captured. The striae and fragments due to adhesive wear were evident (Figure 5.11b-e).
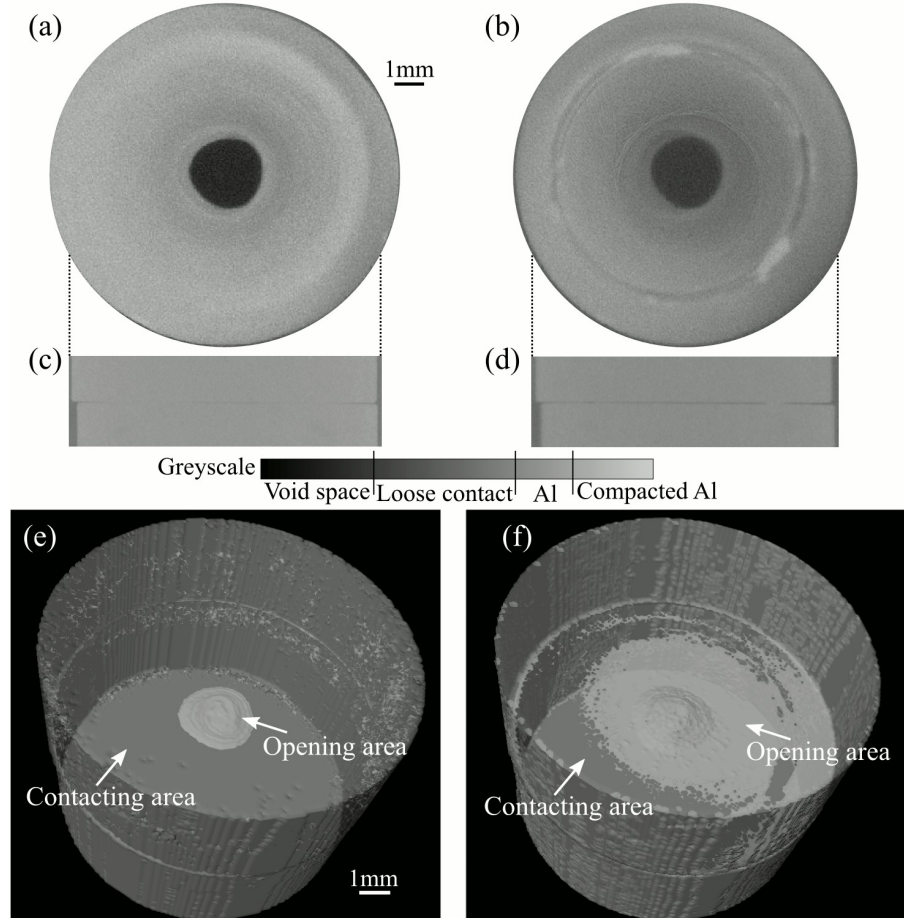
Figure 5.10: Reconstructed µCT scan images (with enhanced contrast) of the shear surface (a) before rotation and (b) after 2π of rotation. (c) and (d) are vertical slices at the same location demonstrating the dilatation induced by aluminum fragments. (e) and (f) are 3D rendering view of the segmented volumes. Before shearing, the sliding interface was in close contact (i.e., can "see through") except for the central indentation (dull-white colored) area; whereas after 360° of rotation, the contacting area has been decreased significantly by approximately 50% due to the microscopic roughness.
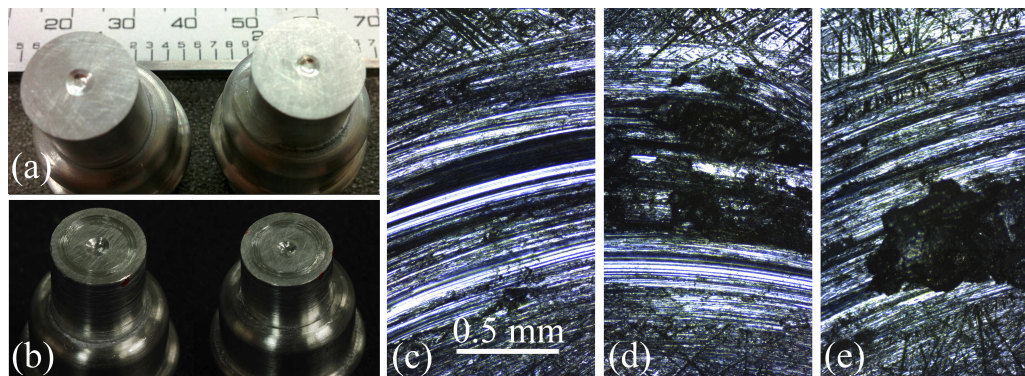
Figure 5.11: Aluminum specimen, before and after the rotary shear test. (a) Aluminum sample before the test, (b) Aluminum sample after the test, (c) striae created by the frictional sliding, and (d) & (e) material deposits on the striae. (c)-(e) are viewed using optical microscope with a 60X magnification.

5.7 Conclusions

Physical and mechanical properties of geomaterials are strongly influenced by their microscopic features, making the ERDμ-T apparatus very suitable to study their response under shear as it allows for inspecting the rock interior, continuously in time and space, without introducing undesired perturbation. Thanks to the ERDμ-T, large amount of information from the μCT imagery is available, allowing a more comprehensive interpretation of the frictional sliding behaviour than that solely relying on mechanical data. Preliminary test results demonstrate the capabilities of ERDμ-T in accurately measuring friction and concurrently linking it to the damage process of the frictional interface.

The analysis of the deformation and frictional strength of rock asperity under μCT opens up promising opportunities in exploring microscopic rock features. Moreover, at micrometric resolution, the ERDμ-T can be utilized to observe the role of gouge materials on rock friction. In addition to the capabilities demonstrated in this paper, the ERDμ-T apparatus can be further developed to conduct seismic wave attenuation tests, linking the evolution of rock asperities to its dynamic elastic moduli. Acoustic emission sensors can also be attached to the vessel, which can be used to study the triggering of earthquake (i.e., microseismic) events.

Supplementary material

This supplementary material includes the detailed derivations of the friction equations (5.3)–(5.5).

The sample, taking the bottom part as an example, has an inner radius of R_0 and an outer radius of R. We calculate the friction coefficient (μ) using the ratio between the shear stress (τ) and the normal stress (σ)

$$\mu = \frac{\tau}{\sigma}, \tag{5.7}$$

where σ can be calculated from the normal load (N) and the area of the shear surface (A), and τ needs to be calculated from the measured torque (M).
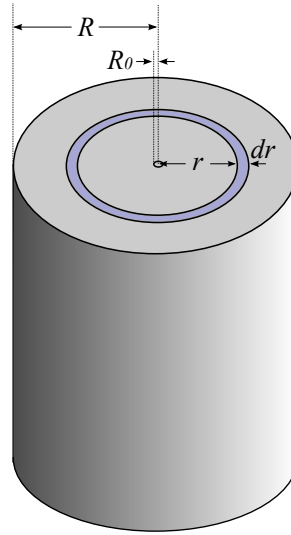
Figure 5.12: Schematic diagram of the bottom part of the sample.

Torque is calculated as the product of force (F) and distance (L): $M = FL$. Now we first investigate an infinitesimal ring at distance r from the center, with a width of dr and an area of dA. The infinitesimal force dF on this ring can be expressed as $dF = \tau dA$, which gives the torque on this ring dM:

$$dM = \tau r dA, \tag{5.8}$$

where

$$dA = \pi(r + dr)^2 - \pi r^2. \tag{5.9}$$

M is the calculated through an integral of dM over the radius range of the shear surface:

$$M = \int_A \tau r dA = \int_{R_0}^{R} 2\pi \tau r^2 dr, \tag{5.10}$$

which gives:

$$M = \frac{2\pi\tau(R^3 - R_0^3)}{3}.$$
(5.11)

Thus, the shear stress is calculated using the torque as:

$$\tau = \frac{3M}{2\pi(R^3 - R_0^3)}.$$
(5.12)

Knowing that

$$\sigma = \frac{N}{\pi(R^2 - R_0^2)},$$
(5.13)

the friction coefficient can be calculated by

$$\mu = \frac{\tau}{\sigma} = \frac{3M(R^2 - R_0^2)}{2N(R^3 - R_0^3)}.$$
(5.14)

Specially, if the center indentation is very small that $R_0 \ll R$, the friction coefficient is then simplified as:

$$\mu \approx \frac{3M}{2NR}.$$
(5.15)

The error associated with μ can be estimated through error propagation:

$$\sigma\mu = \sqrt{\left(\frac{\partial\mu}{\partial M}\right)^2 + \left(\frac{\partial\mu}{\partial N}\right)^2}$$
(5.16)

which gives

$$\sigma\mu = \mu\sqrt{\left(\frac{\sigma M}{M}\right)^2 + \left(\frac{\sigma N}{N}\right)^2}$$
(5.17)

where σM and σN are the errors associated with torque and normal force measurements, respectively.

ERDμ-T control GUI

A graphic user interface (GUI) to control and monitor the ERDμ-T apparatus and a detail diagram of the fluid circuit system are provided in Appendix C.

Chapter 6

Direct observation of faulting by means of a rotary shear test under X-ray micro-computed tomography

Abstract

Friction, fault surface evolution, and energy budget are critical aspects in earthquake studies, and they have been puzzling scientists for decades. Here we present the preliminary result from a novel experimental approach that combines rotary shear testing with X-ray micro-computed tomography (μCT) technology. An artificial fault was sheared at small incremental rotational steps under the normal stress of 2.5 MPa. During shearing, mechanical data including normal force and torque were measured and used to calculate the friction coefficient (μ). After each rotation increment, a μCT imagery data set was acquired to observe the sample structure. The careful and quantitative μCT image analysis allowed for direct and semi-continuous observation of the fault evolution. We observed that (1) fracturing due to asperity interlocking and breakage dominate the initial phase of slipping; (2) frictional behaviour stabilized after ∼1 mm slip distance, which inferred the critical slip distance (D_c); (3) the real contact area on the fault is ∼10% of the nominal fault area; and (4) the energy consumed by generating secondary fractures and seismic wave radiation is approximately 0.1–0.4% and 14.0–15.8% of the total released energy, respectively.

6.1 Introduction

The frictional strength of faults during earthquakes is an essential but unknown parameter controlling earthquake physics. Laboratory and field observations suggest that earthquake initiation, propagation, and termination are related to how friction varies as a function of time, stress, sliding velocity, slipping distance, and contact geometry (Brace et al., 1966; Byerlee, 1978; Scholz, 1998; Reches and Lockner, 2010; Di Toro et al., 2011). Despite extensive investigations, there are still many unanswered questions related to the frictional slip behaviour on faults, for example, the evolution of fault surfaces and the energy budget of earthquake events.

To study friction in faults, laboratory shear experiments have been conducted on a large variety of rocks under different conditions, and these studies contributed greatly to the understanding of earthquake physics (e.g., Beeler et al., 1996; Marone, 1998; Mair and Marone, 1999; Di Toro et al., 2004; Reches and Lockner, 2010; Di Toro et al., 2011; Goldsby and Tullis, 2011; Tisato et al., 2012). Some measurements have been the foundation of theoretical models that describe friction in rocks from a microscopic perspective by considering the interaction of surface asperities (e.g., Dieterich, 1978; Sammis and Biegel, 1989). Many studies suggested that frictional behaviour is also intimately related to mineral composition, fluid, and gouge material properties (e.g., Biegel et al., 1989; Marone and Scholz, 1989; Di-

eterich and Kilgore, 1996; Kanamori and Heaton, 2000; Morrow et al., 2000; Mair et al., 2002; Anthony and Marone, 2005; Niemeijer et al., 2010a,b; McLaskey and Glaser, 2011). On the other hand, fault surface roughness, at various scales, is also an important factor to the frictional behaviour (e.g., Power et al., 1988; Power and Tullis, 1991; Schmittbuhl et al., 1993; Chester and Chester, 2000; Ma et al., 2003; Sagy et al., 2007; Bistacchi et al., 2011; Candela et al., 2011; Shervais and Kirkpatrick, 2016). To date, these laboratory studies allowed only post-mortem examination of the deformed samples, making microscopic analysis of the fault challenging. In fact, to characterize and observe the deformed specimen, the sample assembly is typically removed from the testing facility and opened. This leads to a loss of fault gauge and asperity alignment.

X-ray micro-computed tomography (μCT), which provides a non-destructive technique to inspect the internal structure of the sample, is increasingly used to study geomaterials (e.g., Raynaud et al., 1989; Johns et al., 1993; Renard et al., 2004; Ritman, 2004; Viggiani et al., 2004; Desrues et al., 2006; Vanorio et al., 2011; Tisato et al., 2014, 2015; Zhao et al., 2015a; Renard et al., 2016). μCT discretizes the sample into three-dimensional (3D) micrometric subdomains (i.e., voxel) and measures the X-ray attenuation coefficient of each subdomain. The attenuation coefficient, usually represented by grayscale values, can be assumed to be proportional to the material density (Ritman, 2004). Zhao et al. (2017) developed a new rotary shear test apparatus (ERDμ-T) that allows performing rotary shear experiments while the internal structure of the samples and the slipping surface is observed by means of μCT.

In this study, a rotary shear experiment was conducted on an artificial fault using the ERDμ-T apparatus. The artificial fault (referred to as the fault in the following discussion) was created using micro-fine calcium sulphate cement mortar (i.e., Flowstone) to resemble the surface geometry and strength of natural limestone faults. The fault surfaces (i.e., shear surfaces) were characterized using 3D surface scan prior to the test. The fault was then sheared at incremental rotational steps, and during shearing, mechanical data including normal force and torque were measured. After each step, an X-ray μCT scan was acquired. Thorough analysis of the mechanical and μCT imagery provided direct observation of important features such as the real contact area on the fault, the surface area of shear induced fractures, and the wearing of the fault surfaces. These observations provide key information for improving the understanding of the frictional behaviour and energy budget of earthquake events. Moreover, this work provides a framework to study faulting using μCT technology.

6.2   Material and methods

6.2.1   Sample preparation

The sample used for the rotary shear experiment was made of the gypsum mortar: Flowstone by King Concrete Products. Flowstone is mechanically similar to natural limestones (Table 6.1) and is an appropriate material for the purpose of studying rock friction and shear-induced asperity degradation (Tatone, 2014).

The Flowstone sample was prepared using the following procedure: (1) a Teflon tube with 12 mm inner diameter and 32 mm length was prepared as a mold; (2) tap water at room temperature was degassed in a vacuum chamber for 10 minutes; (3) the degassed water and Flowstone powder were mixed in a clean container at a weight ratio of 1:4; (4) the mixture was stirred to a "batter-like" consistency and then poured into the mold on a vibration table; (5) the sample was allowed to cure at room temperature in the mold for 1 day and then removed from the mold by means of a 12 mm diameter piston; (6) the sample was allowed to further cure for approximately 12 months (note that the strength of the Flowstone increases with curing time, and after 100 days, the change in strength is minimal (Tatone, 2014)); (7) a ∼0.25 mm deep groove was carefully carved (using a tube cutter) along the circumference at the midheight of the recomposed Flowstone sample; (8) the sample was then transversely divided in the middle into two semi-samples by means of three-point bending (ASTM, 2002), which resulted in a tensile fracture nucleated from the groove, representing the initial fault surfaces; (9) a cylindrical hole of 2.5 mm diameter and 3 mm depth was drilled in the centre of one of the semi-samples, and this semi-sample served as the top of the sample assembly.

Note that the hole was drilled because of the concern that the centre area of the shear surface undergoes too little or no displacement that may result in failure due to compression instead of shearing. Moreover, a small piece of biotite fragment was unintentionally mixed in the Flowstone while casting and exposed on the surfaces of the fault. This artifact, however, did not show obvious influence on the frictional behaviour based on our subsequent interpretation.

Prior to the test, a strip of thin copper tape was glued vertically to the side of the recomposed sample and then cut along the fault. The copper tape served as a marker and when the ERDμ-T vessel was closed and placed inside the μCT, it was visualized under the X-ray radiation allowing for (1) aligning of the two semi-samples before testing and (2) checking the imposed rotation of the top semi-sample with respect to the bottom semi-sample during testing. The semi-samples were glued onto the sample holders with Loctite 454 Prism Instant Adhesive Gel, and then securely attached to the top and bottom part of the apparatus. A shrink tube was used to cover the fault to prevent gouge material from escaping

Table 6.1: Properties of the Flowstone, after Tatone (2014).

Material property	Value	Unit
Bulk density, ρ	1780	kg/m^3
Porosity[1], ϕ	26	%
Young's modulus, E	15	GPa
Poisson's ratio, ν	0.24	–
Uniaxial compressive strength, σ_c	50.3	MPa
Internal friction, f_i	0.42	–
Cohesion, c	16.4	MPa
Tensile strength, σ_t	2.6	MPa
Mode I fracture toughness, K_{Ic}	0.55	MPa m$^{1/2}$

[1] Helium pycnometer measurement.

during the rotary shear test.

6.2.2 Shear surface topography characterization

In order to characterize the initial condition of the shear surfaces, they were scanned using the Advanced Topometric Sensor (ATOS) II system manufactured by GOM. The ATOS II topometric system measures 3D coordinates of the surface via the projection of various structured white-light fringe patterns onto the surface. Images of these patterns are recorded by two digital cameras from two different angles, and 3D coordinates of each pixel in the images are computed with high accuracy using a triangulation method and digital image processing (Tatone and Grasselli, 2009). The 3D point cloud was used to create a triangulated surface where each triangle was defined by vertices and the orientation of the vector normal to the plane of the triangle. This information was stored in the computer using the stereolithography (i.e., STL) format.

6.2.3 Experiment set-up and procedure

The rotary shear test was performed using the following steps, similar to those indicated by Zhao et al. (2017):

(1) Test preparation. The ERDμ-T vessel containing the sample was mounted on the 5-axis computer numerical control (CNC) rotation stage of the μCT scanner (Figure 6.1). The stage was moved to a distance from the X-ray source ensuring a voxel resolution of 25 μm. The ERDμ-T apparatus was then powered, and before starting the test, we waited 15 minutes to allow for warming-up to ensure stable readings.

(2) Torque baseline test. While the semi-samples were still separate, we imposed a 360° rotation to the top semi-sample and measured the torque. This test allowed us to obtain the systematic error
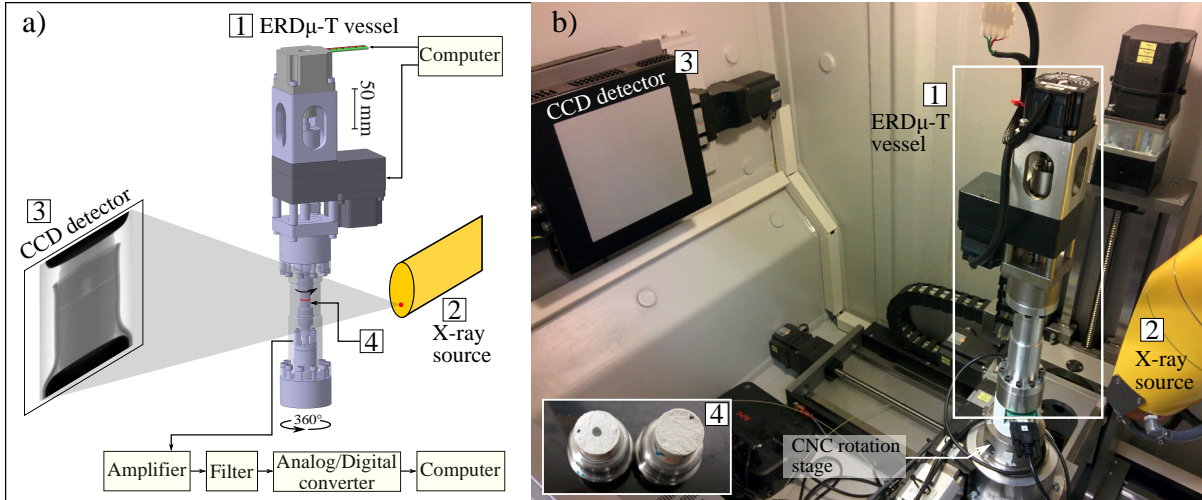
Figure 6.1: (a) Schematic illustration of the ERDμ-T experiment set-up. (b) The actual set-up of an ERDμ-T experiment. (1) The ERDμ-T vessel placed inside the X-ray μCT machine, mounted on the CNC rotation stage, (2) the X-ray source, (3) the CCD detector, and (4) the Flowstone sample.

of the torque measurement resulted from the calibration error, electronic noise introduced by the rotary motor operation, and the friction offered by the jacket covering the fault. Such an error was then averaged to estimate the torque baseline value, which was subtracted from the torque measurements in successive tests.

(3) X-ray μCT scan. Prior to the experiment, a μCT scan was conducted on the undisturbed specimen. The scan was carried out at 100 kV voltage and 249 μA current. During the scan, the ERDμ-T vessel was rotated 360° in 1080 equally spaced increments; meanwhile, the X-ray beam irradiated the external surface of the ERDμ-T vessel. At each angle, five 800 ms exposure time projections, were acquired and averaged to obtain a 16-bit greyscale image.

(4) Fault closure. The top semi-sample was first rotated till the two strips of copper tapes aligned so that fault surfaces were in matching position. Then, it was carefully moved down by the linear electromechanical motor until the top and bottom semi-samples were ~0.5 mm apart.

(5) Shear test initialization. The initialization was used to establish the contact between the top and bottom semi-samples and zero the normal force reading (see detailed description in Zhao et al. (2017)). After the first initialization, a normal load of 280 N was applied to the sample. Given the sample dimensions, the resultant normal stress was approximately 2.5 MPa. We then conducted a μCT scan.

(6) Mechanical tests.

(i) Prior to each rotation step, the normal stiffness test was performed, which allowed us to measure the apparent normal stiffness of the entire sample. However, because the vertical-shortening sensor was not calibrated, the results provided only qualitative information about how the apparent stiffness of the sample varied with vertical deformation. The results are provided in the supplementary material for completeness.

(ii) Finally, the rotary shear test was conducted. In particular, the top semi-sample was rotated incrementally for two 3° rotation steps (Rot. I and II) and four 6° steps (Rot. III to VI). During each rotation, the top semi-sample was accelerated to 3°/s in 0.1 second and stopped almost instantaneously when the desired amount of rotation was reached. During rotation, normal force (N) and torque (M) were recorded at 250 kHz, and the rotation distance was monitored every 0.06° of rotation. Note that the torque signal exceeded the full scale of the instrument (1.5 N m) during Rot. II. To avoid this from reoccurring, the full scale of the torque acquisition channel was doubled for the successive tests. Moreover, after each incremental rotation step, we acquired a μCT dataset allowing for *in-situ* and *in-operando* imaging of the morphological evolution of the sample.

(7) Steps 5–6 were repeated until a stable frictional behaviour was observed after ∼30° of rotation.

6.3   Results and data analysis

6.3.1   Surface topography scan results

The ATOS II scanner digitized the undisturbed fault surfaces at 44 μm grid interval and with a vertical accuracy of 1 μm (Figure 6.2a&b). These surfaces matched since they were created by tensile fracturing, and for the sake of simplicity, in the following analysis, we focus on the bottom surface.

The best-fit plane of the digitized surface was first obtained, and then, the coordinate system was transformed such that the best-fit plane was horizontal. Taking this horizontal plane as the reference (i.e., $z = 0$), the elevation of the rough surface was calculated. Elevation ranged from -0.34 to 0.33 mm, resulting in an overall surface amplitude of 0.67 mm. The region with the largest surface amplitude was located 5.6 mm from the centre of the surface. The surface scan also provided an accurate measurement of the surface size: the outer radius of the surface was $R = 5.95$ mm, and inner radius (i.e., radius of the centre indentation) was $R_0 = 1.25$ mm. Therefore, the nominal contact area (A_n) of the fault was 106 mm^2.

Even though rotary shear is a commonly used method to study fault evolution, a quantitative ap-
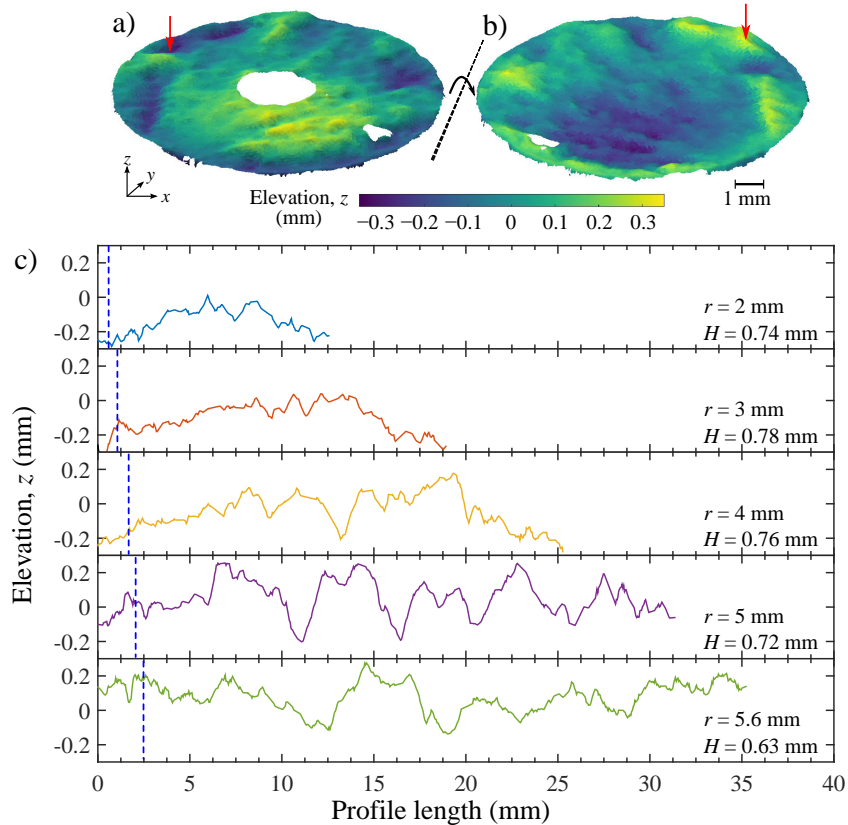
Figure 6.2: 3D surfaces scan of the faults. (a) The top surface and (b) the bottom surface. The red arrows indicate the location with the largest surface amplitude. (c) Five example profiles extracted from the scanned surface, at radii $r = 2, 3, 4, 5$, and 5.6 mm, respectively. The blue dashed lines indicate the total shear distances at different radii. The Hurst exponent (H) of these example profiles are also provided.

proach to evaluate the roughness of the rotary shear sample does not exist. Fault surface at different radii experienced different slipping distances and were subjected to different slipping rates. To account for this fact, we extracted five circular profiles at five different radii from the digitized 3D surface. Then we used roughness characterization methods to gain insights about the roughness of the initial fault surface (Figure 6.2c).

To characterize these profiles, we first employed the power spectral density (PSD) method (Brown and Scholz, 1985; Candela et al., 2009). This method describes the profiles using spectral amplitude and spatial frequency (i.e., wavenumber), which typically exhibit linear relation in log-log scale. The amplitude of the power spectrum indicates how steep a profile is (i.e., roughness); while the slope of the spectrum, referred to as the Hurst exponent (H) (Hurst, 1951), indicates how the roughness changes across scales (Figure 6.3).

The amplitudes of the PSD curves with radii $r \geq 3$ mm were higher than the ones with $r < 3$ mm,
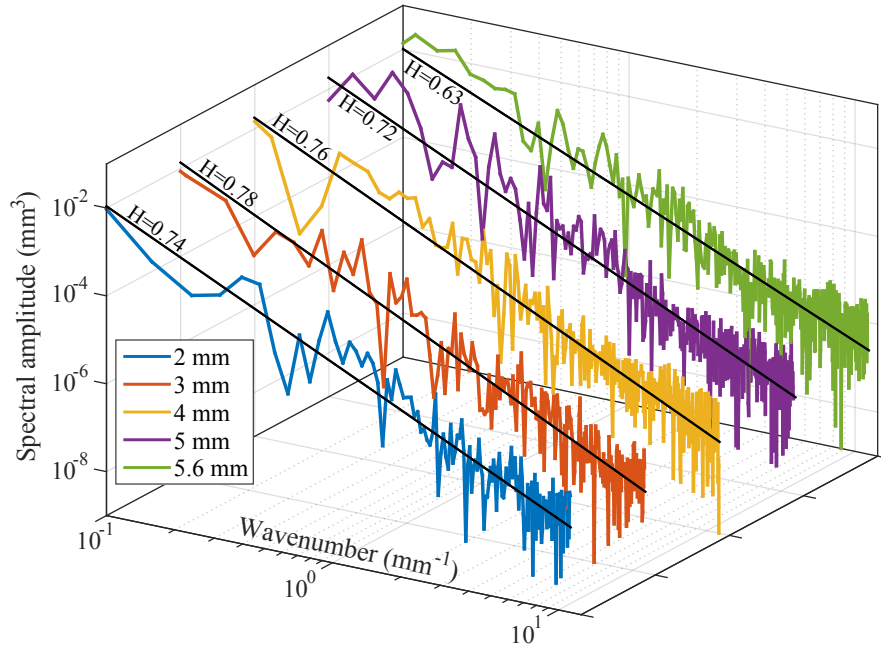
Figure 6.3: Power spectral density curves and their fitted curves of the example profiles extracted from the surface at radii of $r = 2$, 3, 4, 5, and 5.6 mm, respectively. The Hurst exponent (H) of these example profiles are presented with the fitted curves.

showing that the shear surface was rougher at the outer region than the centre region. This was confirmed by visual inspection of the scanned surface that the elevation variation was more significant when $r \geq 3$ mm. The location of the largest elevation variation was located at the radius of 5.6 mm (Figure 6.2). On the other hand, H of the profiles fluctuated between 0.54 and 0.84, reporting an average value of 0.73. However, no clear relation between H and r was observed.

6.3.2 Mechanical data

The shear stress (τ) and friction (μ) were calculated using measured torque (M), normal force (N), and the outer and inner radii of the shear surface (R and R_0) following Zhao et al. (2017):

$$\tau = \frac{3M}{2\pi \left(R^3 - R_0^3\right)}, \tag{6.1}$$

and

$$\mu = \frac{3M \left(R^2 - R_0^2\right)}{2N \left(R^3 - R_0^3\right)}. \tag{6.2}$$

For the data where the torque channel was saturated at 1.5 N m (i.e., during Rot. II) the torque was assumed to be 1.5 N m. The systematic error of torque measurement, which was 0.02 N m according to the torque baseline test, was subtracted from the torque data when calculating the friction.
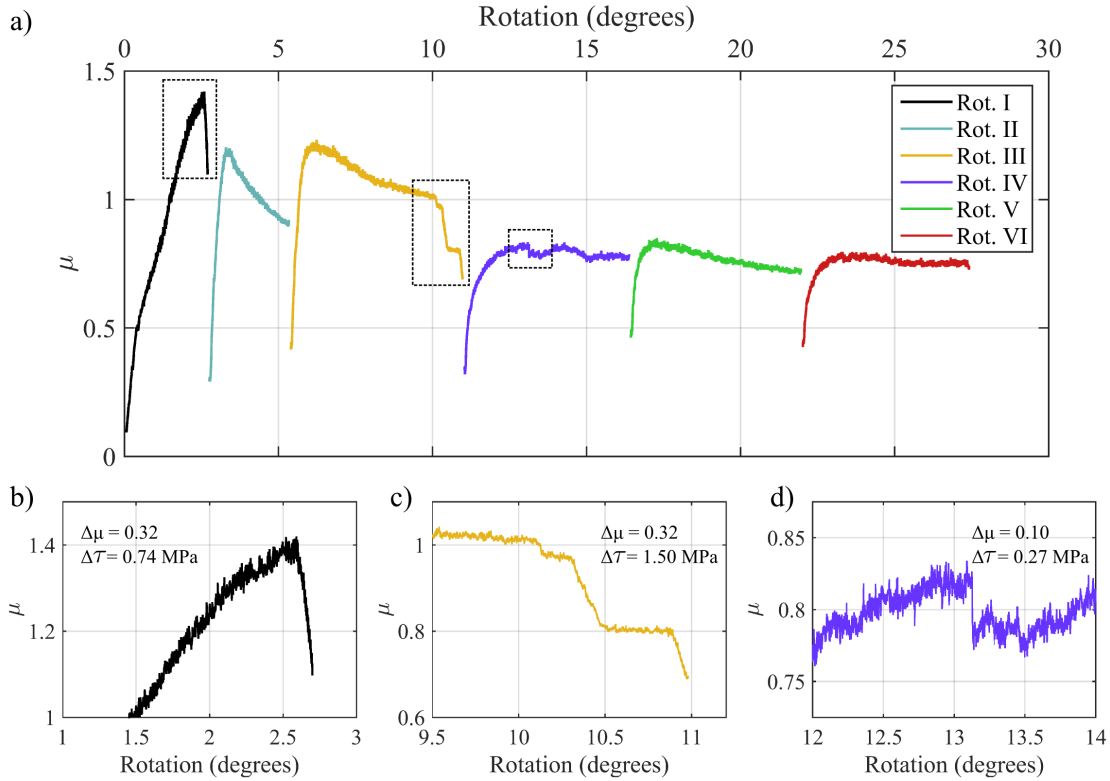
Figure 6.4: (a) Friction coefficient (μ) as a function of rotation distance for rotation steps Rot. I to Rot. VI. Note that μ at Rot. II was relatively low compared to Rot I&III, which is caused by the saturated torque measurement signal. (b)–(d) Zoom-in view of significant friction drops during first three rotation steps.

For Rot I, the initial friction value (μ_i) was 0.1. For consecutive rotation steps, μ_i varied between 0.3 and 0.5 (Figure 6.4a). The peak friction coefficients (μ_p) recorded during the first three steps were > 1, and at the end of Rot. I, friction reached the maximum value of 1.4. After this point a significant ($\sim 20\%$) drop in friction occurred (Figure 6.4b). For Rot. II, μ_p was relatively low compared with Rot I. and Rot. III, which may be related to the saturated torque measurement signal. Judging from the general trend of friction variation, μ_p of Rot. II maybe approximately 1.3, slightly higher than the 1.2. At the end of Rot. III, three consecutive friction drops occurred, and the friction decreased from 1 to 0.7 (Figure 6.4c). During Rot. IV, the μ_p was 0.84 and a small (< 10%) drop of friction occurred (Figure 6.4d). These friction drops corresponded to the shear stress drops of 0.74 MPa, 1.5 MPa, and 0.27 MPa, respectively. During the last two rotation steps (Rot. V and VI), no significant drops were observed, and the residual friction (μ_r) stabilized around ~ 0.7. In general, μ_p and μ_r showed exponential decay as a function of shear distance (Figure 6.5).

Since the rotation of the top sample was monitored at each 0.06° rotation interval, the angular rotation speed (ω) during each interval was calculated by the ratio between 0.06° and the elapsed time.
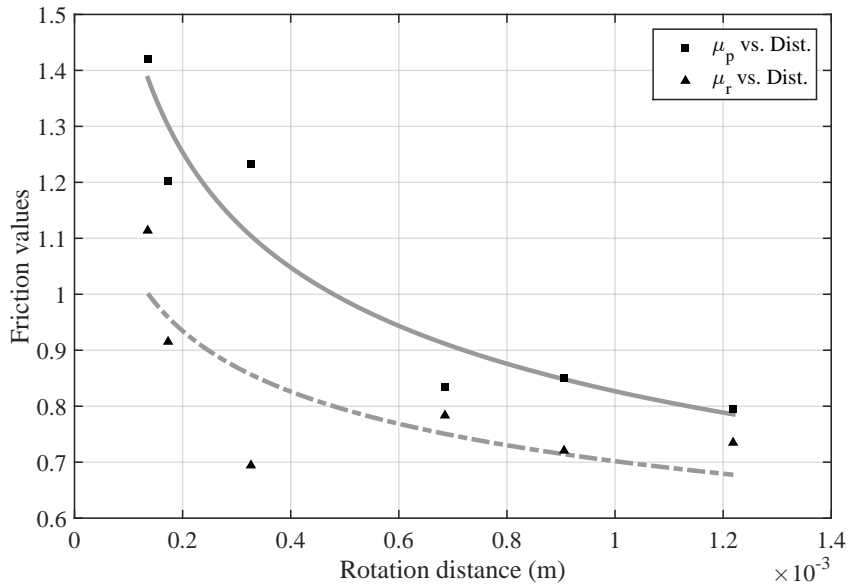
Figure 6.5: Peak (μ_p) and residual (μ_r) friction values as function of shear distance.

The averaged velocity (v) was then calculated as:

$$v = \frac{\omega \pi \left(R + R_0\right)}{360°}.$$

(6.3)

The average friction in each rotation interval, were examined against the averaged velocity (Figure 6.6).

6.3.3 X-ray ERDµ-T imaging results

Each µCT scan generated 1080 16-bit grayscale images having field-of-view of 794×1024 pixels and resolution of 25 µm (Figure 6.7a). These images were reconstructed into a 3D volume (Figure 6.7b) using the Phoenix X-ray datos-x-reconstruction software (v.1.5.0.22), using the following settings: a beam hardening correction of 3/10, an automatic ring artifact reduction, and a manual scan optimization that compensates for small drifts of the specimen during the scan and accurately locates the centre of reconstruction (Tisato et al., 2015). The reconstructed 3D volume comprised of 1024 794×794 16-bit grayscale images, discretizing the sample into approximately 65 million voxels.

The quality of the reconstructed volume that was close to the sample holders was highly influenced by the high density of the stainless-steel sample holders (due to beam hardening and scattering effects). Thus, we selected 620 slices with consistent image quality, located from ∼6.46 mm above to ∼9.06 mm below the fault, for further analysis.

The selected volume was filtered with an edge-preserving non-local means (NLM) filter by means of
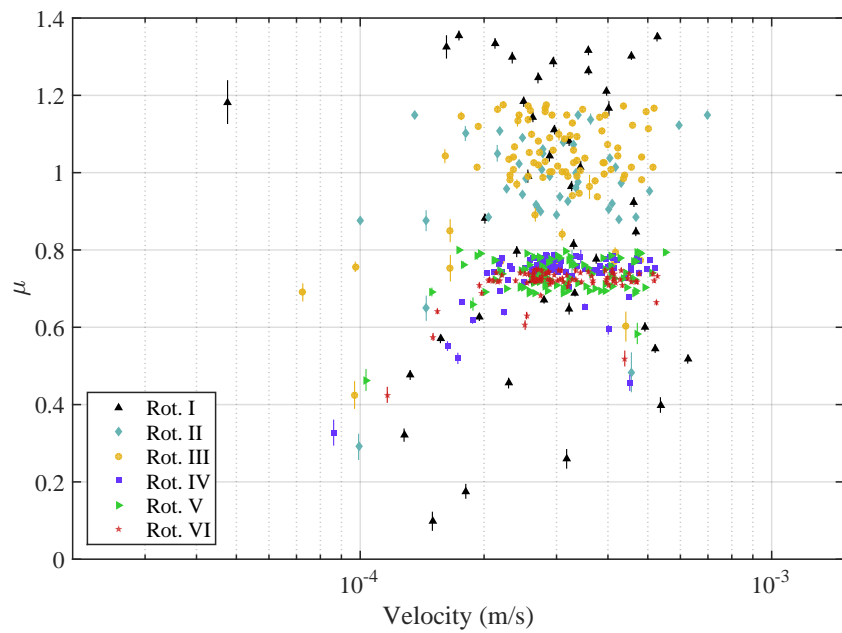
Figure 6.6: Friction coefficient as a function of shearing velocity and associated errors indicated by the vertical bars.
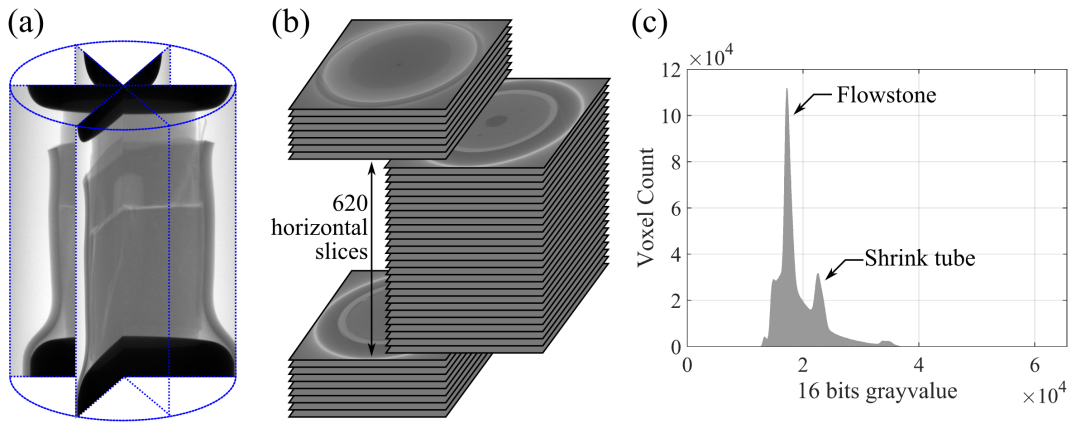
Figure 6.7: (a) 2D radiographs (i.e., shadow projections) acquired during a μCT scan with a field of view of 794×1024. (b) Reconstructed volume shown as an image stack and the 620 slices with consistent image quality were used for further analysis. (c) Histogram of the grayvalue of 620 slices showing the peaks in voxel counts that correspond to different materials.
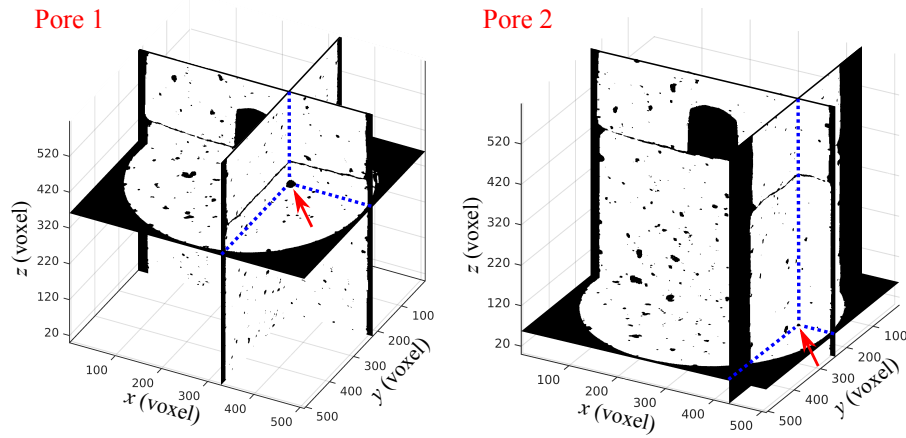
Figure 6.8: Three orthogonal and intersecting slices of the segmented images at the initial condition, showing the pores selected for checking the sample deformation (indicated by the red arrows).

the Non-local Means Denoising plugin that is available with the open source software Fiji (Buades et al., 2005). The parameters used for the plugin were: noise level at 280 and smoothing parameter at 1. This filtering process reduced the noise level by 75%, while ensuring minimal disturbance to features such as fractures and pores (Figure 6.9a–d).

The filtered image stack was then cropped to the volume containing the sample and segmented using grayvalue thresholds. The segmentation was carried out following Zhao et al. (2017) for each data set individually. The thresholds used in the segmentation and the results are listed in Table 6.3. The averaged segmented total sample volume was 1724 mm^3, comparable to the actual bulk volume of the sample, 1710 mm^3. Taking this mean volume as the reference, we estimated the error associated to the segmentation using the volume deviated from the reference value. The segmentation for all data sets showed high consistency with the maximum error of 1.3%; while most data sets had errors less than 0.5%.

Next, we evaluated the deformation of the sample using two isolated pores located in the bottom semi-sample as markers (Figure 6.8). The vertical location of the lower bound (h_1) and the upper bound (h_2) of these pores were located. Based on such information, the vertical location of the centres of these pores were calculated (c), and then, the vertical distance between them (d) was calculated. d stayed constant for all the rotation steps, but was slightly different from the initial condition (Table 6.2). This slight difference maybe related to the applied torque.

Two key assumptions were then made, which were critical to the area estimation in the following section: (1) no gouge material escaped from the fault zone, which was assured because of the shrink tube covering the sample; and (2) the sample deformation due to the applied stress was negligible, which

Table 6.2: Locations of the two selected pores and their vertical distance, examined for all data sets. Values are normalized to the resolution, i.e., 25 μm.

Data set	Initial	Rot. I&II	Rot. III	Rot. IV	Rot. V	Rot. VI
Pore 1 h_1	352	353	352	353	353	353
Pore 1 h_2	375	375	376	375	375	375
Pore 1 c	363.5	364	364	364	364	364
Pore 2 h_1	51	51	51	51	51	51
Pore 2 h_2	63	63	63	63	63	63
Pore 2 c	57	57	57	57	57	57
d	306.5	307	307	307	307	307

was suggested by the aforementioned result and the volumetric strain of <0.01%, calculated based on the sample properties and stress conditions. However, even though the total sample deformation was assumed to be negligible, the microscopic structures adjacent to the fault surface that were below the resolution (i.e., < 25 μm) were subjected to significant deformation.

The segmentation resulted in the binarization of the reconstructed volume where white (i.e., 1) represents the solid sample and black (i.e., 0) represents the pore space (Figure 6.9e). Note that due to the noise and minor differences between scans, the sizes and total number of pores varied from scan to scan. In order to suppress the influence of pore space in further quantitative analysis of the images, a morphological pore-filling operation (see supplementary material) was performed to eliminate all the isolated pores in the segmented volume (Figure 6.9f) (Gonzalez and Woods, 2002).

To aid visual interpretation, we then created the 3D rendering of the pore-filled volume. Specifically, in order to view the fault and fractures, we represented the sample using surfaces enclosing the pore and fracture space (Figure 6.10). The 3D renderings show that a fracture formed when the initial normal force was applied (Figure 6.10a). This fracture, considered as the initial fracture, was not fully open and the segmentation procedure did not capture its whole geometry (Figure 6.10a). After the first two rotation steps (Rot. I & II), the initial fracture opened and propagated causing the bottom semi-sample to split (Figure 6.10b). During Rot. III, a fracture formed in the middle of the bottom semi-sample, and two fractures formed close to the periphery of the top semi-sample (Figure 6.10c). During Rot. IV, a small fracture formed at the bottom semi-sample, connecting the two fractures formed in the earlier steps (Figure 6.10d). No significant fractures were created in Rot. V and VI (Figure 6.10e&f); however, our subsequent interpretation showed that the gouge layer was forming during these rotation steps.

We compared the μCT images data and the surface topography results. This analysis showed that the initial fracture was caused by the misalignment of the bigger asperities. By taking advantage of the fully digitized sample volume, we investigated this region by extracting a vertical 2D slice of the sample volume at the radius of 5.6 mm (Figure 6.11). To avoid loss of information during segmentation, we
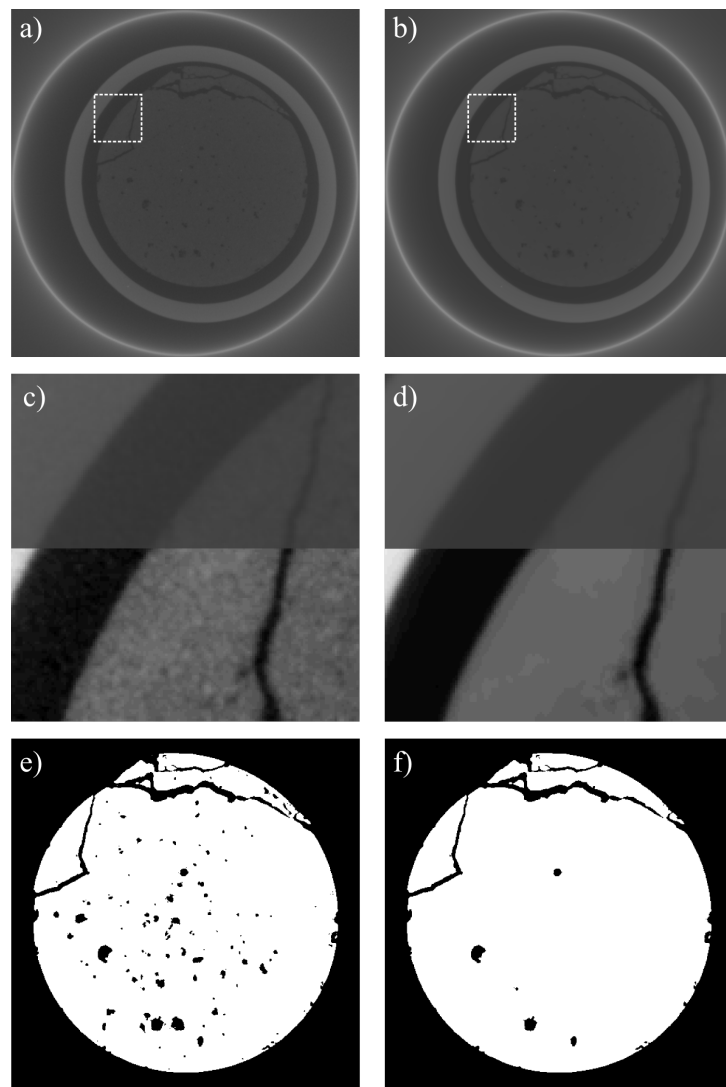
Figure 6.9: Image processing steps, taking a horizontal slice of the scan after Rot. VI as an example. (a) A horizontal slice of the reconstructed μCT image and (b) the same slice after the application of the NLM filter. (c) and (d) are zoom-in views of the areas highlighted by the dashed squares in (a) and (b), respectively. The contrast of the bottom halves of these images are enhanced to demonstrate the advantage of the NLM filter. (e) Segmented result of (b) shown as binary image, and (f) binary image after pore filling.
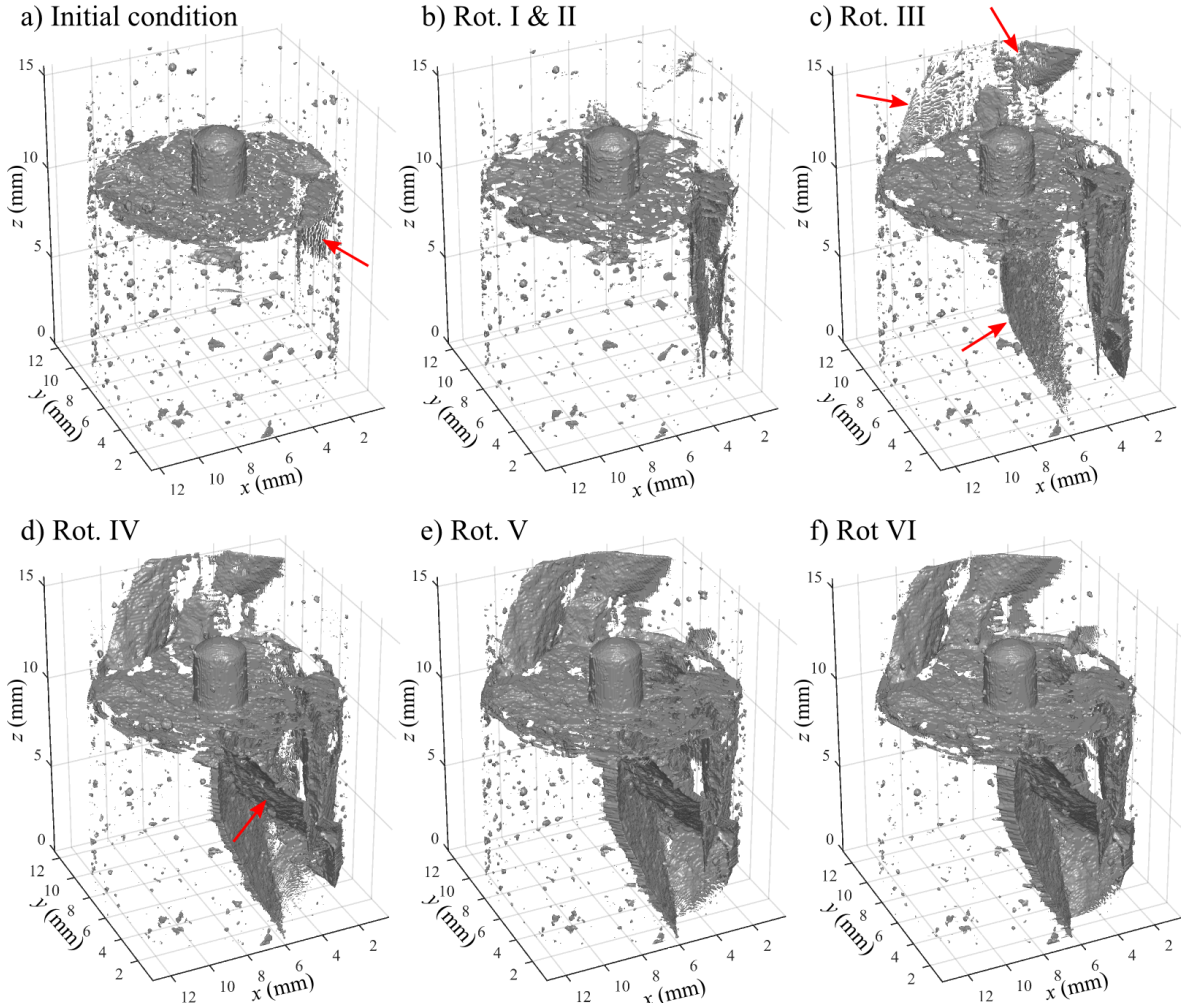
Figure 6.10: 3D rendering of void space surfaces in the digitized sample volume illustrating the damage process of the Flowstone specimen. (a) Before the rotary shear test with 280 N normal force applied; (b–f) after the rotation steps I–VI, respectively. Red arrows indicate the newly formed fractures in the corresponding steps. Note that the pores shown were located on the outer surface of the sample, which were not eliminated by the pore-filling process.
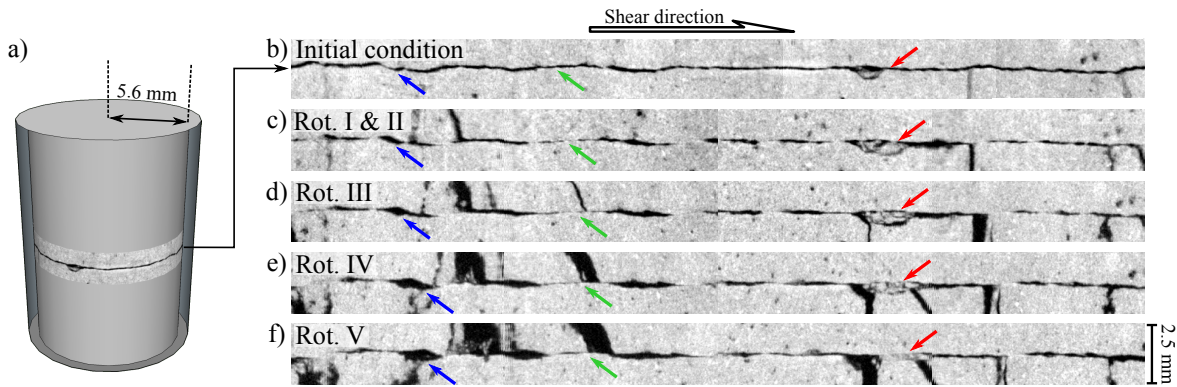
Figure 6.11: Expanded view of the shear surface at the radius of 5.6 mm. (a) The extraction of the vertical 2D slice. (b)–(f) The evolution of the fault viewed from the extracted slice. The hollow arrow indicates the shear direction (i.e., right-lateral). Three sets of coloured arrows indicate key features: slip induced opening (blue), induced secondary faulting (green), and gouge formation (red).

used the reconstructed image and enhanced the grayvalue contrast. This 2D slice can be viewed as a right-lateral fault, and allowed us to visually observe the evolution of the shear surfaces by comparing the same 2D slice extracted from data sets at incremental shear steps.

Although additional information can be gathered from these slices, here we list three key observations: (i) progressive aperture opening creating void space on the fault zone (i.e., blue arrows in Figure 6.11), (ii) the engagement of counteracting asperities and the formation of tensile cracks, similar to secondary faulting (i.e., green arrows in Figure 6.11), and (iii) the degradation of the fault wall material, from intact into fine powder, i.e., the formation of fault gouge (i.e., red arrows in Figure 6.11).

After the experiment, the ERDμ-T was removed from the μCT scanner and opened. This allowed visual inspection of the tested sample (Figure 6.12). The shear surface experienced minimal damage, except for the secondary fractures splitting the sample. Some areas of the shear surface were covered with a thin layer of fine powder, which could also be observed in the 2D slices (Figure 6.11f).

6.3.4   Real contact area and fracture surface area

Assessing the real contact area is essential to understand friction in natural materials, and it is often studied using transparent materials, such as polymethyl methacrylate (PMMA), or inferred from indirect measurement, such as fault normal elastic stiffness (e.g., Ben-David et al., 2010a; Dieterich and Kilgore, 1994; Rubinstein et al., 2004; Nagata et al., 2014; Selvadurai and Glaser, 2017). On the other hand, estimating the fracture surface area is achieved using techniques such as particle size distribution (PSD) and Barrett–Emmett–Teller (BET) N_2 adsorption method (Chester et al., 2005; Wilson et al., 2005). In this study, we used a novel approach to estimate the fracture and real contact area by means of μCT
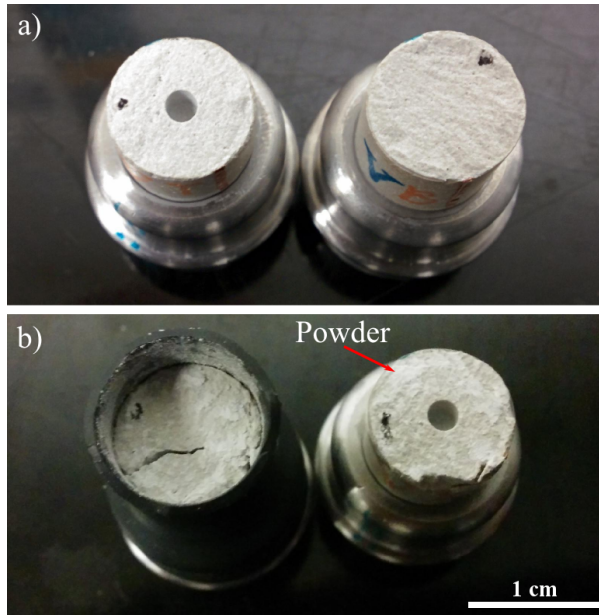
Figure 6.12: Photograph of the Flowstone sample (a) before and (b) after the rotary shear test. Note the gouge formed on the slipping surface.

image analysis.

We examined the segmented-and-pore-filled images by representing the sample volume using surfaces enclosing solid material (Figure 6.13). Then we divided the total surface area (A_t) into three components: (i) the initial surface area (A_i) including the outer surface area of the sample, the initial fracture surface area, and the surface of the hole in the top semi-sample; (ii) the non-contacting surface area on the fault (A_{nc}), and (iii) the shear induced secondary fracture surface area formed during rotations (A_f).

The total surface area in the sample volume (A_t) was estimated by counting the voxels belonging to all the surface boundaries, which was calculated as the difference between the segmented-and-pore-filled volume and the morphologically eroded volume (see supplementary material) (Gonzalez and Woods, 2002).

To estimate the non-contacting surface area (A_{nc}), we first calculated the real contact area (A_c). The locations on the fault, where there is no void space (i.e., air) between the top and bottom semi-samples were considered as "in contact". A_c was estimated by evaluating the area with zero void voxel throughout the fault, using the following procedure:

(1) 50 horizontal segmented-and-pore-filled binary slices that contained the fault were inverted so that void space was represented by 1 and solid material was represented by 0.

(2) These inverted slices were then added together through a simple summation of values at the same $x - y$ location (i.e., stacking). The stacked image was essentially a 2D matrix representing the

A_i {
- ☐1 Outer surface   ☐3 Secondary fracture surface, A_f
- ☐2 Indentation surface   ☐4 Non-contacting surface, A_{nc}
- Inital fracture surface   ☐5 Real contact area, A_c
  (not shown in figure)
}
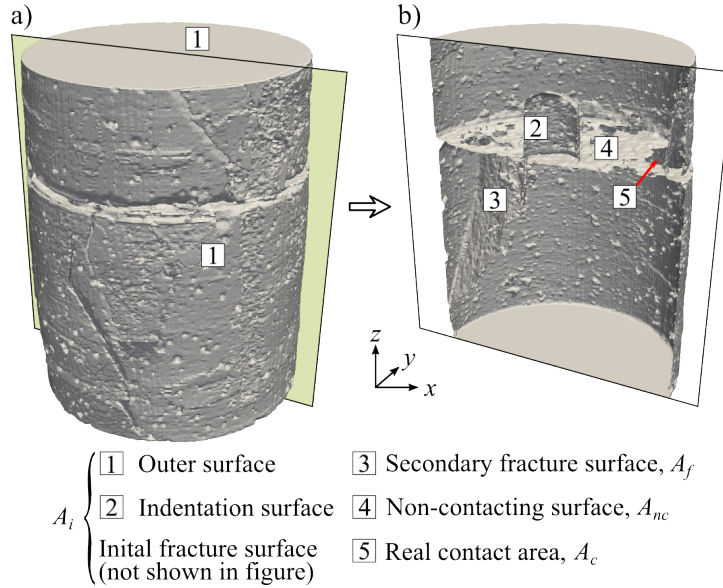
Figure 6.13: 3D surface rendering view illustrating different types of surfaces in the sample volume. The data set after Rot. III is taken as an example.

number of void voxels throughout the examined vertical range (Figure 6.14). Thus, pixels with zero were considered as the real contact area (A_c).

(3) The ratio between A_c and the nominal contact area (A_n) was then calculated.

A_{nc} can then be calculated from the A_n and A_c using:

$$A_{nc} = 2 \left(A_n - A_c \right), \tag{6.4}$$

where the multiplier 2 accounts for the fact that we are considering top and bottom sides of the non-contacting surface.

At the initial condition, the total area, A_t, was divided into A_{nc} and A_i:

$$A_t = A_{nc} + A_i. \tag{6.5}$$

We considered A_i to be unchanged throughout the test based on the assumption that the measured bulk sample volume deformation was negligible. For the successive rotation steps, shear induced secondary fractures formed, and the area of these fractures (A_f) was also a part of A_t:

$$A_t = A_f + A_{nc} + A_i. \tag{6.6}$$
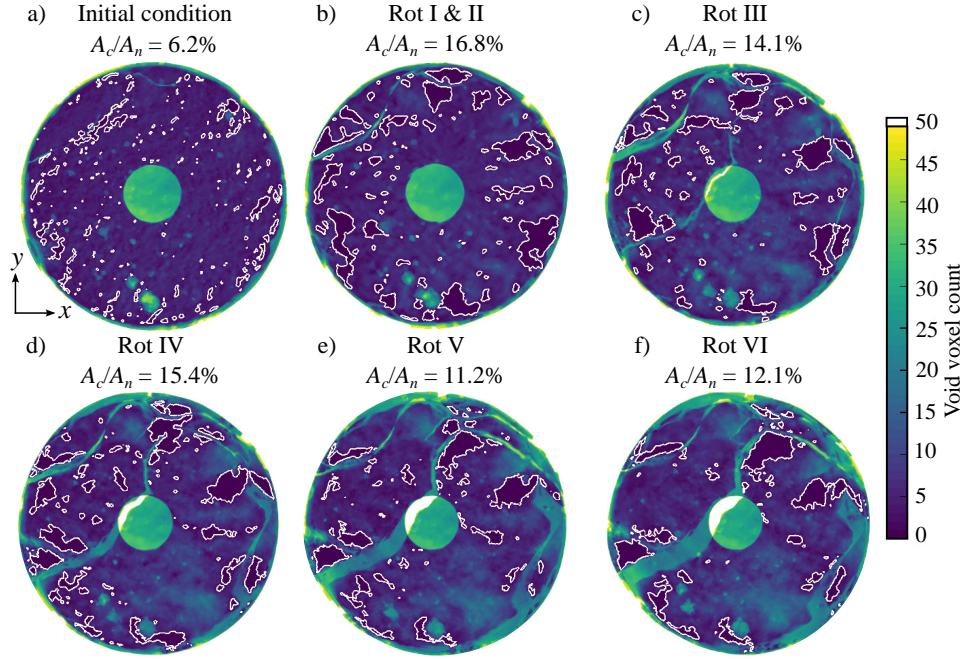
Figure 6.14: Estimated real contact area at (a) the initial condition and (b–f) after each 6° of rotation. The color indicates the total number of voxels representing air in a specific x–y location, and the contours highlight the real contact area (i.e., no air).

A_t and A_{nc} were calculated for each data set; thus, A_f can be estimated by:

$$A_f = A_t - A_i - A_{nc}, \qquad (6.7)$$

and the fracture area created in each rotation step was simply computed as the difference of A_f between two consecutive steps.

A summary of the analysis results is provided in Table 6.3. Note that after Rot. VI, A_t and A_f decreased slightly, and a close inspection of the image (Figure 6.10e&f) suggested that there were no new fractures formed. The closure of fractures and the formation of gouge filling the fractures may have caused the decrease of A_f between Rot. V and VI.

Table 6.3: Summary of segmentation and morphological process results.

Data set	Grayvalue thresholds (upper, lower)	Segmented volume (mm^3)	Error (%)	Real contact area, A_c (mm^2)	Fracture surface area, A_f (mm^2)
Initial	18685, 21200	1722	0.1	6.9	0
Rot. I&II	17700, 20300	1731	0.4	18.7	60.8
Rot. III	17755, 20449	1717	0.4	15.7	347.6
Rot. IV	17600, 20560	1702	1.3	17.1	516.9
Rot. V	19578, 22453	1732	0.5	12.5	584.1
Rot. VI	16058, 19077	1740	0.9	13.5	561.2

6.3.5 Energy budget

During a fault slip event, the accumulated potential energy (W), which includes elastic strain energy (E_s) and gravitational energy (E_g), is partially released, and the released energy (ΔW) is partitioned into friction energy loss (E_F), fracture energy (E_G), and radiated energy (E_R) (Beeler, 2006; Kanamori, 2001; Kanamori and Heaton, 2000; Kanamori and Rivera, 2006). In the rotary shear experiment, different from earthquake events, the specimen was driven by mechanical energy input (W_I) from the rotary motor. The energy budget can be written as follows:

$$\Delta W + W_I = E_F + E_G + E_R. \tag{6.8}$$

Now we address each component in Equation 6.8:

(1) The rotary shear test was conducted with the vertical position of the top and bottom semi-samples fixed; therefore, we neglected the gravitational energy change and considered only E_s in ΔW. E_s was further divided into the change in elastic energy due to normal force change ΔE_s^n and due to torque change ΔE_s^t (Parrish and Camm, 1973):

$$\Delta E_s^n = \frac{\left(N_r^2 - N_i^2\right) L}{2 E A_n}, \tag{6.9}$$

and

$$\Delta E_s^t = \frac{\left(M_r^2 - M_i^2\right) L}{2 G J}. \tag{6.10}$$

where N_i and N_r are the normal force measured at the start and end of the rotation, M_i and M_r are the corresponding torque measurements, L is the total sample length, E is the Young's modulus, G is the shear modulus that can be estimated through E and Poisson's ratio (ν) by $G = E/(2(1 + \nu))$, and J is the polar moment of inertia ($J = \pi R^4/2$).

Moreover, the strain energy variation due to the elastic deformation of the apparatus needs to be considered. The stainless steel (SS304) vertical shaft and the load-and-torque cell were under compression and torsion, while the aluminum (7075-T6) vessel was under tension and torsion. The strain energy variation of these parts was estimated using Equations 6.9 & 6.10, with their corresponding geometries and material properties. The total strain energy released from the sample and the apparatus at each 6° rotation was 0.14 mJ, 0.54 mJ, 0.48 mJ, 0.25 mJ, 0.25 mJ, and 0.18 mJ, respectively.

(2) W_I was calculated from the torque (M) and the angular shear distance (Ω) (Kleppner and

Kolenkow, 2013):

$$W_I = \int_\Omega M \mathrm{d}\Omega. \tag{6.11}$$

(3) E_F was estimated from the shear stress (τ) that was calculated from the torque recorded during the test (Equation 6.1) (Kanamori and Rivera, 2006):

$$E_F = A_n \int_u \tau(u)\mathrm{d}u, \tag{6.12}$$

where the averaged shear distance, u, was calculated using the angular shear distance (Ω):

$$u = \frac{\Omega\pi\,(R + R_0)}{360°}. \tag{6.13}$$

(4) Energy consumed by fracturing, E_G, was estimated from the newly created surface area (ΔA) and fracture energy. As the µCT images suggested, the fractures created due to the interlocking of asperities propagated in tensile mode (i.e., mode I); thus, it was reasonable to use the mode I fracture energy, G_{Ic}, to calculate the fracture surface energy (Chester et al., 2005):

$$E_G = \frac{\Delta A}{2} G_{\mathrm{Ic}}. \tag{6.14}$$

where half of the created fracture surface area was considered for the fact that fractures have two identical sides. G_{Ic} can be related to the fracture toughness (K_{Ic}) following (Atkinson, 1984):

$$G_{\mathrm{Ic}} = \frac{K_{Ic}^2}{E}. \tag{6.15}$$

(5) The radiated energy, E_R, is the only energy term that can be directly measured with seismological methods in the field. However, wave radiation was not recorded in the current experiment set-up; and because the remaining terms in Equation 6.8 were calculated, E_R can be easily inferred.

The total released energy (ΔW) during each 6° rotation increment was 106.72 mJ, 170.00 mJ, 102.19 mJ, 101.16 mJ, and 93.47 mJ, respectively. The energy consumed by friction work (E_F) was 87.49 mJ, 144.60 mJ, 87.30 mJ, 86.43 mJ, and 80.24 mJ, respectively. The energy consumed by creating new fracture surfaces (E_G) was 0.15 mJ, 0.73 mJ, 0.43 mJ, and 0.17 mJ, respectively. E_F consumed 81.98–85.85% of the total released energy and E_G consumed only 0.15–0.43% of the total released energy (Figure 6.15). Thus, the remaining 14.15–17.87% of the total released energy was assumed to be in the form of seismic radiation (E_R).
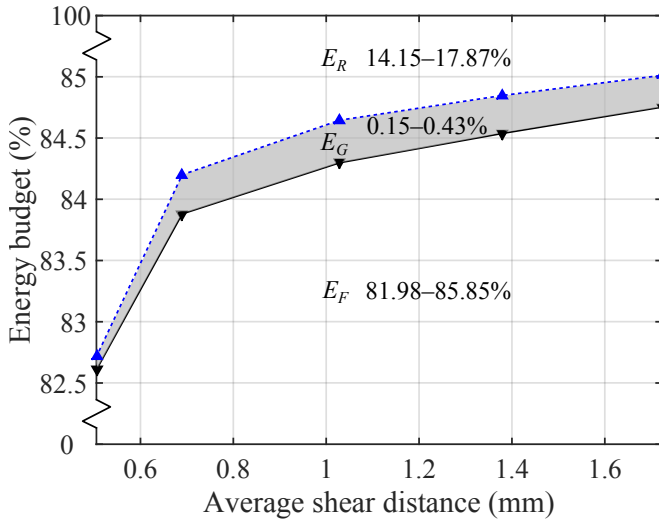
Figure 6.15: Energy budget shown as the relative amount of friction energy loss (E_F), fracture energy (E_G), and radiated energy (E_R). The dashed line indicates the upper and lower bounds of E_G and E_R, respectively.

6.4 Interpretation and discussion

6.4.1 Friction evolution

The initial friction value (μ_i) of the first rotation was 0.1, which may be the result of the application of vertical loading on the slightly misaligned asperity contacts (Figure 6.11b & Figure 6.16a). At the end of each rotation step, the asperities were deformed elastically and held the residual normal and shear stresses, σ_n^r and τ^r, (Figure 6.16b). The initiation procedure prior to each rotation step disturbed the residual stresses (Figure 6.16c). However, since the initial stress conditions (σ_n^i and the resultant τ^i) of the next rotation step was applied to the fault at the exact position as the previous step (Figure 6.16d), we do not consider such a disturbance.

The friction showed no velocity dependency (Figure 6.6), similar to shear tests conducted on limestone at similar low slip rate (Delle Piane et al., 2016). However, the initial friction scattered in a broad range – between 0.8 and 1.4 – before converging to a stable value – between 0.7 and 0.8 – in the latter three rotation steps. The friction drops observed during Rot. I may have been caused by the opening of the initial fracture created by the application of the normal stress; whereas, the sudden drops of friction value during rotation steps Rot. III and IV were associated with the formation of new fractures, highlighting the importance of the development of secondary fractures in the breakdown of fault strength.

Peak friction (μ_p) and residual friction (μ_r) decreased with increasing shear distance and reached typical rock friction values at similar stress conditions (Di Toro et al., 2004, 2011). The shear distance that was required to reach a stable value (~ 0.7) was relatively short: approximately 1 mm (i.e., $\sim 12°$ of
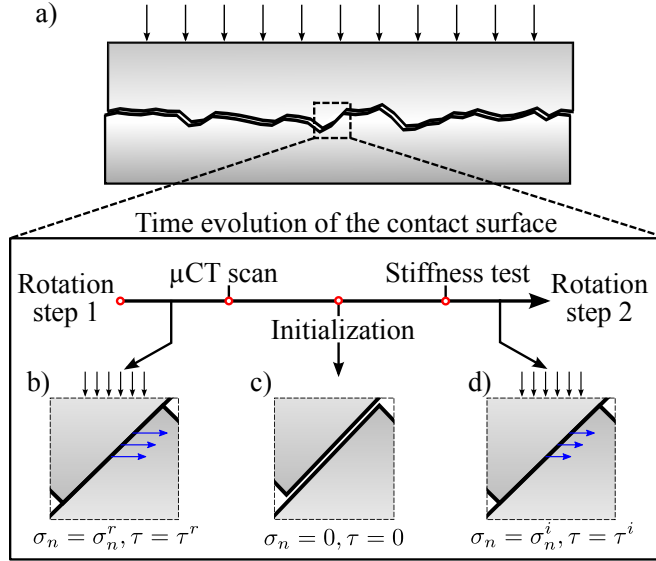
Figure 6.16: (a) Schematic diagram of the variation of stress conditions due to the interactions between asperities. (b) After a rotation step, the shear surface held the residual normal stress (σ_n^r) and the residual shear stress (τ^r), (c) during the initiation, the stresses were released, and (d) initial normal stress (σ_n^i), was applied prior to the next rotation step, resulted in the initial shear stress (τ^i).

rotation). This distance may be regarded as the critical slip distance (D_c), which is interpreted as the slip distance that must occur before the sliding surfaces change from one steady-state friction condition to another (Scholz, 1998).

D_c was observed to have a positive correlation with surface roughness (Okubo and Dieterich, 1984). In general, D_c ranges from $\sim 10^{-5}$ m for laboratory measurements to $\sim 10^{-2}$ m for natural earthquakes (Dieterich, 1978, 1979, 1981; Okubo and Dieterich, 1984; Scholz, 1988). D_c inferred from our experiment (i.e., $\sim 10^{-3}$ m) was larger than values reported in laboratory measurements but smaller than values from natural earthquakes, the reason lies in the fact that the tested fault surface was a fresh fracture that was much rougher than the flat surfaces used in most laboratory tests. The quantitative correlation between roughness and friction may provide key information for upscaling our interpretations to field scale.

6.4.2   Real contact area

Using the innovative ERDµ-T system, we overcame these limitations and imaged the entire shear process without disturbing the shear surface. As a result, continuous estimation of the real contact area was achieved. At the initial condition of the experiment, the top and bottom semi-samples were not in perfect matching contact due to a slight misalignment between them, which was reflected by a relatively small contact area (A_c) that was 6.2% of the nominal contact area. After a small shear distance, A_c

increased more than two times, suggesting a better matching contact between the two fault surfaces. With the increase in slip distance, A_c decreased gradually and stabilized to be approximately 10% of the nominal contact area, similar to the value reported in the literature Dieterich and Kilgore (1994). This result suggests that the real contact area of rock material can be assessed with the ERDµ-T system.

6.4.3 Fracturing and energy consideration

Secondary faulting and fracturing alongside the main fault are observed among a wide range of scales, from 10^{-2} m to 10^2 m, in forms of, for example, en echelon fractures and pseudotachylytes (Belardinelli et al., 2000; Di Toro et al., 2005). Understanding these co-seismic fracturing phenomena can provide critical information on the *in-situ* dynamic stress conditions of the earthquakes, improving our understanding of earthquake physics including rupture mechanisms and propagation speed, energy budget, and gouge formation (Di Toro et al., 2005; Mitchell et al., 2011; Wilson et al., 2005).

Studies regarding the relative amount of energy consumed by fracturing is inconclusive, field observations reported inconsistent values from $< 1\%$ to $> 50\%$ (Chester et al., 2005; Wilson et al., 2005); while laboratory experiments and theoretical models suggested much smaller values at 0.01–0.1% (Scholz, 1990; Yoshioka, 1986). The disagreement about the relative size of E_G is related to the difficulty in assessing the fracture surface area. With the careful estimation of fracture surface area from the µCT images, we quantitatively estimated the fracture surface area, which accounted for 0.1–0.4% of the total energy released during slip, in agreement with most values reported in the literature, except for Wilson et al. (2005). In fact, in the latter study, a large percentage of the energy was assumed to be consumed by rock pulverization.

The thin layer of fine powder (fault gouge) that covered part of the surface at the end of the test was created by fracturing and crushing processes. The grain size of this powder layer was below the resolution of the µCT imaging (i.e., <25 µm). Therefore, quantitative assessment of the actual grain size and the surface area of the fault gouge was not possible. This may result in substantial underestimation of the fracture energy (E_G). Moreover, the estimation of fracture energy was based on Griffith theory of brittle fracture (Griffith, 1920), and the non-elastic deformation near the crack tip that leads to the dissipation of energy was ignored (Orowan, 1949; Irwin, 1957). Therefore, the estimated E_G in this study may suggest the lower bound of the energy consumed by fracturing.

The ratio between E_R and the total released energy is defined as the seismic efficiency (η), and the values we obtained were within the range of 0.15–0.17, qualitatively in agreement with the η value calculated using near-field seismograms (Wang, 2004); however, higher than the proposed upper bound of

$\eta \leq 0.06$ for laboratory and mining-induced earthquakes by McGarr (1994). This discrepancy supports the discussion that the estimated E_G is a lower bound value, and as a consequence, the estimated E_R may represent the upper bound of the radiated energy.

6.4.4   The importance of fault surface roughness

Most conventional rotary shear studies are carried out on flattened surfaces or artificial gouge. In this study, we have shown the critical role of surface roughness on the shearing processes: (1) under low normal stress conditions only a fraction ($\sim$10%) of the surface contributed to the frictional sliding behaviour; (2) the formation of secondary fractures was related to asperity interactions; and (3) the critical slip distance, D_c, was related to the scale of the roughness.

Fault and rock joint surface roughness has been investigated in many laboratory experiments and field studies (e.g., Boneh et al., 2014; Power et al., 1988; Reches and Lockner, 2010; Sagy et al., 2007; Wang and Scholz, 1994), and some hypothesis regarding fault evolution proposed in these studies are in agreement with our direct observation of the shear surface. For example, the asperity interaction mechanism proposed in the work of Boneh et al. (2014) can be observed from the 2D slice image (Figure 6.11), and the creation of powder from the surface wearing that lubricates the fault, as discussed in the work of Reches and Lockner (2010), was also directly observed.

Considering the aforementioned discussion, we can obtain a general picture on how surface roughness plays a dominant role in the initial sliding phase of a fresh fault. First, when the shear distance is less than D_c, asperities interact and secondary fractures form, resulting in large variation of friction values. During this period, the real contact area decreases with increasing shear distance as the two sides of the fault become misaligned. After that, when the shear distance is larger than D_c, asperity interaction and fracturing is not dominating and the friction value becomes stable. During this period, the real contact area stays relatively constant, and on the fault surface, grains are crushed into fine powder that may lubricate the fault.

6.5   Conclusion and implications

Friction of faults is strongly influenced by microscopic features, such as asperities and gouge. This makes the ERDμ-T apparatus very suitable to study frictional behaviour of rough rock surfaces as it allows inspecting the rock interior, continuously in time and space, without introducing undesired perturbations. Large amounts of information can be gathered from μCT imagery, making possible for a more comprehensive interpretation of the frictional sliding behaviour than those solely relying on

mechanical data. Some important features of fault evolution that can hardly be accessed in conventional studies, such as the real contact area, fracture surface area, and wearing of the shear surface were obtained through the X-ray µCT image data.

We demonstrated the dominant importance of roughness in the initial phase of fault slipping. The real contact area on the frictional surface was estimated to be stabilized at about 10% of the nominal contact area. More importantly, we obtained the energy budget during slipping. The lower bound of the fracture energy and upper bound of the seismic wave radiated energy was approximately 0.1–0.4% and 14.0–15.8% of the total energy budget, respectively. These observations may help to improve our understanding of earthquake physics. Moreover, this work demonstrated that the µCT technology is a powerful tool for the study of earthquake physics and established a framework for the upcoming experiments using the ERDµ-T apparatus.

Supplementary material

Normal stiffness test results and discussion

The apparent normal stiffness of each sample was measured by varying the length of the piezoelectric motor beneath the load cell (see Zhao et al. (2017) for detailed explanation of the apparatus). However, the resultant displacement was distributed to all the components along the vertical axis of the ERDµ-T vessel: the piezoelectric motor, the load and torque cell, the sample, the vertical shaft, the ball bearing system, and the stroke of the electromechanical motor. Due to the drastic contrast in stiffness between the sample and the steel components, and considering that the synthetic fault may be even less stiff than the intact material, we assume the strain created by the piezoelectric motor to be entirely concentrated on the Flowstone sample. The loading and unloading path was then represented by the normal force reading and the displacement of the piezoelectric motor (Figure 6.17).

For all the tests, the loading and unloading curves showed obvious hysteresis for the first loading and unloading cycle, but negligible hysteresis for the second cycle. The significant hysteresis during the first cycle may be related to the mobilization of asperities (i.e., slight adjustment of the contact). After the first loading cycle, the sample behaved more "elastically". Interestingly, the unloading curves from the two cycles coincide closely. The apparent stiffness (E_e) was calculated by linear fitting of the estimated strain and normal stress variation ($\Delta\sigma_n$) for the unloading curves. E_e of the sample with the fresh synthetic fault surface was 2.37 GPa, slightly higher than those from the successive tests, which were in the range of 2.03 to 2.26 GPa.

Morphological dilation and pore-filling

Morphological dilation is an image analysis operation that expands the boundaries of objects in an image. It overlaps non-zero elements (i.e., pixel in 2D or voxel in 3D) in the input image with the center of the so-called structure element (e.g., Figure 6.18a) and outputs the morphological union of the two (Figure 6.18 b&c) (Gonzalez and Woods, 2002). The most common structure element for 3D image processing, a 3×3×3 array with non-zero elements representing a 3D cross (Figure 6.18d), was used in the current study.

In order to achieve pore-filling and noise reduction, the segmented binary image (e.g., Figure 6.19a) is first inverted to create the mask of dilation (Figure 6.19b). During the dilation operation, only elements with a true value (i.e., 1) in the corresponding mask elements are modified; therefore, this mask prevents the dilation from crossing the boundaries of the objects in the image. Then an image with the same
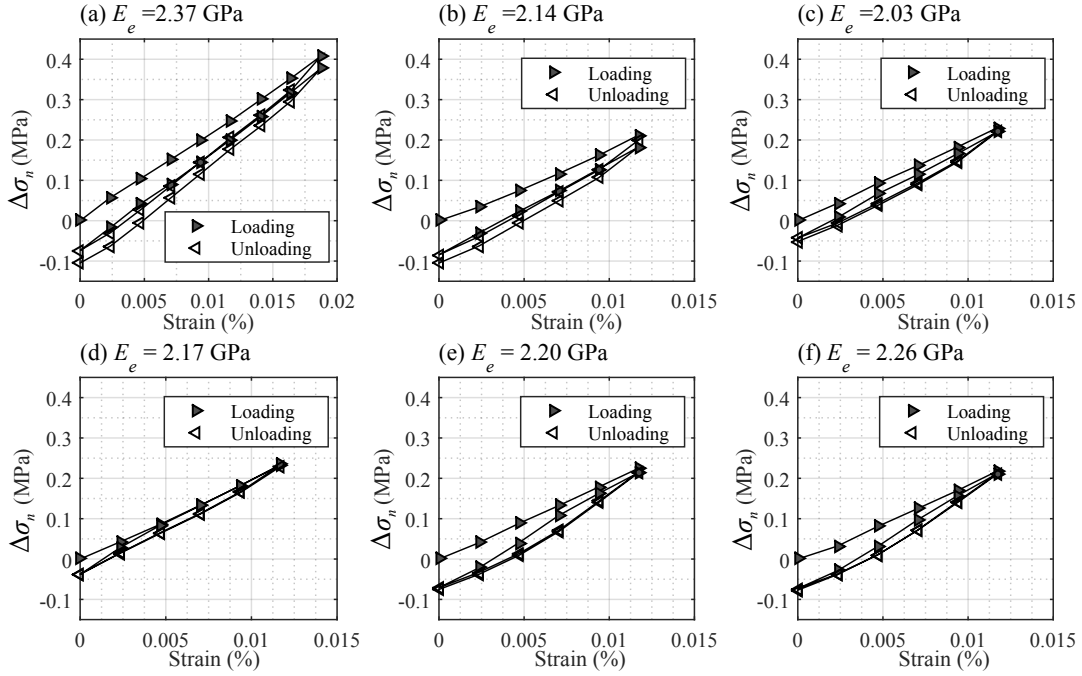
Figure 6.17: Stiffness test results. (a)–(f) Loading and unloading cycles (two cycles for each test) of the stiffness tests, prior to Rot. I–V, respectively. The changes in normal force N were displayed and the loading–unloading curves start at $\Delta N = 0$. Note that the first stiffness test was carried out with slightly larger maximum strain.
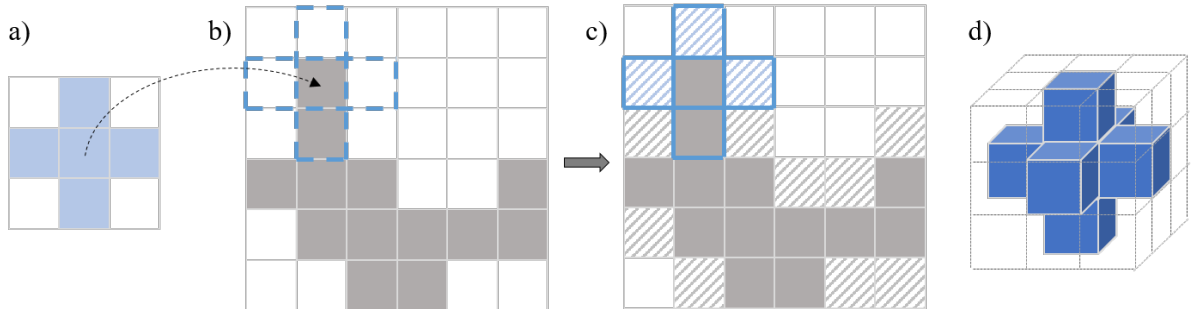
Figure 6.18: Schematic illustration of morphological dilation (in 2D for better illustration). (a) A 2D structure element. (b) Aligning the centre of the structure element with every non-zero element of the target image. (c) Expanding non-zero elements as a result of the morphological union. (d) 3D structure element used in the pore-filling algorithm in the current study.
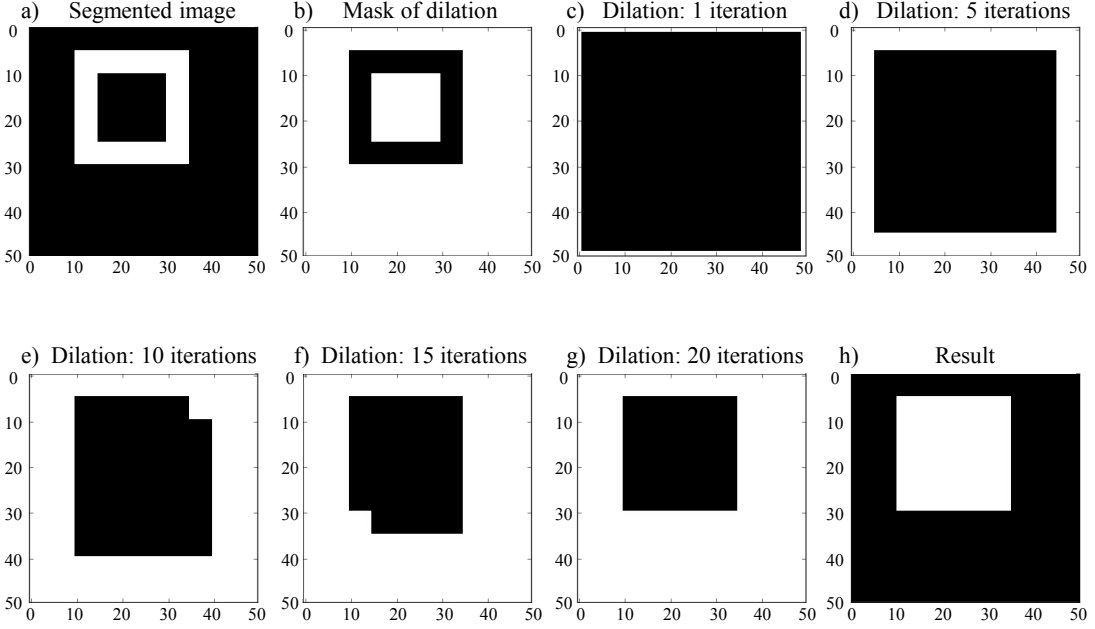
Figure 6.19: 2D example showing the pore filling process using morphological dilation.

size as the segmented image and full of zeros is created as the input image. An iterative morphological dilation operation expanding the border of the input image inwards is carried out (Figure 6.19c–g). The iteration stops when the output image coincides with the result from the previous iteration. Finally, the image is inverted for the pore-filled result (Figure 6.19h). This pore-filling procedure fills all the isolated pore space (i.e., not connected to the fractures).

Morphological erosion and surface area calculation

Morphological erosion is an operation opposite to the previously described morphological dilation, and it shrinks the boundaries of objects in the input image. The erosion is carried out by overlapping the structure element with non-zero elements in the input image, and if local shape of the input image matches the shape of structure element, the corresponding elements in the input image will be replaced by zeros, except for the centre element (Figure 6.20a–c) (Gonzalez and Woods, 2002). After one iteration of erosion, the objects in the input image will be shrunk, and the difference between the original image and the eroded image represents the boundaries of the objects in the image (Figure 6.20d). The surface area of these objects are calculated by counting the number of elements on the boundaries.
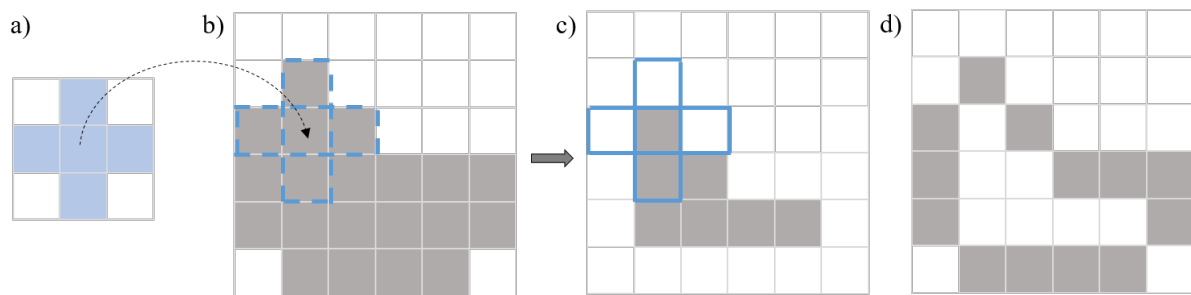
Figure 6.20: Schematic illustration of morphological erosion (in 2D for better illustration). (a) Structure element. (b) Overlapping the structure element with non-zero pixels of the target image. (c) Result of erosion after one iteration. (d) Detection of object boundary as a result of difference between (b) and (c).

Chapter 7

Numerical modelling of a laboratory shear experiment using the combined finite-discrete element method (FDEM)

This chapter will be submitted to *Computer and Geotechnics* as: Zhao, Q., Abdelaziz A., Ha J., and Grasselli, G. (2017). Numerical modelling of a laboratory shear experiment using the combined finite-discrete element method (FDEM).

7.1   Introduction

Experimental studies under μCT provided unprecedented direct and detailed observation of the evolution of a sample under shear. The combination of rotary shear experiment and μCT imaging demonstrated the dominant role of surface roughness at the initial portion of slipping, the formation and accumulation of gouge, and the shear-induced secondary fractures. The experiment was carried out at small incremental shear steps, and the observation of the fault evolution was only available at discrete time points coincident with each rotation step; while an actual time-continuous observation is still in lack.

Numerical simulation has been extensively used to study the shear behaviour of rocks and provided insights into the shear behaviour of rock joints (e.g., Mora and Place, 1998; Place and Mora, 2001; Karami and Stead, 2008; Park and Song, 2009; Rasouli and Harrison, 2010; Asadi et al., 2012; Bahaaddini et al., 2013; Lambert and Coll, 2014; Tatone, 2014). In this study, we used the combined finite-discrete element method (FDEM) to simulate a rotary shear experiment. FDEM is a numerical method that combines continuum mechanics principles with discrete element method (DEM) to simulate interaction, deformation, and fracturing of materials (Munjiza et al., 1995; Munjiza, 2004). FDEM has the ability to explicitly capture the entire deformation and fracturing process and the associated seismic activity (Mahabadi et al., 2012a; Lisjak et al., 2013; Zhao et al., 2014, 2015b).

To fully simulate the behaviour of a rotary shear experiment is a challenging task, and may require a three-dimensional (3D) model (Hazzard and Mair, 2003). However, owing to the limited computation power, a 3D model capturing the entire sample geometry and shear process is not practical. On the other hand, the use of the two-dimensional (2D) simulation has the merit of reducing the computational demand, and it has been shown to provide insights into the shear behaviour in rocks (Tatone, 2014).

We reproduced a rotary shear experiment using a carefully built and calibrated 2D FDEM model and focused on investigating three aspects that are hardly accessible by the experiment: (1) the continuous variation of stresses, (2) the progressive failure of the shear zone, and (3) the shear induced seismicity. Our simulation demonstrated that a carefully calibrated numerical model was able to reproduce realistic emergent rock mechanical and frictional behaviours.

In the following sections, we first outline the simulation procedures of FDEM, and then we introduce the implementation of a new clustering algorithm that helps to improve the understanding of the simulated seismic activity. After that, the model setup and simulation procedure is presented. Then, major findings of this study are analyzed and discussed.
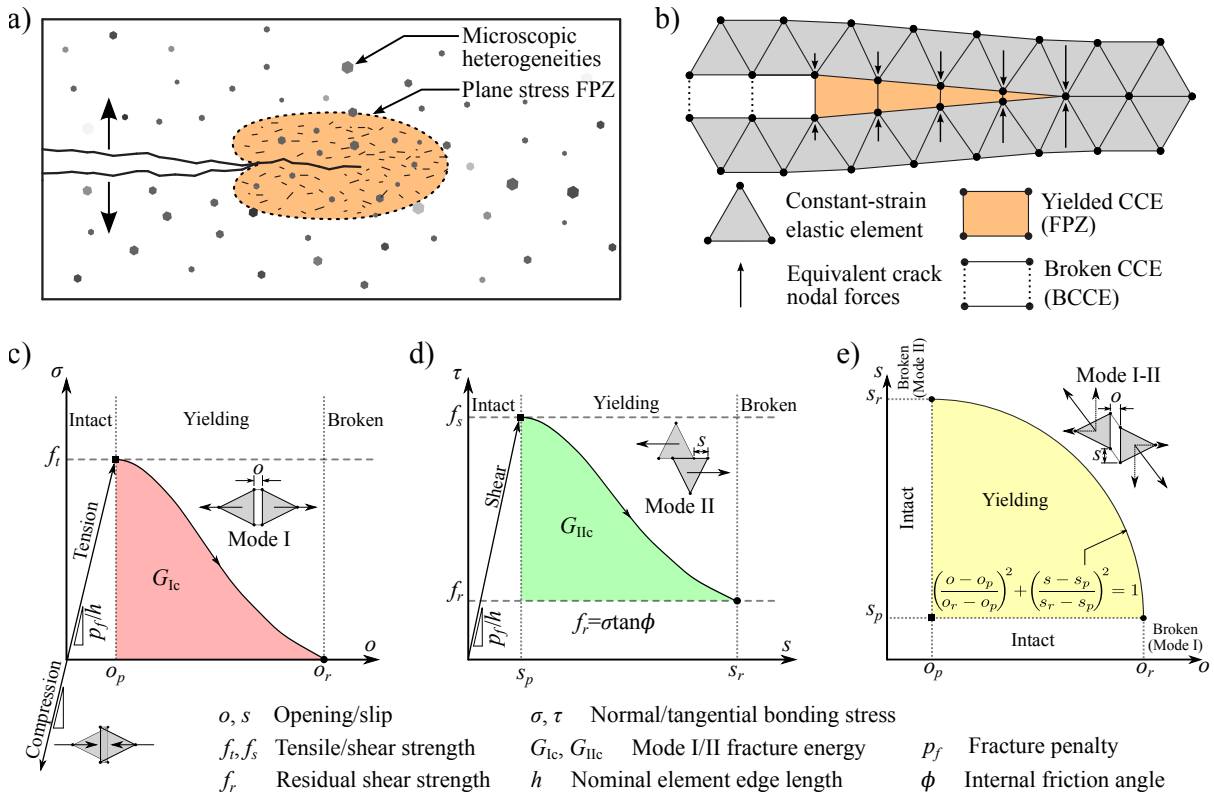
Figure 7.1: Schematic diagram showing the FDEM approach of simulating material failure. (a) Propagation of a tensile fracture and the creation of fracture process zone (FPZ) (Modified after Labuz et al., 1985; Lisjak et al., 2013). (b) Realization of the fracturing process in FDEM that involves the yielding and breakage of cohesive crack elements (CCE) (Modified after Lisjak et al., 2013; Zhao et al., 2014). (c)–(e) Deformation and failure criteria of the CCE (Modified after Tatone and Grasselli, 2015a).

7.2 Material and methods

7.2.1 The combined finite-discrete element method

In a FDEM model, the simulated material is meshed based on a finite element mesh consisting of nodes and triangular elements. The model is then enriched by inserting a four-node cohesive crack element (CCE) between each adjacent triangular element pair. An explicit time integration scheme is used to solve the equations of motion for the discretized system and update the nodal coordinates at each simulation step (Munjiza, 2004).

FDEM models the progressive failure of rock material according to the principles of non-linear elastic fracture mechanics (Dugdale, 1960; Barenblatt, 1962; Munjiza, 2004). It captures the fracturing behaviour of solids by modelling the entire failure path including elastic deformation, plastic yielding, and breakage (Figure 7.1).

Depending on the local stress and deformation field, the CCE first undergoes elastic deformation,

and upon its microscopic peak strength, it yields and experiences plastic deformation, simulating the development of the fracture process zone (FPZ) (Labuz et al., 1985). When the deformation of the CCE overcomes an energy based displacement threshold, the CCE breaks and releases the strain energy accumulated in the elastic triangular elements, resembling the energy release process of seismic activities. The broken cohesive crack element (BCCE) is then considered as a new fracture. At laboratory scale, this failure process is referred to as acoustic emission (Lockner, 1993); while at engineering scale, it is referred to as microseismicity (Reyes-Montes et al., 2005).

7.2.2 Analysis of simulated seismic activity in FDEM

There are two main reasons for modelling seismic activity in rocks, as suggested by Hazzard and Young (2002). First, the quantitative seismic information from the models, together with the simulated mechanical behaviour and damage observations, can provide an additional tool to validate the model. Second, a successfully validated model can be used to investigate the relationships between simulated seismicity, damage characteristics, and model properties.

FDEM simulated seismic activity has been analyzed using two approaches: (1) internal monitoring of the node motions during crack propagation and (2) seismic source inversion of the simulated seismograms (Lisjak et al., 2013; Grasselli et al., 2012). The latter approach is limited to models with simple geometry and stress conditions, and in this study, we further develop the former approach to obtain more insight into the fracturing process.

In the internal monitoring approach, the occurrence time, kinetic energy release, coordinates, and failure mode of each BCCE are recorded (Lisjak et al., 2013). A limitation of this approach is that it considers each BCCE as one seismic event, whose properties are highly dependent on the element size. While under certain laboratory scale simulations, the breakage of CCEs can be regarded as acoustic emissions associated with the breakage of mineral grains and boundaries (e.g., Lisjak et al., 2013; Zhao et al., 2015b), in most cases, the mesh dependency needs to be addressed to obtain a better physical meaning of the BCCEs. Zhao et al. (2014) implemented a clustering algorithm based on the spatial and temporal distribution of BCCEs using a non-parametric approach. The method used therein was able to cluster BCCEs successfully; however, a major improvement was required to constrain the clustering by considering the rupture velocity of cracks.

Crack propagation velocity (v_f) is controlled by the driving force at the crack tip (i.e., stress intensity factor) (Atkinson, 1987). Analytical and numerical calculations demonstrated that the maximum crack propagation velocity (i.e., terminal fracture propagation velocity, v_T) for mode I and mode II cracking are
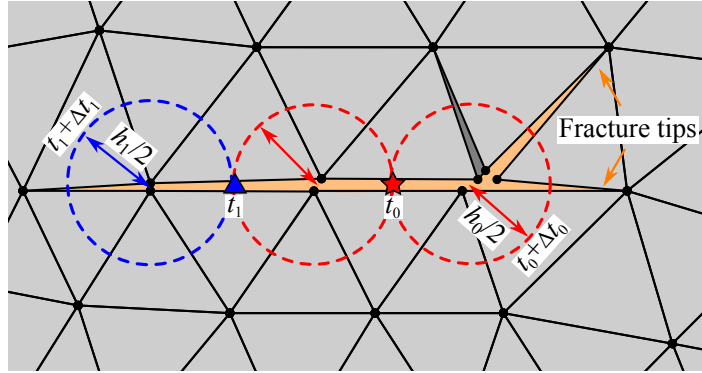
Figure 7.2: Schematic diagram illustrating the clustering algorithm. The red star indicates the centre of the first BCCE in this region that occurred at time t_0 (i.e., hypocenter), the fracture propagated in two directions and the adjacent BCCEs occurring within a radius of h_0 and time delay of Δt_0 were clustered into the same seismic event. The clustering continues searching for all BCCE based on the newly clustered fracture tip (e.g., blue triangle) until no BCCEs satisfy the clustering criteria.

Rayleigh-wave velocity (v_R) and P-wave velocity (v_P), respectively (Freund, 1972; Burridge, 1973; Andrews, 1976). These calculations were verified by experimental observations (Washabaugh and Knauss, 1994; Xia et al., 2004). However, v_T up to wave speeds were obtained for weak interfaces lacking intrinsic strength, and crack propagating in intact materials showed slower velocities due to energy dissipation in the FPZ (Ravi-Chandar and Knauss, 1984a,b; Washabaugh and Knauss, 1994). For mode I cracks, the reported v_f mostly falls in the range of 0.2–0.57v_R (as reviewed by Zhang and Zhao, 2014). On the other hand, there are barely any published data available for v_f of mode II cracking of intact materials; however, it was convenient to assume a constant v_f of 0.5v_S as a first approximation (Madariaga, 1976; Hazzard and Young, 2002).

In FDEM, the cohesive crack model mimics the effect of the FPZ and yielding and breakage of the CCEs consume energy (Figure 7.1). Stemming from the discussion above, we assumed $v_f = 0.5v_R$ and $0.5v_S$ for the clustering of mode I and II crack propagation in FDEM, respectively. v_R can be estimated from the Poisson's ratio (ν) and v_S (Freund, 1998):

$$v_R = \frac{0.862 + 1.14\nu}{(1+\nu)v_s}. \tag{7.1}$$

The clustering algorithm has been implemented as a post-processing tool, where all the BCCEs recorded during the simulation are clustered after the simulation. The process is demonstrated using a simple example (Figure 7.2):

(1) In this examined area, a CCE breaks at time t_0. Considering this initial BCCE as a fracture with negligible thickness, its centre point is considered as the hypocentre (red star) of this clustered

seismic event. The searching for other BCCEs belonging to this event starts from both ends (i.e., fracture tips) of the initial BCCE.

(2) Using the two fracture tips as the centres and the half-length ($h_0/2$) of the initial BCCE as the radius, BCCEs occurred in such a region within a time delay of Δt are clustered into the same seismic event (e.g., the BCCE occurred at t_1, indicated by the blue triangle). Δt is calculated using the fracture rupture velocity associated with the dominant failure mode as $\Delta t = h_0/2v_f$, which ensures that these BCCEs belong to one rupture process. The searching radius of $h_0/2$ ensures that BCCEs clustered together are connected fractures.

(3) The same searching algorithm is applied to the new BCCEs clustered into the current event, and their ends are treated as fracture tips and half-lengths as searching radii.

(4) The searching for BCCEs belonging to the current seismic event continues until no further BCCEs satisfy the criteria. Then this cluster of BCCEs is considered as one seismic event, and its source parameters are calculated. This includes:

   (a) Event time, which is the breakage time of the first BCCE in this cluster;

   (b) Source mechanism, which is represented by a scalar number ζ and calculated as a weighted average of the failure mode of all BCCEs in this cluster:

$$\zeta = \frac{\sum\limits_{i=1}^{n} E_k^i \gamma^i}{\sum\limits_{i=1}^{n} E_k^i}; \tag{7.2}$$

where the kinetic energy release by the formation of the ith BCCE (E_k^i) is taken as its weight, n is the total number of BCCEs clustered in this seismic event, and γ^i is the failure mode of the ith BCCE. $\zeta = 1$ and 2 represent pure tensile and shear events, respectively, while events having $1 < \zeta < 2$ have tensile and shear failure components.

   (c) Hypocentre location, which is the coordinates of the centre of the initial BCCE in this cluster; and

   (d) Energy released by the event, which is the sum of kinetic energy release of all BCCEs in this cluster (i.e., $\sum\limits_{i=1}^{n} E_k^i$).

(5) Proceed to the next cluster, until all recorded BCCEs are processed.

In this way, multiple BCCEs that were created by a single rupture process are clustered into one seismic event, resulting in a more realistic estimation of the source mechanism and event energy.

7.2.3 Calibration of numerical parameters

FDEM models synthesize the macroscopic behaviour of materials from the interaction of micro-mechanical constituents. As a result, the macroscopic mechanical properties measured by standard laboratory tests cannot be used directly, and an iterative calibration is required to obtain the correct input parameters (Tatone, 2014). The Flowstone cementitious material used in the rotary shear experiment was calibrated by Tatone and Grasselli (2015a) using the open source FDEM code, Y-Geo (Mahabadi et al., 2012a). We adapted the numerical parameters and re-calibrated them (Table 7.1) for the FDEM software Irazu (version 3.1.0, by Geomechanica Inc.), because of the modified implementations of penalties and viscous damping coefficient.

Major changes of the numerical parameters were (1) the fracture penalty (P_f) was ten times smaller; (2) a viscous damping factor (α) of 1, instead of a uniform damping coefficient for the entire model, was used; and (3) strength related parameters were fine tuned. $\alpha = 1$ means that the viscous damping of each triangular element is calculated as the critical damping coefficient (k_s) (Munjiza, 2004; Lisjak et al., 2016):

$$k_s = 2h\sqrt{E\rho}, \tag{7.3}$$

where E is the Young's modulus of the simulated material, ρ is the element density, and h is the average edge length of the element. Equation 7.3 provides an approximation of the theoretical critical damping assuming a single element of size h, that behaves as a one-degree-of-freedom mass-spring-dashpot system (Munjiza, 2004). The implementation of element-specific damping improved the simulation quality by avoiding improperly damped conditions especially when the model has a graded mesh.

The averaged laboratory test results were used as the calibration targets; namely, the unconfined compressive strength, $\sigma_c = 50.3$ MPa, the Young's modulus, $E = 15.0$ GPa, the Poisson's ratio, $\nu = 0.24$, and the indirect tensile strength, $\sigma_t = 2.6$ MPa. An unconfined compressive strength test model and a Brazilian disc test model were created to calibrate the numerical parameters. The corresponding emergent macro-mechanical properties of the calibrated numerical material were 49.9 MPa, 15.0 GPa, 0.24, and 2.7 MPa, respectively; in good agreement with the experimental values. In addition, according to the simulated elastic properties, the P- and S-wave velocities (v_P and v_S) of the simulated material were 2967 m/s and 1884 m/s, respectively.

7.2.4 Model setup

In order to reproduce the rotary shear experiment, we built the model based on the sample used in the experiment. The sample assembly consisted of the top and bottom semi-samples, with an artificial fault

Table 7.1: Input parameters for the calibrated FDEM model.

Property (unit)	Value
Density, ρ (kg·m^{-3})	1704
Young's modulus, E (GPa)	15.6
Poisson's ratio, ν (-)	0.22
Internal friction angle, ϕ (°)	24.5
Internal cohesion, c (MPa)	17.5
Tensile strength, σ_t (MPa)	2.55
Mode I fracture energy, G_{Ic} (J·m^{-2})	3.8
Mode II fracture energy, G_{IIc} (J·m^{-2})	90
Fracture penalty, P_f (GPa)	156
Viscous damping factor, α	1

between them created via a three point bend testing configuration (Figure 7.3a). However, due to the limitation of the 2D simulation, the geometry of the fault could not be directly modelled. Instead, we analyzed the 3D surface scan results and extracted the circular profiles with the largest amplitude, which corresponds to the radius of 5.6 mm (Figure 7.3b&c). Despite the slight difference at the location with a large pore, which the surface scan was unable to resolve, the extracted surface profiles were consistent with the μCT image.

These profiles were adjusted to recreate the initial experiment conditions according to the μCT image (Figure 7.3d). We first aligned the profiles laterally according to the μCT image, then the top profile was rotated 0.15 degree clockwise for better matching. The slight rotation in the μCT image indicated that in the experiment, the top semi-sample was not perfectly aligned with the bottom semi-sample.

The surface was scanned at a horizontal grid interval of 44 μm, and creating a numerical model meshed to such a fine resolution is impractical. We sub-sampled the profiles to a 0.1 mm nominal grid interval, which was chosen as an acceptable compromise between computation time and accuracy in representing the surface geometry. In addition, to mimic the rotary shear behaviour, the two ends of the profiles were extended by 3 mm, using the same geometry as their opposite ends to create an effective periodic boundary (Figure 7.3d). These carefully prepared profiles formed the initial shear interface of the numerical model.

The bodies of the top and bottom semi-samples were made to be 15 mm thick, resulting in a total vertical length of 30 mm, similar to the sample used in the laboratory experiment. The corners at the ends of the shear surfaces were filleted with a radius of 0.2 mm to avoid stress concentration that may result in unrealistic damage. To reduce the computation time required to close the aperture, the vertical distance between the top and bottom semi-samples was adjusted so that the closest point between them was 2×10^{-6} mm. Moreover, two boxes were added to simulate sample holders and the shrink tube that covered the sample in the experiment.
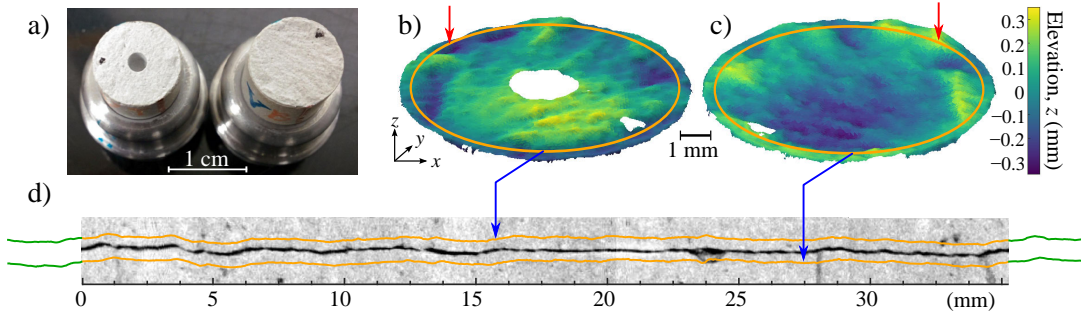
Figure 7.3: Preparation of 2D surface profiles for the model setup. (a) The top (left) and bottom (right) semi-samples used in the rotary shear experiment. (b)–(c) 3D surface scan of the shear surfaces. Red arrows indicate the location with the largest surface amplitude. (d) Comparison of the adjusted profiles with the μCT image showing the initial condition of the shear simulation. Note that the top and bottom profiles were vertically offset for clearer illustration.

With regard to meshing, the region of interest (i.e., 1 mm adjacent to the shear surfaces) was discretized with a constant nominal element size of 0.1 mm. The remaining parts of the model were meshed with linearly increasing mesh size as a function of the distance from the shear interface, with the coarsest element size being 3 mm. As a result, the model was meshed into 20,240 triangular elements. These elements were assigned with the calibrated numerical properties (Section 7.2.3); while the boxes had stainless steel properties with infinite stiffness. The model was simulated under plane stress condition.

7.2.5 Simulation procedure and boundary conditions

The rough and slightly misaligned initial contact between the top and bottom semi-samples resulted in a reduced apparent stiffness (E_e) compared to the intact sample, which was tested prior to performing the shear simulation. A simulation was carried out to evaluate E_e by loading the sample vertically at a constant velocity of 0.2 mm/ms. The result of this simulation measured the E_e of the simulated sample, and provided the vertical strain associated with 2.5 MPa, which is the initial normal stress condition of the experiment. Note that the loading speed used in the study is significantly higher than those used in laboratory experiments; however, it has been verified to ensure a quasi-static loading condition while allowing a reasonable computation time (Mahabadi, 2012).

The simulation of the shear test was conducted in three phases (Table 7.2). In phase 1, the normal stress was applied by compressing the sample to a strain that corresponds to 2.5 MPa. In phase 2, shear velocity increased gradually over time to (i) allow the oscillation induced by the instantaneous stop of normal loading to damp out and (ii) mitigate the transient motion due to the instantaneous application of shear velocity. In phase 3, the top and bottom boxes were fixed in the vertical position, and moved in the horizontal direction at a constant velocity until the desired shear displacement was reached.
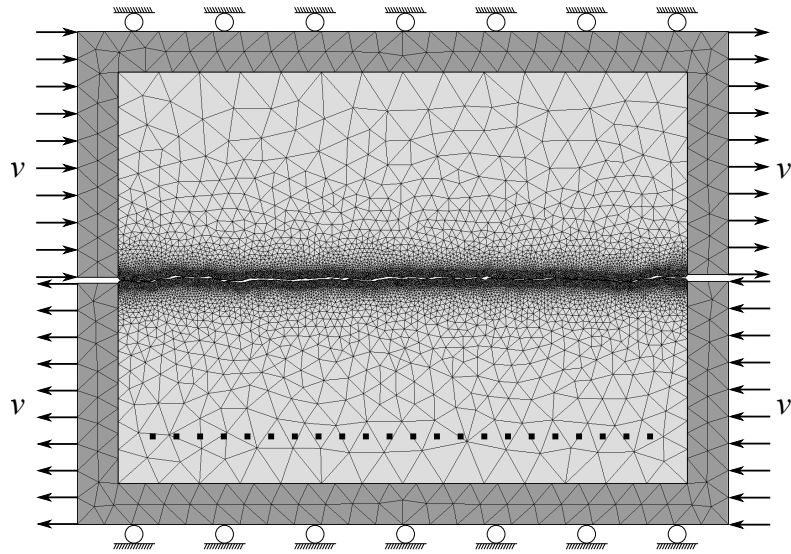
Figure 7.4: Mesh topology and boundary conditions of the shear test simulation. The top and bottom semi-samples were first loaded in the normal direction to 2.5 MPa, and then the vertical position of the parts were fixed (i.e., by rollers) and shear velocity was applied to shear the top and bottom semi-samples by a total shear displacement of 3 mm. The dotted line indicates the location of the virtual strain gauge.

Table 7.2: Boundary conditions applied to the model throughout the shear simulation and the resultant shear distance.

Phase	Purpose	Simulation steps	v_x (mm/ms)[1]	v_y (mm/ms)[2]	u (mm)
1	Normal load	1–66,400	0	0.1	0
2	Transition	66,401–964,000	0–0.15[3]	0	0–0.02
3	Shear test	964,001–26,000,000	0.15	0	0.02–3.02

[1] Positive ($\rightarrow$) on the top box and negative ($\leftarrow$) on the bottom box.
[2] Negative ($\downarrow$) on the top box and positive ($\uparrow$) on the bottom box.
[3] Linearly interpolated every time step to ramp up the shear velocity gradually.

A virtual measurement line recording the normal and shear stresses of each element along this line was placed adjacent to the bottom of the sample (Figure 7.4). This measurement line monitored the stress conditions every 13,000 simulation steps, equivalent to a 200 Hz monitoring rate. The recorded element stresses were then averaged to obtain the overall normal stress (σ_n) and shear stress (τ), which were used to calculate the apparent friction coefficient:

$$\mu = \frac{\tau}{\sigma_\mathrm{n}}. \tag{7.4}$$

The model simulated approximately 3 mm of shear displacement in 26 million simulation steps, and each step represents a simulation time of 4×10^{-7} ms. In addition to the above-mentioned optimizations for computation time, the Irazu FDEM simulation software is also parallelized on GPU (i.e., graphics processing unit), which significantly improved the simulation speed. The simulation took roughly 5 days
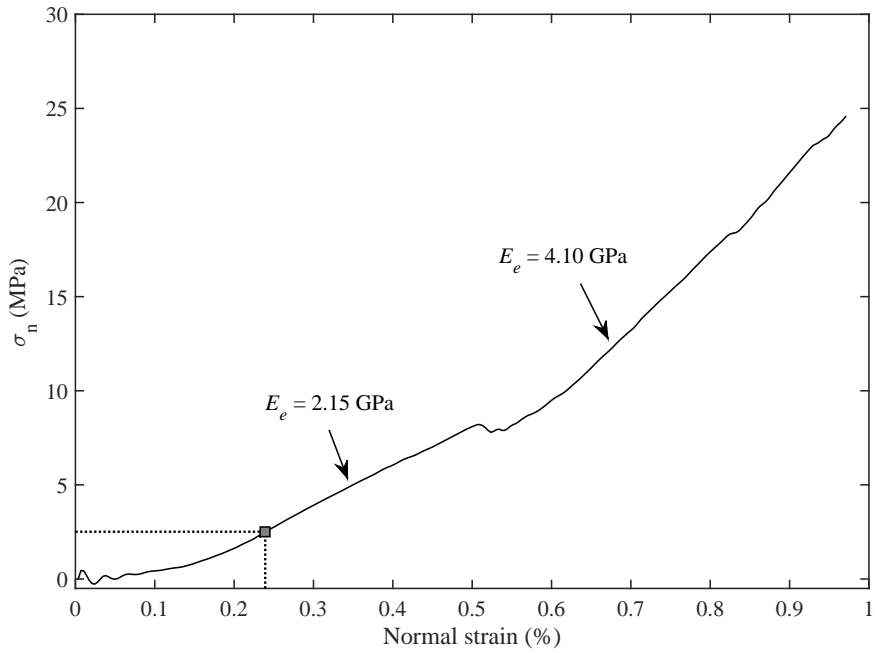
Figure 7.5: Simulation result of the apparent normal stiffness test. The square indicates the location where the apparent normal stress was 2.5 MPa. Arrows indicate the two linear portions of the stress-strain curve with different apparent normal stiffness (E_e) values. Note that the wiggle at the initial portion of the loading curve was the oscillation due to the instantaneous application of the vertical loading, and this oscillation was damped out after a short period of time, not affecting the overall behaviour.

to complete, with a computer equipped with an AMD Radeon R9 390 GPU and a 4.0 GHz Intel i7 CPU (i.e., central processing unit).

7.3 Results and data analysis

7.3.1 Application of normal stress

The initial portion of the stress-strain curve of the simulated apparent normal stiffness test was non-linear (Figure 7.5), and at approximately 0.15% strain, the normal stress (σ_n) started to climb almost linearly with a slope (i.e., apparent normal stiffness, E_e) of 2.15 GPa. When σ_n reached 7.5 MPa, a minor stress drop occurred. This drop was related to the development of a sub-vertical fracture started from an asperity with high stress concentration. After that, σ_n increased at a higher E_e, until the sample was entirely fractured. The first linear portion, has an E_e closely resembling the value measured in the laboratory experiment (Figure 6.17).

7.3.2 Frictional behaviour

The shear stress (τ) experienced a significant amount of fluctuation. These fluctuations were related to the stress disturbance due to the breakage of material and associated seismic activity on the shear surface, and some of them resulted in an overall tensional stress condition in the shear direction (i.e., $\tau < 0$). These seismic activities will be investigated in the following section.

In general, τ increases prior to $\sim$1 mm of shear displacement (u), and reached the peak value of 2.13 MPa. After that, τ showed no obvious correlation with u. σ_n increased continuously with increasing shear displacement (Figure 7.6), and the fluctuations were relatively small compared to its magnitude. At $u = 3$ mm, σ_n reached 24 MPa. This overall increasing trend was caused by the slightly tilted top shear surface, which acted as long-wavelength unevenness that induced dilation throughout the shearing process.

The calculated friction coefficient fluctuated, as a result of the fluctuation of τ, and it reached the peak value of $\mu = 0.25$ at $u \simeq 0.3$ mm. Note that the peak shear stress and peak friction coefficient did not occur at the same point. After that, the magnitude of the fluctuation decreased gradually as σ_n kept increasing. μ stabilized at approximately 0.07. The overall range of the friction coefficient was significantly lower than the value reported in the laboratory experiment; however, the frictional behaviour qualitatively matched the experiment observations well (i.e., Figure 6.4).

The laboratory experiment was carried out at incremental shear steps, and the stress condition varies between rotation steps due to the creep/relaxation and the initiation step (Section 6.4.1). Nonetheless, a closer look at the stress conditions and the friction coefficient of the initial $\sim$0.3 mm of shear displacement, which corresponds to the first rotation step of the laboratory shear experiment, showed intriguing similarities between the values measured in the laboratory experiment and the simulated results (Figure 7.7).

The initial portion of the frictional behaviour of the experimental data can be divided into four stages (Figure 7.7a): (I) τ, σ_n, and μ ramped up gradually; (II) τ experienced a stable stage with minor increase, and σ_n decreased continuously, causing τ to increase gradually; (III) τ increased to a peak shear stress, and σ_n also increased but at a slower rate than τ, causing μ to increase to the peak value; and (IV) τ, σ_n, and μ dropped quickly.

Comparing the simulated results with the experimental data, it was clear that these stages were qualitatively captured by the simulation (Figure 7.7b). However, the simulated shear stress and resultant friction coefficient were much lower than the experimental results, and the simulation had more fluctuations. To further investigate this interesting behaviour, we examined the local stress conditions
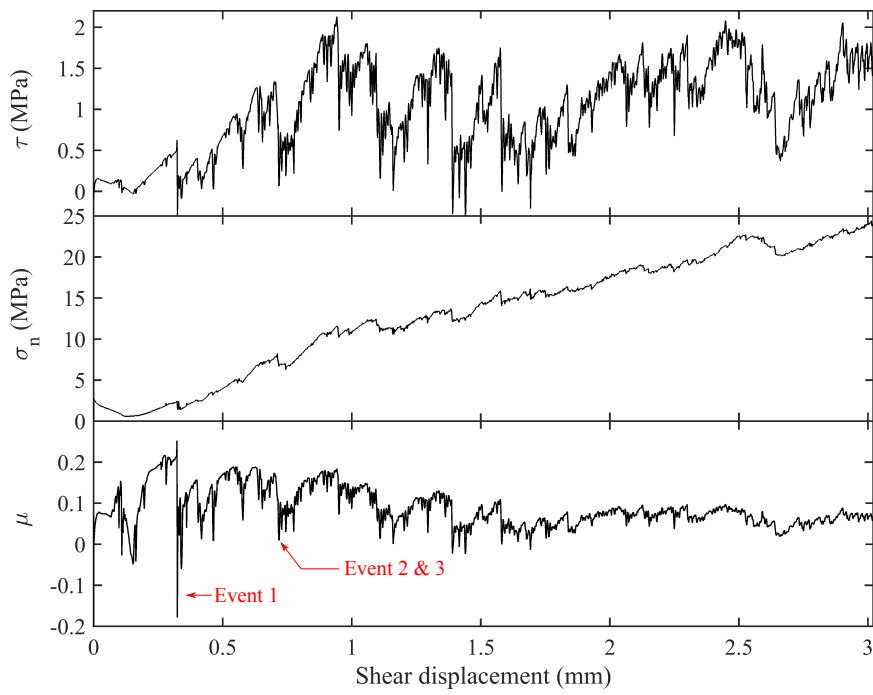
Figure 7.6: Apparent shear and normal stresses and the calculated friction coefficient. Red arrows indicate significant drops of frictional resistance that were considered to be associated with seismic events, which are investigated in Section 7.3.3.
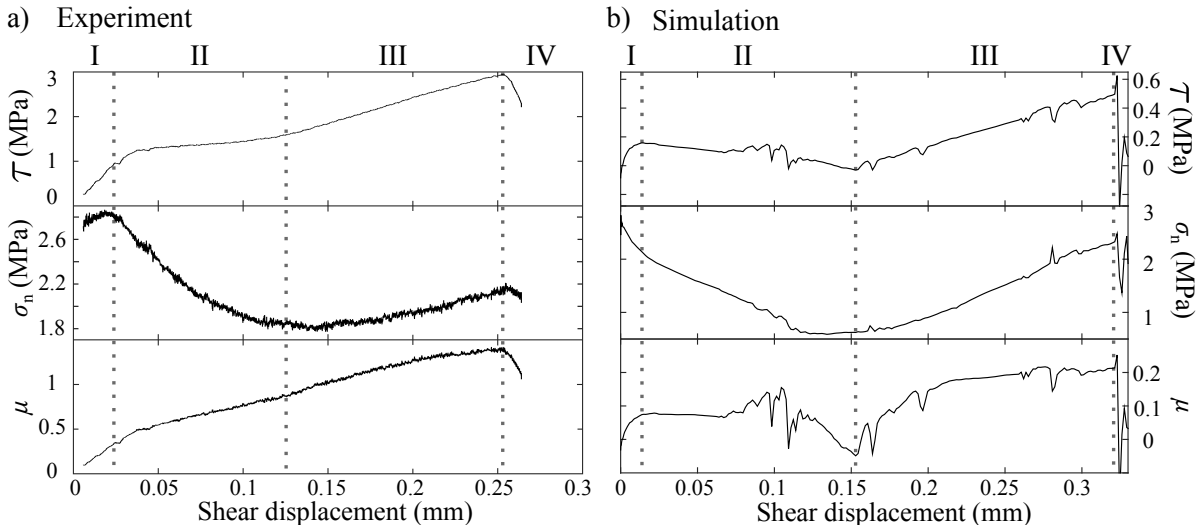
Figure 7.7: Comparison of stresses and friction coefficient of the initial portion of slipping between (a) the laboratory data and (b) the simulated data.

at the asperity associated with the stress drop at stage IV (Figure 7.8). The detailed review of this region clearly demonstrated that the stress variation was due to the shifting of contacts and asperity interaction.
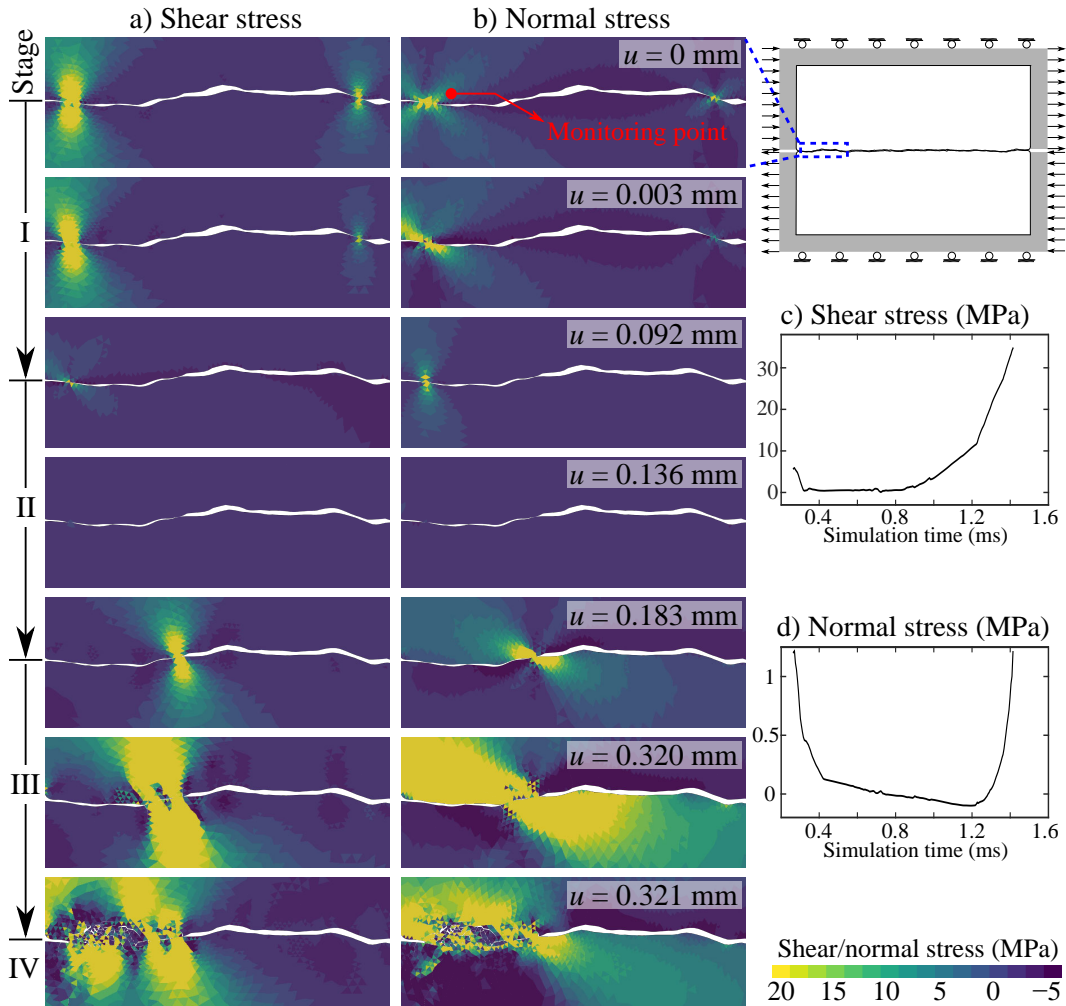
Figure 7.8: Zoom-in view of the asperity associated with the stress drop at stage IV. Local shear stress (panel a) and normal stress (panel b) are illustrated as a function of shear distance (u). (c) and (d) are the shear and normal stress conditions at the monitoring point, respectively.

7.3.3 Simulated gouge formation and microseismic activity

Large amount of material failure occurred during shearing, which was simulated by the breakage of cohesive crack elements (BCCEs). These BCCEs were used to evaluate the progressive damage of the shear surface and the formation of the gouge zone (Figure 7.9).

The first several BCCEs occurred at the location where the top and bottom semi-samples were the closest. However, significant damage started to appear at both ends of the shear surface after

approximately 0.5 mm of shear displacement. The damage was mostly concentrated adjacent to the shear surface prior to 1.5 mm of shear displacement, and then sub-vertical fractures penetrating into the sample body started to develop. Most of the BCCEs adjacent to the shear surface failed in shear mode (mode II), and almost all sub-vertical fractures propagated in tensile mode (mode I). As experimentally observed, the accumulation of gouge material was not uniform on the shear surface, in fact, even at the end of the simulation, a portion of the shear surface was still intact and without gouge material.

A total amount of 7,557 CCEs were broken throughout the simulation, and they were clustered into 5,293 events. The magnitude of these seismic events ranged from -11.4 to -4.4, with an averaged magnitude of -7.9, in agreement with simulated and experimental laboratory earthquakes (e.g., McLaskey et al., 2014; Goodfellow and Young, 2014; Zhao et al., 2015b). In general, large magnitude events tended to be shear dominant failure; while the small magnitude events tended to be tensile dominant failure (Figure 7.10). On the other hand, the magnitudes of the events did not show any correlation with their spatial locations. The vertical fractures, despite their significant extent, did not release large amounts of energy. In fact, these events had magnitude range from -9.9 to -5.6, with an averaged magnitude of -8.2.

Here, we chose three seismic events as examples and further examine them to demonstrate some detailed results we obtained from the simulation. Event 1 was related to the significant friction drop at approximately 0.3 mm of shear displacement, and Events 2 and 3 were two consecutive events that occurred closely in time.

Examining the particle velocity field and orientation of the maximum principal stress of the model (Figure 7.11), we found that prior to every event, the location of the event was experiencing a shear velocity lower than the loading velocity. These zones were related to the interlocking of asperities and referred to as interlocking zones (ILZs) in the following discussion. Stress concentrated at ILZs and eventually broke the asperities, releasing the accumulated strain energy. The seismic wave associated with such an energy release process was observed. At the source region, the seismic wave had particle velocity that was two orders of magnitude higher than that of the ILZ.

The initial BCCEs related to Events 2 and 3 were 12.5 mm and 0.005 ms apart, in space and time, respectively. Considering that the P-wave velocity is 2967 m/s, the P-wave induced by Event 2 travelled 14.8 mm when Event 3 occurred. This fact suggests that Event 3 may be triggered by the perturbation of the stress wave radiated from Event 2. However, due to the limited output frequency, the exact stress perturbation associated with such a triggering event was not captured.
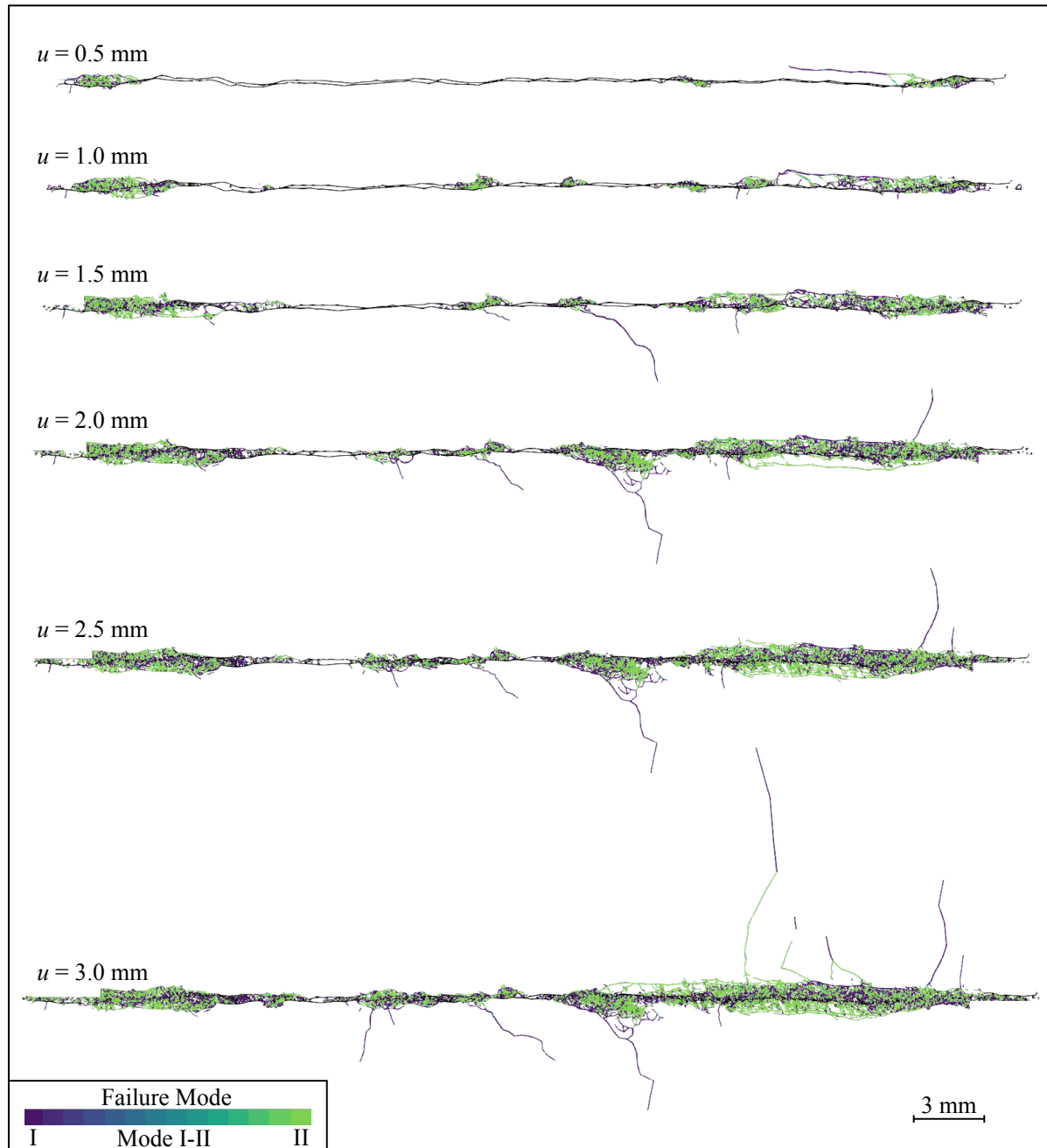
Figure 7.9: Broken CCEs at different shear displacement (u), indicating the damage of the shear surface and the accumulation of gouge material with increasing u.
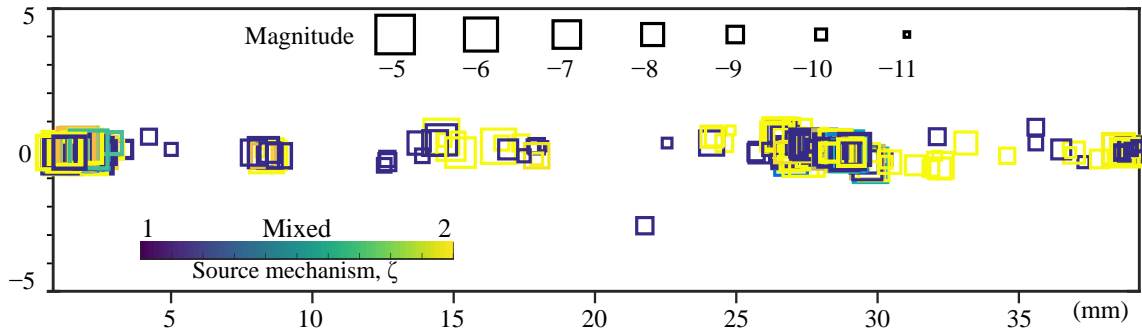
Figure 7.10: Magnitude, location, and failure mode of the clustered seismic activity. Only the largest and smallest 100 events in magnitude were plotted.

7.3.4 Energy budget

During an earthquake event, the accumulated potential energy (W) is partially released (ΔW) and partitioned into friction energy loss (E_F), fracture energy (E_G), and radiated energy (E_R) (Beeler, 2006; Kanamori, 2001; Kanamori and Heaton, 2000; Kanamori and Rivera, 2006):

$$\Delta W = E_R + E_F + E_G. \tag{7.5}$$

In the numerical model, E_F can be estimated from the nominal shear interface area (A_n), shear stress (τ), and the shear displacement (u), using (Kanamori and Rivera, 2006):

$$E_F = A_n \int_u \tau(u)\mathrm{d}u, \tag{7.6}$$

where A_n is calculated from the nominal shear surface length by assuming the model to be unit thickness.

Energy consumed by creating new fractures, E_G, was directly calculated using the energy consumed by creating the BCCEs:

$$E_G = \sum_{i=1}^{n} A(i)G_\mathrm{c}(i), \tag{7.7}$$

where $A(i)$ is the area of the ith BCCE calculated using its averaged edge length (h) and assuming unit thickness, and $G_\mathrm{c}(i)$ is the fracture energy based on its dominant mode of failure (Table 7.1).

The radiated energy, E_R, is calculated using the kinetic energy release associated with the breakage of BCCEs, following the work by Lisjak et al. (2013):

$$E_R = \sum_{i=1}^{n} E_k(i), \tag{7.8}$$

where $E_k(i)$ is the kinetic energy release by the ith BCCE.
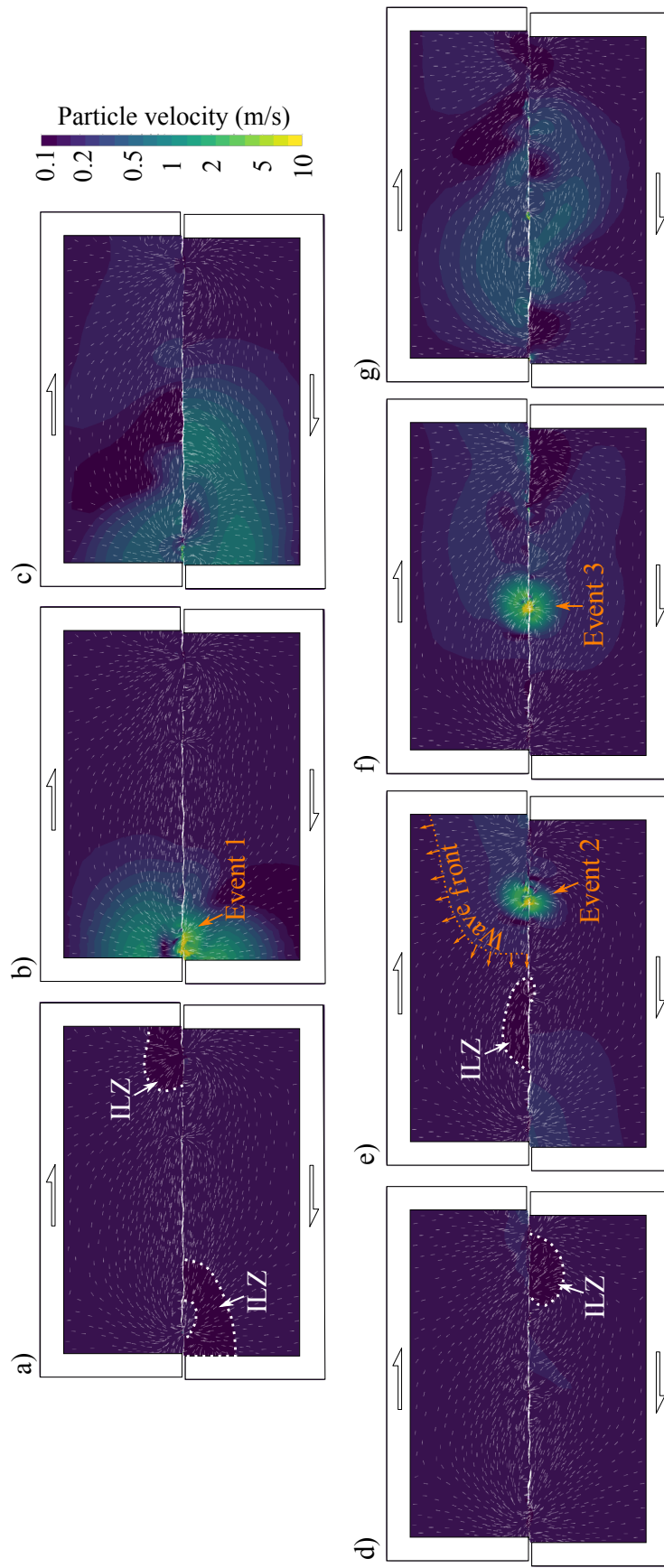
Figure 7.11: Particle velocity is indicated by the colour map and the orientation of the maximum principal stress is represented by the overlaying dashes. Note that particle velocity was shown in log scale for better illustration. Patches with particle velocity lower than 0.15 mm/ms (i.e., the loading velocity of each half of the sample) were highlighted as interlocking zones (ILZs).
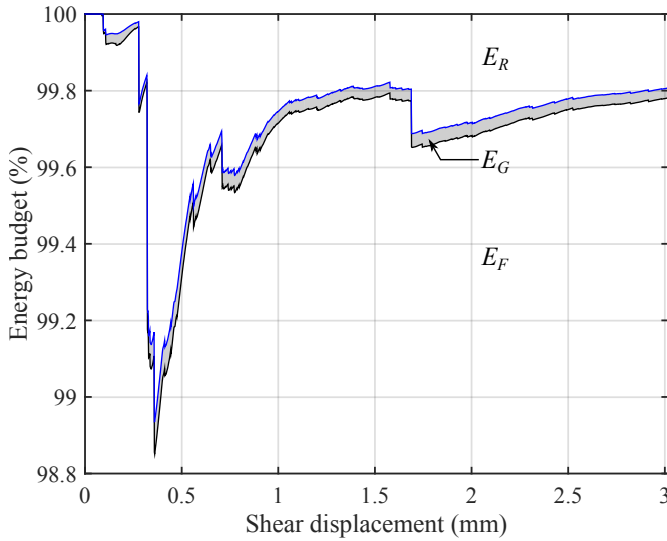
Figure 7.12: Energy budget shown as the relative percentage of friction work (E_F), fracture energy (E_G), and radiated energy (E_R).

As a result, we obtained the energy budget of the entire shear process (Figure 7.12). E_F consumed more than 98.8%, E_R accounted for up to 1.1%, and E_G consumed no more than 0.09% of the total released energy. The abrupt increase in radiated energy was related to the large magnitude seismic events. For example, the highest relative percentage of E_R was associated with Event 1.

7.4   Discussion

7.4.1   Apparent normal stiffness

The apparent normal stiffness (E_e) is influenced by the initial actual contact area, surface roughness, material strength, deformability of the asperities, and properties of infill material (Bandis et al., 1983). The overall stress-strain curve showed a hyperbola shape, which was related to the closure of the aperture. However, when studying the stress-strain curve, two segments were revealed, and the slope of the first portion (i.e., $E_e = 2.15$) closely matched the laboratory measurements. This verifies the apparent normal stiffness test conducted by the ERDµ-T apparatus, and showed that the existence of a rough fracture surface significantly altered the normal stiffness of the sample.

7.4.2   Frictional behaviour

Initial portion of the shear behaviour qualitatively resembled the laboratory test results very well. This suggests that the 2D profile we used in the simulation, which had the largest amplitude and was pos-

tulated to be associated with the formation of the first fracture in the experiment, was indeed the controlling factor of the initial portion of shearing.

Combining the experimental data (Figure 7.7a), the μCT image (Figure 7.3d), and the simulation results (Figure 7.7b and Figure 7.8), we can explain the laboratory observations and achieve a better comprehension of how the interaction between asperities controlled the frictional behaviour of the initial portion of slipping in the laboratory shear experiment (i.e., stages I–IV).

(I) During stage I, the shear stress increased gradually due to frictional resistance of the contact points under normal stress. Note that the minor normal stress increase measured in the experiment at this stage was not captured by the numerical model. This may be related to the interaction of the asperities in the direction perpendicular to shear, which was not captured by the simulation.

(II) During stage II, the top and bottom surfaces adjusted to a more conforming contact, which resulted in a decrease of the normal stress at the asperity contact. The asperities rarely interacted at this stage; therefore, the shear stress did not increase with the increasing shear displacement.

(III) During stage III the contact points shifted and asperities started to engage and interlock, causing the shear stress to increase quickly and reach the peak shear stress at the end of this stage. The asperities stayed intact and "climbed" onto each other, causing dilation and increased the normal stress.

(IV) At the beginning of stage IV, the asperity under high stress concentration broke and released the accumulated normal and shear strain locally, resulting in the drop of shear and normal stresses.

After the initial portion of shear displacement, no direct comparison can be made between the experimental and simulation results. However, as the laboratory test was limited to small incremental shear steps, the simulation had the merit of providing the time-continuous information of the shear behaviour.

The simulation shows that the shear surface did not slip as an entire body, rather, the slipping consisted of numerous shifting of contacts between asperities. Local asperities in contact were first broken and formed the gouge layer. This gouge layer accumulated and separated the top and bottom shear surfaces. Moreover, some parts of the shear surface remained intact throughout the shearing process. These observations agree with the laboratory observations on the post-mortem sample, and suggest the importance of surface roughness in controlling the formation of the gouge layer.

Sub-vertical fractures started to appear after approximately 1.5 mm of shear displacement (u), when significant amount of damage had already accumulated on the shear surface (Figure 7.9). This suggests

that when $u < 1.5$ mm, only local asperities (i.e., millimetric scale roughness) was controlling the frictional behaviour, and when $u > 1.5$ mm, the unevenness of the shear surface (i.e., centimetric scale roughness) becomes influential. The unevenness caused the normal stress (σ_n) to increase continuously, and at $u = 3$ mm, σ_n was approaching the peak σ_n measured in the simulation of the apparent normal stiffness test.

The stresses suffered significant fluctuations and the friction coefficient was much lower than the experimental measurement, which is a common limitation of the 2D simulations. The laboratory experiment by Frye and Marone (2002) and the numerical simulation by Hazzard and Mair (2003) demonstrated that 2D numerical models exhibit friction values notably lower than 3D models and laboratory measurements; meanwhile they suffer from much more fluctuation due to the lack of particle motion in the third dimension. To fully capture the shear behaviour of the rotary shear experiment, a 3D model capturing the surface geometry and asperity interaction on the entire shear surface will be required.

7.4.3 Seismic activity

The energy release by the breakage of asperities and degradation of intact material in the gouge layer was recorded and clustered into seismic events. Majority of the CCEs were not clustered and treated as single-CCE seismic events. This maybe due to the fact that the numerical parameters used in the model were calibrated to simulate quasi-static condition, which caused the fractures to "grow" gradually, instead of propagating dynamically. Nonetheless, the seismic events we obtained still provided insight into the location, mechanism, and magnitude of the shear induced seismic activity.

Shear dominant events were related to the breakage of asperities and crushing of intact materials, which occurred on the shear surface. On the other hand, sub-vertical fractures that penetrated into the sample body were all tensile dominant events. Considering that shear dominant events tend to have higher magnitude than tensile failure dominant events, this result suggests that almost all energy release occurred in the shear zone.

Local asperity interlocking zones (i.e., ILZs) led to seismic events that released accumulated strain energy. More interestingly, observations on two closely related events (Figure 7.11) suggested that the stress wave induced by one seismic event may trigger events at other locations.

Field observations showed that field seismic wave and near field dynamics deformation can dynamically trigger earthquakes (Gomberg et al., 2001, 2003), and laboratory experiment also demonstrated that the small strain (10^{-6} to 10^{-4}) due to seismic wave perturbation (Johnson and Jia, 2005) is sufficient to trigger seismic events. Our results agree with these observations and indicate that mechanical

based numerical simulation is a useful tool to investigate this aspect.

The energy budget derived from the model showed that almost all the energy was consumed by friction work, and fracturing consumed less than 0.1% of the total energy. Moreover, the relative percentage of the radiated energy, which is known as the seismic efficiency (η), was approximately 1% at the largest seismic event. The relative percentages of E_R and E_G were low compared to the values in the literature (e.g., McGarr, 1994; Wang, 2004), and the reason may be twofold: (1) the minimum mesh size of 0.1 mm restricted the capability of modelling crushing below such element size, which caused underestimation of E_G, and (2) the entire yielding and failure process of the BCCEs may release kinetic energy, and the absence of the consideration of such a process caused the underestimated E_R. On the other hand, the overall energy budget is qualitatively in agreement with the reported values and we demonstrated first time that a micromechanical based numerical model may help to understand the energy budget of earthquakes.

7.5 Conclusion

In this study, we used a carefully built and calibrated numerical model to reproduce the rotary shear experiment. The model was able to capture the mechanical and frictional behaviour observed in the laboratory experiment, providing detailed information of the continuous variation of stresses and the progressive evolution of the shear surface. With these observations, we were able to explain the laboratory measured stress variations. We introduced a clustering algorithm to improve the understanding of the simulated seismic events. The simulated seismicity suggested that the material damage and degradation in the shear zone released much more energy than the sub-vertical tensile fractures. Moreover, we observed a dynamically triggered seismic event on the shear surface. These results also demonstrated that mechanical based numerical simulation is a capable approach to study earthquake fault behaviour.

Supporting material[*]

Figure 7.13: Animated view of the particle velocity field associated with seismic event 1, as presented in Figure 7.11a–c.

---

[*]Animations can be viewed using *Adobe Acrobat (Pro, Standard, or Reader) DC* under Mac or Windows operating system.

Figure 7.14: Animated view of the particle velocity field associated with seismic events 2 and 3, as presented in Figure 7.11d–g.

Chapter 8

Conclusion

8.1   Overall conclusion

The main purpose of this dissertation was to investigate the different stages of progressive rock failure using numerical simulations and laboratory experiments. The combined finite-discrete element method (FDEM) was employed to analyze the influence of rock fabrics on hydraulic fracturing and associated seismicity (Chapter 2). Several seismic analysis tools were developed, including frequency-magnitude distribution (b-value), fractal dimension (D-value), and seismic events clustering. These simulations demonstrated that at local scale, fractures tended to propagate following the rock mass fabric; while at reservoir scale, they developed in the direction perpendicular to the minimum *in-situ* stress direction.

A numerical experimentation was then conducted to investigate the influence of *in-situ* stress on seismic activity (Chapter 3). The results demonstrated that the seismic signature (i.e., b-value, D-value, and seismic rate) can help to distinguish different phases. To further investigate the different phases of progressive failure, a uniaxial compression experiment, coupled with a time-lapse ultrasonic tomography, was carried out (Chapter 4). In addition, a FDEM model was built to reproduce the experiment. Using this combination of technologies, the entire deformation and failure processes were studied at macroscopic and microscopic scales. The results not only illustrated the rock failure and seismic behaviours at different stress levels, but also suggested several precursory behaviours indicating the catastrophic failure of the rock.

The research then focused on the frictional behaviour of rock fractures. Chapter 5 introduces a newly developed rock physics experimental apparatus (ERDµ-T) that was paired with X-ray micro-computed tomography (µCT) to inspect *in-situ* and *in-operando* deformation of the tested specimen.

This technology allowed for the direct observation of how two rough surfaces interact and deform without perturbing the experimental conditions (Chapter 6). Some intriguing observations were made regarding key areas of the study of fault evolution and frictional behaviour, including influence of surface roughness, real contact area, and energy budget.

Lastly, a carefully calibrated FDEM model that was built based on the rotary experiment (Chapter 7) to investigate aspects that the experiment was not able to. The implementation of a new clustering algorithm that helps to improve the understanding of the simulated seismic activity was first introduced, and then discussion on the mechanical behaviour of the shear interface and the shear induced seismicity was presented.

8.2   Contributions

This dissertation resulted in several original contributions and they can be broadly classified into two categories:

(1) Numerical simulation and analysis of brittle rock failure and associated seismicity.

  (i) The influence of bedding planes, discrete fracture network (DFN), and *in-situ* stress condition was systematically studied;

 (ii) A series of tools for analyzing FDEM simulated seismic events were developed, these include b-value, D-value, and fracture clustering; and

(iii) Integration of FDEM modelling with laboratory experiments was achieved by building and calibrating the model honouring the experimental sample and testing conditions.

   These contributions represented the first set of seismic analysis tools developed for the FDEM simulated seismic activity. The clustering approach eases the mesh dependency of the simulated events and enriches the physical meaning of the simulated fractures. Moreover, it was demonstrated for the first time that carefully built and calibrated FDEM model can reproduce and potentially predict rock behaviour.

(2) Rock physics experiment under μCT.

  (i) The ERDμ-T apparatus was installed, calibrated, and tested. A complete MATLAB script package for monitoring the system and conducting experiment was developed; and

(ii) A time-lapse 3D non-destructive observation of fault evolution was achieved using the ERDμ-T. Direct estimation of fracture surface area and the associated energy consumption was obtained.

These contributions represented the first rotary shear experiment apparatus that can be coupled with the μCT to provide *in-situ* and *in-operando* observation of the fault evolution. This new apparatus and the preliminary results obtained from it provided tantalizing direct observations and quantitative information of several crucial aspects of earthquake studies, including: fault surface evolution, development of secondary fractures, and energy budget. These aspects had never been directly observed or calculated.

8.3   Future directions

Based on the results reported in this dissertation, the following recommendations are proposed for future work:

1. Improve the understanding of simulated fracture propagation in FDEM.

   The cohesive crack model approach is the key component to realizes the continuum-discontinuum simulation in FDEM. This approach mimics the behaviour of the fracture process zone; however, quantitative relation between the related numerical parameters (e.g., fracture energy) and the fracture propagation velocity has not been studied in depth. Research in this direction may yield an additional way to calibrate FDEM models.

2. Deepen the comprehension of the controlling factors of hydraulic fracturing and associated seismicity and suggest a "traffic light" system.

   The influence of geological background such as bedding planes and *in-situ* stress condition were investigated separately in this dissertation. On the other hand, some precursory behaviours of catastrophic rock failure have been observed. A combined understanding of these results may help to establish a "traffic light" system to improve the safety of hydraulic fracturing operations.

3. Conduct 3D numerical modelling of rock failure.

   The importance of the third dimension has been emphasized in previous studies. In a 2D model, some 3D factors are neglected, for example the rotation of stress, the effect of the intermediate principal stress, and the particle motion in the third dimension. 3D models are likely to provide more accurate results by taking these factors into consideration. In addition, the digital surface

obtained by 3D surface scan and digital volume created from μCT images can be used as the framework to build 3D models. These could significantly improve the accuracy of the numerical model and may enable the prediction of rock behaviour.

4. Carry out confined rotary shear experiment and apply pore fluids.

   The rotary shear experiment in this study was unconfined that the fractures extended to sizes comparable to the main fault. Applying confining pressure may constrain the fracturing to the fault zone, allowing for the investigation of fault evolution and its interaction with fluid.

5. Improve the experimental approach for better understanding of the source mechanism and energy budget related to fault slip.

   There are two critical aspects that were not available for the rotary shear experiment in this study: radiated energy and sub-resolution fracture surface area. The radiated energy can be assessed by attaching acoustic emission sensors to the sample; while the sub-resolution fracture surface area can be estimated using a particle size distribution analysis of the post-mortem gouge material. Moreover, temperature sensors can be embedded to monitor the temperature change due to friction work.

6. Examine fault surface roughness as a function of slipping.

   Even though the continuous evolution of the sample volume was examined from the careful analysis of the μCT images, resolving the surface roughness variation as a function of slipping is challenging. However, further studies on this aspect is important to improve the understanding of frictional behaviour and may provide key information for upscaling laboratory interpretations to field scale.

Bibliography

Adachi, J., Siebrits, E., Peirce, A., and Desroches, J. (2007). Computer simulation of hydraulic fractures. *International Journal of Rock Mechanics and Mining Sciences*, 44(5):739–757.

Adams, L. H. and Williamson, E. D. (1923). On the compressibility of minerals and rocks at high pressures. *Journal of the Franklin Institute*, 195(4):475–529.

Aghababaei, R., Warner, D. H., and Molinari, J.-F. (2016). Critical length scale controls adhesive wear mechanisms. *Nature communications*, 7.

Aki, K. (1965). Maximum likelihood estimate of b in the formula logN=a−bM and its confidence limits. *Bull. Earthquake Res. Inst., Tokyo Univ.*, 43:237–239.

Aki, K. and Lee, W. H. K. (1976). Determination of three-dimensional velocity anomalies under a seismic array using first P arrival times from local earthquakes: 1. A homogeneous initial model. *Journal of Geophysical Research*, 81(23):4381–4399.

Al-Busaidi, A., Hazzard, J. F., and Young, R. P. (2005). Distinct element modeling of hydraulically fractured Lac du Bonnet granite. *Journal of Geophysical Research: Solid Earth*, 110(B6).

Amitrano, D. (2003). Brittle-ductile transition and associated seismicity: Experimental and numerical studies and relationship with the b value. *Journal of Geophysical Research: Solid Earth*, 108(B1).

Amitrano, D. (2012). Variability in the power-law distributions of rupture events. *The European Physical Journal-Special Topics*, 205(1):199–215.

Amitrano, D., Grasso, J.-R., and Hantz, D. (1999). From diffuse to localised damage through elastic interaction. *Geophysical Research Letters*, 26(14):2109–2112.

Amorese, D., Grasso, J.-R., and Rydelek, P. A. (2010). On varying b-values with depth: results from computer-intensive tests for Southern California. *Geophysical Journal International*, 180(1):347–360.

Andrews, D. J. (1976). Rupture velocity of plane strain shear cracks. *Journal of Geophysical Research*, 81(32):5679–5687.

Anthony, J. L. and Marone, C. (2005). Influence of particle characteristics on granular friction. *Journal of Geophysical Research-Solid Earth*, 110(B8).

Asadi, M. S., Rasouli, V., and Barla, G. (2012). A bonded particle model simulation of shear strength and asperity degradation for rough rock fractures. *Rock Mechanics and Rock Engineering*, 45(5):649–675.

ASTM (2002). Standard Test Method for Flexural Strength of Concrete (Using Simple Beam with Third-Point Loading). Technical report, American Society for Testing and Materials, West Conshohocken, PA, USA.

Atkinson, B. K. (1984). Subcritical crack growth in geological materials. *Journal of Geophysical Research: Solid Earth*, 89(B6):4077–4114.

Atkinson, B. K. (1987). *Fracture mechanics of rock.* Academic Press.

Babuška, V. (1984). P-wave velocity anisotropy in crystalline rocks. *Geophysical Journal International*, 76(1):113–119.

Bahaaddini, M., Sharrock, G., and Hebblewhite, B. (2013). Numerical direct shear tests to model the shear behaviour of rock joints. *Computers and Geotechnics*, 51:101–115.

Bandis, S., Lumsden, A., and Barton, N. (1983). Fundamentals of rock joint deformation. *International Journal of Rock Mechanics and Mining Sciences & Geomechanics Abstracts*, 20(6):249 – 268.

Barenblatt, G. (1959). The formation of equilibrium cracks during brittle fracture. General ideas and hypotheses. Axially-symmetric cracks. *Journal of Applied Mathematics and Mechanics*, 23(3):622–636.

Barenblatt, G. I. (1962). The mathematical theory of equilibrium cracks in brittle fracture. *Advances in applied mechanics*, 7:55–129.

Barree, R. D., Fisher, M. K., and Woodroof, R. A. (2002). A Practical Guide to Hydraulic Fracture Diagnostic Technologies.

Barton, N. (1974). *A Review of the Shear Strength of Filled Discontinuities in Rock: Review of a New Shear Strength Criterion for Rock Joints. N. Barton.* Norges Geotekniske Institutt. Norwegian Geotechnical Institute.

Beeler, N. M. (2006). Inferring earthquake source properties from laboratory observations and the scope of lab contributions to source physics. In R. Abercrombie A. McGarr, G. D. T. and Kanamori, H., editors, *Earthquakes: Radiated Energy and the Physics of Faulting*, pages 99–119, Washington, DC.

Beeler, N. M., Tullis, T. E., Blanpied, M. L., and Weeks, J. D. (1996). Frictional behavior of large displacement experimental faults. *Journal of Geophysical Research: Solid Earth*, 101(B4):8697–8715.

Belardinelli, M. E., Bonafede, M., and Gudmundsson, A. (2000). Secondary earthquake fractures generated by a strike-slip fault in the South {Iceland} Seismic Zone. *Journal of Geophysical Research: Solid Earth*, 105(B6):13613–13629.

Ben-David, O., Cohen, G., and Fineberg, J. (2010a). The dynamics of the onset of frictional slip. *Science*, 330(6001):211–214.

Ben-David, O., Rubinstein, S. M., and Fineberg, J. (2010b). Slip-stick and the evolution of frictional strength. *Nature*, 463(7277):76–79.

Bender, B. (1983). Maximum-Likelihood Estimation of B-Values for Magnitude Grouped Data. *Bulletin of the Seismological Society of America*, 73(3):831–851.

Biegel, R. L., Sammis, C. G., and Dieterich, J. H. (1989). The frictional properties of a simulated gouge having a fractal particle distribution. *Journal of Structural Geology*, 11(7):827–846.

Bistacchi, A., Griffith, W. A., Smith, S. A. F., Di Toro, G., Jones, R., and Nielsen, S. (2011). Fault roughness at seismogenic depths from LIDAR and photogrammetric analysis. *Pure and Applied Geophysics*, 168(12):2345–2363.

Boneh, Y., Chang, J. C., Lockner, D. A., and Reches, Z. (2014). Evolution of wear and friction along experimental faults. *Pure and Applied Geophysics*, 171(11):3125–3141.

Botev, Z. I., Grotowski, J. F., and Kroese, D. P. (2010). Kernel density estimation via diffusion. *The Annals of Statistics*, 38(5):2916–2957.

Brace, W. F. and Byerlee, J. D. (1966). Stick-slip as a mechanism for earthquakes. *Science*, 153(3739):990–992.

Brace, W. F., Paulding, B. W., and Scholz, C. (1966). Dilatancy in the fracture of crystalline rocks. *Journal of Geophysical Research*, 71(16):3939–3953.

Brown, S. R. and Scholz, C. H. (1985). Broad bandwidth study of the topography of natural rock surfaces. *J. geophys. Res*, 90(B14):12575–12582.

Buades, A., Coll, B., and Morel, J.-M. (2005). A non-local algorithm for image denoising. In *2005 IEEE Computer Society Conference on Computer Vision and Pattern Recognition (CVPR'05)*, volume 2, pages 60–65. IEEE.

Burridge, R. (1973). Admissible speeds for plane-strain self-similar shear cracks with friction but lacking cohesion. *Geophysical Journal of the Royal Astronomical Society*, 35(4):439–455.

Byerlee, J. (1978). Friction of Rocks. *Pure and Applied Geophysics*, 116(4-5):615–626.

Cai, M., Kaiser, P. K., Tasaka, Y., Maejima, T., Morioka, H., and Minami, M. (2004). Generalized crack initiation and crack damage stress thresholds of brittle rock masses near underground excavations. *International Journal of Rock Mechanics and Mining Sciences*, 41(5):833–847.

Candela, T., Renard, F., Bouchon, M., Brouste, A., Marsan, D., Schmittbuhl, J., and Voisin, C. (2009). Characterization of fault roughness at various scales: Implications of three-dimensional high resolution topography measurements. *Pure and Applied Geophysics*, 166:1817–1851.

Candela, T., Renard, F., Bouchon, M., Schmittbuhl, J., and Brodsky, E. E. (2011). Stress drop during earthquakes: effect of fault roughness scaling. *Bulletin of the Seismological Society of America*, 101(5):2369–2387.

Chambon, G., Schmittbuhl, J., and Corfdir, A. (2002). Laboratory gouge friction: Seismic-like slip weakening and secondary rate-and state-effects. *Geophysical research letters*, 29(10):1–4.

Chang, S.-H. and Lee, C.-I. (2004). Estimation of cracking and damage mechanisms in rock under triaxial compression by moment tensor analysis of acoustic emission. *International Journal of Rock Mechanics and Mining Sciences*, 41(7):1069–1086.

Chen, C.-C., Wang, W.-C., Chang, Y.-F., Wu, Y.-M., and Lee, Y.-H. (2006). A correlation between the b-value and the fractal dimension from the aftershock sequence of the 1999 Chi-Chi, Taiwan, earthquake. *Geophysical Journal International*, 167(3):1215–1219.

Chester, F. M. and Chester, J. S. (2000). Stress and deformation along wavy frictional faults. *Journal of Geophysical Research: Solid Earth*, 105(B10):23421–23430.

Chester, J. S., Chester, F. M., and Kronenberg, A. K. (2005). Fracture surface energy of the Punchbowl fault, San Andreas system. *Nature*, 437(7055):133–136.

Delle Piane, C., Giwelli, A., Clennell, M. B., Esteban, L., Kiewiet, L., Kager, S., and Raimon, J. (2016). Frictional and Hydraulic Behaviour of Carbonate Fault Gouge During Fault Reactivation — An Experimental Study. *Tectonophysics*, 690:21–34.

Desrues, J., Viggiani, G., and Besuelle, P. (2006). *Advances in X-ray Tomography for Geomaterials.* Wiley Online Library.

Di Toro, G., Goldsby, D. L., and Tullis, T. E. (2004). Friction falls towards zero in quartz rock as slip velocity approaches seismic rates. *Nature*, 427(6973):436–439.

Di Toro, G., Han, R., Hirose, T., De Paola, N., Nielsen, S., Mizoguchi, K., Ferri, F., Cocco, M., and Shimamoto, T. (2011). Fault lubrication during earthquakes. *Nature*, 471(7339):494–498.

Di Toro, G., Nielsen, S., and Pennacchioni, G. (2005). Earthquake rupture dynamics frozen in exhumed ancient faults. *Nature*, 436(7053):1009–1012.

Diederichs, M. S., Kaiser, P. K., and Eberhardt, E. (2004). Damage initiation and propagation in hard rock during tunnelling and the influence of near-face stress rotation. *International Journal of Rock Mechanics and Mining Sciences*, 41(5):785–812.

Dieterich, J. H. (1978). Time-dependent friction and the mechanics of stick-slip. *Pure and Applied Geophysics*, 116(4-5):790–806.

Dieterich, J. H. (1979). Modeling of Rock Friction .1. Experimental Results and Constitutive Equations. *Journal of Geophysical Research*, 84(B5):2161–2168.

Dieterich, J. H. (1981). Constitutive properties of faults with simulated gouge. In *Mechanical Behavior of Crustal Rocks*, volume 24, pages 103–120. AGU, Washington, DC.

Dieterich, J. H. and Kilgore, B. D. (1994). Direct observation of frictional contacts: New insights for state-dependent properties. *Pure and Applied Geophysics*, 143(1-3):283–302.

Dieterich, J. H. and Kilgore, B. D. (1996). Imaging surface contacts: power law contact distributions and contact stresses in quartz, calcite, glass and acrylic plastic. *Tectonophysics*, 256(1):219–239.

Dugdale, D. S. (1960). Yielding of steel sheets containing slits. *Journal of the Mechanics and Physics of Solids*, 8(2):100–104.

Dusseault, M. B. (2013). Geomechanical aspects of shale gas development. *Rock Mechanics for Resources, Energy and Environment*, page 39.

Efron, B. and Tibshirani, R. (1986). Bootstrap methods for standard errors, confidence intervals, and other measures of statistical accuracy. *Statistical science*, pages 54–75.

Ezazi, M. A., Quazi, M. M., Zalnezhad, E., and Sarhan, A. A. D. (2014). Enhancing the tribo-mechanical properties of aerospace AL7075-T6 by magnetron-sputtered Ti/TiN, Cr/CrN & TiCr/TiCrN thin film ceramic coatings. *Ceramics International*, 40(10):15603–15615.

Falls, S. D. and Young, R. P. (1998). Acoustic emission and ultrasonic-velocity methods used to characterise the excavation disturbance associated with deep tunnels in hard rock. *Tectonophysics*, 289(1):1–15.

Falls, S. D., Young, R. P., and Carlson, S. R. (1992). Ultrasonic tomography and acoustic emission in hydraulically fractured Lac du Bonnet grey granite. *Journal of Geophysical Research: Solid Earth*, 97(B5):6867–6884.

Freund, L. B. (1972). Energy flux into the tip of an extending crack in an elastic solid. *Journal of Elasticity*, 2(4):341–349.

Freund, L. B. (1998). *Dynamic fracture mechanics*. Cambridge university press.

Frye, K. M. and Marone, C. (2002). The effect of particle dimensionality on granular friction in laboratory shear zones. *Geophysical Research Letters*, 29(19):22–1–22–4. 1916.

Fusseis, F., Steeb, H., Xiao, X., Zhu, W.-l., Butler, I. B., Elphick, S., and Mäder, U. (2014). A low-cost X-ray-transparent experimental cell for synchrotron-based X-ray microtomography studies under geological reservoir conditions. *Journal of synchrotron radiation*, 21(1):251–253.

Gale, J. F. W., Reed, R. M., and Holder, J. (2007). Natural fractures in the Barnett Shale and their importance for hydraulic fracture treatments. *AAPG bulletin*, 91(4):603–622.

Gerstenberger, M., Wiemer, S., and Giardini, D. (2001). A systematic test of the hypothesis that the b value varies with depth in California. *Geophysical Research Letters*, 28(1):57–60.

Goebel, T. H. W., Becker, T. W., Schorlemmer, D., Stanchits, S., Sammis, C., Rybacki, E., and Dresen, G. (2012). Identifying fault heterogeneity through mapping spatial anomalies in acoustic emission statistics. *Journal of Geophysical Research: Solid Earth*, 117(B3):B03310.

Goldsby, D. L. and Tullis, T. E. (2011). Flash heating leads to low frictional strength of crustal rocks at earthquake slip rates. *Science*, 334(6053):216–218.

Gomberg, J., Bodin, P., and Reasenberg, P. A. (2003). Observing earthquakes triggered in the near field by dynamic deformations. *Bulletin of the Seismological Society of America*, 93(1):118–138.

Gomberg, J., Reasenberg, P., Bodin, P., and Harris, R. (2001). Earthquake triggering by seismic waves following the landers and hector mine earthquakes. *Nature*, 411(6836):462–466.

Gonzalez, R. C. and Woods, R. E. (2002). *Digital image processing.* Prentice-Hall Inc., Upper Saddle River, New Jersey.

Goodfellow, S. D., Flynn, J. W., Reyes-Montes, J. M., Nasseri, M. H. B., and Young, R. P. (2014). Acquisition of Complete Acoustic Emission Amplitude Records during Rock Fracture Experiments. *Journal of Acoustic Emission*, 32.

Goodfellow, S. D. and Young, R. P. (2014). A laboratory acoustic emission experiment under in situ conditions. *Geophysical Research Letters*, 41(10):3422–3430.

Grasselli, G., Zhao, Q., Lisjak, A., and Liu, Q. (2012). Numerical simulation of acoustic emission in rocks using fem/dem. In Zhao, J. and Li, J., editors, *Rock dynamics and applications – State of the art*, pages 149–159. CRC Press.

Greenleaf, J. F., Johnson, S. A., Lee, S. L., and Hermant, G. T. (1974). *Algebraic reconstruction of spatial distributions of acoustic absorption within tissue from their two-dimensional acoustic projections.* Springer.

Griffith, A. A. (1920). The phenomena of rupture and flow in solids. *Philosophical Transactions of the Royal Society of London. Series A, Containing Papers of a Mathematical or Physical Character*, 221:163–198.

Grob, M. and van der Baan, M. (2011). Inferring in-situ stress changes by statistical analysis of microseismic event characteristics. *The Leading Edge*, 30(11):1296–1301.

Gutenberg, B. (1956). The energy of earthquakes. *Quarterly Journal of the Geological Society*, 112(1-4):1–14.

Gutenberg, B. and Richter, C. F. (1944). Frequency of earthquakes in California. *Bulletin of the Seismological Society of America*, 34(4):185–188.

Han, R., Hirose, T., and Shimamoto, T. (2010). Strong velocity weakening and powder lubrication of simulated carbonate faults at seismic slip rates. *Journal of Geophysical Research: Solid Earth*, 115(B3).

Handin, J. (1966). Strength and ductility. *Geological Society of America Memoirs*, 97:223–290.

Hanks, T. C. (1992). Small earthquakes, tectonic forces. *Science*, 256(5062):1430–1432.

Hardy, H. R. (2003). *Acoustic emission/microseismic activity: Volume 1: Principles, Techniques and Geotechnical Applications* . Balkema, Lisse.

Hazzard, J. F. and Mair, K. (2003). The importance of the third dimension in granular shear. *Geophysical research letters*, 30(13):1708.

Hazzard, J. F. and Young, R. P. (2000). Simulating acoustic emissions in bonded-particle models of rock. *International Journal of Rock Mechanics and Mining Sciences*, 37(5):867–872.

Hazzard, J. F. and Young, R. P. (2002). Moment tensors and micromechanical models. *Tectonophysics*, 356(1-3):181–197.

Healy, J. H., Rubey, W. W., Griggs, D. T., and Raleigh, C. B. (1968). The Denver earthquakes. *Science*, 161(3848):1301–1310.

Henderson, J. R., Barton, D. J., and Foulger, G. R. (1999). Fractal clustering of induced seismicity in the Geysers geothermal area, California. *Geophysical Journal International*, 139(2):317–324.

Hillerborg, A., Modéer, M., and Petersson, P. E. (1976). Analysis of crack formation and crack growth in concrete by means of fracture mechanics and finite elements. *Cement and Concrete Research*, 6(6):773–781.

Hirata, T. (1987). Omori's Power Law aftershock sequences of microfracturing in rock fracture experiment. *Journal of Geophysical Research: Solid Earth*, 92(B7):6215–6221.

Hirata, T., Satoh, T., and Ito, K. (1987). Fractal Structure of Spatial-Distribution of Microfracturing in Rock. *Geophysical Journal of the Royal Astronomical Society*, 90(2):369–374.

Hubbert, M. K. and Willis, D. G. (1957). Mechanics of hydraulic fracturing. *Transactions of the American Institute of Mining and Metallurgical Engineers*, 210(6):153–163.

Hudson, J. A. and Harrison, J. P. (2000). *Engineering rock mechanics: an introduction to the principles*. Elsevier.

Hurst, H. E. (1951). Long-term storage capacity of reservoirs. *Trans. Amer. Soc. Civil Eng.*, 116:770–808.

Ida, Y. (1972). Cohesive force across the tip of a longitudinal-shear crack and Griffith's specific surface energy. *Journal of Geophysical Research*, 77(20):3796–3805.

Imoto, M. (1991). Changes in the magnitude-frequency b-value prior to large (M $\geqslant$ 6.0) earthquakes in japan. *Tectonophysics*, 193(4):311–325. Earthquake prediction.

Interface, Inc. (2007). *Model SGA strain gauge transducer amplifier user manual.*

Irwin, G. R. (1957). Analysis of stresses and strains near the end of a crack traversing a plate. *Journal of Applied Mechanics*, 24:361–364.

Jackson, M. E., Beuschel, C. A., McAteer, J. A., and Williams, J. C. (2008). Morphology of Major Stone Types, As Shown by Micro Computed Tomography (micro CT). *AIP Conference Proceedings*, 1049(1):333–337.

Jaeger, J. C., Cook, N. G. W., and Zimmerman, R. W. (2007). *Fundamentals of Rock Mechanics.* BlackWell Publishing, 4th edition.

Jansen, D. P., Carlson, S. R., Young, R. P., and Hutchins, D. A. (1993). Ultrasonic imaging and acoustic emission monitoring of thermally induced microcracks in lac du bonnet granite. *Journal of Geophysical Research: Solid Earth*, 98(B12):22231–22243.

Jasinski, R. J., Nelson, E. B., and Norman, W. D. (1996). Hydraulic fracturing process and compositions.

Jing, L. and Stephansson, O. (1995). Mechanics of rock joints: Experimental aspects. In Selvadurai, A. P. S. and Boulon, M. J., editors, *Mechanics of Geomaterial Interfaces*, volume 42 of *Studies in Applied Mechanics*, pages 317–342. Elsevier.

Johns, R. A., Steude, J. S., Castanier, L. M., and Roberts, P. V. (1993). Nondestructive measurements of fracture aperture in crystalline rock cores using x ray computed tomography. *Journal of Geophysical Research: Solid Earth*, 98(B2):1889–1900.

Johnson, E. (1992). Process Region Changes for Rapidly Propagating Cracks. *International Journal of Fracture*, 55(1):47–63.

Johnson, P. A. and Jia, X. (2005). Nonlinear dynamics, granular media and dynamic earthquake triggering. *Nature*, 437(7060):871–874.

Johnston, D. H. and Toksöz, M. N. (1980). Ultrasonic P and S wave attenuation in dry and saturated rocks under pressure. *Journal of Geophysical Research: Solid Earth*, 85(B2):925–936.

Kanamori, H. (2001). Energy budget of earthquakes and seismic efficiency. In Renata Dmowska, James R. Holton, H. T. R., editor, *Earthquake Thermodynamics and Phase Transformations in the Earth's Interior*, volume 76, pages 293–305. Academic Press.

Kanamori, H. and Heaton, T. H. (2000). Microscopic and macroscopic physics of earthquakes. In John B. Rundle, D. L. T. and Klein, W., editors, *Geocomplexity and the Physics of Earthquakes*, pages 147–163. Wiley Online Library.

Kanamori, H. and Rivera, L. (2006). Energy partitioning during an earthquake. In Abercrombie, R., McGarr, A., Di Toro, G., and Kanamori, H., editors, *Earthquakes: Radiated Energy and the Physics of Faulting*, pages 3–13. American Geophysical Union.

Karami, A. and Stead, D. (2008). Asperity degradation and damage in the direct shear test: A hybrid fem/dem approach. *Rock Mechanics and Rock Engineering*, 41(2):229–266.

Kern, H. (1993). P-and S-wave anisotropy and shear-wave splitting at pressure and temperature in possible mantle rocks and their relation to the rock fabric. *Physics of the Earth and Planetary Interiors*, 78(3):245–256.

Ketcham, R. A. and Carlson, W. D. (2001). Acquisition, optimization and interpretation of X-ray computed tomographic imagery: applications to the geosciences. *Computers & Geosciences*, 27(4):381–400.

Kleppner, D. and Kolenkow, R. (2013). *An introduction to mechanics.* Cambridge University Press.

Kranz, R. L. (1983). Microcracks in rocks: a review. *Tectonophysics*, 100(1):449–480.

Labuz, J., Shah, S., and Dowding, C. (1985). Experimental analysis of crack propagation in granite. *International Journal of Rock Mechanics and Mining Sciences & Geomechanics Abstracts*, 22(2):85–98.

Lakshmipathy, J. and Kulendran, B. (2014). Reciprocating wear behaviour of 7075Al/S_iC and 6061Al/Al_2O_3 composites: a study of effect of reinforcement, stroke and load. *Tribology in Industry*, 36(2):117–126.

Lambert, C. and Coll, C. (2014). Discrete modeling of rock joints with a smooth-joint contact model. *Journal of Rock Mechanics and Geotechnical Engineering*, 6(1):1–12.

Lei, X., Kusunose, K., Rao, M. V. M. S., Nishizawa, O., and Satoh, T. (2000). Quasi-static fault growth and cracking in homogeneous brittle rock under triaxial compression using acoustic emission monitoring. *Journal of Geophysical Research: Solid Earth*, 105(B3):6127–6139.

Lei, X., Masuda, K., Nishizawa, O., Jouniaux, L., Liu, L., Ma, W., Satoh, T., and Kusunose, K. (2004). Detailed analysis of acoustic emission activity during catastrophic fracture of faults in rock. *Journal of Structural Geology*, 26(2):247–258.

Lei, X. and Satoh, T. (2007). Indicators of critical point behavior prior to rock failure inferred from pre-failure damage. *Tectonophysics*, 431(1):97–111.

Lipták, B. G. (2013). *Process Control: Instrument Engineers' Handbook.* Butterworth-Heinemann.

Lisjak, A. and Grasselli, G. (2014). A review of discrete modeling techniques for fracturing processes in discontinuous rock masses. *Journal of Rock Mechanics and Geotechnical Engineering*, 6(4):301–314.

Lisjak, A., Liu, Q., Zhao, Q., Mahabadi, O. K., and Grasselli, G. (2013). Numerical simulation of acoustic emission in brittle rocks by two-dimensional finite-discrete element analysis. *Geophysical Journal International*, 195(1):423–443.

Lisjak, A., Mahabadi, O. K., Kaifosh, P., and Grasselli, G. (2014a). A New Geomechanical Modeling Approach for Simulating Hydraulic Fracturing and Associated Microseismicity in Fractured Shale Formations. *ARMA e-Newsletter*, Special Issue: Geomechanics of Hydraulic Fracturing in Shale Formations:9–12.

Lisjak, A., Mahabadi, O. K., Kaifosh, P., Vietor, T., and Grasselli, G. (2014b). A preliminary evaluation of an enhanced FDEM code as a tool to simulate hydraulic fracturing in jointed rock masses. In Alejano Perucho, A., Olalla, C., Jimenez, R., L. R., editor, *Rock Engineering and Rock Mechanics: Structures in and on Rock Masses*, pages 1427–1432. CRC Press.

Lisjak, A., Tatone, B. S. A., Mahabadi, O. K., and Kaifosh, P. (2016). *Irazu FDEM Theory Manual.* Geomechanica Inc.

Lo, T., Toksöz, M. N., Xu, S., and Wu, R. S. (1988). Ultrasonic laboratory tests of geophysical tomographic reconstruction. *Geophysics*, 53(7):947–956.

Lockner, D. A. (1993). The Role of Acoustic-Emission in the Study of Rock Fracture. *International Journal of Rock Mechanics and Mining Sciences & Geomechanics Abstracts*, 30(7):883–899.

Lockner, D. A., Byerlee, J., Kuksenko, V., Ponomarev, A., and Sidorin, A. (1991). Quasi-static fault growth and shear fracture energy in granite. *Nature*, 350(6313):39–42.

Lockner, D. A., Walsh, J. B., and Byerlee, J. D. (1977). Changes in seismic velocity and attenuation during deformation of granite. *Journal of Geophysical Research*, 82(33):5374–5378.

Ma, K.-F., Brodsky, E. E., Mori, J., Ji, C., Song, T.-R. A., and Kanamori, H. (2003). Evidence for fault lubrication during the 1999 Chi-Chi, Taiwan, earthquake (Mw7.6). *Geophysical Research Letters*, 30(5):1244.

Madariaga, R. (1976). Dynamics of an expanding circular fault. *Bulletin of the Seismological Society of America*, 66(3):639–666.

Mahabadi, O. K. (2012). *Investigating the influence of micro-scale heterogeneity and microstructure on the failure and mechanical behaviour of geomaterials.* PhD thesis, University of Toronto.

Mahabadi, O. K., Grasselli, G., and Munjiza, A. (2010). Y-GUI: A graphical user interface and pre-processor for the combinedfinite-discrete element code, Y2D, incorporating material heterogeneity. *Computers & Geosciences*, 36(2):241–252.

Mahabadi, O. K., Lisjak, A., Munjiza, and Grasselli, G. (2012a). Y-Geo: New Combined Finite-Discrete Element Numerical Code for Geomechanical Applications. *International Journal of Geomechanics*, 12(6):676–688.

Mahabadi, O. K., Randall, N. X., Zong, Z., and Grasselli, G. (2012b). A novel approach for micro-scale characterization and modeling of geomaterials incorporating actual material heterogeneity. *Geophysical Research Letters*, 39(1):L01303.

Mahabadi, O. K., Tatone, B. A., and Grasselli, G. (2014). Influence of microscale heterogeneity and microstructure on the tensile behavior of crystalline rocks. *Journal of Geophysical Research: Solid Earth*, 119(7):5324–5341.

Main, I. G., Meredith, P. G., and Jones, C. (1989). A reinterpretation of the precursory seismic b-value anomaly from fracture mechanics. *Geophysical Journal International*, 96(1):131–138.

Mair, K., Frye, K. M., and Marone, C. (2002). Influence of grain characteristics on the friction of granular shear zones. *Journal of Geophysical Research: Solid Earth*, 107(B10):2219.

Mair, K. and Marone, C. (1999). Friction of simulated fault gouge for a wide range of velocities and normal stresses. *Journal of Geophysical Research: Solid Earth*, 104(B12):28899–28914.

Marone, C. (1998). Laboratory-derived friction laws and their application to seismic faulting. *Annual Review of Earth and Planetary Sciences*, 26:643–696.

Marone, C. and Scholz, C. H. (1989). Particle-size distribution and microstructures within simulated fault gouge. *Journal of Structural Geology*, 11(7):799–814.

Martin, C. D. (1993). *The strength of massive Lac du Bonnet granite around underground openings.* PhD thesis, University of Manitoba.

Mavko, G., Mukerji, T., and Dvorkin, J. (1998). The Rock Physics Handbook: Tools forSeismic Analysis in Porous Media.

McGarr, A. (1994). Some comparisons between mining-induced and laboratory earthquakes. *pure and applied geophysics*, 142(3):467–489.

McLaskey, G. C. and Glaser, S. D. (2011). Micromechanics of asperity rupture during laboratory stick slip experiments. *Geophysical Research Letters*, 38(12):L12302.

McLaskey, G. C., Kilgore, B. D., Lockner, D. A., and Beeler, N. M. (2014). Laboratory generated M-6 earthquakes. *Pure and Applied Geophysics*, 171(10):2601–2615.

Meglis, I., Chow, T., Martin, C., and Young, R. (2005). Assessing in situ microcrack damage using ultrasonic velocity tomography. *International Journal of Rock Mechanics and Mining Sciences*, 42(1):25–34.

Michaels, J. E. (2008). Detection, localization and characterization of damage in plates with an in situ array of spatially distributed ultrasonic sensors. *Smart Materials and Structures*, 17(3):35035.

Mignan, A. and Woessner, J. (2012). Estimating the magnitude of completeness for earthquake catalogs. *Community Online Resource for Statistical Seismicity Analysis.*

Mitchell, T. M., Ben-Zion, Y., and Shimamoto, T. (2011). Pulverized fault rocks and damage asymmetry along the Arima-Takatsuki Tectonic Line, Japan. *Earth and Planetary Science Letters*, 308(3-4):284–297.

Mora, P. and Place, D. (1998). Numerical simulation of earthquake faults with gouge: toward a comprehensive explanation for the heat flow paradox. *Journal of Geophysical Research-Solid Earth*, 103(B9):21067–21089.

Morrow, C. A., Moore, D. E., and Lockner, D. A. (2000). The effect of mineral bond strength and adsorbed water on fault gouge frictional strength. *Geophysical research letters*, 27(6):815–818.

Munjiza, A. (2004). *The Combined Finite-Discrete Element Method.* John Wiley & Sons, Ltd.

Munjiza, A., Owen, D. R. J., and Bicanic, N. (1995). A combined finite-discrete element method in transient dynamics of fracturing solids. *Engineering Computations*, 12(2):145–174.

Nagata, K., Kilgore, B., Beeler, N., and Nakatani, M. (2014). High-frequency imaging of elastic contrast and contact area with implications for naturally observed changes in fault properties. *Journal of Geophysical Research: Solid Earth*, 119(7):5855–5875.

Neumann-Denzau, G. and Behrens, J. (1984). Inversion of seismic data using tomographical reconstruction techniques for investigations of laterally inhomogeneous media. *Geophysical Journal International*, 79(1):305–315.

Niemeijer, A., Marone, C., and Elsworth, D. (2010a). Fabric induced weakness of tectonic faults. *Geophysical Research Letters*, 37(3):L03304.

Niemeijer, A., Marone, C., and Elsworth, D. (2010b). Frictional strength and strain weakening in simulated fault gouge: Competition between geometrical weakening and chemical strengthening. *Journal of Geophysical Research: Solid Earth*, 115(B10):B10207.

Nuannin, P., Kulhanek, O., and Persson, L. (2005). Spatial and temporal b value anomalies preceding the devastating off coast of nw sumatra earthquake of december 26, 2004. *Geophysical Research Letters*, 32(11):L11307.

Nur, A. and Simmons, G. (1969). Stress-induced velocity anisotropy in rock: An experimental study. *Journal of Geophysical Research*, 74(27):6667–6674.

Okubo, P. G. and Dieterich, J. H. (1984). Effects of physical fault properties on frictional instabilities produced on simulated faults. *Journal of Geophysical Research: Solid Earth*, 89(B7):5817–5827.

Orowan, E. (1949). Fracture and strength of solids. *Reports on progress in physics*, 12(1):185.

Osborn, S. G., Vengosh, A., Warner, N. R., and Jackson, R. B. (2011). Methane contamination of drinking water accompanying gas-well drilling and hydraulic fracturing. *Proceedings of the National Academy of Sciences*, 108(20):8172–8176.

Paige, C. C. and Saunders, M. A. (1982). LSQR: An algorithm for sparse linear equations and sparse least squares. *ACM transactions on mathematical software*, 8(1):43–71.

Park, J.-W. and Song, J.-J. (2009). Numerical simulation of a direct shear test on a rock joint using a bonded-particle model. *International Journal of Rock Mechanics and Mining Sciences*, 46(8):1315–1328.

Parrish, A. and Camm, F. J. (1973). *Mechanical engineer's reference book*. Butterworths, London.

Paterson, M. S. and Wong, T.-f. (2005). *Experimental rock deformation: the brittle field*. Springer.

Place, D. and Mora, P. (2001). *Numerical Simulation of Localisation Phenomena in a Fault Zone*, pages 1821–1845. Birkhäuser Basel, Basel.

Power, W. L. and Tullis, T. E. (1991). Euclidean and fractal models for the description of rock surface roughness. *Journal of Geophysical Research: Solid Earth*, 96(B1):415–424.

Power, W. L., Tullis, T. E., and Weeks, J. D. (1988). Roughness and wear during brittle faulting. *Journal of Geophysical Research: Solid Earth*, 93(B12):15268–15278.

Rabinowicz, E. (1965). *Friction and wear of materials*. Wiley, New York.

Rasouli, V. and Harrison, J. (2010). Assessment of rock fracture surface roughness using riemannian statistics of linear profiles. *International Journal of Rock Mechanics and Mining Sciences*, 47(6):940–948.

Ravi-Chandar, K. and Knauss, W. G. (1984a). An experimental investigation into dynamic fracture: Ii. microstructural aspects. *International Journal of Fracture*, 26(1):65–80.

Ravi-Chandar, K. and Knauss, W. G. (1984b). An experimental investigation into dynamic fracture: Iii. on steady-state crack propagation and crack branching. *International Journal of Fracture*, 26(2):141–154.

Raynaud, S., Fabre, D., Mazerolle, F., Geraud, Y., and Latière, H. J. (1989). Analysis of the internal structure of rocks and characterization of mechanical deformation by a non-destructive method: X-ray tomodensitometry. *Tectonophysics*, 159(1):149–159.

Reches, Z. and Lockner, D. A. (2010). Fault weakening and earthquake instability by powder lubrication. *Nature*, 467(7314):452–455.

Renard, F., Bernard, D., Thibault, X., and Boller, E. (2004). Synchrotron 3D microtomography of halite aggregates during experimental pressure solution creep and evolution of the permeability. *Geophysical Research Letters*, 31(7):L07607.

Renard, F., Cordonnier, B., Dysthe, D. K., Boller, E., Tafforeau, P., and Rack, A. (2016). A deformation rig for synchrotron microtomography studies of geomaterials under conditions down to 10 km depth in the Earth. *Journal of Synchrotron Radiation*, 23(4):1030–1034.

Reyes-Montes, J. M., Rietbrock, A., Collins, D. S., and Young, R. P. (2005). Relative location of excavation induced microseismicity at the Underground Research Laboratory (AECL, Canada) using surveyed reference events. *Geophysical Research Letters*, 32(5):L05308.

Ritman, E. L. (2004). Micro-computed tomography-current status and developments. *Annu. Rev. Biomed. Eng.*, 6:185–208.

Ritter, F., Boskamp, T., Homeyer, A., Laue, H., Schwier, M., Link, F., and Peitgen, H.-O. (2011). Medical Image Analysis: A visual approach. *IEEE Pulse*, 2(6):60–70.

Rubinstein, S. M., Cohen, G., and Fineberg, J. (2004). Detachment fronts and the onset of dynamic friction. *Nature*, 430(7003):1005–1009.

Rutledge, J. T. and Phillips, W. S. (2003). Hydraulic stimulation of natural fractures as revealed by induced microearthquakes, Carthage Cotton Valley gas field, east Texas. *Geophysics*, 68(2):441–452.

Rydelek, P. A. and Sacks, I. S. (1989). Testing the completeness of earthquake catalogues and the hypothesis of self-similarity. *Nature*, 337(6204):251–253.

Sagy, A., Brodsky, E. E., and Axen, G. J. (2007). Evolution of fault-surface roughness with slip. *Geology*, 35(3):283–286.

Sammis, C. G. and Biegel, R. L. (1989). Fractals, fault-gouge, and friction. In *Fractals in geophysics*, pages 255–271. Springer.

Sanchez-Santana, U., Rubio-Gonzalez, C., Gomez-Rosas, G., Ocana, J. L., Molpeceres, C., Porro, J., and Morales, M. (2006). Wear and friction of 6061-T6 aluminum alloy treated by laser shock processing. *Wear*, 260(7):847–854.

Sayers, C. M. and Kachanov, M. (1995). Microcrack-induced elastic wave anisotropy of brittle rocks. *Journal of Geophysical Research: Solid Earth*, 100(B3):4149–4156.

Schmittbuhl, J., Gentier, S., and Roux, S. (1993). Field measurements of the roughness of fault surfaces. *Geophysical Research Letters*, 20(8):639–641.

Scholz, C. H. (1988). The critical slip distance for seismic faulting. *Nature*, 336(6201):761–763.

Scholz, C. H. (1990). *The Mechanics of Earthquakes and Faulting*. Cambridge University Press.

Scholz, C. H. (1998). Earthquakes and friction laws. *Nature*, 391(6662):37–42.

Schorlemmer, D., Wiemer, S., and Wyss, M. (2005). Variations in earthquake-size distribution across different stress regimes. *Nature*, 437(7058):539–542.

Sellers, E. J., Kataka, M. O., and Linzer, L. M. (2003). Source parameters of acoustic emission events and scaling with mining-induced seismicity. *Journal of Geophysical Research: Solid Earth*, 108(B9).

Selvadurai, P. and Glaser, S. (2017). Asperity generation and its relationship to seismicity on a planar fault: a laboratory simulation. *Geophysical Journal International*, 208(2):1009–1025.

Shervais, K. A. H. and Kirkpatrick, J. D. (2016). Smoothing and re-roughening processes: The geometric evolution of a single fault zone. *Journal of Structural Geology*, 91:130–143.

Stanchits, S., Vinciguerra, S., and Dresen, G. (2006). Ultrasonic velocities, acoustic emission characteristics and crack damage of basalt and granite. *Pure and Applied Geophysics*, 163(5-6):975–994.

Sudhakar, I., Madhu, V., Reddy, G. M., and Rao, K. S. (2015). Enhancement of wear and ballistic resistance of armour grade AA7075 aluminium alloy using friction stir processing. *Defence Technology*, 11(1):10–17.

Tatone, B. S. A. (2014). *Investigating the evolution of rock discontinuity asperity degradation and void space morphology under direct shear.* PhD thesis, University of Toronto.

Tatone, B. S. A. and Grasselli, G. (2009). A method to evaluate the three-dimensional roughness of fracture surfaces in brittle geomaterials. *Review of Scientific Instruments*, 80(12):125110.

Tatone, B. S. A. and Grasselli, G. (2015a). A calibration procedure for two-dimensional laboratory-scale hybrid finite-discrete element simulations. *International Journal of Rock Mechanics and Mining Sciences*, 75:56–72.

Tatone, B. S. A. and Grasselli, G. (2015b). Characterization of the effect of normal load on the discontinuity morphology in direct shear specimens using X-ray micro-CT. *Acta Geotechnica*, 10(1):31–54.

Tisato, N., Di Toro, G., De Rossi, N., Quaresimin, M., and Candela, T. (2012). Experimental investigation of flash weakening in limestone. *Journal of Structural Geology*, 38:183–199.

Tisato, N., Quintal, B., Chapman, S., Madonna, C., Subramaniyan, S., Frehner, M., Saenger, E. H., and Grasselli, G. (2014). Seismic attenuation in partially saturated rocks: Recent advances and future directions. *The Leading Edge*, 33(6):640–646.

Tisato, N., Torriani, S. F. F., Monteux, S., Sauro, F., De Waele, J., Tavagna, M. L., D'Angeli, I. M., Chailloux, D., Renda, M., Eglinton, T. I., and Bontognali, T. R. R. (2015). Microbial mediation of complex subterranean mineral structures. *Scientific reports*, 5(15525).

Tocher, D. (1957). Anisotropy in rocks under simple compression. *Eos, Transactions American Geophysical Union*, 38(1):89–94.

Togo, T. and Shimamoto, T. (2012). Energy partition for grain crushing in quartz gouge during subseismic to seismic fault motion: an experimental study. *Journal of Structural Geology*, 38:139–155.

Tullis, J. and Yund, R. A. (1977). Experimental Deformation of Dry Westerly Granite. *Journal of Geophysical Research*, 82(36):5705–5718.

Utsu, T. (1999). Representation and analysis of the earthquake size distribution: A historical review and some new approaches. *Pure and Applied Geophysics*, 155(2-4):509–535.

Vanorio, T., Nur, A., and Ebert, Y. (2011). Rock physics analysis and time-lapse rock imaging of geochemical effects due to the injection of CO_2 into reservoir rocks. *Geophysics*, 76(5):O23–O33.

Vervoort, A., Wevers, M., Swennen, R., Roels, S., Van Geet, M., and Sellers, E. (2004). Recent advances of X-ray CT and its applications for rock material. *X-ray CT for Geomaterials*, pages 79–91.

Viggiani, G., Lenoir, N., Bésuelle, P., Di Michiel, M., Marello, S., Desrues, J., and Kretzschmer, M. (2004). X-ray microtomography for studying localized deformation in fine-grained geomaterials under triaxial compression. *Comptes rendus Mécanique*, 332(10):819–826.

Wang, J.-H. (2004). The seismic efficiency of the 1999 chi-chi, taiwan, earthquake. *Geophysical Research Letters*, 31(10):L10613.

Wang, W. and Scholz, C. H. (1994). Wear processes during frictional sliding of rock: A theoretical and experimental study. *Journal of Geophysical Research: Solid Earth*, 99(B4):6789–6799.

Washabaugh, P. D. and Knauss, W. G. (1994). A reconciliation of dynamic crack velocity and Rayleigh wave speed in isotropic brittle solids. *International Journal of Fracture*, 65(2):97–114.

Weeks, J., Lockner, D. A., and Byerlee, J. (1978). Change in b-values during movement on cut surfaces in granite. *Bulletin of the Seismological Society of America*, 68(2):333–341.

Wiemer, S. and Wyss, M. (2000). Minimum magnitude of completeness in earthquake catalogs: Examples from alaska, the western united states, and japan. *Bull. Seism. Soc. Am.*, 90:859–869.

Wilson, B., Dewers, T., Reches, Z., and Brune, J. (2005). Particle size and energetics of gouge from earthquake rupture zones. *Nature*, 434(7034):749–752.

Woessner, J. and Wiemer, S. (2005). Assessing the quality of earthquake catalogues: Estimating the magnitude of completeness and its uncertainty. *Bulletin of the Seismological Society of America*, 95(2):684–698.

Wyss, M. (1973). Towards a physical understanding of the earthquake frequency distribution. *Geophysical Journal International*, 31(4):341–359.

Xia, K., Rosakis, A. J., and Kanamori, H. (2004). Laboratory earthquakes: The sub-Rayleigh-to-supershear rupture transition. *Science*, 303(5665):1859–1861.

Yoshioka, N. (1986). Fracture energy and the variation of gouge and surface roughness during frictional sliding of rocks. *Journal of Physics of the Earth*, 34(4):335–355.

Zhang, Q. B. and Zhao, J. (2014). A review of dynamic experimental techniques and mechanical behaviour of rock materials. *Rock Mechanics and Rock Engineering*, 47(4):1411–1478.

Zhao, B., Wang, J., Coop, M. R., Viggiani, G., and Jiang, M. (2015a). An investigation of single sand particle fracture using X-ray micro-tomography. *Géotechnique*, 65(8):625–641.

Zhao, D., Hasegawa, A., and Horiuchi, S. (1992). Tomographic imaging of P and S wave velocity structure beneath northeastern Japan. *Journal of Geophysical Research: Solid Earth*, 97(B13):19909–19928.

Zhao, Q., Lisjak, A., Mahabadi, O. K., Liu, Q., and Grasselli, G. (2014). Numerical simulation of hydraulic fracturing and associated microseismicity using finite-discrete element method. *Journal of Rock Mechanics and Geotechnical Engineering*, 6(6):574–581.

Zhao, Q., Tisato, N., and Grasselli, G. (2017). Rotary shear experiments under X-ray micro-computed tomography. *Review of Scientific Instrument*, 88:15110.

Zhao, Q., Tisato, N., Grasselli, G., Mahabadi, O. K., Lisjak, A., and Liu, Q. (2015b). Influence of in situ stress variations on acoustic emissions: a numerical study. *Geophysical Journal International*, 203(2):1246–1252.

Zoback, M. D., Kohli, A., Das, I., Mcclure, M. W., and Others (2012). The importance of slow slip on faults during hydraulic fracturing stimulation of shale gas reservoirs. In *SPE Americas Unconventional Resources Conference*. Society of Petroleum Engineers.

Appendix A

MATLAB package for FDEM seismic post-processing

A.1 Introduction

The following pieces of MATLAB code are a complete package for analysis of FDEM simulated seismic events. The simulated seismic events can be viewed in Paraview and exported as `.csv` file. The function `csvdatain2D.m` is used in the `FDEM_seismic_tool.m` code to read these `.csv` files, which then prepares a `.mat` file for seismic analysis, including frequency-magnitude relation (`FDEM_b_value.m`), spatial distribution and fractal dimension (`FDEM_D_value.m`), and clustering (`FDEM_clustering.m`). The code package presented here was tested with Irazu 3.1.0., Paraview 5.4.0, and MATLAB R2014b.

A.2 Data preparation

```matlab
1  function data = csvdatain2D(filename)
2  fid = fopen(filename);
3  dataread=textscan(fid,...
4                    '%f%f%f%f%f%f%f%f%f%f%f%f%f%f%d%f%d%f%f%d%f%f%f',...
5                    'Delimiter',',','HeaderLines',1);
6  fclose(fid);
7  for ii=1:22
```

```matlab
8        data(:,ii)=dataread{1,ii}(:,1);
9    end
10   % get rid of DFN (Ek=-1) events at the first frame
11   data(data(:,13)≤0,:)=[];
12   % get rid of zero displacement event
13   % data(data(:,1)==data(:,10) & data(:,4)==data(:,7),:)=[];
14   %% sorting
15   % Parameters can be used to track events:
16   %                Prperties                                column #
17   % (i)   event time step, Te                                 (14)
18   % (ii)  failure time step, Tf                               (16)
19   % (iii) event energy, Ee                                    (13)
20   % (iv)  failure mode                                        (15)
21   % (v)   Kinetic energy at failure, Ekf                      (17)
22   % (vi)  Yeilding time, Ty                                   (19)
23   % (vii) Kinetic energy at yielding, Eky                     (18)
24   % sort the matrix 6 times, using (vi)-(i), respectively
25   % after sorting the row number will be event number
26   data = sortrows(data,18);
27   data = sortrows(data,19);
28   data = sortrows(data,17);
29   data = sortrows(data,15);
30   data = sortrows(data,13);
31   data = sortrows(data,16);
32   % sorting according to failure time is default
33   end
```

```matlab
1    function FDEM_seismic_tool
2    % MATLAB code used to prepare a source.mat file containing
3    % seismic event information (for 2D simulation).
4    % This file can be processed by other codes for:
```

```matlab
5    % clustering , b- and D-values , moment tensor , T-k diadram , etc.
6    %
7    % Input file: *.csv files from paraview output data
8    %
9    % In paraview: save data as .csv file following this steps:
10   % open seismic_event.vtu --> save data --> save point data
11   %
12   % by Q.Zhao @ Grasselli's Geomechanics Group , U of T, 2017

13
14   clear all; close all;clc;
15   set(0,'Defaulttextfontsize',12);
16   set(0,'DefaultAxesfontsize',12);
17   set(0,'DefaultAxesLineWidth',1);
18   set(0,'Defaultlinelinewidth',0.75);
19   set(0,'DefaultlineMarkerSize',5);
20   % Change default axes fonts.
21   set(0,'DefaultAxesFontName', 'Times New Roman');
22   % Change default text fonts.
23   set(0,'DefaultTextFontname', 'Times New Roman');

24
25   %% choose folder
26   dirname = uigetdir('./','Select folder');
27   % find csv files
28   listing = ls([dirname '/*.csv']);
29   if isempty(listing)
30       error('Please export csv files in Paraview.');
31   end

32
33   % get last frame and start from here
34   [fnameLast , ¬]=uigetfile([dirname '/*.csv'],...
35                   'Select last time point file');
36   flast = [dirname '/' fnameLast];
```

```matlab
37
38  rng = 13:19; clumn = 22;
39  data0 = csvdatain2D(flast);
40  % estimate frame number for events
41  nframeID = (data0(:,14)/nPerFrame);
42
43  if isempty(data0)
44      warning('No seismic event up to the selected time point.')
45      return
46  end
47  nEvent  = numel(data0(:,1));
48  nfstart = ceil(min(nframeID));
49  nfend   = ceil(max(nframeID));
50  frames  = nfstart:nfend; % file numbers need to be processed
51  nf      = numel(frames);
52  disp('Processing files...');
53  %% Sort files in numeric order
54  % numerical order: 1, 2,..., 10, 11, ...,
55  %       instead of: 1, 10, 11, 2, 20, ...
56  fstruct = dir([dirname '/*.csv']);
57  filenames = {fstruct.name};
58  % nft = numel(filenames); % total file number
59  maxlen = max(cellfun(@length, filenames));
60  padname = @(s) sprintf(['%0' num2str(maxlen) 's'], s);
61  namesPadded = cellfun(padname, filenames, 'UniformOutput', false);
62  [¬, sortOrder] = sort(namesPadded);
63  fstruct = fstruct(sortOrder);
64  filenames = {fstruct.name}';
65  %% Tracking events
66  for i = 1:nf-1
67      % current file
68      fileCur = strcat(dirname, '/', filenames(frames(i)+1));
```

```matlab
69        % current data
70        dataCur = csvdatain2D(fileCur{1});
71        masterData{i} = dataCur;
72    end
73    masterData{nf} = data0;
74    events = zeros(nEvent,clumn);
75    brkFrameID = nf:-1:1;
76    for i =1:nEvent % get source parameters for each event
77        cmpTmp0 = data0(i,rng);
78        for k = 1:nf
79            % see if in this frame
80            nInframe = numel(masterData{brkFrameID(k)}(:,1));
81            for jk = 1:nInframe
82                cmpTmp1 = masterData{brkFrameID(k)}(jk,rng);
83                if all(cmpTmp0 == cmpTmp1)
84                    events(i,:) = masterData{brkFrameID(k)}(jk,:);
85                else
86                    continue
87                end
88            end
89        end
90    end
91    dataSources.input{1,:}  = paraIn;
92    dataSources.input{2,:}  = para;
93    dataSources.frame0      = nfstart;
94    dataSources.events      = events;
95    save(strcat(dirname, '/source.mat'),'dataSources');
96    disp('All done!')
97    end
```

A.3   Clustering

```matlab
1   function FDEM_clustering
2   % MATLAB code used to cluster seismic events taking into
3   % consideration fracture propagation.
4   %
5   % Input file: source.mat from irazu_seismic_tool.m
6   % Output file: source_clst.mat file containing:
7   %               (1) clst_pool --> row clustered data
8   %               (2) clst_events --> clustered events
9   %               ==> clst_events format:
10  %                   Column   1    2    3   4   5   6
11  %                   Value   time, mode, x,  y,  z,  Ek
12  %
13  % by Q.Zhao @ Grasselli's Geomechanics Group, U of T, 2017
14
15  clear all;close all;clc
16  frac_color='grbkc';
17  % frac_color='kkkkk';
18  set(0,'Defaulttextfontsize',12);
19  set(0,'Defaultaxesfontsize',12)
20  set(0,'DefaultAxesLineWidth',1)
21  set(0,'Defaultlinelinewidth',1);
22  set(0,'DefaultlineMarkerSize',5);
23  % Change default axes fonts.
24  set(0,'DefaultAxesFontName', 'Times New Roman')
25  set(0,'DefaultAxesFontSize', 12)
26  % Change default text fonts.
27  set(0,'DefaultTextFontname', 'Times New Roman')
28  set(0,'DefaultTextFontSize', 12)
29  %% choose file
30  try
31      [fname,pname] = uigetfile('*.mat','Enter data file');
32      filename=[pname fname];
```

```matlab
33        load(filename)

34        data0= dataSources.events;

35        data = data0;

36        N = size(data,1);

37   catch me

38        disp('No data file selected.');

39        return

40   end

41   %% input parameters

42   para        = {'Youngs modulus [Pa]',...

43        'Poissons ratio',...

44        'Density',...

45        'Time step size'};

46   defaulpara = {'15600000000','0.22','1704','0.0000004'};

47   num_line    = [1 50; 1 50; 1 50; 1 50];

48   paraIn      = inputdlg(para,'Input parameters',num_line,defaulpara);

49   E           = str2num(paraIn{1});

50   nu          = str2num(paraIn{2});

51   roh         = str2num(paraIn{3});

52   t_step      = str2num(paraIn{4});

53   %%

54   G     = 0.5*E/(1+nu); % shear modulus

55   vs    = sqrt(G/roh); % S wave velocity m/s

56   % Rayleigh wave velocity m/s [L. B. Freund (1998)]

57   vR    = ((0.862+1.14*nu)/(1+nu))*vs;

58   % Consider fractue propagate at half terminal rupture velocity

59   vf_I  = 0.50*vR;

60   vf_II = 0.50*vs;

61

62   disp('Processing...')

63   ntotal = 0;   % # total clustered events

64   displ  = 1; % plot while processing, set to 0 to turn off
```

```matlab
65  %% clustering
66
67  if displ == 1
68      figure(1)
69      hold on;axis equal;box on;
70  end
71
72  while size(data,1) > 0
73      ntotal = ntotal + 1;
74      esc = 0;
75      %% get first event of current cluster
76      clst_pool{ntotal} = data(1,:);
77      data(1,:) = [];
78      %% data for data pool
79      % coordinates of each cohesive crack element (CCE)
80      % centre
81      x=data(:,20);
82      y=data(:,21);
83      % one end
84      x1=(data(:,1)+data(:,10))/2;
85      y1=(data(:,2)+data(:,11))/2;
86      % the other end
87      x2=(data(:,4)+data(:,7))/2;
88      y2=(data(:,5)+data(:,8))/2;
89      t = data(:,16)*t_step; % failure time for each CCE
90      %% searching for current cluster
91      while esc == 0
92          esc_counter = 0;
93          for i = 1:size(clst_pool{ntotal},1)
94              %% data for event pool
95              % centre
96              x_ev = clst_pool{ntotal}(i,20);
```

```matlab
 97                    y_ev = clst_pool{ntotal}(i,21);
 98                    % one end
 99                    x1_ev = (clst_pool{ntotal}(i,1)+...
100                                clst_pool{ntotal}(i,10))/2;
101                    y1_ev = (clst_pool{ntotal}(i,2)+...
102                                clst_pool{ntotal}(i,11))/2;
103                    % the other end
104                    x2_ev = (clst_pool{ntotal}(i,4)+...
105                                clst_pool{ntotal}(i,7))/2;
106                    y2_ev = (clst_pool{ntotal}(i,5)+...
107                                clst_pool{ntotal}(i,8))/2;
108                % failure time for each CCE
109                t_ev = clst_pool{ntotal}(i,16)*t_step;
110                % failure mode for each CCE
111                md   = clst_pool{ntotal}(i,15);
112                %% find first clustering layer from connecting CCEs
113                 % searching radius
114                r   = (sqrt((x1_ev-x2_ev)^2+(y1_ev-y2_ev)^2))/2;
115                if md ≥ 1.5
116                    vf = vf_II;
117                else
118                    vf = vf_I;
119                end
120                dt = r/vf; % time delay
121                % 4 ways of connection between 2 CCEs
122                cl_1 = find(sqrt((x1-x1_ev).^2 + (y1-y1_ev).^2) ≤ r...
123                                            & t - t_ev ≤ dt);
124                cl_2 = find(sqrt((x2-x2_ev).^2 + (y2-y2_ev).^2) ≤ r...
125                                            & t - t_ev ≤ dt);
126                cl_3 = find(sqrt((x1-x2_ev).^2 + (y1-y2_ev).^2) ≤ r...
127                                            & t - t_ev ≤ dt);
128                cl_4 = find(sqrt((x2-x1_ev).^2 + (y2-y1_ev).^2) ≤ r...
```

```matlab
129                                                    & t - t_ev <= dt);
130             cl_ID    = [cl_1; cl_2; cl_3; cl_4];
131             cl_ID    = unique(cl_ID);
132             if ~isempty(cl_ID)
133                 % put connecting CCEs within dt into event pool
134                 clst_pool{ntotal} = ...
135                     [clst_pool{ntotal}; data(cl_ID,:)];
136                 %% refresh data for data pool
137                 data(cl_ID,:) = [];
138                 x(cl_ID) = []; x1(cl_ID) = []; x2(cl_ID) = [];
139                 y(cl_ID) = []; y1(cl_ID) = []; y2(cl_ID) = [];
140                 t(cl_ID) = [];  % failure time for each CCE
141             else
142                 esc_counter = esc_counter + 1;
143             end
144
145             if esc_counter == size(clst_pool{ntotal},1)
146                 esc = 1;
147             end
148         end
149     end
150
151     if displ == 1
152         plot(clst_pool{ntotal}(:,20),clst_pool{ntotal}(:,21),...
153             'o','color',frac_color(mod(ntotal,5)+1))
154         drawnow
155     end
156 end
157
158 for i = 1: size(clst_pool,2)
159     % calculate clustered event properties
160     %    Column    1    2    3    4    5
```

```matlab
161        %     Value    time,  mode,  x,   y,    Ek
162        t_ev     = clst_pool{i}(1,16)*t_step;
163        Ek_ev    = sum(clst_pool{i}(:,17));
164        wt       = clst_pool{i}(:,17)/sum(clst_pool{i}(:,17));
165        mode_ev = sum(clst_pool{i}(:,15).*wt);
166        x_ev     = clst_pool{i}(1,20);
167        z_ev     = zeros(numel(y_ev),1);
168        clst_events(i,:) = [t_ev,mode_ev,x_ev,y_ev,z_ev,Ek_ev];
169    end
170
171    % saving
172    disp('*************** Results ******************');
173    disp([num2str(N) ' broken joints before clustering']);
174    disp([num2str(ntotal) ' event(s) after clustering']);
175    disp('*******************************************');
176    save([pname 'source_clst.mat'],'clst_pool','clst_events')
177    disp('All done!')
178
179    end
```

A.4 b-value

```matlab
1    function b = FDEM_b_value
2    % MATLAB code for b-value
3    % keywords: b-value, G-R, bin, maximum likelyhood, bootstrap
4    % Input file: source.mat from irazu_seismic_tool.m
5    %
6    % by Q.Zhao @ Grasselli's Geomechanics Group, U of T, 2017
7
8    clear all; close all;
9    set(0,'Defaulttextfontsize',12);
```

```matlab
10  set(0,'DefaultAxesfontsize',12);
11  set(0,'DefaultAxesLineWidth',1);
12  set(0,'Defaultlinelinewidth',1.2);
13  set(0,'DefaultlineMarkerSize',8);
14  % Change default axes fonts.
15  set(0,'DefaultAxesFontName', 'Times New Roman')
16  % Change default text fonts.
17  set(0,'DefaultTextFontname', 'Times New Roman')
18  %% choose file
19  try
20      [fname,pname] = uigetfile('*.*','Enter data file');
21      filename=[pname fname];
22      load(filename)
23      data = dataSources.events;
24  catch me
25      disp('No data file selected.');
26      return
27  end
28  %% settings
29  prompt2 = 'Units used (1-[m,s,kg]; 2-[mm,ms,micro-g]): ';
30  unittype = input(prompt2); % 1-[m,s,kg]; 2-[mm,ms,micro-g]
31  prompt3 = 'Triggering magnitude: ';
32  trig_mag = input(prompt3); % 1-[m,s,kg]; 2-[mm,ms,micro-g]
33  n_truncate=0; dM=0.1; % no truncation, bin size=0.1
34  %%
35  data=sortrows(data,13); % sort rows according to Ek
36  data(data(:,13)<=0,:)=[];
37  if unittype == 2
38      Ek=data(:,13)./10^9; % (nanoJ) to (J)
39  elseif unittype == 1
40      Ek=data(:,13); % (J)
41  end
```

```matlab
42  mag0=real(2*(log10(Ek)-4.8)/3);      % magnitude
43  mag0=mag0';
44  while max(mag0)<trig_mag
45      warning(['Triggering magnitude too large! M(max)='...
46          num2str(max(mag0))])
47      prompt4 = 'Re-enter triggering magnitude: ';
48      trig_mag = input(prompt4); % 1-[m,s,kg]; 2-[mm,ms,micro-g]
49  end
50  mag0=sort(mag0);
51  mag0(mag0<trig_mag)=[]; % events larger than trig_mag
52  mag=mag0;
53  NN=length(mag);
54  disp([num2str(NN) ' events, estimating b-value...']);
55
56  %% calculate b-value
57  bin=(floor(min(mag)/dM))*dM:dM:(ceil(max(mag)/dM))*dM;
58  bincount=zeros(length(bin),1);
59  % divide data into bins
60  for j=1:NN
61      for k=1:length(bin)
62          if mag(j)>=bin(k)-dM/2 && mag(j)<bin(k)+dM/2
63              bincount(k)=bincount(k)+1;
64
65          end
66          bincum(k)=NN-sum(bincount(1:k-1));
67      end
68  end
69
70  Mc_bin_n=find(bincount==max(bincount));
71  % if several bins have same count, use largest magnitude one
72  Mc_bin_n=Mc_bin_n(1);
73  Mc=bin(Mc_bin_n);
```

```matlab
74  Mc_bincum=sum(bincount(1:Mc_bin_n));
75
76  %% choose Mc here if needed
77  figure(1); hold on;
78  plot(bin-0.5*dM,log10(bincount),'ko'); % plot non-cumulative count
79  plot(bin-0.5*dM,log10(bincum),'ks','MarkerFaceColor',[.6,.6,.6]);
80  xlabel('Magnitude');
81  ylabel('log(Number of events)');
82  box on;
83  set(gca,'XMinorTick', 'on');
84  plot(Mc-0.5*dM,log10(bincount(Mc_bin_n)),'ro');
85
86  Mc_set = 'Y';
87  prompt_Mc =...
88      'Use default magnitude of completeness (red circle)? (Y/N): ';
89  Mc_set = input(prompt_Mc, 's');
90
91  if Mc_set == 'N' | Mc_set == 'n'
92      disp('Please select the Mc location on the graph...')
93      [Mc_x,Mc_y]=ginput(1);
94      [Mc_bin_numm,Mc_bin_n]=min(abs(bin-Mc_x));
95      Mc=bin(Mc_bin_n);
96      Mc_bincum=sum(bincount(1:Mc_bin_n));
97  end
98  plot(Mc-0.5*dM,log10(bincount(Mc_bin_n)),'go');
99
100 % find Mmax_num here
101 % Mmax_bin_num=round((-7.5-bin(1))/binsize);
102 Mmax_bin_num=(length(bin)-n_truncate);
103 Mmax=bin(Mmax_bin_num);
104 Mmax_bincum=sum(bincount(1:Mmax_bin_num));
105
```

```matlab
106  meanmag=mean(mag(Mc_bincum+1:Mmax_bincum));
107  b=log10(exp(1))/(meanmag-Mc+dM/2);% MLM
108  n_es=log10(bincum(Mc_bin_n))-b*(bin-Mc);% MLM estimated N
109  n_real=log10(bincum(Mc_bin_n:Mmax_bin_num));%
110  mag_real=bin(Mc_bin_n:Mmax_bin_num);
111  resid=log10(bincum(Mc_bin_n:Mmax_bin_num))-...
112      n_es(Mc_bin_n:Mmax_bin_num);
113  ss_res=sum(resid.^2);
114  ss_tot=sum((n_real-mean(log10(bincum(Mc_bin_n:Mmax_bin_num)))).^2);
115  %      rsqr_MLM(i)=1-ss_res/ss_tot;
116  %% bootstrap for MLM standard error
117  nReps=1000; % re-sampling number
118  samp_length=Mmax_bin_num-Mc_bin_n+1;
119  for nbt=1:nReps
120      for iii=1:samp_length
121          samp_id(iii)=floor((samp_length-1).*rand(1)+1);
122      end
123      samp_data=mag_real(samp_id);
124      samp_meanmag=mean(samp_data);
125      samp_b(nbt)=log10(exp(1))/(samp_meanmag-Mc+dM/2);
126  end
127  se=std(samp_b);
128
129  %% plotting final figure
130  close all
131  figure(2); hold on;
132  plot(bin-0.5*dM,log10(bincount),'ko'); % plot non-cumulative count
133  plot(bin-0.5*dM,log10(bincum),'ks','MarkerFaceColor',[.6,.6,.6]);
134  xlabel('Magnitude');
135  ylabel('log(Number of events)');
136  box on;
137  set(gca,'XMinorTick', 'on');
```

```matlab
138  % the b_MLM line
139  plot(bin(ceil(0.7*Mc_bin_n):end)-0.5*dM,...
140      n_es(ceil(0.7*Mc_bin_n):end),'b');
141  text(bin(1),1.1*log10(NN),...
142  ['{\itb} = ' num2str(b,'%6.2f') '\pm' num2str(se,'%6.2f')],...
143  'color','b');
144  plot([bin(Mc_bin_n)-0.5*dM,bin(Mc_bin_n)-0.5*dM],...
145      [0,log10(NN)+0.5],'r--');
146  disp(['M_c = ' num2str(Mc,'%6.2f')]);
147  disp(['b-value = ' num2str(b,'%6.2f') ', +- ' num2str(se,'%6.2f')]);
148  print('-dpdf',figure(2),[filename '_b-value.pdf']);
```

A.5 D-value

```matlab
1   function D = FDEM_D_value
2   % MATLAB code for D-value
3   % Input file: source.mat from irazu_seismic_tool.m
4   %
5   % by Q.Zhao @ Grasselli's Geomechanics Group, U of T, 2017
6
7   clear all; close all;
8   set(0,'Defaulttextfontsize',15);
9   set(0,'DefaultAxesfontsize',15);
10  set(0,'DefaultAxesLineWidth',1.5);
11  set(0,'Defaultlinelinewidth',0.5);
12  set(0,'DefaultlineMarkerSize',5);
13  set(0,'DefaultAxesFontName', 'Times New Roman')
14  set(0,'DefaultTextFontname', 'Times New Roman')
15
16  clr={[.15,.15,.15],[1,0.8,0.2],[1,0,.2],...
17      [0,1,.4],[.6,.2,0.2],[0,.4,1]};
```

```matlab
18   mkr={'s','^','+','>','d','o'};
19   %% choose file
20   try
21        [fname,pname] = uigetfile('*.*','Enter sample file');
22        filename=[pname fname];
23        load(filename) % TODO!!!!!!!!!!!!!!!!!!!
24        data = dataSources.events;
25   catch me
26        disp('No data file.');
27        return
28   end
29   %% settings
30   % prompt1 = 'Time step size: ';
31   % timestepsize = input(prompt1);
32   prompt2 = 'Units used (1-[m,s,kg]; 2-[mm,ms,micro-g]): ';
33   unittype = input(prompt2); % 1-[m,s,kg]; 2-[mm,ms,micro-g]
34   prompt3 = 'Triggering magnitude: ';
35   trig_mag = input(prompt3);
36   prompt4 = 'Minimum element size: ';
37   min_elem_size = input(prompt4);
38   %%
39   data=sortrows(data,13); % sort rows according to Ek
40   data(data(:,13)<=0,:)=[]; % get rid of Ek=-1 events
41   x=data(:,20); y=data(:,21);
42   xmax=max(abs(x));ymax=max(abs(y));
43   lmax=2*sqrt(xmax^2+ymax^2);
44   % mode=data(:,3); t=data(:,9);
45   if unittype == 2
46        Ek=data(:,13)./10^9; % (nanoJ) to (J)
47   elseif unittype == 1
48        Ek=data(:,13); % (J)
49   end
```

```matlab
50  mag=2*(log10(Ek)-4.8)/3;    %  magnitude
51
52  NN=length(data);
53  count=0;
54  temp=[];
55  for j=1:length(data)
56      if mag(j)>trig_mag
57          count=count+1;
58          temp(end+1,:)=[x(j),y(j)];
59      end
60  end
61
62  N=length(temp);
63  disp([num2str(N) ' events > ' num2str(trig_mag)...
64      ', estimating D-value...'])
65
66  %% prepare for plotting (not used in fitting)
67  dp=min_elem_size:min_elem_size:lmax;
68  D_countp=zeros(length(dp),1);
69  for n=1:N-1
70      for nn=n+1:N
71          dist=sqrt((temp(n,1)-temp(nn,1))^2+...
72              (temp(n,2)-temp(nn,2))^2);
73          for dd=1:length(dp)
74              if dist<dp(dd)
75                  D_countp(dd)=D_countp(dd)+1;
76              end
77          end
78      end
79  end
80  cp=2*D_countp/(count*(count-1));
81  cp=cp';
```

```matlab
82  esc=0;
83  while esc == 0
84
85  figure(1);
86  hdd=loglog(dp,cp,'bo');
87  set(hdd,'Color',clr{1},'Marker',mkr{1});
88
89  range_set = 'Y';
90  prompt_range = 'Use the sample size as the range? (Y/N): ';
91  range_set = input(prompt_range, 's');
92  if range_set == 'N' | range_set == 'n'
93      disp('Please select the upper limit on the graph...')
94      [pos_x,pos_y]=ginput(1);
95  else
96      pos_x = lmax;
97  end
98
99  d=min_elem_size:min_elem_size:pos_x;
100 D_count=zeros(length(d),1);
101
102 for n=1:N-1
103     for nn=n+1:N
104         dist=sqrt((temp(n,1)-temp(nn,1))^2+...
105             (temp(n,2)-temp(nn,2))^2);
106
107         for dd=1:length(d)
108             if dist<d(dd)
109                 D_count(dd)=D_count(dd)+1;
110             end
111         end
112     end
113 end
```

```matlab
114  c=2*D_count/(count*(count-1));
115  c=c';
116
117  %% fitting
118  [fitresult, gof]=loglogFit(d,c);
119  rsqr=gof.rsquare;
120  se=sqrt(gof.sse/(NN-2));
121  D=fitresult.d;
122
123  %% plot final figure
124  close all
125  figure(2);
126  hdd=loglog(dp,cp,'bo');
127  set(hdd,'Color',clr{1},'Marker',mkr{1});
128  hold on;
129  loglog(d,10.^(fitresult.a+D*log10(d)),'Color',clr{1});
130  text(d(1),10.^(fitresult.a+D*log10(d(1))),['{\itD} = '...
131      num2str(D,'%6.3f') ', {R^2} = ' num2str(rsqr,'%6.3f')],...
132      'color',clr{1});
133  ylabel('Correlation Integral, \it{C}');
134  if unittype == 2
135      xlabel('Source distance (mm)');
136  else
137      xlabel('Source distance (m)');
138  end
139  set(gcf,'PaperUnit','inches','PaperPosition',[0 0 8 6]);
140  set(gcf,'PaperSize',[8 6]);
141  % if happy with the result?
142  hpy = 'Y';
143  prompt_hpy = 'Happy with the result? (Y/N): ';
144  hpy = input(prompt_hpy, 's');
145  if hpy == 'Y' | hpy == 'y'
```

```matlab
146      esc=1;
147      print('-dpdf','-r1200',figure(2),[filename '_D-value.pdf']);
148  end
149  end
150
151  end
152
153  function [fitresult, gof] = loglogFit(d, c)
154  [xData, yData] = prepareCurveData( d, c );
155  ft = fittype( '10^(a+d*(log10(x)))',...
156      'independent', 'x', 'dependent', 'y' );
157  opts = fitoptions( ft );
158  opts.Display = 'Off';
159  opts.Lower = [-Inf -Inf];
160  opts.Upper = [Inf Inf];
161  opts.StartPoint = [d(1) c(1)];
162  [fitresult, gof] = fit( xData, yData, ft, opts);
163  end
```

Appendix B

Additional notes on the calibration of the load and torque cell of the ERDμ-T

B.1   Strain gauges

Three mechanical parameters are measured using strain gauges that are glued to the load and torque cell (LTC): normal force, torque, and shortening, as detailed in Chapter 5. These strain gauges were configured using the Wheatstone (full) bridge, whose output voltage (i.e., analogue signal transmitted to signal conditioners) can be calculated using:

$$V_{out} = \left[\frac{R_3}{R_1 + R_3} - \frac{R_4}{R_2 + R_4} \right] V_{in}, \tag{B.1}$$

where V_{in} is the supplied voltage.

The shortening sensor, however, has not been calibrated. Re-calling the design, the two arc-shaped beryllium copper cantilevers, where strain gauges for shortening measurement are attached to, connect the stainless steel bottom of the vessel and the LTC. Therefore, it measures the shortening of the LTC, not the sample. Thus, it is difficult to calibrate the shortening sensor, because the correlation between the voltage reading and the actual shortening will vary as a function of the stiffness contrast between the sample and the LTC.
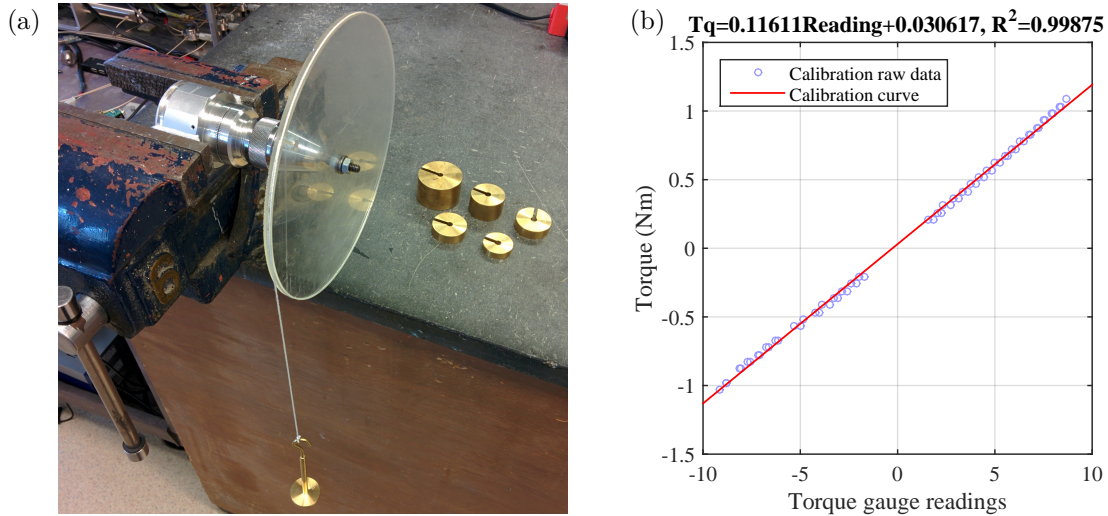
Figure B.1: Calibration of the torque gauge. (a) A polymethyl methacrylate (PMMA) wheel, standard weights, and a rope were assembled to calibrate the torque gauge. (b) Calibration raw data of readings on the torque gauge and applied torque, and the calibration curve using a first order polynomial fitting.

B.2   Torque gauge calibration

In order to achieve a good torque calibration result, the torque gauge itself was firstly calibrated, using a polymethyl methacrylate (PMMA) wheel with a groove on the edge, standard weights, and a string. The centre of the wheel was fixed to the torque gauge, and different torque was applied by hanging different weights to string that warped around the wheel (Figure B.1). The torque gauge was held in a vice and kept horizontal to ensure the accuracy of the calculation of the applied torque, and torque in both clockwise and counterclockwise directions were calibrated. Such a practice correlated the readings of the torque gauge to actual torque (Tq), and we used this result to calibrate the torque sensor in ERDµ-T.

B.3   Correlation between measurements

B.3.1   Correlation between torque and normal load

During the calibration, it is demonstrated that normal force (Fn) and torque are cross-correlated resulting in an error of 5% at full scale. During the post-processing, it is recommended to compensate also for such effect, especially at high torque.
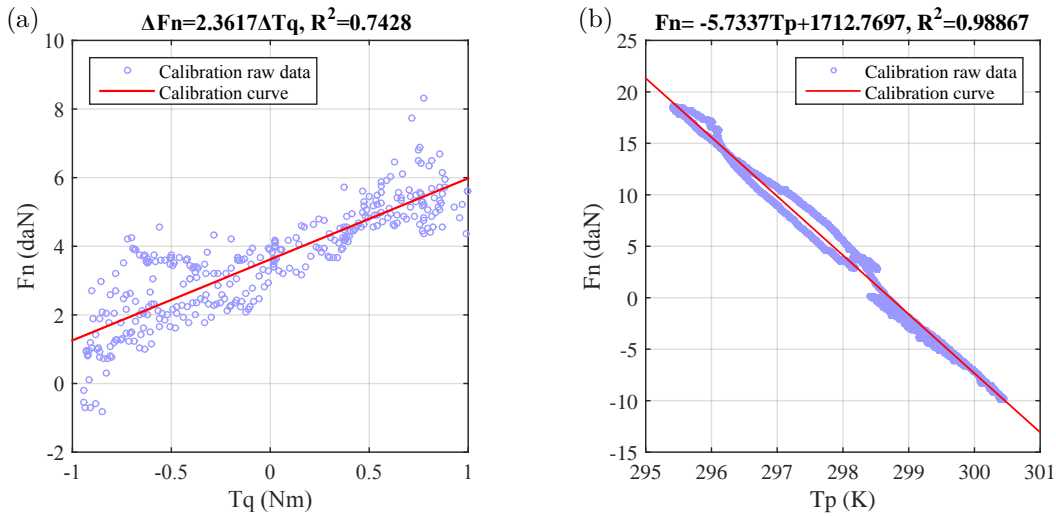
Figure B.2: Cross-calibration of torque and normal load and the influence of temperature on normal force. (a) Raw data of applied torque and the resulted normal force, and the calibration curve using a first order polynomial fitting. (b) Raw data of temperature and the resulted normal force variation.

B.3.2 Correlation between temperature and normal load

Temperature influences the normal force measurement due to the significant difference in temperature sensitivity of the fixed resistors and strain gauges. Temperature related variation of normal force reading was dealt with in Chapters 5 and 6 by the initiation process. However, this procedure disturbs the stress condition on the frictional surface. Therefore, a calibration of the dependence of normal load measurement on temperature was carried out, and the obtained relation can be used to correct the normal force reading to compensate for temperature variation. Note that in the calibration curve, for 3.18 K of temperature variation, error of normal force measurement at full scale is 1.89%; whereas during the test, temperature variation in the CT machine cabinet is usually 0.5 K.

B.4 Error assessment

e_l for each loading cycle is calculated using:

$$e_l = \frac{max|\eta_d - \eta'_{cal}|}{F.S.} \times 100\%, \tag{B.2}$$

where $F.S.$ is the voltage output range at full scale, η'_{cal} is the voltage calculated by $(\kappa_{cal} - b')/a'$, and a' and b' were obtained using a first order polynomial fitting of the voltage reading from ERDμ-T (i.e., η_d) in this cycle.

Table B.1: Normal force calibration errors at full scale.

Loading cycle	1st cycle	2nd cycle	Unit
Nonlinearity error	3.80	1.87	%F.S.
Repeatability error	2.75	1.55	%F.S.
Hysteresis error	4.27	2.13	%F.S.
Total error		5.43	%F.S.

Table B.2: Torque calibration errors at full scale.

Loading direction	1st cycle	2nd cycle	Unit
Nonlinearity error	3.21	1.59	%F.S.
Repeatability error	2.38	1.97	%F.S.
Hysteresis error	3.16	1.74	%F.S.
Total error		4.28	%F.S.

e_h is calculated using:

$$e_h = \frac{max|\eta_{cal}^{upscale} - \eta_{cal}^{downscale}|}{F.S.} \times 100\%, \tag{B.3}$$

where superscription denotes the direction of loading.

e_r is calculated using calibration data of two cycles:

$$e_r = \frac{max|\eta_{cal}^{1} - \eta_{cal}^{2}|}{F.S.} \times 100\%, \tag{B.4}$$

where superscription denotes the number of the loading cycle.

e_t is calculated based on two cycles of calibration data:

$$e_t = \frac{max|\eta_d - \eta_{cal}|}{F.S.} \times 100\%. \tag{B.5}$$

Table B.1 and B.2 provides the detailed calibration results for each loading cycle, which produced the total error reported in Chapter 5.

Appendix C

ERDµ GUI and schematic diagram of the fluid circuit system

C.1 ERDµ-T GUI

This GUI is used to control and monitor the ERDµ system. A README text can be accessed by clicking the help button on the GUI, also included as follows.

Figure C.1: ERDµ-T GUI

>>>>>>>>>>>>>>>>>>>>>>>>>> README for GUI_ERDu_control <<<<<<<<<<<<<<<<<<<<<<<<<<

GUI description:

This GUI is used to control motors:

(1) confining pressure, Pc,

(2) fluid pressure IN, Pi,

(3) fluid pressure OUT, Po,

(4) Normal force, Fn, and

(5) Rotary motor, Tq.

========================= Haydon motors (1-4) ===========================

* pop-up menu (top-right):

  used to set calibration parameters (a to t)

  click [write] to write value to Olimex temporarily

  Readings will be updated once written

  click [save] to save to the memory

* sliders:

  minor step (arrow) --> move 1000 steps

  major step (click slider) --> move 2000 steps

  push button (<</>>) --> move to lower/upper limits

  Note: moving to the left is retracting

* pop-up menu (beside each slide bar):

  Velocity of the motot in step/s

* [Position to go] can be set by:

  (1) edit text box, and (2) move slider

  click [start] to move to [Position to go]

  click [stop] to stop motor whenever you want

========================= Oriental motors (5) ===========================

* position of Oriental motor is in degrees

* velocity can be modified on-the-fly by

```
  (1) edit text box, and (2) push plus/minus button

  positive velocity --> clockwise (top view)

  negative velocity --> counter-clockwise (top view)


* Oriental motor command speed range calculation:

  80-4000 rpm-->with 200 ratio-->0.4-20 rpm at sample-->2.4-120 degree/s

  Speed step: 0.03 degree/s

  !!! input velocity will be rounded to closest (0.03 times an integer) !!!


* acceleration is the time it takes to accelerate to assigned velocity

  in seconds, range [2-150]*0.1 s


* decceleration is set to ~0 (i.e., instantaneous stop)


==================== Analog Acquisition Setting =========================
%% analog acquisition for ERDu-T test
%//////////////////////////////////////////////////////////
%~channel   description                               ~
%~========================================================~
%~ 0        Load Cell                           Fn ~
%~ 1        Strain sensor                       S1 ~
%~ 2        Torque sensor                       N1 ~
%~ 3        Fluid pressure in (motor 2)         Pi ~
%~ 4        Fluid pressure out (motor 3)        Po ~
%~ 5        Confining pressure                  Pc ~
%~ 6        Conductivimeter in (P0.0 to select) Ci ~
%~ 7        Rotation (only shear machine)       R1 ~
%~ 11       Temperature                         Tp ~
%//////////////////////////////////////////////////////////
%% Offset settings (SW2)
%BIT    1   2   3   4   5   6   7   8
%CH0    on  off off on  on  off off off (Box 1) Fn
%CH1    on  off on  on  on  on  off on  (Box 2) S1
```

```
%CH2    off on  off off on  on off off (Box 3) Tq
```

```
%% Gain settings (SW1)
%BIT    1  2  3  4  5  6  7  8
%CH0    off off off on off off on  off (Box 1) Fn
%CH1    off off off on off off on  off (Box 2) S1
%CH2    off off off off off off on off (Box 3) Tq
```

C.2   Confining and pore fluid circuit system

The fluid circuit diagram is created according to the actual layout of the apparatus (Figure 5.3a). The confining and pore fluid circuit system can be connected to either the ERDμ-T or ERDμ-Q vessels.
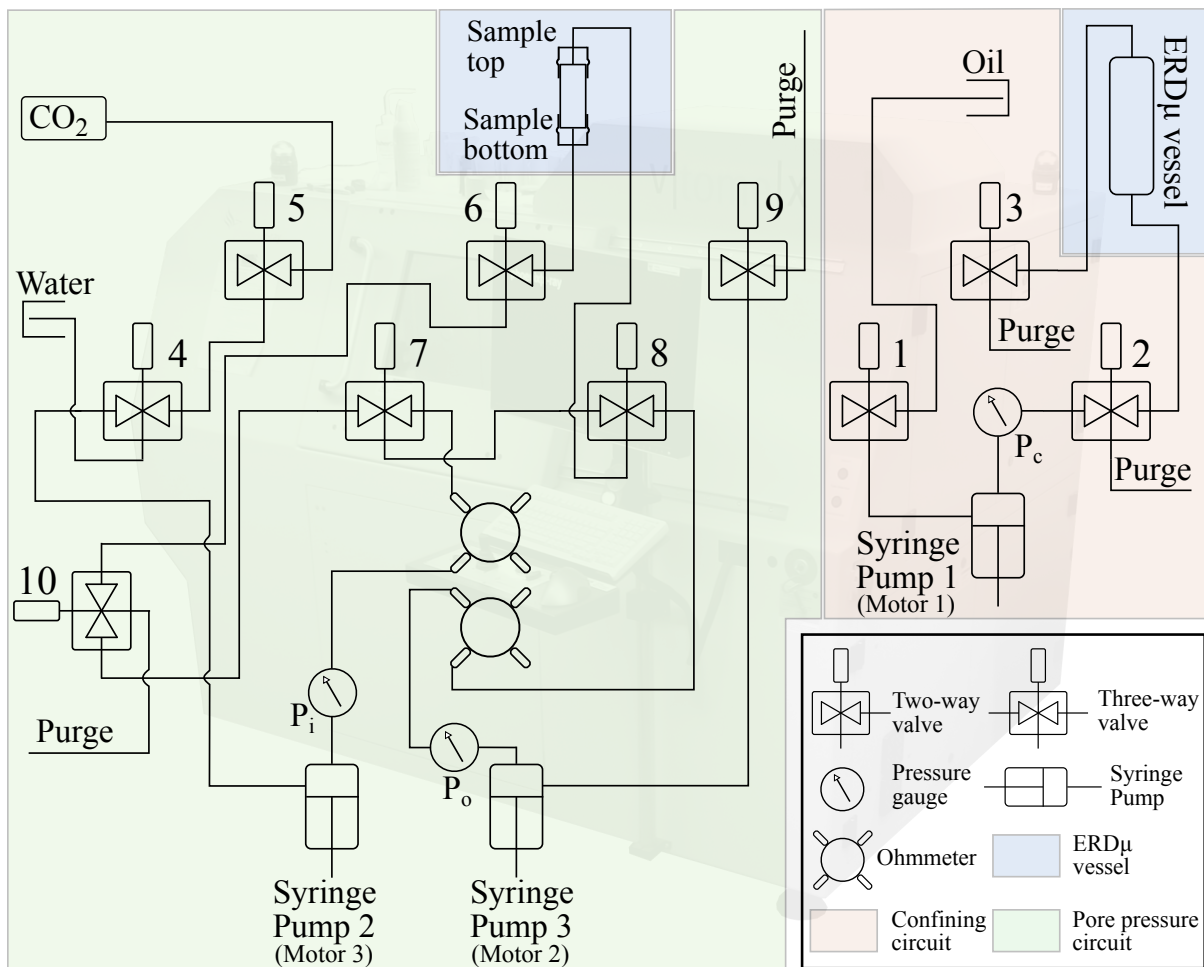

Figure C.2: ERDμ confining and pore (i.e., saturation) fluid circuit system